ISSN 0915 6364

NIFS-DATA--41

NATIONAL INSTITUTE FOR FUSION SCIENCE

Atomic Nuclear Charge Scaling for Dielectronic Recombination to Be-like Ions

K. Moribayashi and T. Kato

(Received - Mar. 26, 1997)

NIFS-DATA-41 Apr. 1997

NAGOYA, JAPAN

Atomic Nuclear Charge Scaling for Dielectronic Recombination to Be-like Ions

Kengo Moribayashi and Takako Kato

National Institute for Fusion Science, Chikusaku Nagoya 464, Japan

Abstract

The atomic nuclear charge (Z) scaling for the dielectronic recombination (DR) rate coefficient (α) to the O^{4+}, Ne^{6+}, Mg^{8+}, P^{11+}, Ar^{14+}, Ca^{16+}, V^{19+}, Fe^{22+} ions as well as the auger energy (ΔE), the radiative transition probability (Ar), and the autoionization rate (Aa) for the Be-like ions is studied. For the calculation of the energy levels, Ar, and Aa values, Cowan's code is employed. Not only the doubly excited $1s^2 2pnl$ states but also the $1s^2 3lnl'(l = s, p, d)$ are considered as the autoionization ones. In the DR processes, at low Z, only the $1s^2 2pnl \rightarrow 1s^2 2snl$ and $1s^2 3pnl \rightarrow 1s^2 2snl$ processes give a significant contribution. While, at high Z, the $1s^2 3s(\text{or } d)nl \rightarrow 1s^2 2pnl$ and $1s^2 2pnl \rightarrow 1s^2 2pn'l'$ processes also become important. The dielectronic recombination rate coefficient to the final excited $1s^2 2snl$ show weak Z-dependence, on the other hand, those to the final excited $1s^2 2pnl$ states have a strong Z-dependence.

Keywords

dielectronic recombination rate coefficient, Beryllium-like ion, energy level, radiative transition probability, autoionization rate, atomic nuclear charge scaling, autoionzation state, Cowan's code

1. Introduction

The dielectronic recombination (DR) process, which is defined by the following process,

$$A^{Z+1}(i_0) + e^- \rightarrow A^{Z**}(i) \rightarrow A^{Z*}(f) + h\nu, \tag{1}$$

is important in high temperature plasma such as tokamak and solar corona[1, 2]. Here A^{Z**} expresses the autoionization state of the A^Z and i_0, i, and f are the initial state, the autoionization (doubly excited) state, and the final excited state, respectively. In this paper, the A^Z ion is treated as Be-like ion. To obtain the population of the excited states of ions in plasma with use of collisional radiative model[3], the DR rate coefficient given by

$$\alpha(i_0, f) = \frac{C(T_e)}{g_0} \sum_i \frac{g(i) Aa(i, i_0) Ar(i \rightarrow f)}{\sum\limits_{all\ i'_0} Aa(i, i'_0) + \sum\limits_{all\ f'} Ar(i \rightarrow f')} \exp(-\frac{\Delta E_i}{kT_e}), \tag{2}$$

is requested[4, 5]. Here Ar,Aa, T_e, g_0 and ΔE_i represent radiative transition probability, autoionization rate, electron temperature, statistical weight of the initial state (i_0), and auger energy, that is, the energy difference between the autoionization state (i) and the initial state (i_0), respectively.

In our previous paper[6, 7], we studied the DR processes to Be-like C^{2+} and Fe^{22+} ions. Then we considered the $1s^22pnl$ states and $1s^23lnl'$ states as the autoionization states. We found that in the C^{2+} ion, the α value for the DR process through the $1s^22pnl$ state is always much larger than that through the $1s^23lnl'$ all over the T_e values. On the other hand, in the case of Fe^{22+} ion, the $1s^22pnl$ and the $1s^23lnl'$ dominated at low and at high T_e, respectively. From atomic nuclear charge (Z) scaling of ΔE, Ar, Aa, and α, we can understand the reason why the different mechanism between two ions occurs. Further, this paper showed that there are five important processes for the DR processes to Be-like ions, and in each process, a characteristic mechanism exists. Here the following five processes, $1s^22pnl \rightarrow 1s^22pn'l'$ $1s^22pnl \rightarrow 1s^22snl$, $1s^23snl \rightarrow 1s^22pnl$, $1s^23pnl \rightarrow 1s^22snl$, and $1s^23dnl \rightarrow 1s^22pnl$ are considered. Since the Z-scaling for the DR processes to the Be-like ions is very complicated, we should study the mechanism for Z-scaling in more detailed.

For the DR processes to the Be-like ions, a lot of papers exist[6-17]. However, as far as we know, there are no paper in which the mechanism for Z-scaling is discussed fully, for example, the estimation of the contribution of each autoionization states to the DR process or contribution of each process mentioned before. Therefore, in this paper, we estimate the important autoionization state and the important final bound states in the DR process to some Be-like ions. Furthermore, the mechanism of Z-scaling for each process is also studied. When we study the DR processes to the ions with many electrons, approximation methods are requested because the exact calculation is very difficult. Then the knowledge of the mechanism for the DR processes will be very useful for making a model.

The autoionization states (i in Eq.(1)) considered in this paper are the $1s^2 2pnl$, $1s^2 3snl$, $1s^2 3pnl$, and $1s^2 3dnl$ and the final bound states (f in Eq.(1)) are the $1s^2 2snl$ and $1s^2 2pnl$. The five processes mentioned before are considered as an important process. In order to understand the Z-scaling, we treat Be-like O^{4+}, Ne^{6+}, Mg^{8+}, P^{11+}, Ar^{14+}, Ca^{16+}, and V^{19+} ions in addition to Be-like C^{2+} and Fe^{22+} ions as A^Z ion in Eq.(1). We study the Z-scaling for the ΔE, Ar, and Aa values as well as the α values. The calculations for the ΔE, Ar, and Aa are executed with use of Cowan's code[18, 19] in which the configuration interaction (CI) method is used. We compare our results with those given by Romanik[13] and Chen[15]. The aims of this paper are (i) to understand the mechanism for Z-scaling of the α values and (ii) to estimate the α values to Be-like ions by Z-scaling.

2. Theory for atomic nuclear charge scaling for radiative transition probability (Ar) and autoionization rate (Aa)

In this section, we describe Z-scaling for Ar and Aa values following the discussion in Ref.[9] in the ideal case where the electron correlation and relativistic effects are removed.

For the real case with these effects, we will discuss in Sec.3-5. The Z value is the nuclear charge minus the number of electrons bound in inner shells. For example, in the case of $1s^2 2pnl$ state in Fe^{22+} ion, it is 24 for the $2p$ electron and 23 for the nl electron, respectively.

The radiative transition probability Ar for emission from state A to state B, is given by

$$Ar = N\sigma^3 S. \tag{3}$$

Here N and σ are the normalization constant and the energy difference between the states A and B, respectively and S is the line-strength given by

$$S = | < \psi_B | \vec{r} | \psi_A > |^2, \tag{4}$$

where $\psi_{A(B)}$ is the wave function of the state A(B). Firstly S decreases according to Z^{-2} because the atomic radius $< r > \propto Z^{-1}$. On the other hand, in order to estimate the Z-scaling for σ, the Z-expansion method[20] is useful. With the use of this method, the energy for large Z can be written as

$$E \cong Z^2(E_0 + E_1/Z), \tag{5}$$

because the second and higher order terms can be neglected for large Z. Here $E_{0(1)}$ is the 0(1)-th expansion coefficient. In the case when the principal quantum numbers n are the same between the states A and B, the E_0 values are the same for state A and state B. Therefore σ can be approximated by

$$\begin{aligned} \sigma &\propto Z^2 \qquad \text{for} \quad \Delta n \neq 0 \\ \sigma &\propto Z \qquad \text{for} \quad \Delta n = 0, \end{aligned} \tag{6}$$

where Δn is the difference between principal quantum number of the transition electron in the state A and that in the state B. From Eqs.(3) and (6), Ar can be given by

$$\begin{aligned} Ar &\propto Z^4 \qquad \text{for} \quad \Delta n \neq 0 \\ Ar &\propto Z \qquad \text{for} \quad \Delta n = 0. \end{aligned} \tag{7}$$

The autoionization rate Aa is given by

$$Aa \sim \frac{2\pi}{\hbar} | < \Psi_{j_1} \Psi_{j_2} | \frac{1}{r_{12}} | \Psi_{j_3} \Psi_i > |^2, \tag{8}$$

where the states j and i express discrete and continuum states, respectively and r_{12} is the distance between two electrons. In Cowan's code[18, 19], a free electron state is assumed to be separable from the bound state. Then the wave function of a free electron, which is of the same form as that for a bound electron, is given by

$$\Psi_{i,\epsilon l m_l m_s}(\vec{r}) = \frac{1}{r} P_{\epsilon l}(r) Y_{l m_l}(\theta, \phi) \Sigma_{m_s}(s_z). \tag{9}$$

with

$$P_{\epsilon l} \sim (\frac{2}{\pi p_c})^{1/2} \frac{1}{r} \sin(p_c r + \delta(r)). \tag{10}$$

Here p_c equals to $\epsilon^{1/2}$ where ϵ is the free electron energy and $\Sigma_{m_s}(s_z)$ is the wave function for the spin of the electron. That is, p_c increases according to

$$\begin{aligned} p_c &\propto Z \qquad \text{for} \quad \Delta n_c \neq 0 \\ p_c &\propto Z^{1/2} \qquad \text{for} \quad \Delta n_c = 0. \end{aligned} \tag{11}$$

Here Δn_c expresses the difference of the principal quantum number between the states j_1 and j_3. Namely,

$$\begin{aligned} \Psi_i &\propto Z^{1/2} \qquad \text{for} \quad \Delta n_c \neq 0 \\ \Psi_i &\propto Z^{3/4} \qquad \text{for} \quad \Delta n_c = 0 \end{aligned} \tag{12}$$

because $r^{-1} \propto Z$. Then Ψ_j and $< r_{12}^{-1} >$ increase according to $Z^{3/2}$ and Z, respectively and $dr_1^3 dr_2^3$ decreases according to Z^{-6}. Therefore Aa becomes

$$\begin{aligned} Aa &\propto Z^0 \qquad \text{for} \quad \Delta n_c \neq 0 \\ Aa &\propto Z^{1/2} \qquad \text{for} \quad \Delta n_c = 0. \end{aligned} \tag{13}$$

After all it is found that the Z-dependence for Aa is weaker than that for Ar.

3. Energy level for autoionization states

The ΔE value is very important for the DR process, because it decides the temperature where the α value takes the maximum as will be mentioned in Sec.6. Table I lists ionization energy (IE), first autoionization state (FAS), and the energy of the FAS from the ionization limit ΔE values for the FAS as a function of Z. Roughly speaking, the IE values increase according to $(Z-3)^2$ because threshold corresponds to $1s^22snl(n \rightarrow \infty)$ state, that is, the energy difference between the ground state and the threshold follows the $\Delta n \neq 0$ case in Sec.2. The α value at very low T_e around 1eV depends on the auger energy ΔE given in Table I as will discuss in Sec.6. Only when the auger energy value is smaller, the dielectronic recombination plays an important role at low T_e.

The energy for the $1s^22pnl$ measured from the $1s^22p(J=1/2)$ state of Li-like ion can be written by

$$E(1s^22pnl) - E(1s^22p) = -\hbar(Z-3)^2/2n^2. \tag{14}$$

Figs.1-1(a)-(d) show the $(E(1s^22pnl) - E(1s^22p))/(Z-3)^2$ $(l = s, p, d, f)$ values as a function of $Z-3$. The threshold energy divided by $(Z-3)^2$ is also plotted by a thick solid line. The states with energy values below and above the threshold represent the bound and auger states, respectively. At large Z value, energy split which comes from the spin-orbit interaction between $J=1/2$ and $3/2$ of the $1s^22p$ state of Li-like ion occurs (see Table II). The $1s^22pnl$ states reach either $1s^22p\ P_{J=1/2}$ or $1s^22p\ P_{J=3/2}$ at large n. As a result, energy split in the $1s^22pnl$ states becomes larger at large Z[6, 7]. Here the J value expresses the total angular momentum. Therefore, the minimum and maximum values of the energy levels for each state are plotted in these figures. Mancini and Safronova[21] also plotted the similar figures to Figs.1-1 for Z=5-18. However, the energy spilt effect were not seen in their figures because the $^3P_0$, $^3S_0$, $^3P_2$ states were selected. The energy values increase slightly for larger l values. This agrees with the result of Mancini and Safronova[21]. As a result, for example, in the Be-like C ion, the $1s^22p4p$ and the $1s^22p4d$ states are the bound and autoionization ones, respectively[17], though both states have the same n value. The $E/(Z-3)^2$ values keep almost the same for different Z as shown in Figs.1. On the other hand, the energy for threshold increases as Z becomes larger. This is due to the fact that the threshold energy $(1s^22s)$ and the energy of the $1s^22pnl$ states

measured from the $1s^22p(J=1/2)$ state increase according to Z and Z^2, respectively[6, 7]. Therefore, the $1s^22pnl$ states often become the bound states at large Z. For example, at $n=7$ and 9, the state becomes bound one above $Z=10$ and 15, respectively. At $n=11$, both bound and autoionization states exist above $Z=20$. This comes from the fact that the energy split increases according to Z^3[22].

Figs.1-2(a)-(g) show the $(E(1s^23lnl')-E(1s^23l))/(Z-3)^2*n^2$ values as a function of $Z-3$. The energy split effects are smaller than those for $1s^22pnl$ states. This is due to the fact that the energy split of the $1s^23l$ state is much smaller than that of the $1s^22p$ as is listed in Table II. For the $1s^23d$ state, the energy split occurs between $J=3/2$ and $J=5/2$. On the other hand, for the $1s^23s$ state, there is no energy split because the J value is always 1/2. It should be noted that the relativistic effect becomes smaller as the principal quantum number increases. In these figures, energy split by different J is ignored because the energy values for different l are much larger. The energy of the threshold $1s^22s$ is much smaller than those for these states Therefore, the energy for the threshold is not plotted. The $E/(Z-3)^2*n^2$ values show almost constant for different Z and n values though the values at small Z and small n are not constant within 20% for $Z>10$, where the strong electron correlation exists. The energies increase very slightly as a function of either l or l' value similar to the case of the $1s^22pnl$ states.

4. Radiative transition probability (Ar)

Fig.2-1 shows the $Ar/(Z-2)$ values for the $1s^22p11l \rightarrow 1s^22s11l$ $(l=s,p,d,f,g)$ transition as a function of $Z-2$. In Fig.2-1, the Ar is given by

$$Ar=\frac{\sum_{S'L'J'SLJ}\sum g(i)Ar(1s^22pnl\ ^{2S+1}L_J\rightarrow 1s^22l''n'l'\ ^{2S'+1}L'_{J'})}{\sum_{SLJ}g(i)}, \qquad (15)$$

where $g(i)$ is the statistical weight of the autoionization state. The Ar values are independent of l. Furthermore, the $Ar/(Z-2)$ values show almost constant for $Z<18$. However, for $Z\geq 18$, as Z increases, the values become larger. This is due to the energy

split by the spin-orbit interaction, which increases according to Z^3[22]. In Figs.2-1-2, the fine structures $^{2S+1}L_J$ are also shown for the transitions with the large Ar values. The energy values which are almost the same for different Z, such like the energy for $^3P_0 - ^3S_1$ transition in Fig.2-1-2(a), are also seen because the states without effect of spin-orbit interaction exist (see Figs.1-1).

Figs.2-2 show the same as Figs.2-1 for the $1s^2 2pnl \rightarrow 1s^2 2pn'l'$ transitions as a function of $Z-3$. Here the $Ar/(Z-3)^4$ values are shown in place of $Ar/(Z-2)$. Two types of transitions exist, that is, $l' = l-1$ and $l' = l+1$. For the $l' = l-1$ transition, the $Ar/(Z-3)^4$ values show almost the constant for different Z as is given by Eq.(7) in Sec.2. Further, they decrease as the n' value becomes larger. On the other hand, for the $l' = l+1$ transition, the different trend appears except for the $1s^2 2p11s \rightarrow 1s^2 2pn'p$ transition. Namely the values are much smaller than those for the $l' = l-1$ transition and almost the same among $n' = 3-6$. They also show almost the constant except for large Z and small Z. For these transitions, the effect of energy split is smaller than that for the $1s^2 2p11l \rightarrow 1s^2 2s11l$ transition because n and n' values of the transition electron are larger. Figs.2-2-2 show the same as Fig.2-2 for the fine structure levels.

Figs.2-3(a)-(h) show the same as Fig.2-2 for the transition form the $1s^2 3l5l'$ and $1s^2 3l7l'$ ($l = s, p, d$, $l' = s, p, d, f, g$) states. The $Ar/(Z-2)^4$ values show almost the constant for different Z roughly as is given by Eq.(7) in Sec.2. Further, from these figures, we found that the effect of the spin-orbit interaction appears only a little. Figs.2-3-2 to Figs.2-3-4 show the same as Fig.2-3 for the fine structure levels of the $1s^2 3snl$, $1s^2 3pnl$, and $1s^2 3dnl$ states, respectively.

The largest Ar values in Figs.2-1-2, Figs.2-2-2, Figs.2-3-2 to Figs.2-3-4 for fine structure transitions are almost the same as the averaged Ar value given by Eq.(15) for the same transitions.

5. Autoionization rate (Aa)

Figs.3-1 (a) and (b) show the average Aa values given by

$$Aa = \frac{\sum_{SLJ} g(i) Aa(1s^2 2pnl\ ^S L_J, i_0)}{\sum_{SLJ} gi} \tag{16}$$

from the $1s^2 2p9l$ and $1s^2 2p11l$ states, respectively. Here the i_0 state represents the final state of the $1s^2 2s\ +\epsilon l'$, where $\epsilon l'$ represents the free electron. In Fig.3-1(a), only the Aa values for $Z \leq 15$ are plotted because the $1s^2 2p9l$ states for $Z \geq 18$ are not autoionization states but bound ones as mentioned in Sec.3. The Aa values for $l = s$ are the largest and seem to show almost the constant for different Z. This result is different from the scaling $Z \propto Z^{1/2}$ given in Eq.(13) in Sec.2. Figs.3-1-2 show the same as Fig.3-1 for the fine structure levels.

Figs.3-2(a)-(f) show the same as Figs.3-1 from the $1s^2 3l5l'$ and $1s^2 3l7l'$ states. For $l = s$, the Aa values for $l' = f$ and g are much smaller than those for $l' = s, p, d$. On the other hand, for $l = p, d$, the Aa values for $l' = f$ and g are comparable with those for $l' = s, p, d$. This is considered due to the electron correlation. Namely, for example, the overlap of wavefunctions between the $3s$ and $5g$ electrons, which corresponds to the strength of electron correlation, is smaller than that between the $3s$ and $5s$ ones and than that between the $3p$ (or d) and $5g$ ones. Then, though the oscillation is seen in these figures at low Z, the Aa values seem to remain almost the constant at large Z as is also given by Eq.(13) in Sec.2. This oscillation also may come from the strong electron correlation. Figs.3-2-2 to Figs.3-2-4 show the same as Figs.3-2 for the fine structure levels of the $1s^2 3snl$, $1s^2 3pnl$, and $1s^2 3dnl$ states, respectively.

Figs.3-3(a)-(f) show the same as Figs.3-2 for the case where the i_0 state represents the states of the $1s^2 2p\ +\epsilon l''$. The oscillation becomes weaker than that in Figs.3-2 except for that from the $1s^2 3s7l'$ state. The Aa values from the $1s^2 3pnl'$ and $1s^2 3dnl'$ to the $1s^2 2p\ +\epsilon l''$ are much larger than those to $1s^2 2s\ +\epsilon l''$, in particular, at small l'. On the other hand, both are comparable in the case of the transition from the $1s^2 3snl'$ state. This comes from the fact that the overlap of wavefunction of the $3p$ (or $3d$) electron with

that of the $2p$ electron is much larger than that of the $2s$ one, while in the case of $3s$ electron, both are comparable. Figs.3-3-2 to Figs.3-3-4 show the same as Figs.3-3 for the fine structure levels of the $1s^2 3snl$, $1s^2 3pnl$, and $1s^2 3dnl$ states, respectively.

In the transitions for fine structure levels, the Aa values from the singlet states give the larger ones than those from the triplet states. The largest Aa value in each figure is larger than the averaged value given by Eq.(16) for the same transitions. As is seen in Fig.3-2-2(d) and Fig.3-2-3(d), the Aa values become much smaller at one Z values. This comes from the fact that rough values for ΔE are used in Cowan's code[18, 19], though Aa value is a function of ΔE as well.

6. Dielectronic recombination rate coefficient (α)

In this section, Z-scaling for the dielectronic recombination to the Be-like ions is studied. The DR process studied here is as follow.

$$\mathrm{A}^{Z+1}(1s^2 2s) + e^- \rightarrow \mathrm{A}^{Z**}(i) \rightarrow \mathrm{A}^{Z*}(f) + h\nu, \tag{17}$$

where A^Z is treated as the Be-like ion. The autoionization states (i) considered here are the $1s^2 2pnl$, $1s^2 3snl$, $1s^2 3pnl$, and $1s^2 3dnl$ states. Further, the final bound states (f) are the $1s^2 2snl$, and $1s^2 2pnl$ states. The important processes for some Be-like ions and the mechanism of Z-scaling for some processes are studied.

Table III lists the total α values given by Eq.(2) for the DR processes to Be-like C^{2+}, O^{4+}, Ne^{6+}, Mg^{8+}, P^{11+}, Ar^{14+}, Ca^{16+}, V^{19+}, Fe^{22+} ions as a function of T_e. The α values given by Romanik[13] and those by Chen[15] for the C^{2+}, O^{4+}, Ne^{6+}, Ar^{14+}, and Fe^{22+} ions are also listed. Our result agrees with Chen's one within 20%, while the error between ours and Romanik's becomes more than 50% at low T_e around 10eV. Romanik used the Coulomb-Born method for the autoionization rate and the experimental oscillator strength for the radiative transition probability, respectively. On the other hand, Chen employed multi-configuration Dirac Fock (MCDF) model[23, 24] and we adapt configuration interaction (CI) method by Cowan's code[18, 19] for both Aa and Ar. The

method employed by Chen and that by us are better than that by Romanik obviously.

Figs.4-1(a)-(i) show the comparison same as Table III. The α values for the five processes considered in this paper, that is, $1s^22pnl \rightarrow 1s^22pn'l'$, $1s^22pnl \rightarrow 1s^22snl$, $1s^23snl \rightarrow 1s^22pnl$, $1s^23pnl \rightarrow 1s^22snl$, and $1s^23dnl \rightarrow 1s^22pnl$ are also plotted. In the C^{2+} ion, only the $1s^22pnl \rightarrow 1s^22snl$ process dominates except for very low T_e around 1eV where $1s^22pnl \rightarrow 1s^22pn'l'$ process gives the most significant contribution. Since the α values through the $1s^23snl$ and $1s^23dnl$ states are much smaller than those through $1s^22pnl$ and $1s^23pnl$, those through the $1s^23snl$ and $1s^23dnl$ states do not appear in Fig.4-1(a) for C^{2+}. In the O^{4+} ion, the contribution through $1s^23pnl$ becomes comparable with that through the $1s^22pnl$ at high T_e around 1000eV. In the Ne^{6+}, Mg^{8+}, P^{11+}, and Ar^{14+} ions, the former is much larger than the latter at high T_e and the DR processes through $1s^23dnl$ and $1s^23snl$ states can not be ignored. In the Ca^{16+}, V^{19+} and Fe^{22+} ions, the α values for the DR processes through $1s^23dnl$ and $1s^23snl$ states become larger than that through the $1s^23pnl$. Furthermore, the $1s^22pnl \rightarrow 1s^22pn'l'$ process plays more important role of the DR process than the $1s^22pnl \rightarrow 1s^22snl$ even at high T_e. The fact that the contribution from the $1s^23lnl'$ becomes larger as Z increases is due to the Z-scaling for the ΔE values because the ΔE_i values determine the place of the peak in the α as a function of T_e. Namely roughly speaking, the ΔE_i values of the $1s^23lnl'$ and those of the $1s^22pnl'$ states increase according to Z^2 and Z, respectively, as mentioned in Refs.[6, 7].

Figs.4-2(a)-(j) show the α value as a function of T_e for the five important processes mentioned before. At low Z, the maximum α value for the processes to the final excited $1s^22snl$ states, that is, the $1s^22pnl \rightarrow 1s^22snl$ and $1s^23pnl \rightarrow 1s^22snl$ processes, shows almost the same values for different Z (see Figs.4-2(a) and (g)). Namely, these processes give weak Z-dependence. While in the transitions to the $1s^22pnl$ state, that is, $1s^22pnl \rightarrow 1s^22pn'l'$, $1s^23snl \rightarrow 1s^22pnl$, and $1s^23dnl \rightarrow 1s^22pnl$ processes, the maximum value becomes larger as Z increases(see Figs.4-2(c), (e), (i)). This comes from the fact that the number of the final $1s^22pnl$ bound states increases for the increase of Z values. The $1s^22pnl$ states of the Be-like ions are either in the bound or in the autoionization states as mentioned in Sec.3. As Z increases, the maximum n value for the bound $1s^22pnl$

states becomes larger. At large Z, the maximum values for α shows almost the same for different Z for all processes. From Figs.4-2, we found that the places of the position in the processes through $1s^23lnl'$ shift faster than those through $1s^22pnl$ as Z increases. This comes from the Z-scaling for ΔE_i, as mentioned before.

At very low T_e around 1eV where only the $1s^22pnl \rightarrow 1s^22pn'l'$ process dominates, the α values are determined by the first auger energy as mentioned in Sec.3. For the C^{2+} ion, the peak place of the α value is the smallest because the auger energy is the lowest (see Table I). Further, the α values for Ar^{14+} and Ca^{16+} ions are much larger than those for V^{19+} and Fe^{22+} ions, since the ΔE_i values for the former ions are much smaller than those for the latter (also see Table I).

7. Conclusion

We study the atomic nuclear charge (Z) scaling for the dielectronic recombination process to the Be-like ions. We calculate the auger energy ΔE, the radiative transition probability (Ar), and autoionization rate (Aa) as well as the dielectronic recombination rate coefficient (α) for different Z from Z=6 to Z=26. For the energy levels, Ar, and Aa values, we employ Cowan's code in order to consider the electron correlation and relativistic effects.

We found that the Z-scaling is affected by the electron-electron correlation for small Z and the relativistic effect for large Z, respectively. Further, the different mechanism between the $\Delta n = 0$ and the $\Delta n \neq 0$ transitions is also seen. Here Δn is the different quantum number between the autoionization state and the final bound state.

At low Z, the process to the $1s^22snl$ state through the autoionization $1s^22pnl$ state dominates for the α values. On the other hand, at high Z, those to the $1s^22pnl$ states become comparable with those to the $1s^22snl$. Further, the processes through the autoionization $1s^22pnl$ states and those through the $1s^23lnl'$ states dominate at low and high temperature, respectively. The maximum α values to the final excited $1s^22snl$ states are almost the same for different Z. On the other hand, those to the final excited $1s^22pnl$

become larger as Z increases.

Acknowledgment

We wish to thank Drs.R.More, J. Duban, and M.Cornille for their useful discussions.

References

[1] A.Burgess, Astrophys. J., **139**, 776(1964), **141**, 1588(1965).

[2] M.J. Seaton and P.J. Storey, "Di-electronic recombination" in "atomic processes and applications" edited by P.G. Burke and B.L. Moisewitsch, North-Holland 1976 p.133.

[3] T. Fujimoto, J. Quant. Spectrosc. Radiat. Transfer, **21**, 439(1979).

[4] I.Murakami, T.Kato, and J.Dubau, NIFS-DATA-35(1996).

[5] I.Murakami, T.Kato, and J.Dubau, Phsica Scripta, **54**, 463(1996).

[6] K. Moribayashi, and T. Kato, NIFS-DATA-36(1996).

[7] K. Moribayashi, and T. Kato, Physica Scripta, **55**, 286(1997).

[8] D.J. McLaughlin and Y. Hahn, Phys.Rev.A, **29**, 712(1984).

[9] Y.Hahn, Adv.Atom and Mol. Phys., **21**, 123(1985).

[10] L.J. Roszman, Phys.Rev.A, **35**, 2122(1987).

[11] D.C. Griffin, M.S. Pindzola, C. Bottcher, Phys. Rev. A, **31**, 568(1985).

[12] D.C. Griffin and M.S. Pindzola, Phys.Rev.A, **35**, 2821(1987).

[13] C.J. Romanik, Astrophys. J., **330**, 1022(1988).

[14] N.R. Badnell, J.Phys. B,**23**, L565(1990).

[15] M.H. Chen, Phys.Rev.A, **44**, 4215(1991).

[16] H. Teng, B.Sheng, W. Zhang, and Z .Xu, Physca Scripta, **49**, 463(1994).

[17] U.I. Safronova, T. Kato, and M. Ohira, NIFS-DATA-37(1996).

[18] R.D. Cowan, J.Opt.Soc.Am., **58**, 808(1968).

[19] R.D. Cowan, "The theory of atomic structure and spectra", University of California Press, 1981.

[20] L.A. Vainshtein and U.I. Safronova, Physica Scripta, **31**, 519(1985).

[21] R.C. Mancini and U.I. Safronova, J. Phys.B, **28**, 3469(1995).

[22] U.I. Safronova, M.S. Safronova, R. Bruch, and L.A. Vainstein, Physica Scripta, **51**, 471(1995).

[23] I.P. Grant, B.J. McKenzie, P.H. Norrington, D.F. Mayers, and N.C. Pyper, Comput. Phys. Commun., **21**, 207(1980).

[24] M.H. Chen, Phys.Rev.A, **31**, 1449(1985).

Figure Captions

Fig.1-1 $(E(1s^2 2pnl) - E(1s^2 2p))/(Z-3)^2$ as a function of $Z-3$: (a)$l=s$, (b)$l=p$, (c)$l=d$, and (d)$l=f$. The $E(1s^2 2pnl)$ is given by Eq.(14) and the configurations indicated mean n value.

Fig.1-2 The $(E(1s^2 3lnl) - E(1s^2 3l))/(Z-3)^2 \times n^2$ values for the $1s^2 3lnl'$ as a function of $Z-3$: (a)$l=s$, $l'=s$, (b)$l=s$, $l'=p$, (c)$l=s$, $l'=d$, (d)$l=p$, $l'=s$, (e)$l=p$, $l'=p$, (f)$l=p$, $l'=d$, (g)$l=d$, $l'=s$, (h)$l=p$, $l'=p$, and (i)$l=p$, $l'=d$. The configurations indicated mean the n value.

Fig.2-1 $Ar/(Z-2)$ values for the $1s^2 2p11l \rightarrow 1s^2 2s11l$ processes as a function of $Z-2$. The averaged Ar values are given by Eq.(15). The configurations indicated mean the l value.

Fig.2-1-2 The same as Fig.2-1 from each fine structure levels: The configurations indicated mean the fine structures ($^{2S+1}L_J$) of autoionzation states ($1s^2 2p11l$) and those of final bound states ($1s^2 2s11l$).

Fig.2-2 The averaged $Ar/(Z-3)^4$ values for $1s^2 2p11l \rightarrow 1s^2 2pn'l'$ processes as a function of $Z-3$: (a)$l=s$, $l'=p$, (b)$l=p$, $l'=s$, (c)$l=p$, $l'=d$, (d)$l=d$, $l'=p$, (e)$l=d$, $l'=f$, (f)$l=f$, $l'=d$, (g)$l=f$, $l'=g$. The configurations indicated mean the n' value.

Fig.2-2-2 The same as Fig.2-2 from each fine structure levels: The configurations indicated mean the fine structures ($^{2S+1}L_J$) of autoionzation states ($1s^2 2p11l$) and those of final bound states ($1s^2 2pn'l'$).

Fig.2-3 $Ar/(Z-2)^4$ values from the $1s^2 3l'nl$ states as a function of $Z-2$: (a)$l'=s$, $n=5$, (b)$l'=s$, $n=7$, (c)$l'=p$, $n=5$, (d)$l'=p$, $n=7$, (e)$l'=d$, $n=5$, and (f)$l'=d$, $n=7$. The configurations indicated mean the l value.

Fig.2-3-2 to Fig.2-3-4 The same as Figs.2-3 from each fine structure levels: The configurations indicated mean the fine structures ($^{2S+1}L_J$) of autoionzation states ($1s^2 3lnl'$) and those of final bound states ($1s^2 2l''nl'$).

Fig.3-1 The averaged Aa given in Eq.(16) from the $1s^2 2pnl$ as a function of Z: (a)$n=9$ and (b)$n=11$. The configurations indicated mean the l value.

Fig.3-1-2 The same as Fig.3-1 from each fine structure: The configurations indicated mean the fine structures ($^{2S+1}L_J$) of autoionzation states ($1s^2 2p11l$).

Fig.3-2 The same as Figs.3-1 from the $1s^2 3l'nl$: (a)$n=5$, $l'=s$, (b)$n=7$, $l'=s$, (c)$n=5$, $l'=p$, (d)$n=7$, $l'=p$, (e)$n=5$, $l'=d$, and (f)$n=7$, $l'=d$. The configurations indicated mean the l value.

Fig.3-2-2 to Fig.3-2-4 The same as Figs.3-2 from each fine structure: The configurations indicated mean the fine structures ($^{2S+1}L_J$) of autoionzation states ($1s^2 3lnl'$).

Fig.3-3 The same as Figs.3-2 to the continuum states of $1s^2 2p + \epsilon l'$.

Fig.3-3-2 to Fig.3-3-4 The same as Figs.3-2 from each fine structure: The configurations indicated mean the fine structures ($^{2S+1}L_J$) of autoionzation states ($1s^2 3lnl'$).

Fig.4-1 Total dielectronic recombination rate coefficients (α) given by Eq.(2) for the DR processes to Be-like ions as a function of T_e: (a)C^{2+}, (b)O^{4+}, (c)Ne^{6+}, (d)Mg^{8+}, (e)P^{11+}, (f)Ar^{14+}, (g)Ca^{16+}, (h)V^{19+}, and (i)Fe^{22+}. The configurations indicated mean the processes.

Fig.4-2 The α values as Figs.4-1 for the different five processes: (a)(b)$1s^2 2pnl \rightarrow 1s^2 2snl$; (c)(d)$1s^2 2pnl \rightarrow 1s^2 2pn'l'$; (e)(f)$1s^2 3snl \rightarrow 1s^2 2pnl$; (g)(h)$1s^2 3pnl \rightarrow 1s^2 2snl$; and (i)(j)$1s^2 3dnl \rightarrow 1s^2 2pnl$. The configurations indicated mean the ions.

Table I Ionization energy (IE) (in unit of 1000cm −1), first autoionization state (FAS), and auger energy (AE) for the FAS (in unit of 1000cm −1) for Be-like ions.

Be-like ion	IE($1000cm^{-1}$)	FAS	AE($1000cm^{-1}$)
C^{2+}	386.	$1s^22p4d$	2.
O^{4+}	919.	$1s^22p6s$	16.
Ne^{6+}	1672.	$1s^22p7s$	14.
Mg^{8+}	2645.	$1s^22p8s$	18.
P^{11+}	4521.	$1s^22p9s$	11.
Ar^{16+}	6900.	$1s\ 22p10s$	9.
Ca^{18+}	8768.	$1s^22p10s$	10.
V^{21+}	11990.	$1s^22p11s$	55.
Fe^{23+}	15730,	$1s^22p11s$	43.

Table II Energy ($1000cm^{-1}$) for $1s^22p$, $1s^23s$, $1s^23p$ and $1s^23d$ states of Li-like ions.

Li-like ion	$1s^22p$		$1s^23s$	$1s^23p$		$1s^23d$	
	J=1/2	J=3/2	J=1/2	J=1/2	J=3/2	J=3/2	J=5/2
C^{3+}	64.	64.	305.	322.	322.	327.	327.
O^{5+}	96.	96.	643.	669.	669.	677.	677.
Ne^{7+}	128.	130.	1103.	1138.	1139.	1150.	1150.
Mg^{10+}	160.	164.	1686.	1730.	1732.	1746.	1747.
P^{13+}	208.	219.	2793.	2851.	2854.	2875.	2876.
Ar^{15+}	258.	283.	4181.	4256.	4260.	4286.	4288.
Ca^{18+}	291.	331.	5263.	5344.	5356.	5385.	5389.
V^{21+}	342.	416.	7125.	7220.	7242.	7277.	7284.
Fe^{24+}	394.	520.	9277.	9386.	9423.	9465.	9477

Table III Comparison among our α values (in unit of 10^{-12}cm^3/s) to the Be-like ions and those by Chen[15] and Romanik[13] as a function of T_e(eV).

T_e(eV)		C^{2+}			O^{4+}	
T_e(eV)	present	Chen	Romanik	present	Chen	Romanik
1.0	18.9		20.2	7.75		7.73
2.0	22.4		28.5	16.2		16.9
3.0	31.8		44.7	25.6		31.0
4.0	36.3		52.7	33.7		44.0
5.0	37.1		54.6	38.6		52.3
6.0	36.1		53.3	40.9		56.5
7.0	34.3		50.7	41.5		57.9
8.0	32.2		47.5	41.0		57.6
9.0	30.1		44.2	39.8		56.2
10.0	28.1	22.8	41.1	38.4	37.7	54.3
20.0	15.4		21.3	24.7		34.4
30.0	10.0	8.42	13.2	17.7	16.3	23.5
40.0	7.19		9.16	13.7		17.5
50.0	5.47	4.64	6.81	11.1	9.53	13.7
60.0	4.35		5.32	9.31		11.1
70.0	3.56		4.30	7.93		9.25
80.0	2.98	2.57	3.57	6.87	5.53	7.87
90.0	2.55		3.02	6.03		6.81
100.0	2.21	1.92	2.60	5.35	4.21	5.96
200.0	0.841		0.957	2.27		2.39
300.0	0.469	0.446	0.527	1.32	1.09	1.36
400.0	0.309		0.345	0.891		0.904
500.0	0.223	0.220	0.247	0.651	0.581	0.656
600.0	0.170		0.189	0.502		0.503
700.0	0.136		0.150	0.403		0.402
800.0	0.111	0.112	0.123	0.332	0.319	0.331
900.0	0.093		0.103	0.280		0.278
1000.0	0.080	0.0819	0.0882	0.240	0.236	0.238

Table III (continue)

	Ne^{6+}			Mg^{8+}	P^{11+}	Ca^{16+}	V^{19+}
T_e(eV)	present	Chen	Romanik	present	present	present	present
1.0	15.8		21.5	18.3	48.1	277.	1.53
2.0	25.9		31.0	34.3	69.5	279.	23.4
3.0	29.7		37.1	37.6	68.7	234.	48.1
4.0	33.7		45.9	39.6	65.7	201.	64.5
5.0	37.3		54.1	41.7	63.7	178.	74.4
6.0	39.7		60.1	43.5	62.7	162.	80.5
7.0	40.9		63.6	44.7	62.2	150.	84.4
8.0	41.2		65.3	45.2	61.8	140.	86.9
9.0	40.9		65.5	45.2	61.2	133.	88.5
10.0	40.1	48.7	64.9	44.8	60.6	127.	89.5
20.0	27.9		46.0	33.4	47.6	90.5	83.9
30.0	20.4	24.6	32.8	24.6	35.8	68.4	70.3
40.0	16.3		25.2	19.6	28.0	53.6	58.0
50.0	13.8	15.6	20.4	16.8	22.9	43.5	48.5
60.0	12.0		17.2	14.9	19.6	36.3	41.2
70.0	10.6		14.8	13.6	17.4	31.0	35.6
80.0	9.55	10.1	13.0	12.6	15.8	27.1	31.3
90.0	8.64		11.5	11.8	14.7	24.2	27.8
100.0	7.88	8.06	10.3	11.1	13.8	21.9	25.1
200.0	3.89		4.73	6.62	9.59	13.6	14.2
300.0	2.40	2.42	2.85	4.43	7.17	11.2	11.6
400.0	1.67		1.95	3.21	5.55	9.57	10.1
500.0	1.24	1.36	1.44	2.45	4.43	8.19	9.00
600.0	0.973		1.12	1.95	3.63	7.07	8.00
700.0	0.788		0.905	1.60	3.05	6.17	7.13
800.0	0.655	0.782	0.750	1.34	2.60	5.43	6.40
900.0	0.555		0.634	1.15	2.25	4.82	5.77
1000.0	0.478	0.597	0.545	0.997	1.97	4.31	5.23

Table III (continue)

	Ar^{14+}			Fe^{22+}		
T_e(eV)	present	Chen	Romanik	present	Chen	Romanik
1.0	112.		127.	9.66		0.703
2.0	133.		190.	72.5		24.9
3.0	131.		179.	113.		66.0
4.0	125.		162.	130.		98.3
5.0	118.		148.	136.		119.
6.0	113.		137.	136.		132.
7.0	109.		130.	134.		139.
8.0	105.		125.	132.		143.
9.0	102.		120.	129.		144.
10.0	99.6	92.8	117.	126.	129.	149.
20.0	75.1		91.4	104.		130.
30.0	56.7	58.2	70.6	86.1	88.5	109.
40.0	44.3		55.8	71.5		91.4
50.0	35.9	37.6	45.7	60.2	62.9	77.2
60.0	30.0		38.5	51.4		66.2
70.0	25.9		33.3	44.6		57.5
80.0	22.9	23.9	29.5	39.2	41.3	50.7
90.0	20.7		26.7	34.9		45.2
100.0	19.0	19.6	24.5	31.4	33.2	40.9
200.0	13.2		16.2	16.3		21.8
300.0	10.9	10.0	13.0	12.5	13.1	16.7
400.0	9.05		10.6	10.9		14.2
500.0	7.59	6.85	8.87	9.85	10.2	12.6
600.0	6.44		7.49	8.92		11.2
700.0	5.54		6.42	8.12		10.1
800.0	4.82	4.49	5.57	7.42	7.73	9.16
900.0	4.24		4.89	6.79		8.33
1000.0	3.77	3.62	4.34	6.24	6.55	7.61

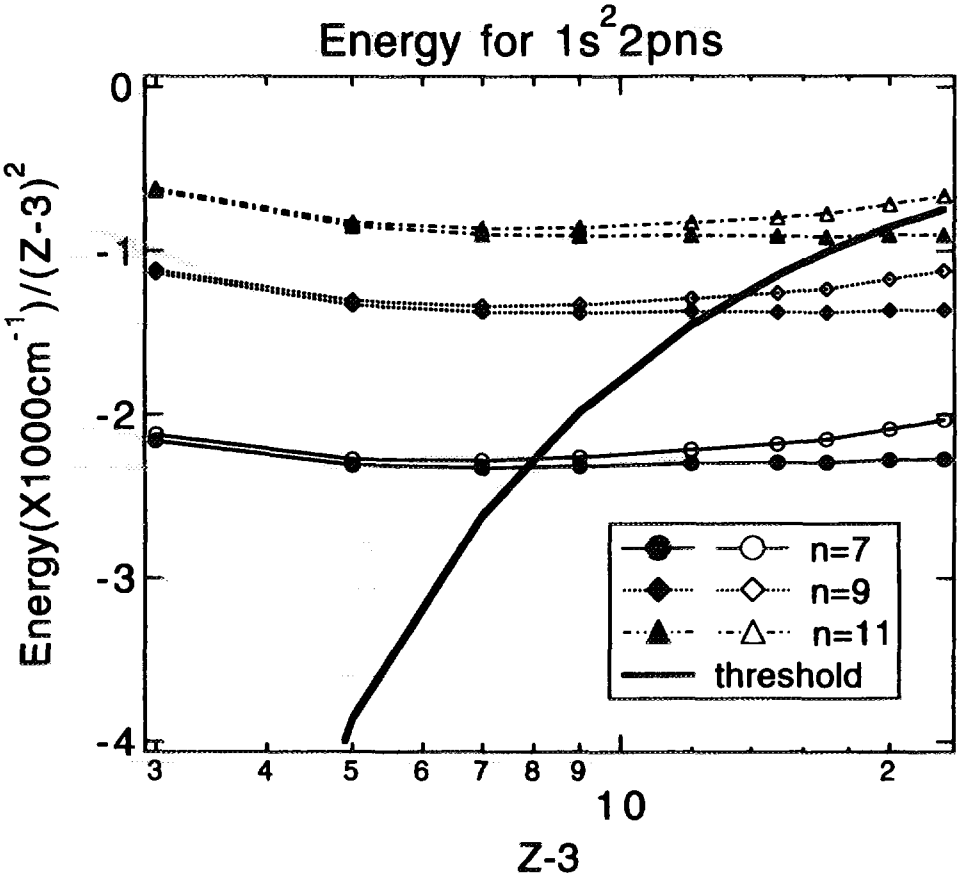

Fig.1-1(a)

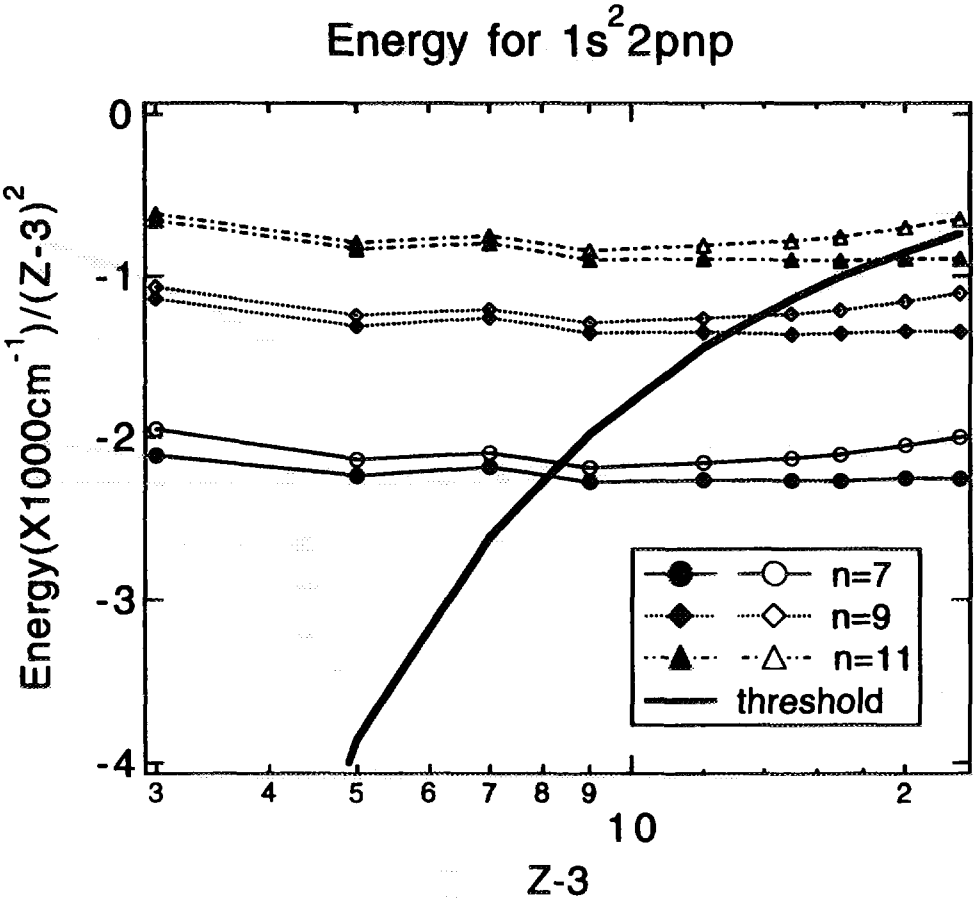

Fig.1-1(b)

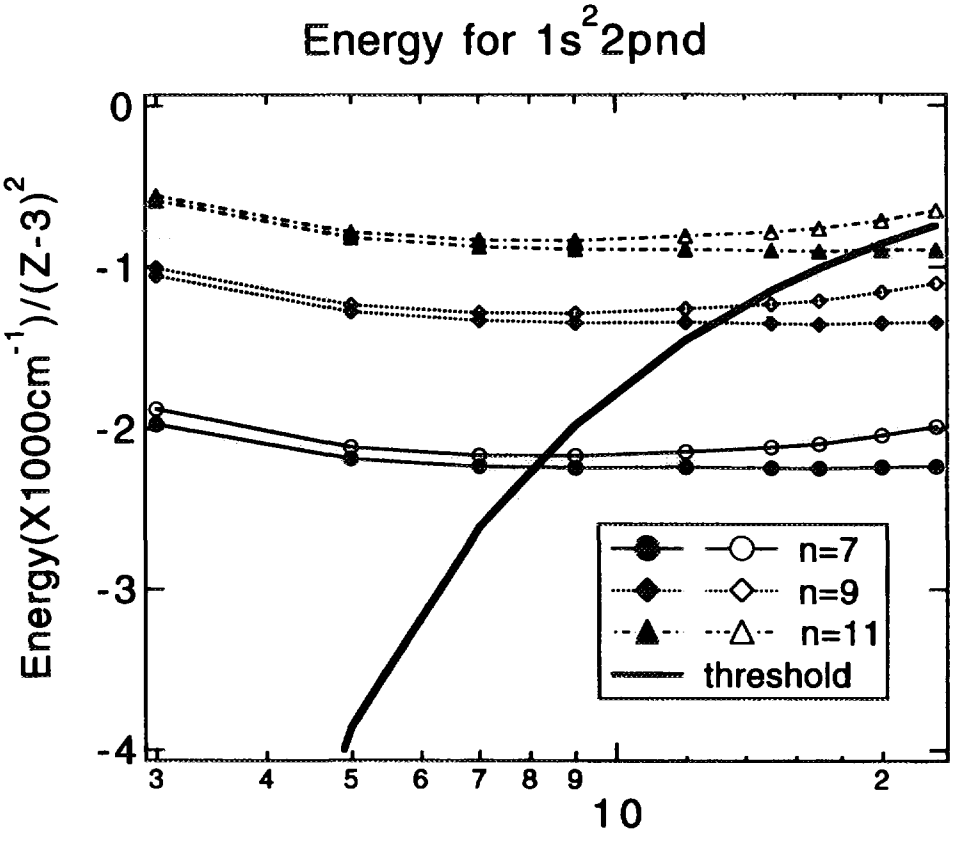

Fig.1-1(c)

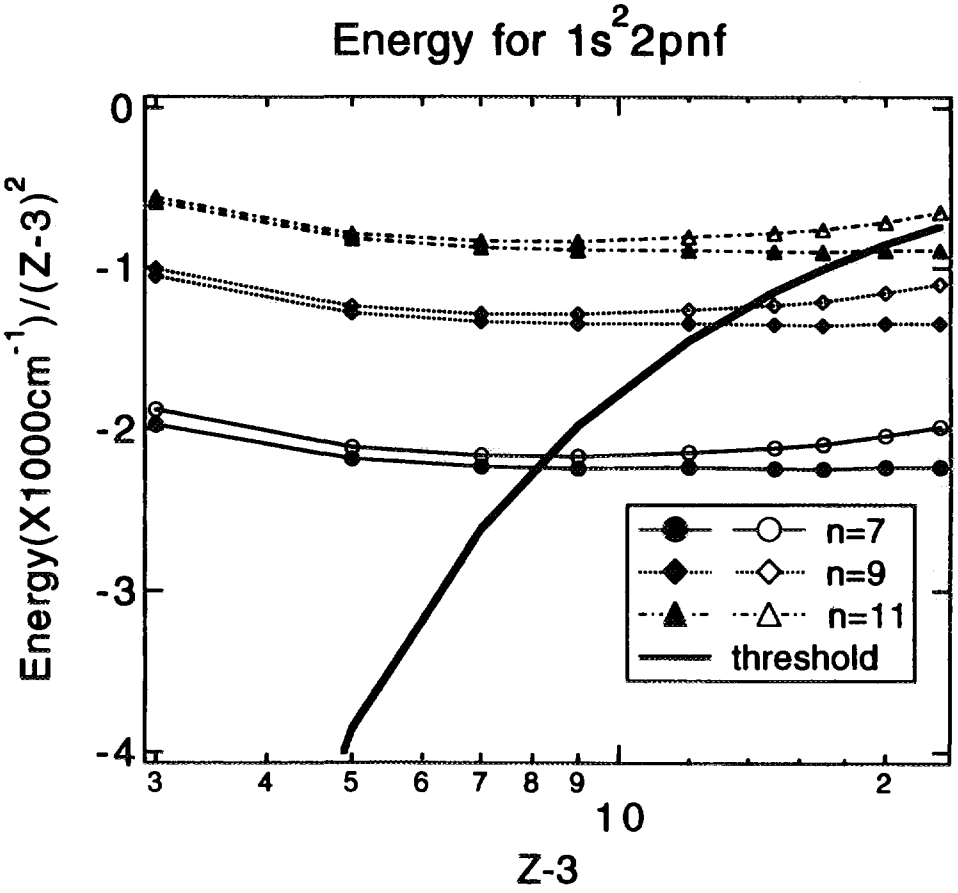

Fig.1-1(d)

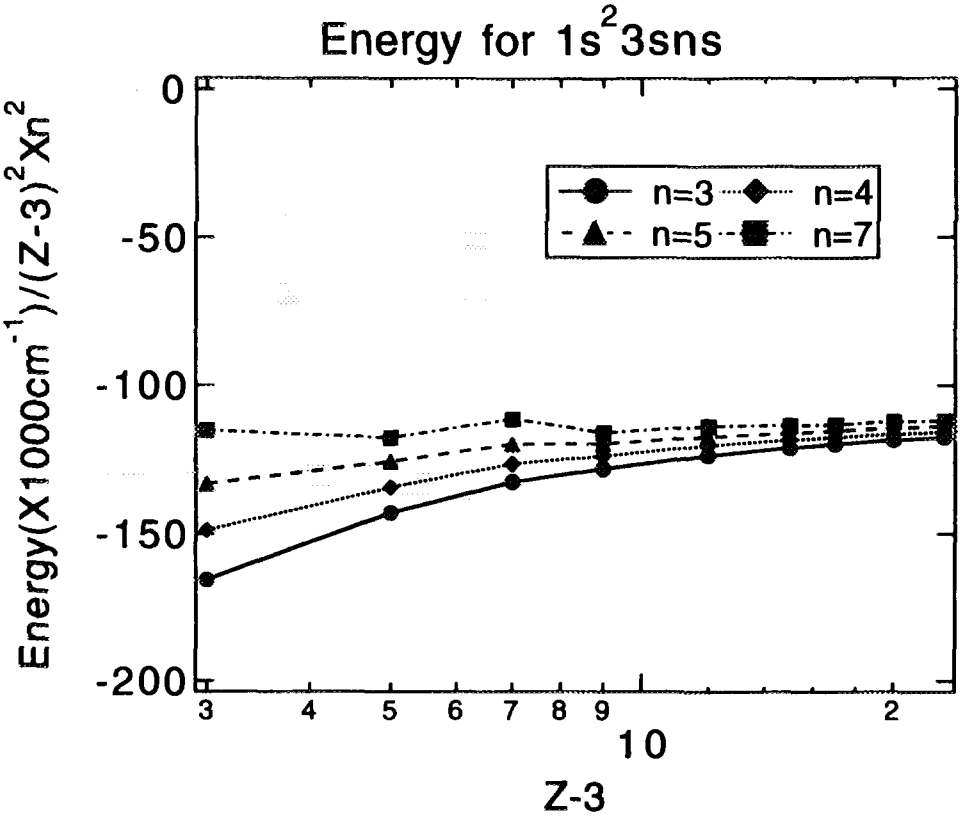

Fig.1-2(a)

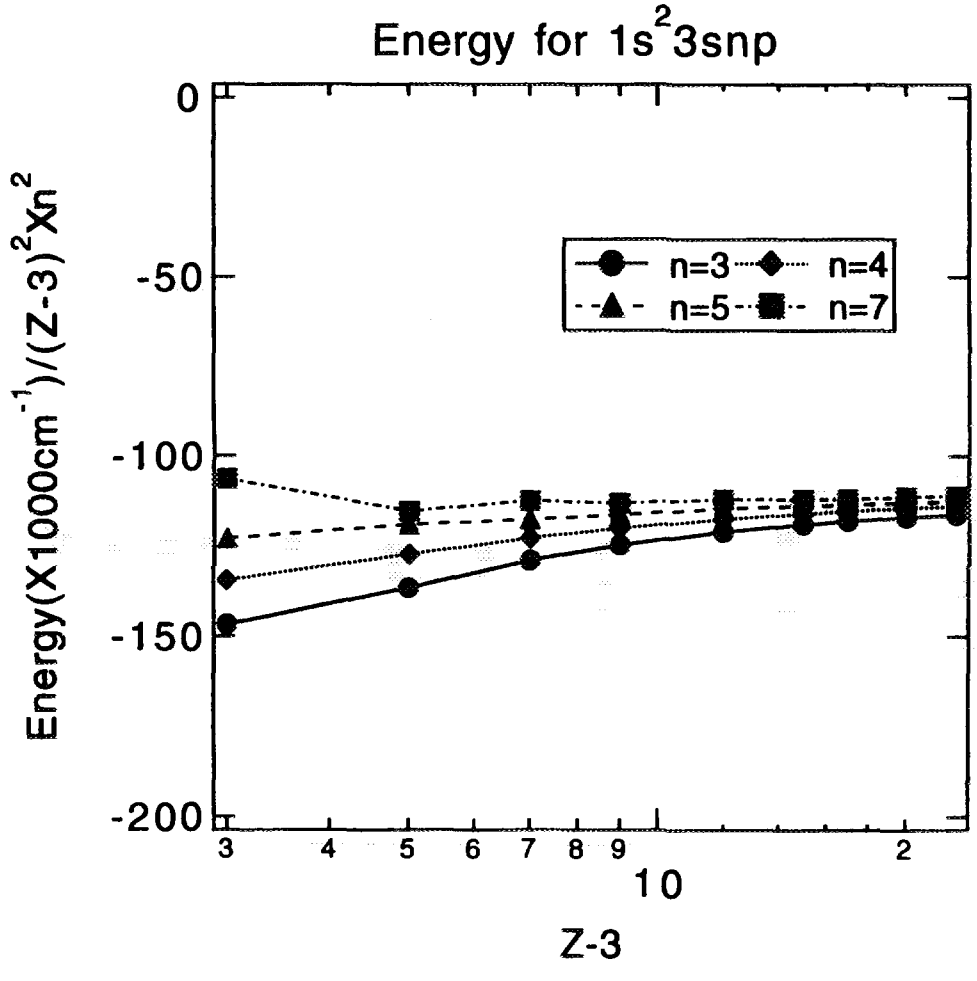

Fig.1-2(b)

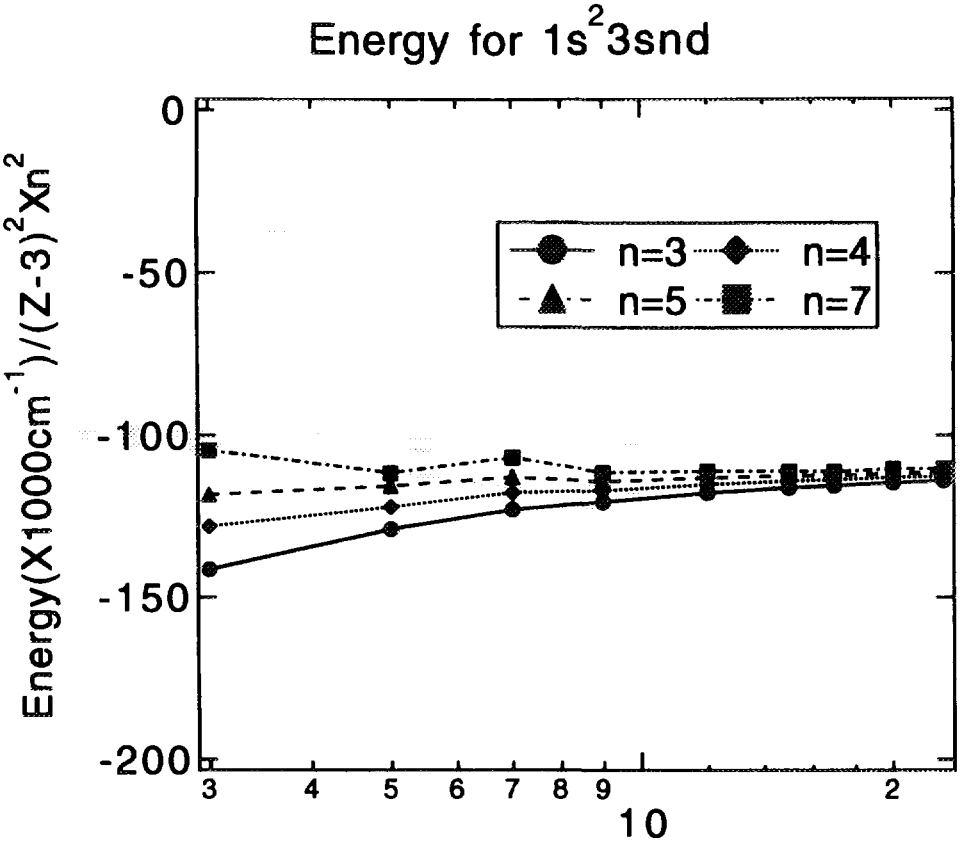

Fig.1-2(c)

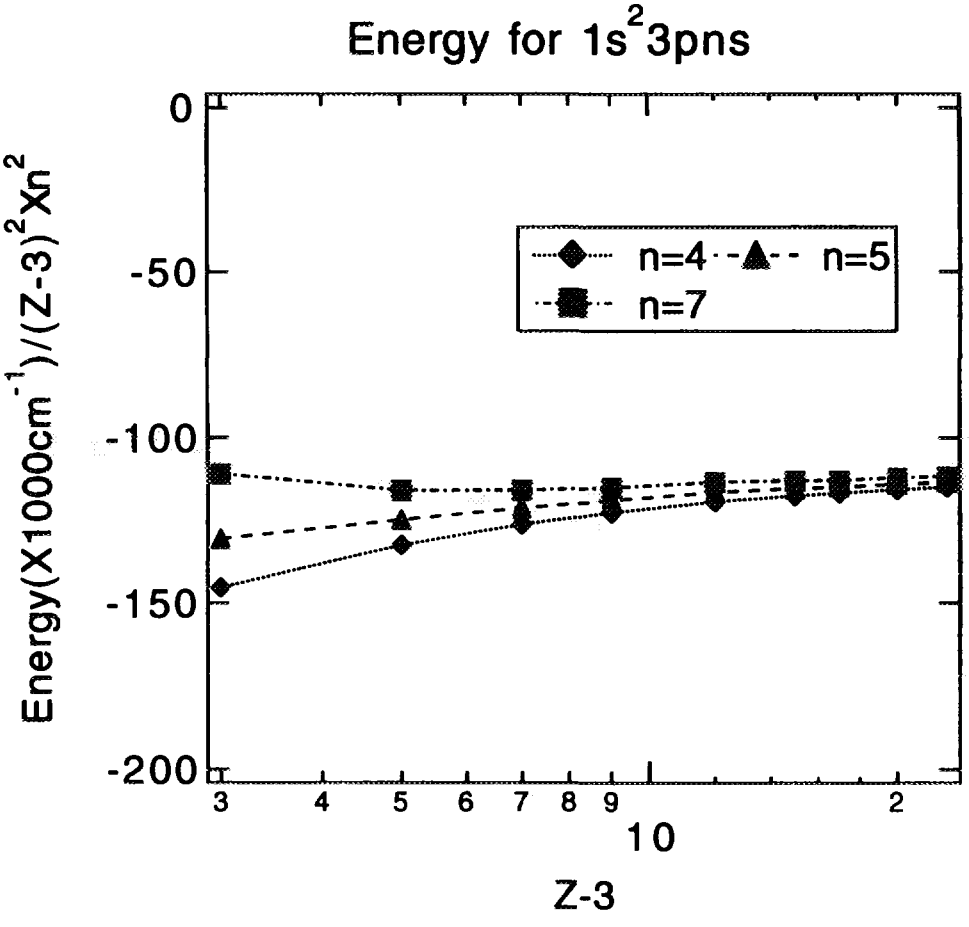

Fig.1-2(d)

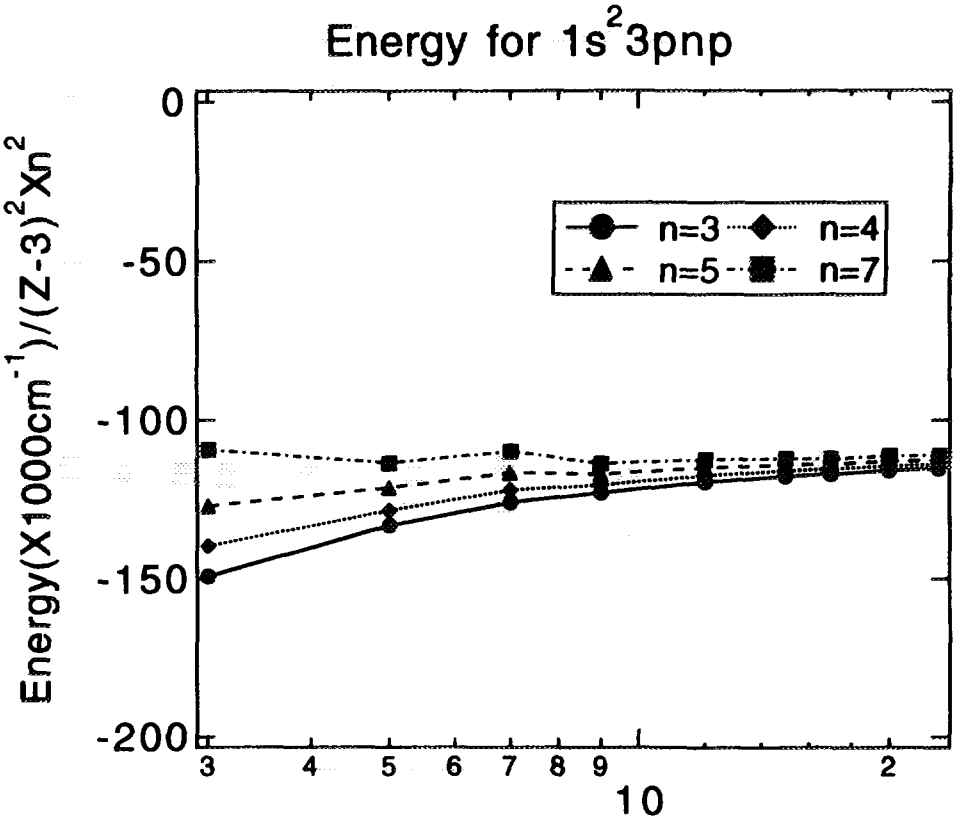

Fig.1-2(e)

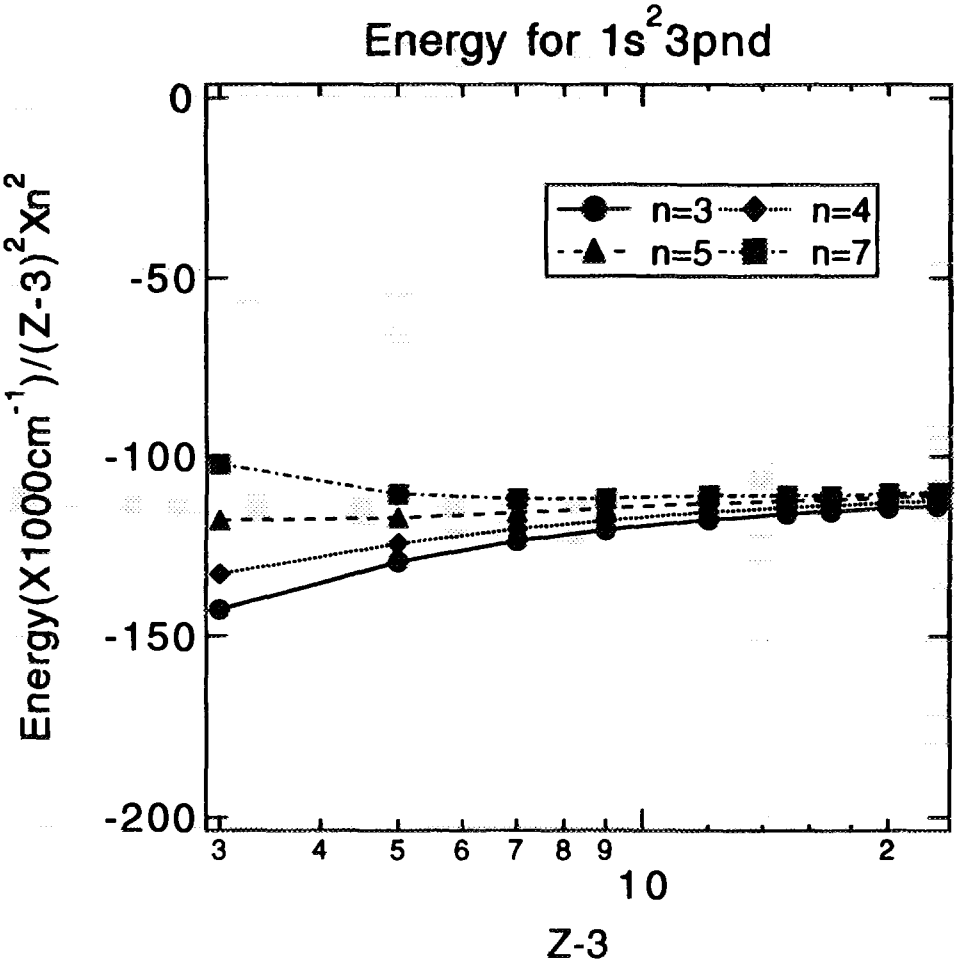

Fig.1-2(f)

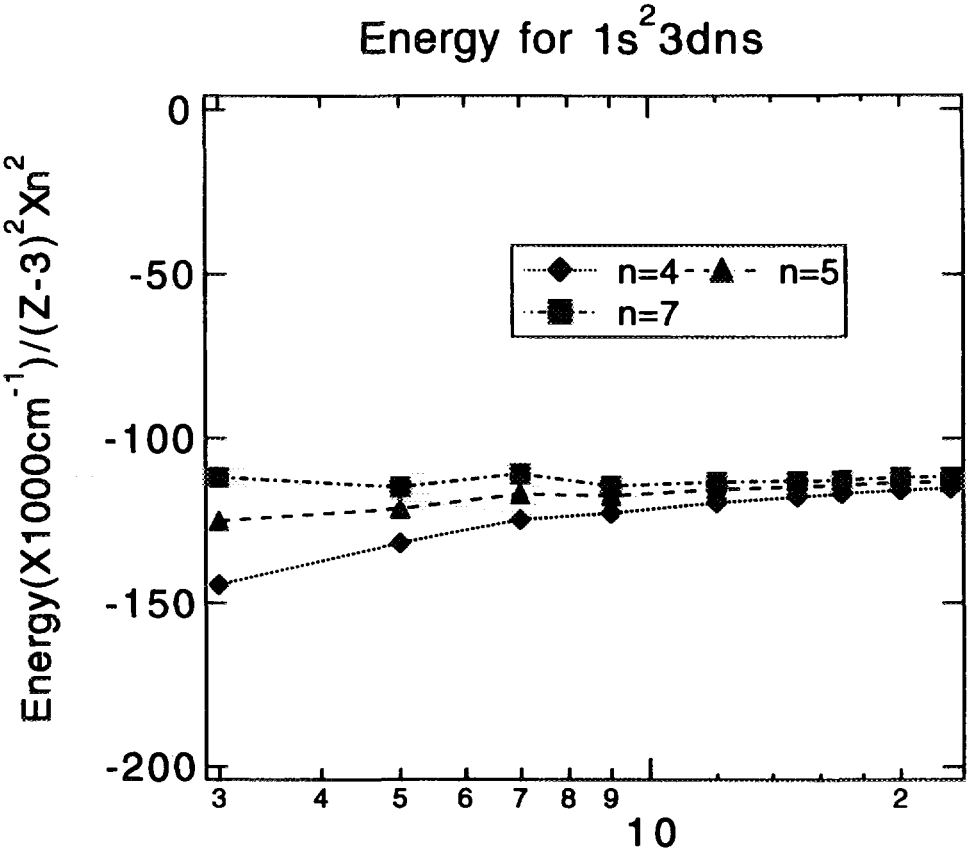

Fig.1-2(g)

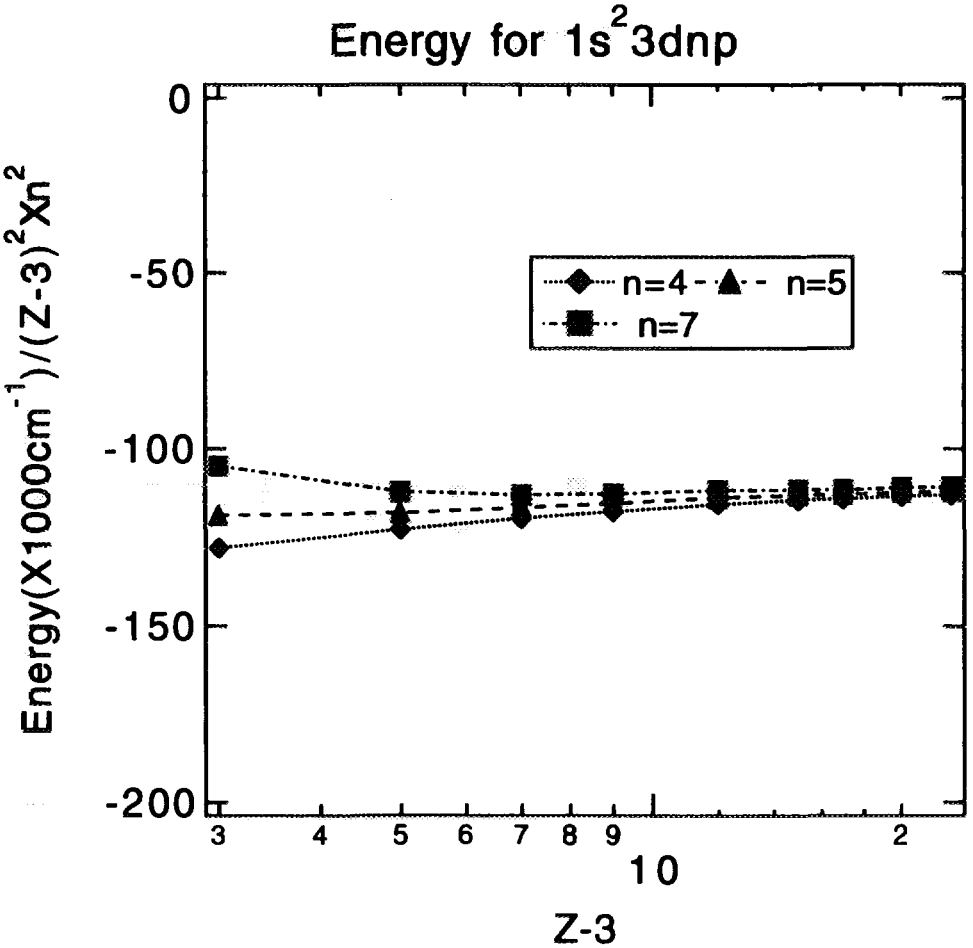

Fig.1-2(h)

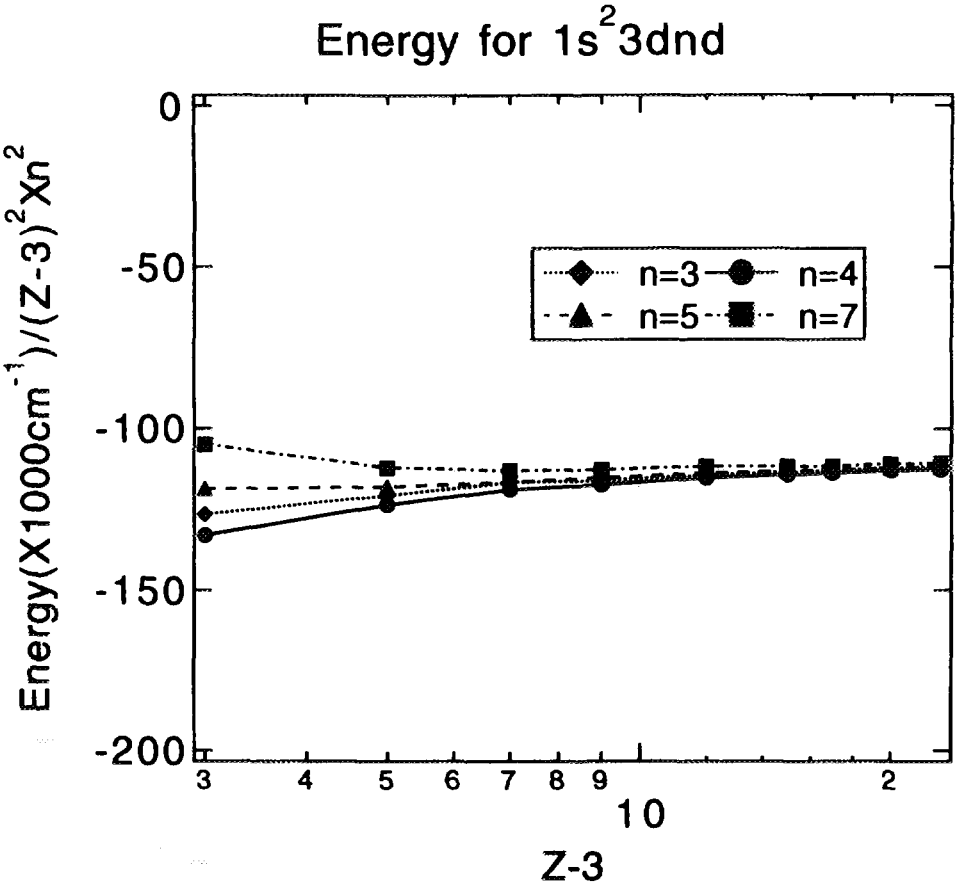
Energy for 1s²3dnd
Energy(X1000cm⁻¹)/(Z-3)²Xn²
0
-50
-100
-150
-200
n=3
n=4
n=5
n=7
3
4
5
6
7
8
9
10
2
Z-3

Fig.1-2(i)

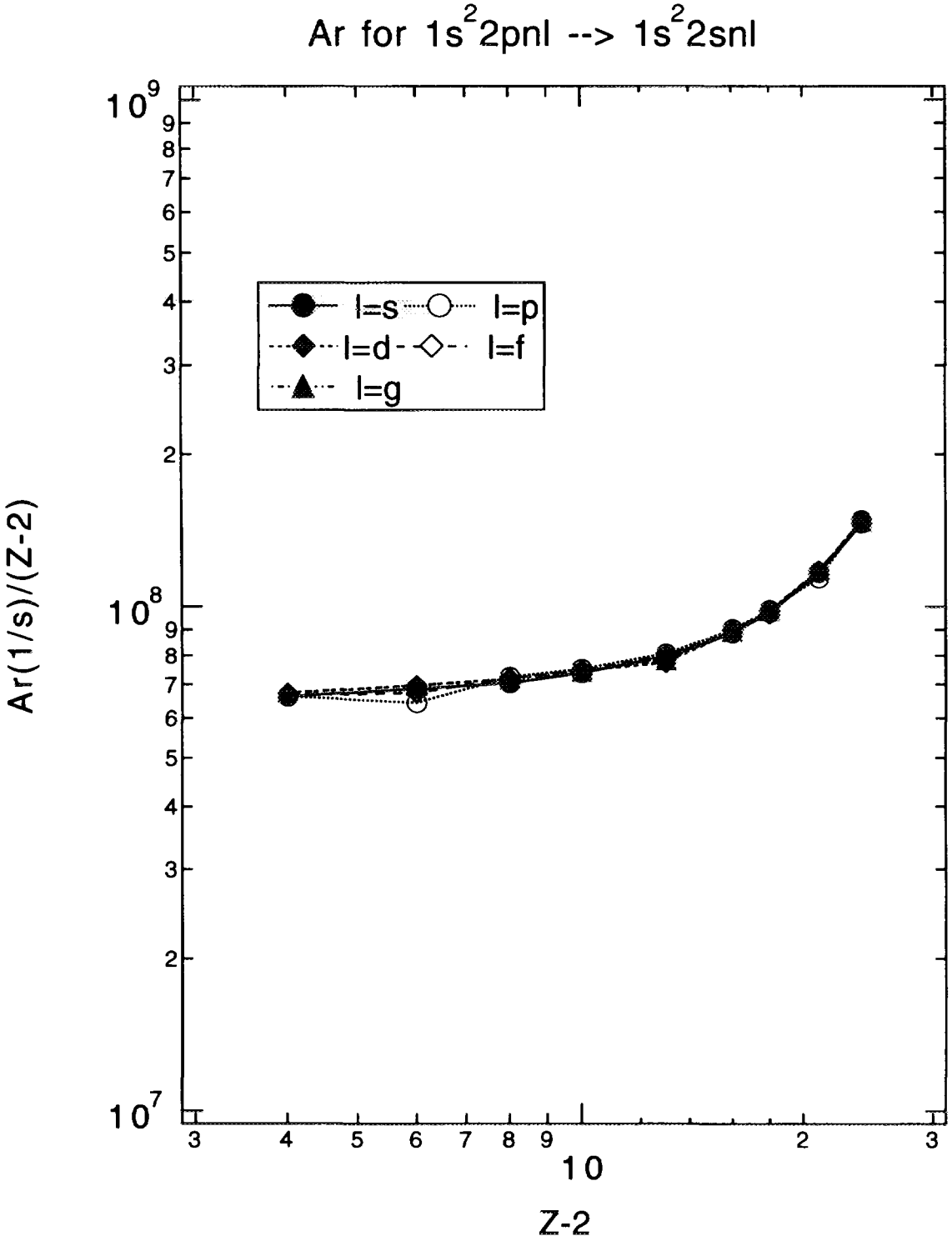
Ar for 1s²2pnl --> 1s²2snl
Ar(1/s)/(Z-2)
Z-2
l=s
l=p
l=d
l=f
l=g
10⁹
10⁸
10⁷
3 4 5 6 7 8 9 10 2 3

Fig.2-1

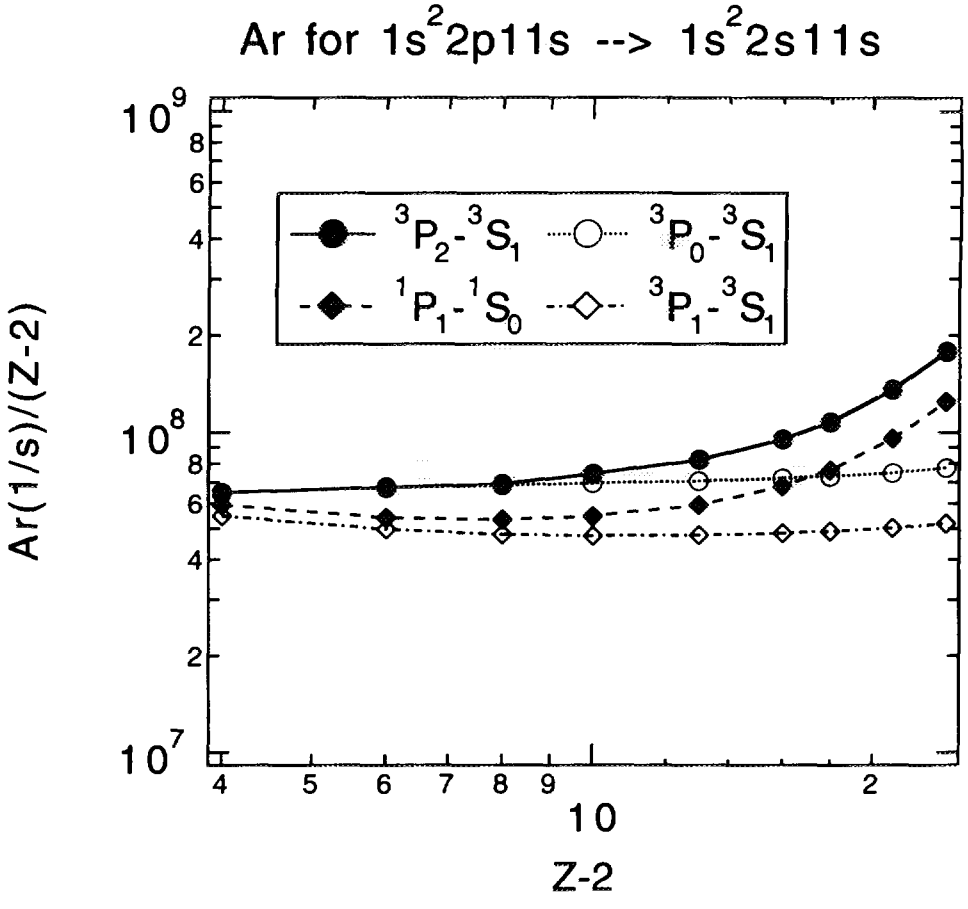

Fig.2-1-2(a)

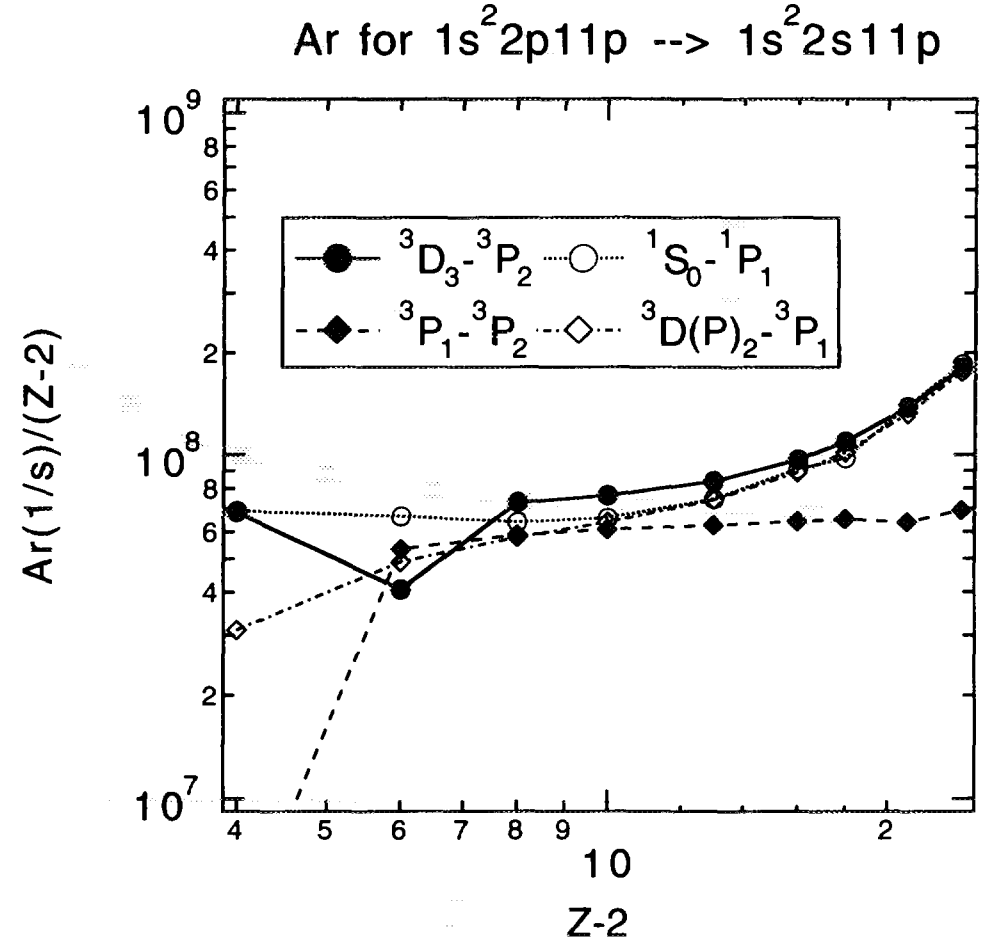

Fig.2-1-2(b)

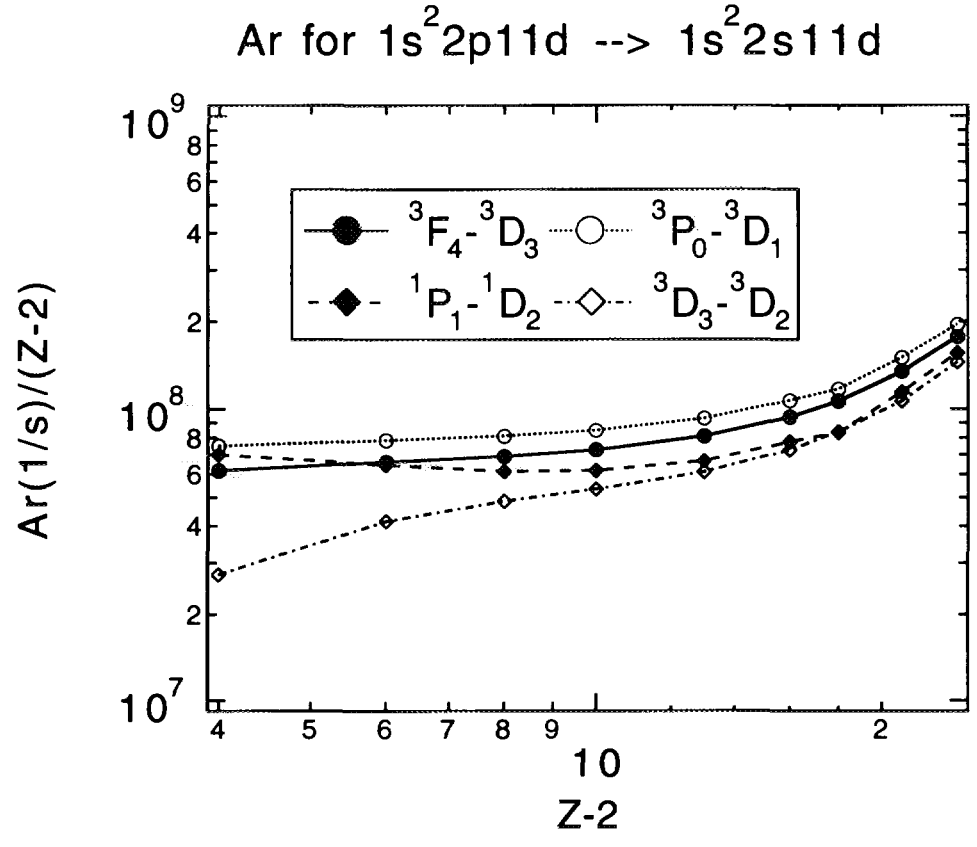

Fig.2-1-2(c)

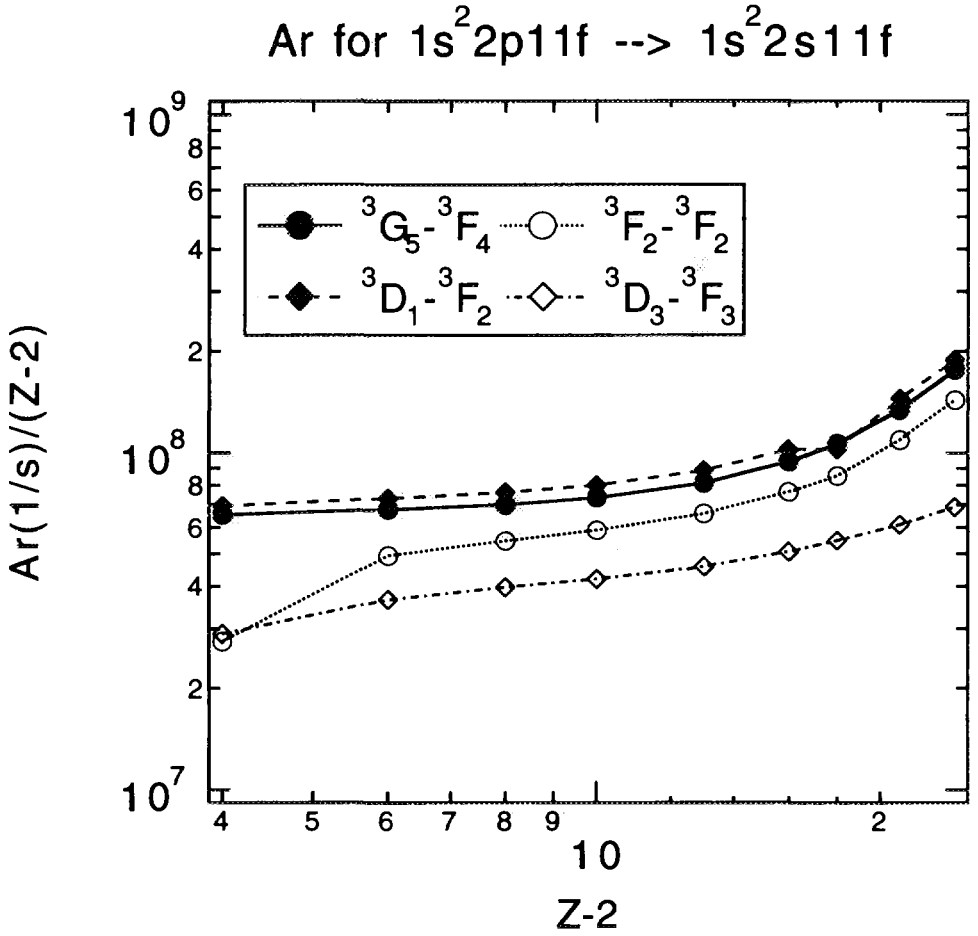

Fig.2-1-2(d)

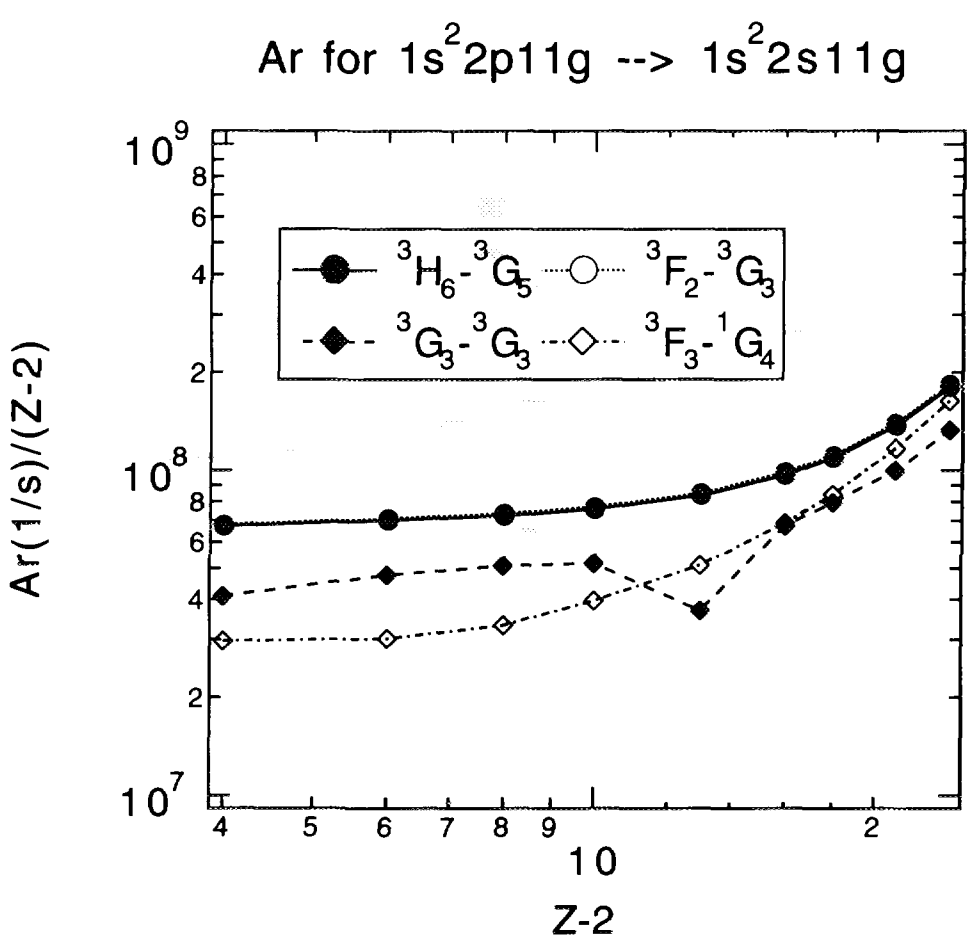
Ar for 1s²2p11g --> 1s²2s11g
Ar(1/s)/(Z-2)
10⁹
8
6
4
2
10⁸
8
6
4
2
10⁷
4
5
6
7
8
9
10
2
Z-2
³H₆-³G₅
³F₂-³G₃
³G₃-³G₃
³F₃-¹G₄

Fig.2-1-2(e)

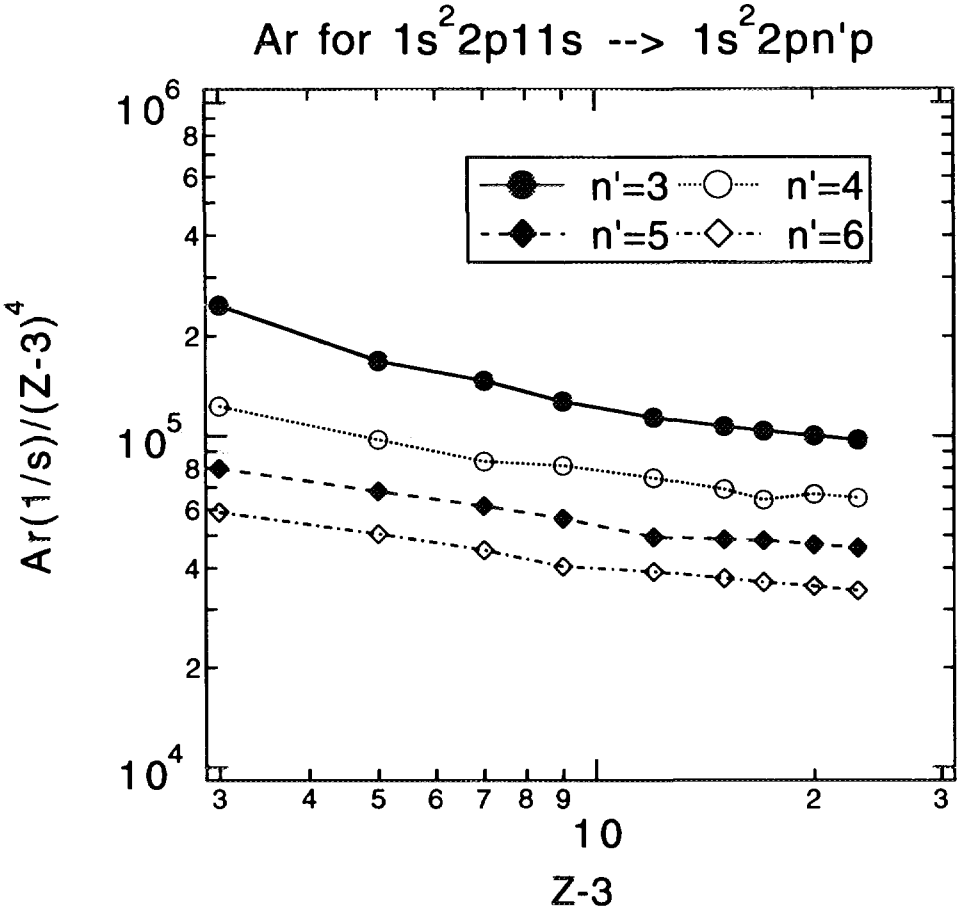
Ar for 1s²2p11s --> 1s²2pn'p
Ar(1/s)/(Z-3)⁴
10⁶
8
6
4
2
10⁵
8
6
4
2
10⁴
n'=3
n'=4
n'=5
n'=6
3
4
5
6
7
8
9
10
2
3
Z-3

Fig.2-2(a)

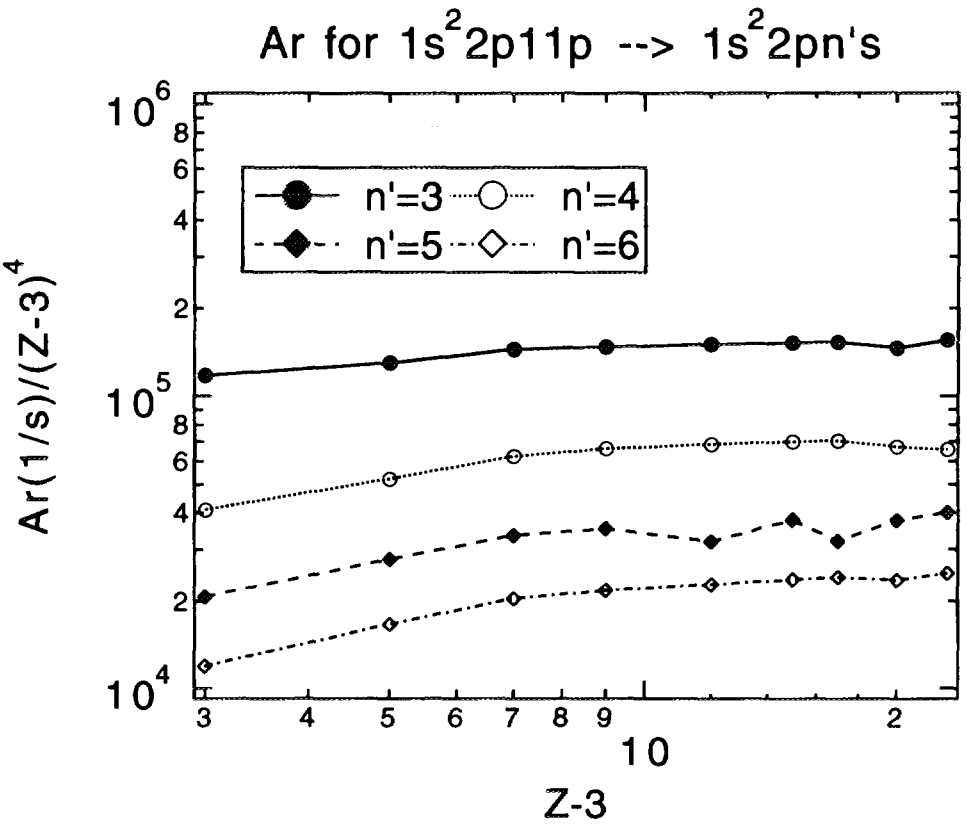

Fig.2-2(b)

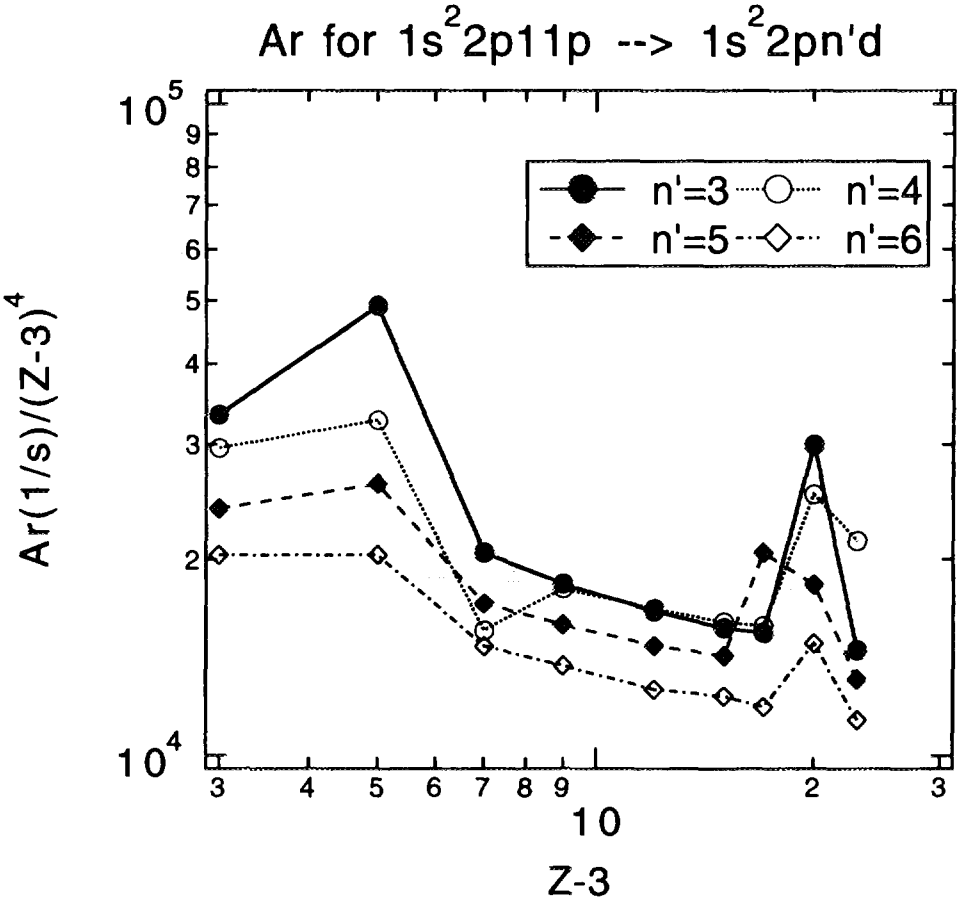

Fig.2-2(c)

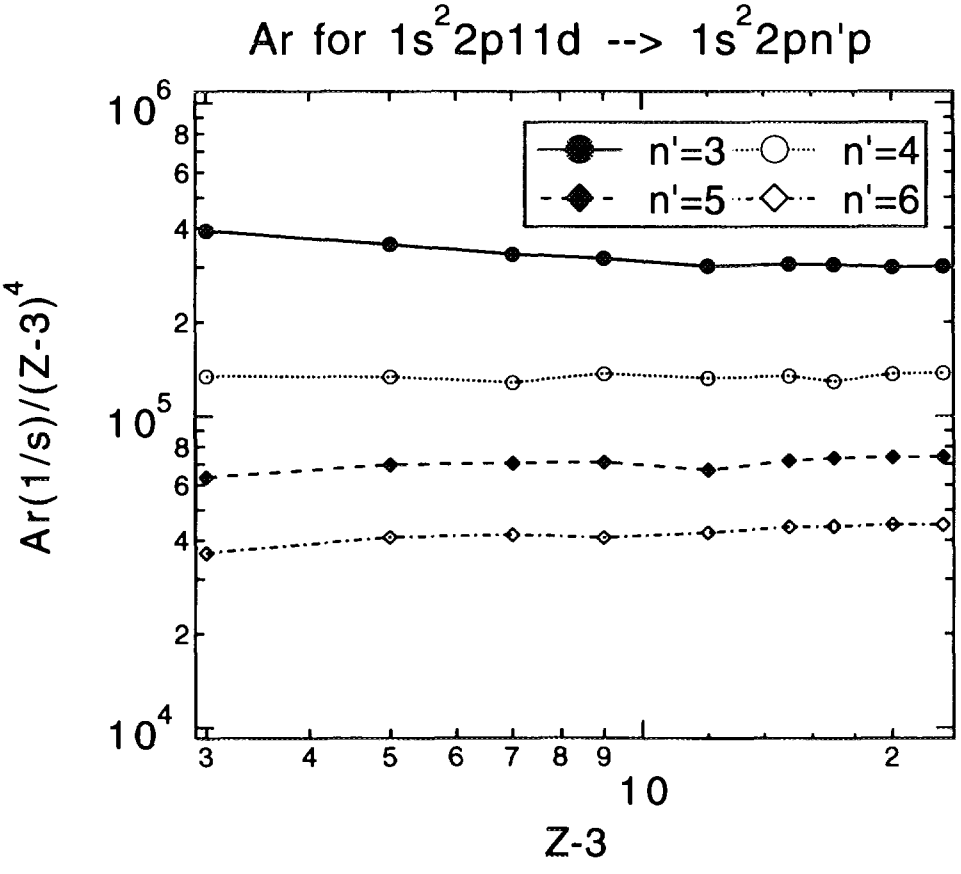

Fig.2-2(d)

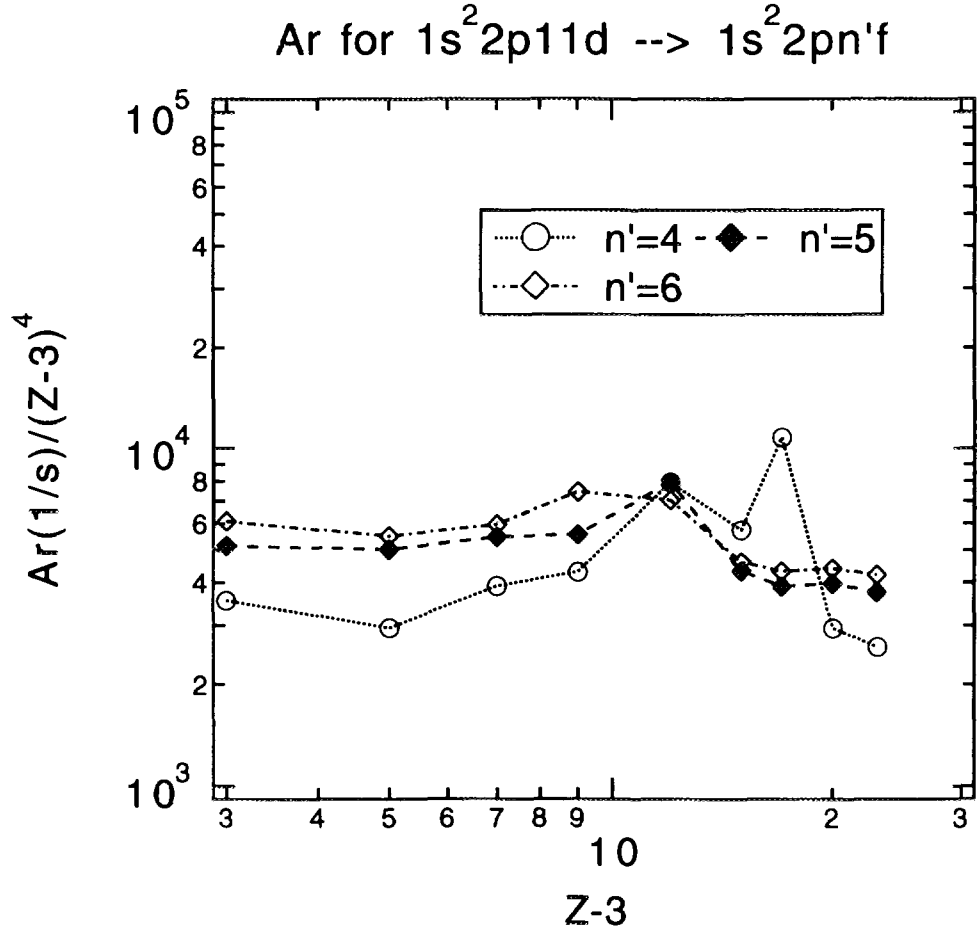

Fig.2-2(e)

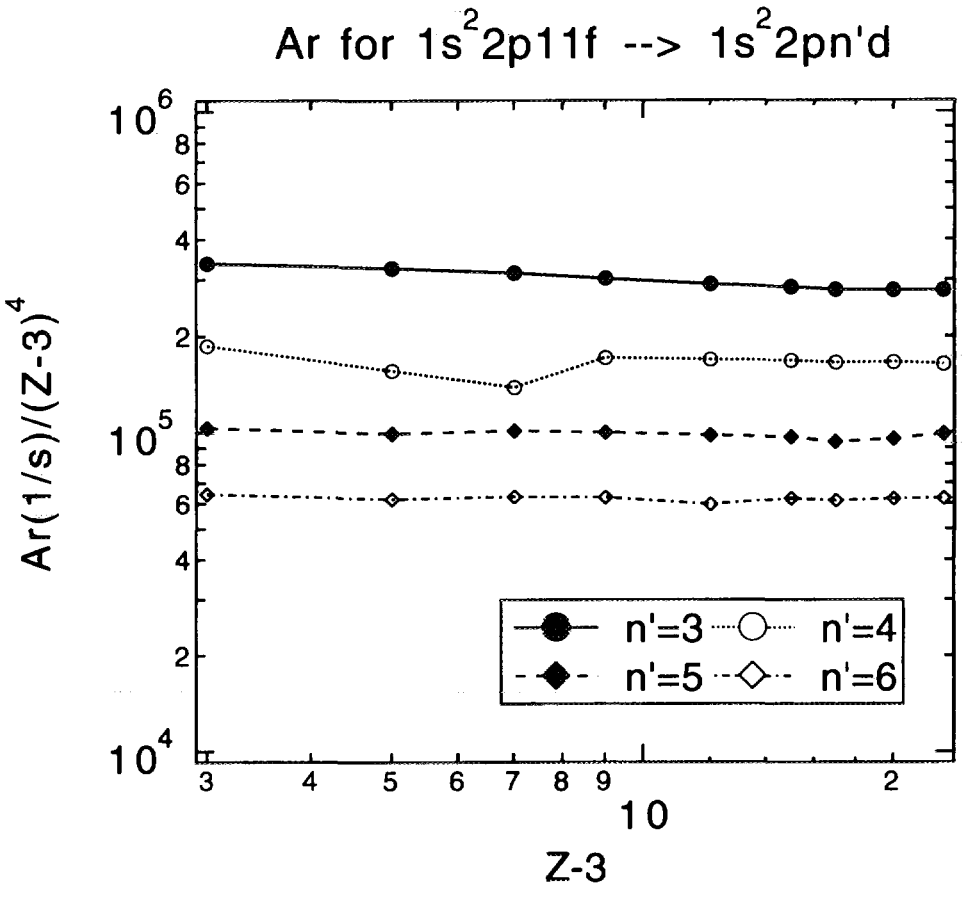

Fig.2-2(f)

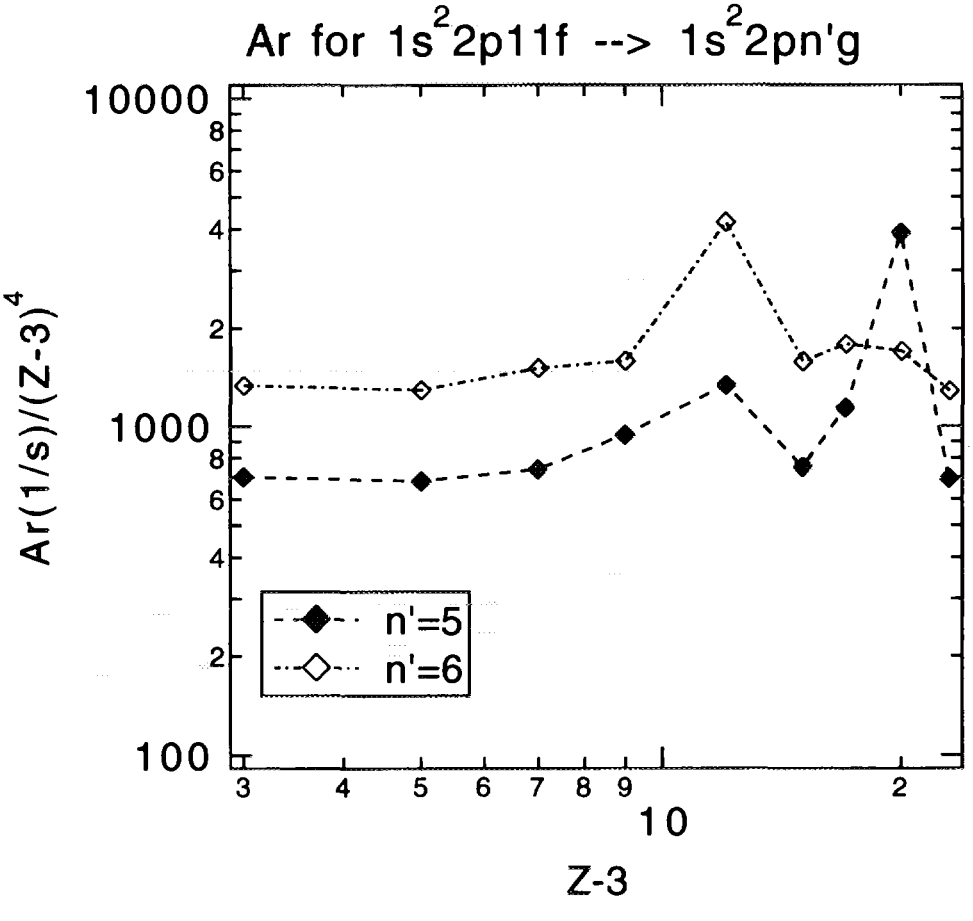

Fig.2-2(g)

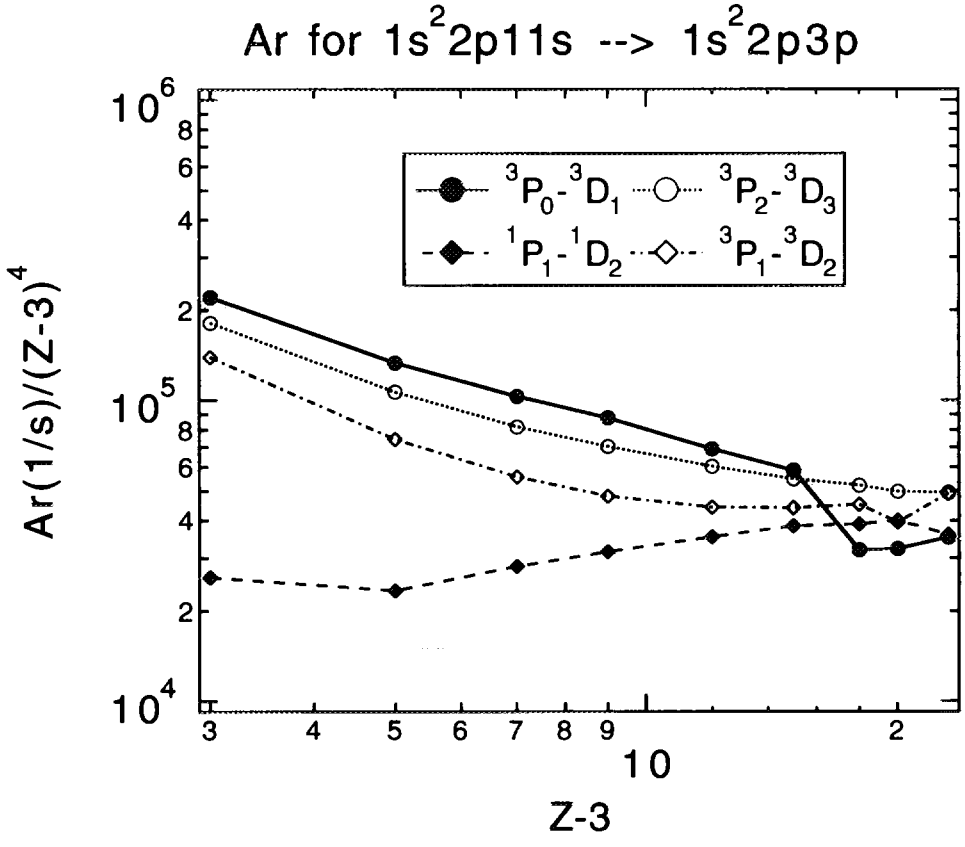

Fig.2-2-2(a)

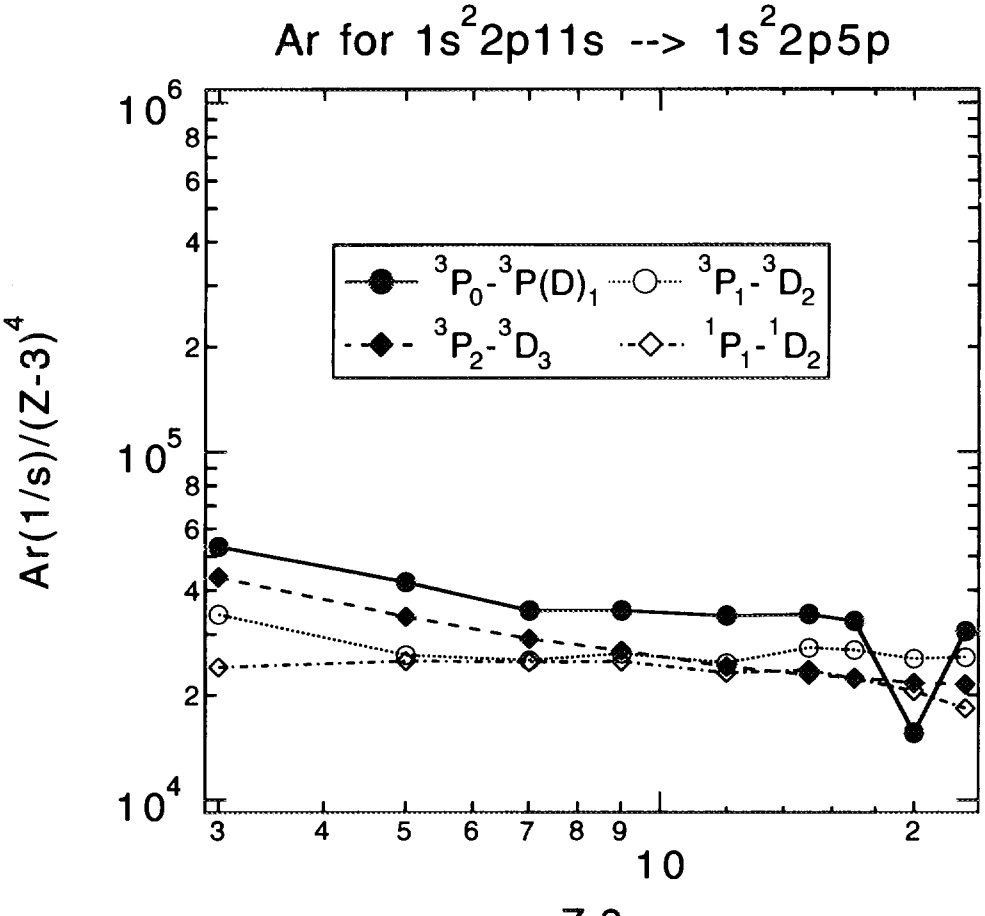

Fig.2-2-2(b)

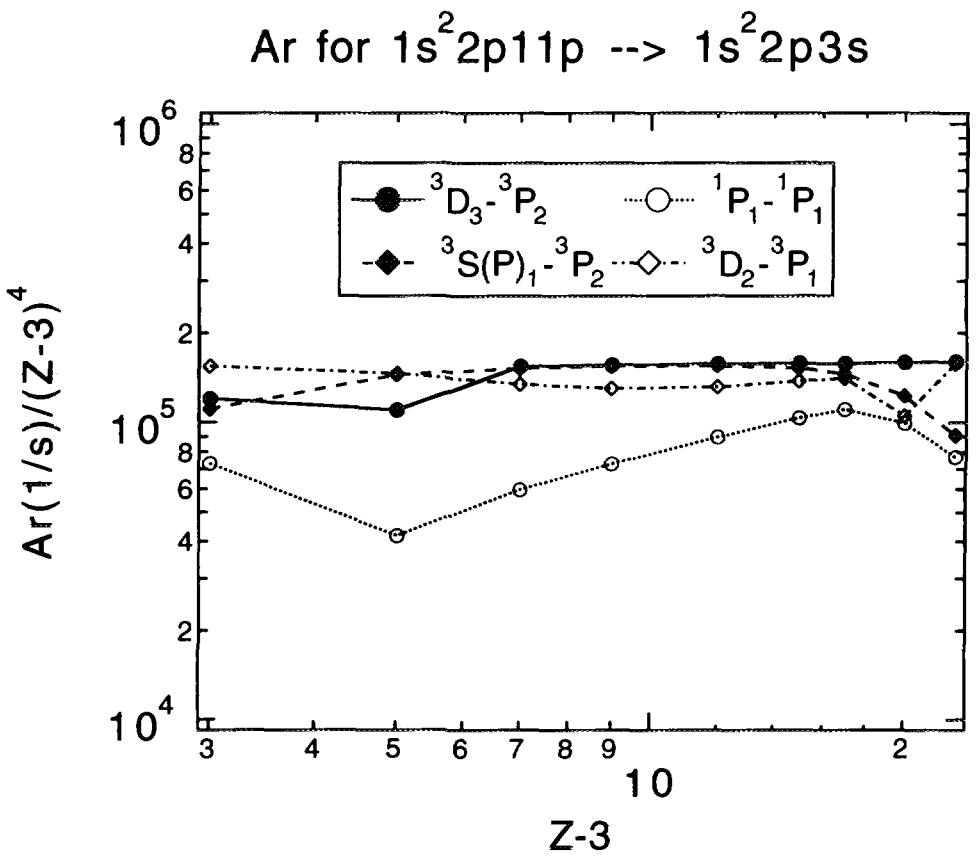

Fig.2-2-2(c)

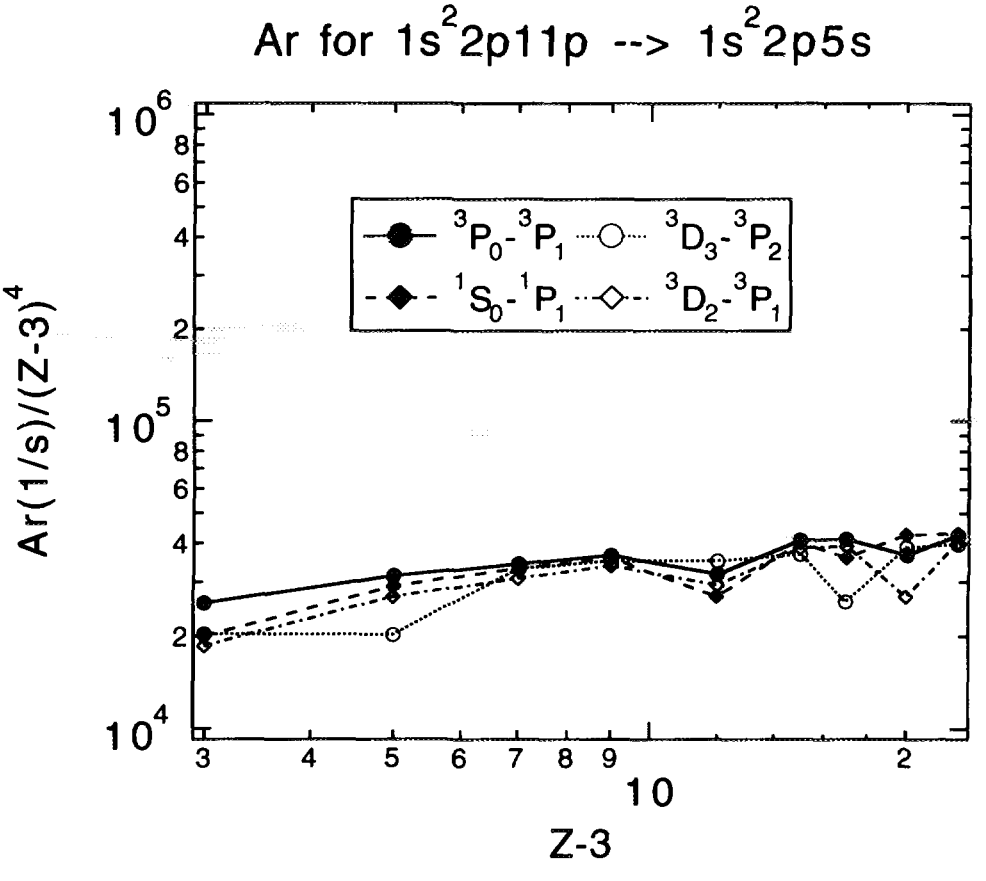

Fig.2-2-2(d)

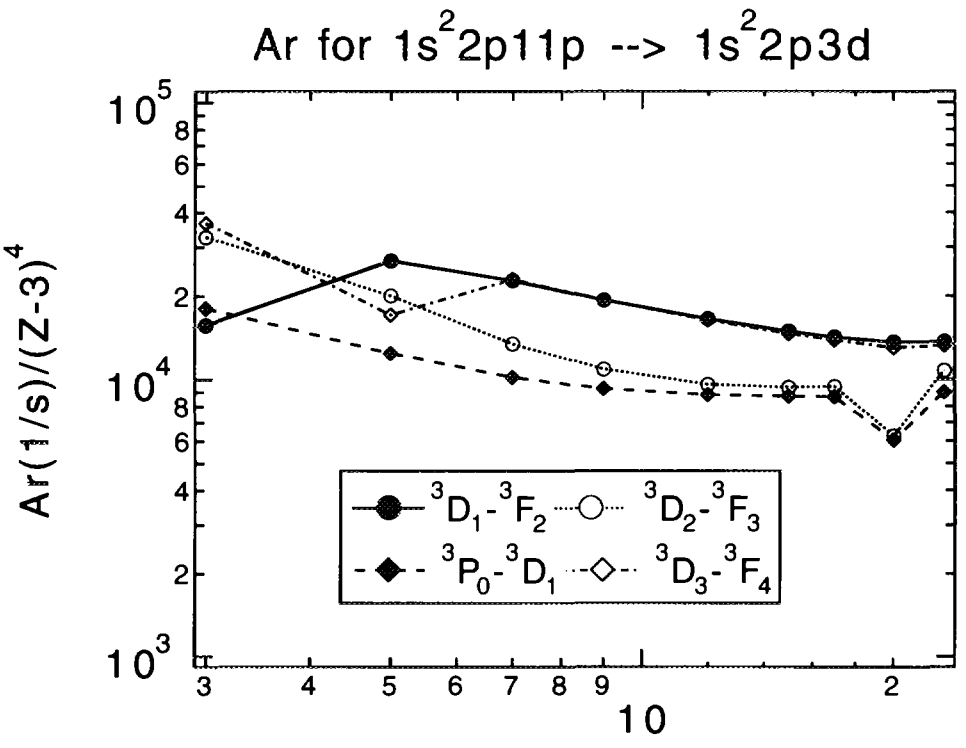

Fig.2-2-2(e)

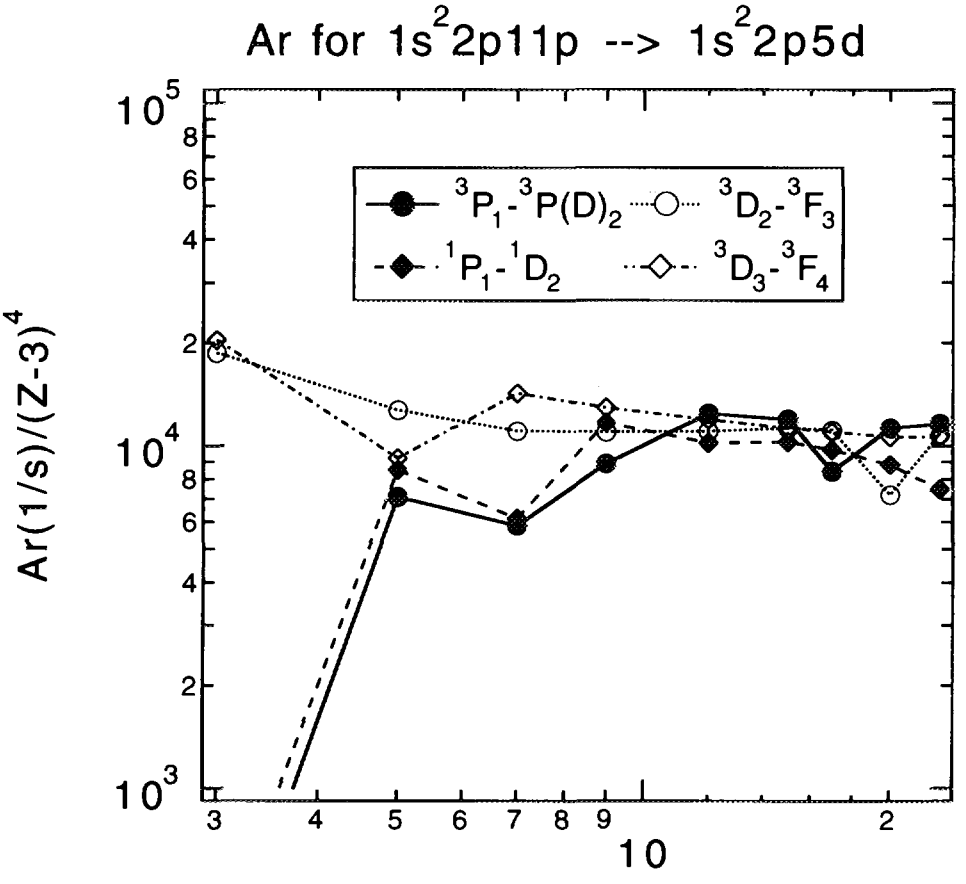

Fig.2-2-2(f)

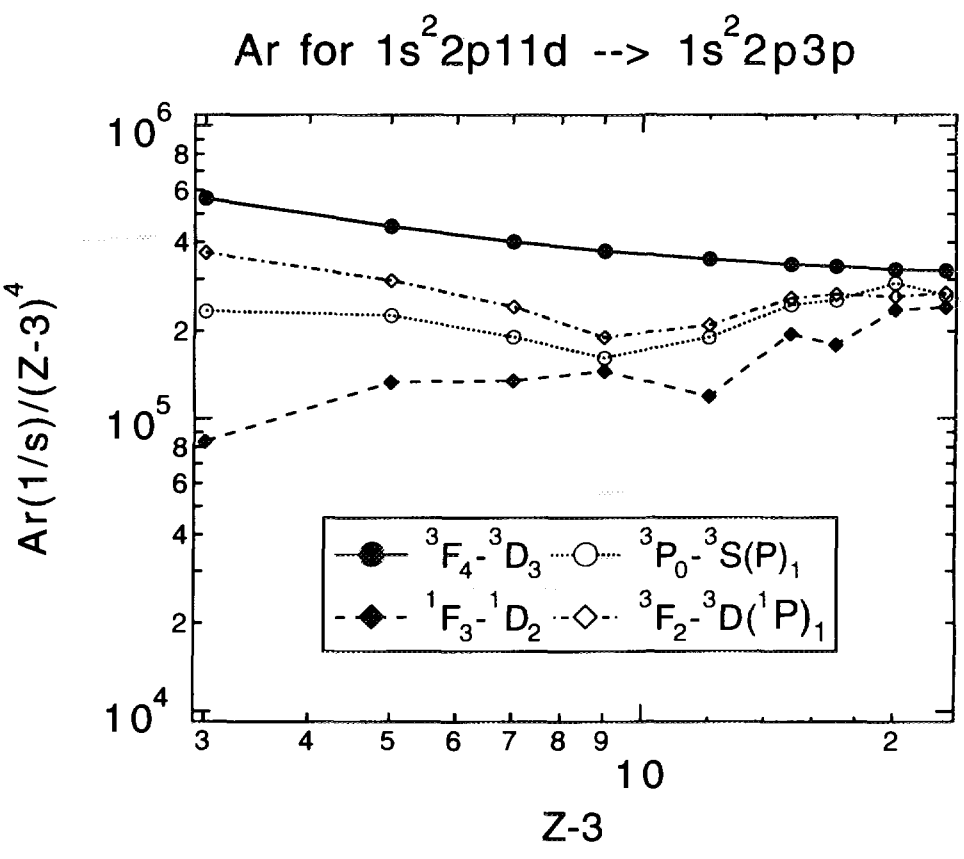

Fig.2-2-2(g)

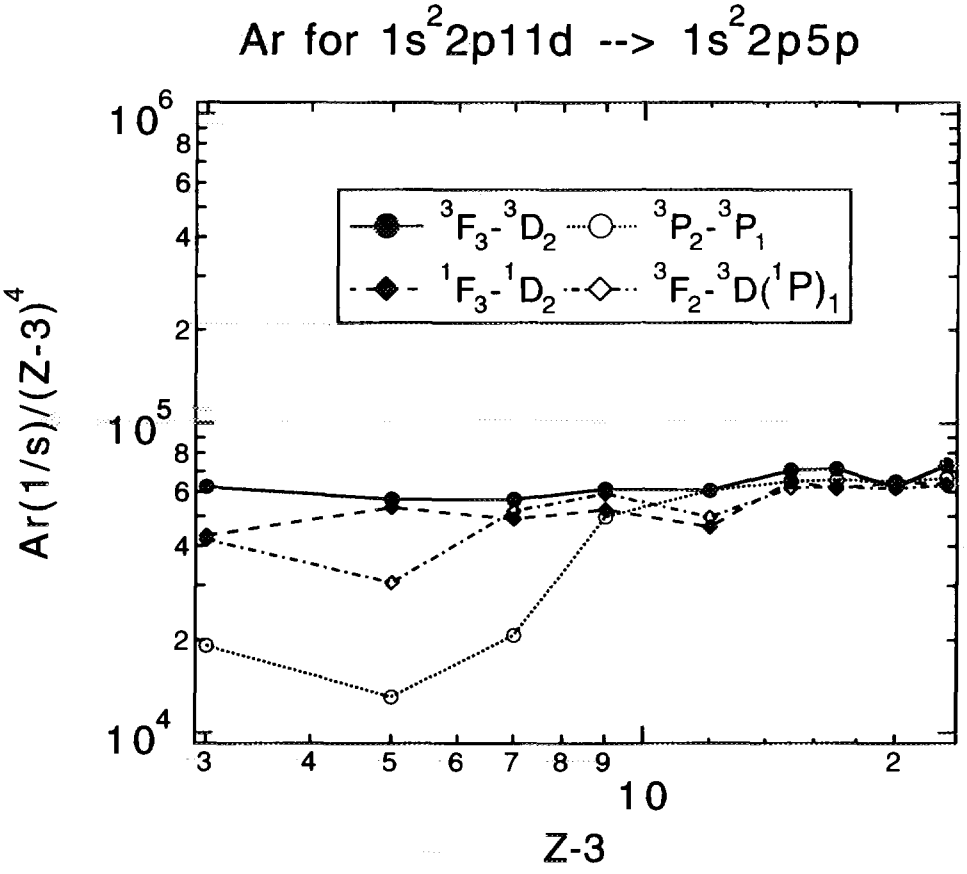

Fig.2-2-2(h)

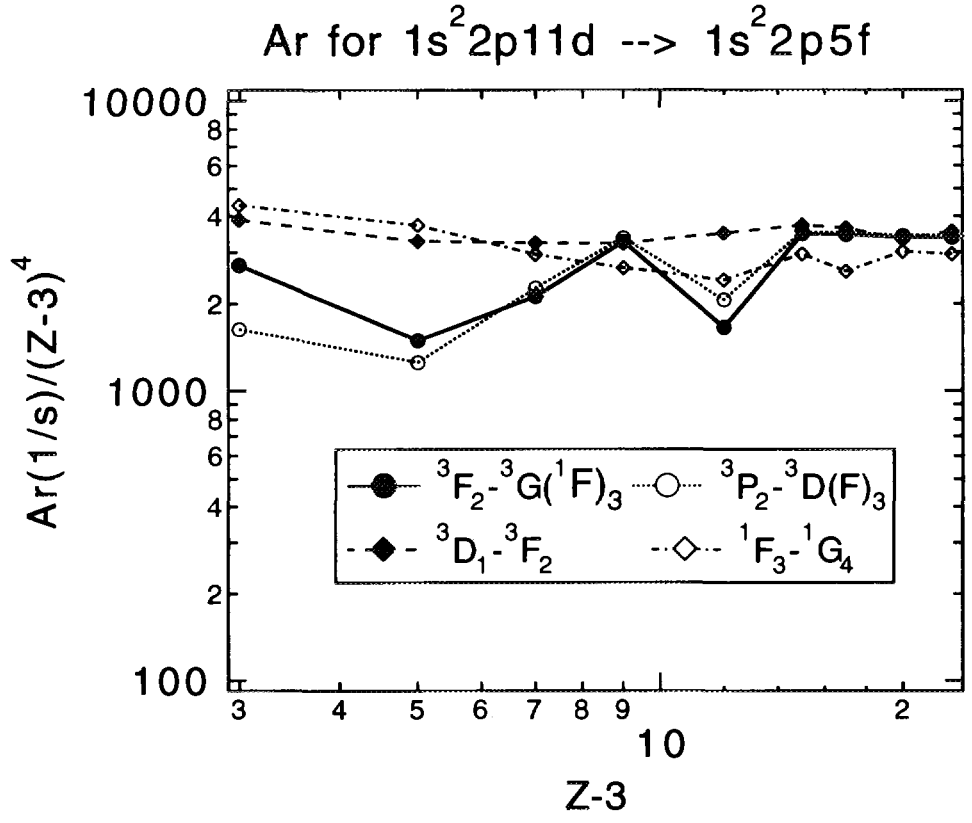

Fig.2-2-2(i)

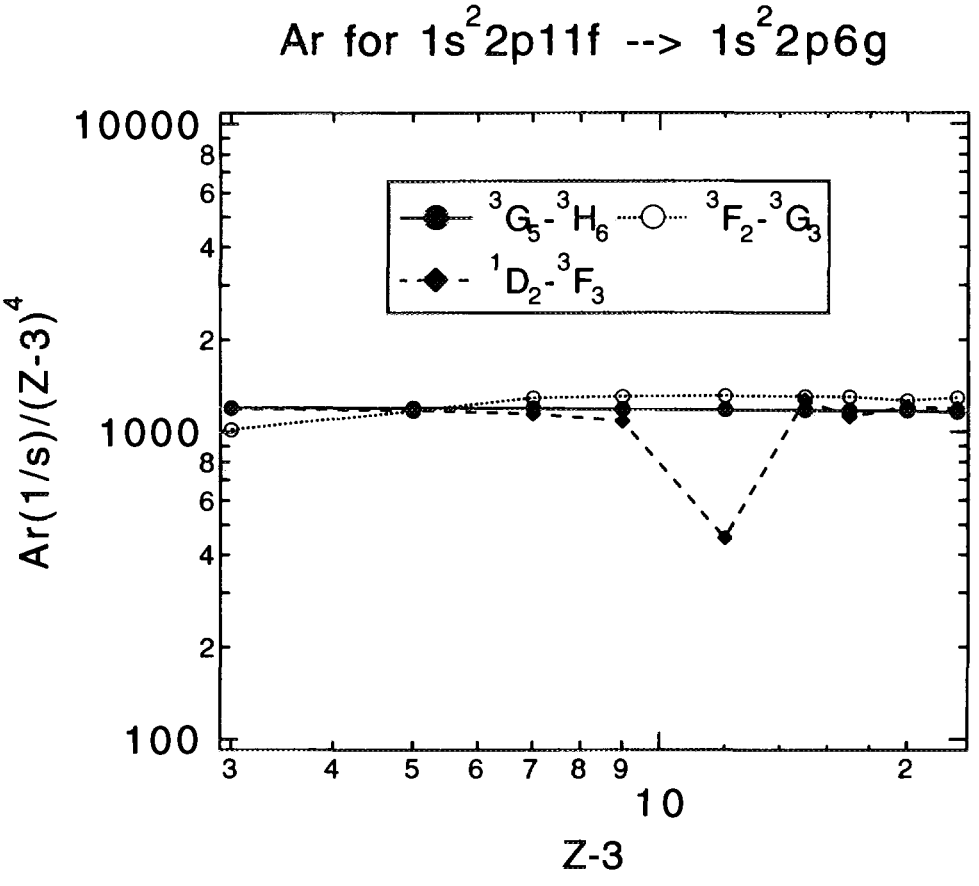

Fig.2-2-2(j)

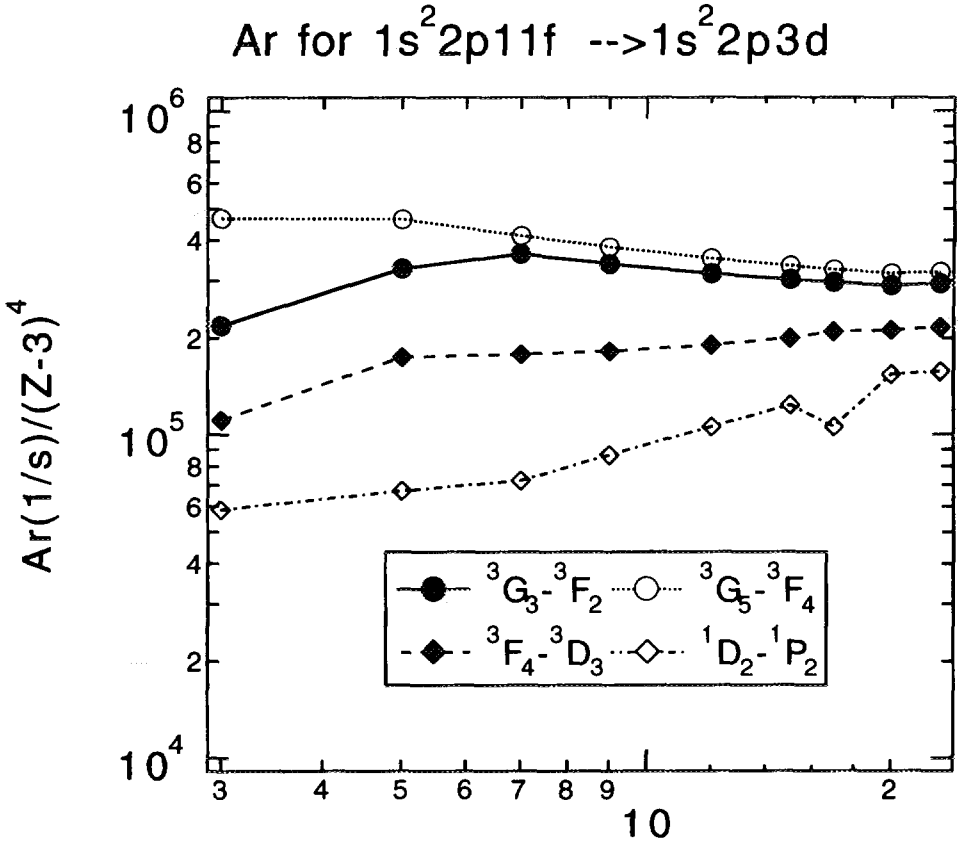

Fig.2-2-2(k)

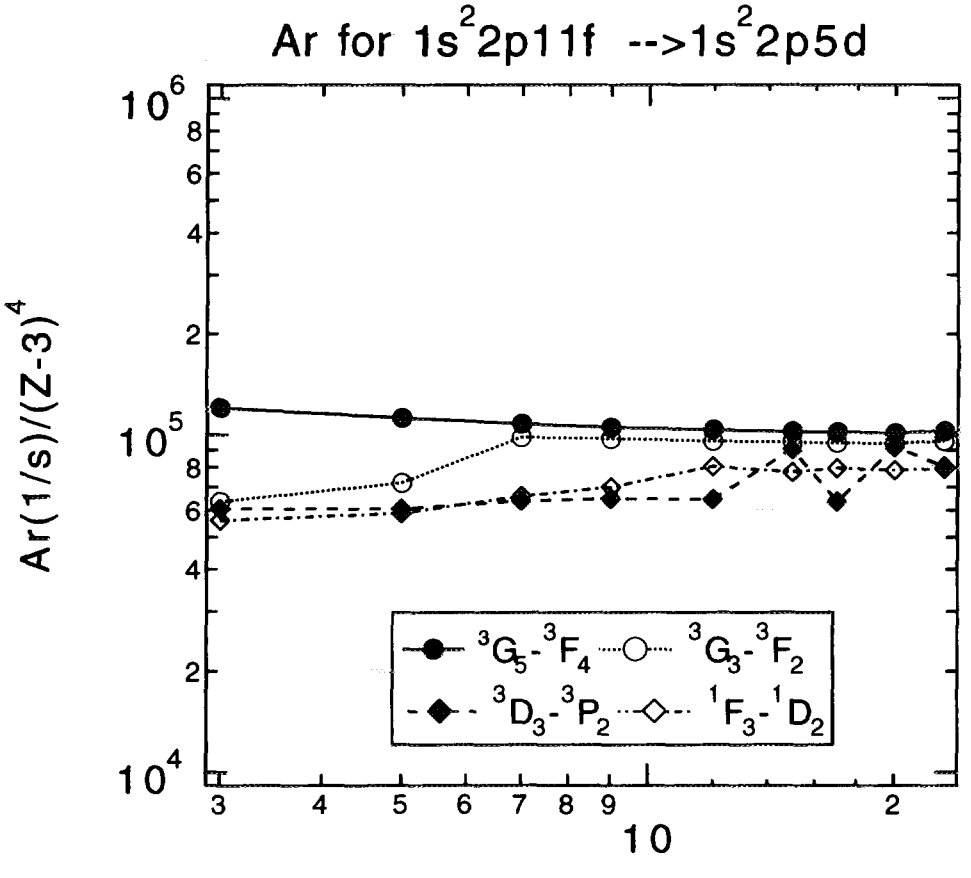

Fig.2-2-2(l)

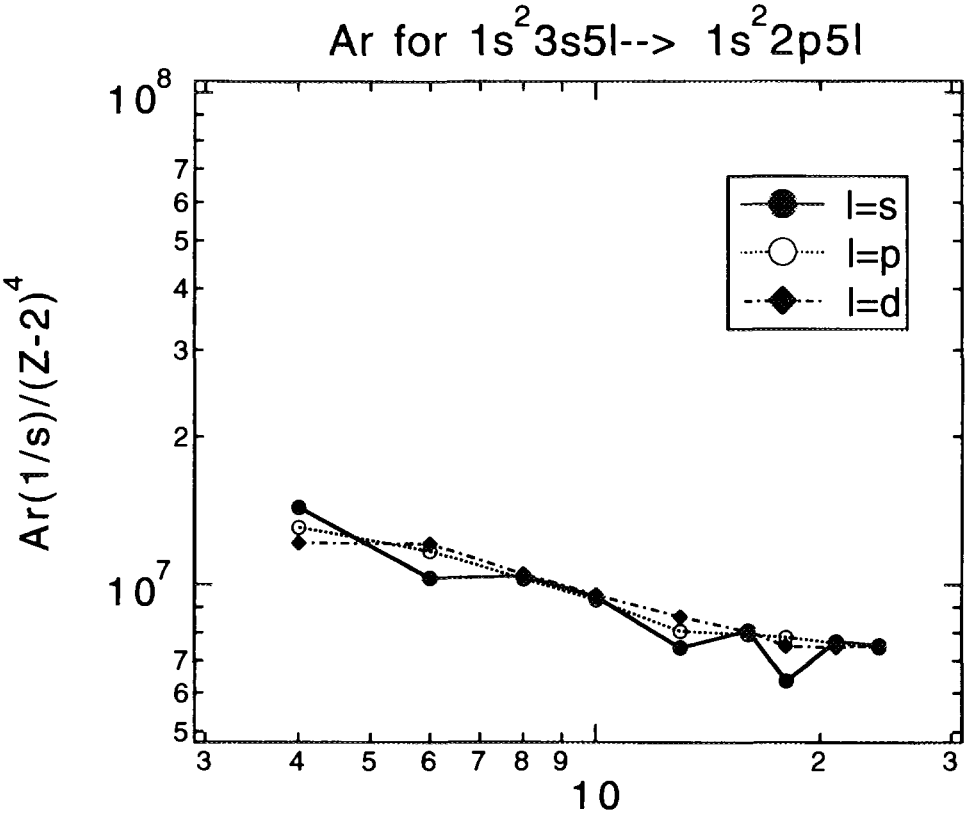

Fig.2-3(a)

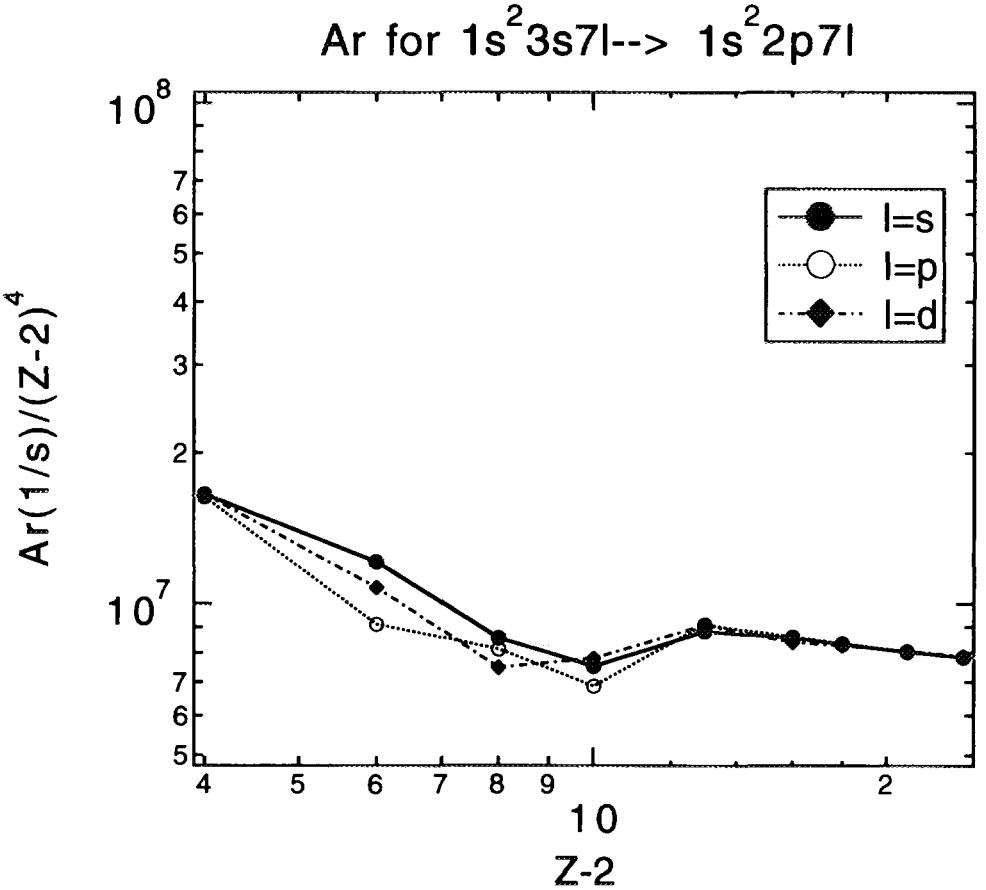

Fig.2-3(b)

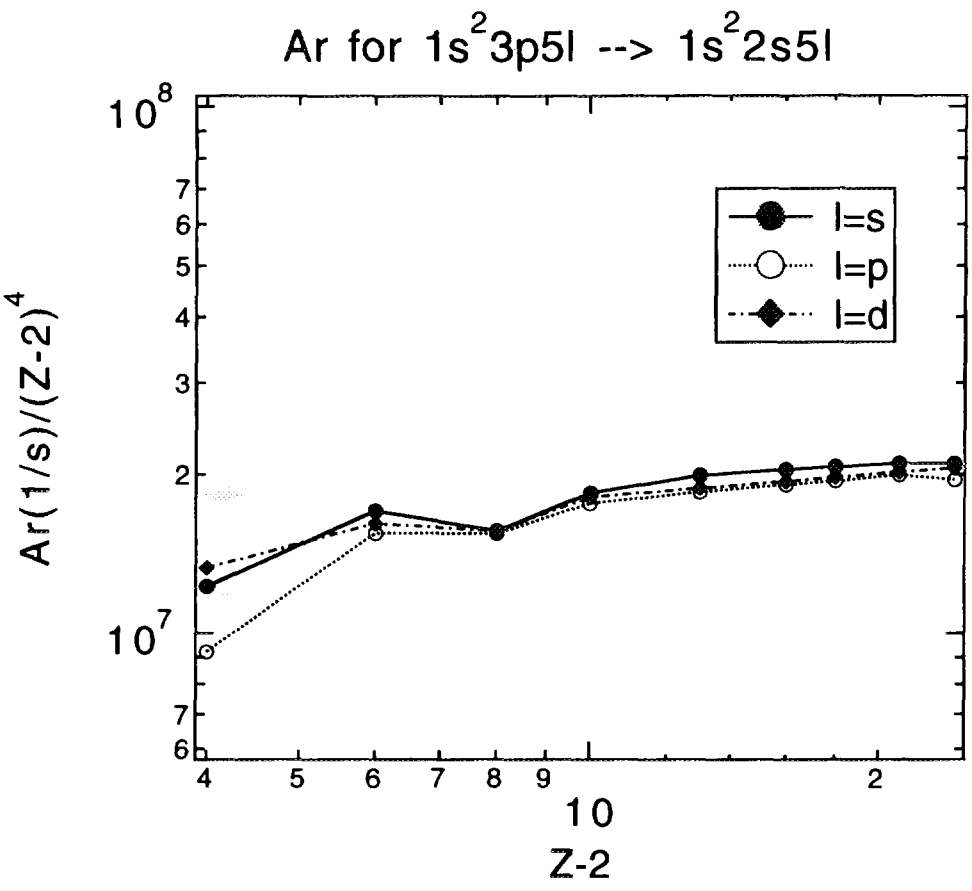

Fig.2-3(c)

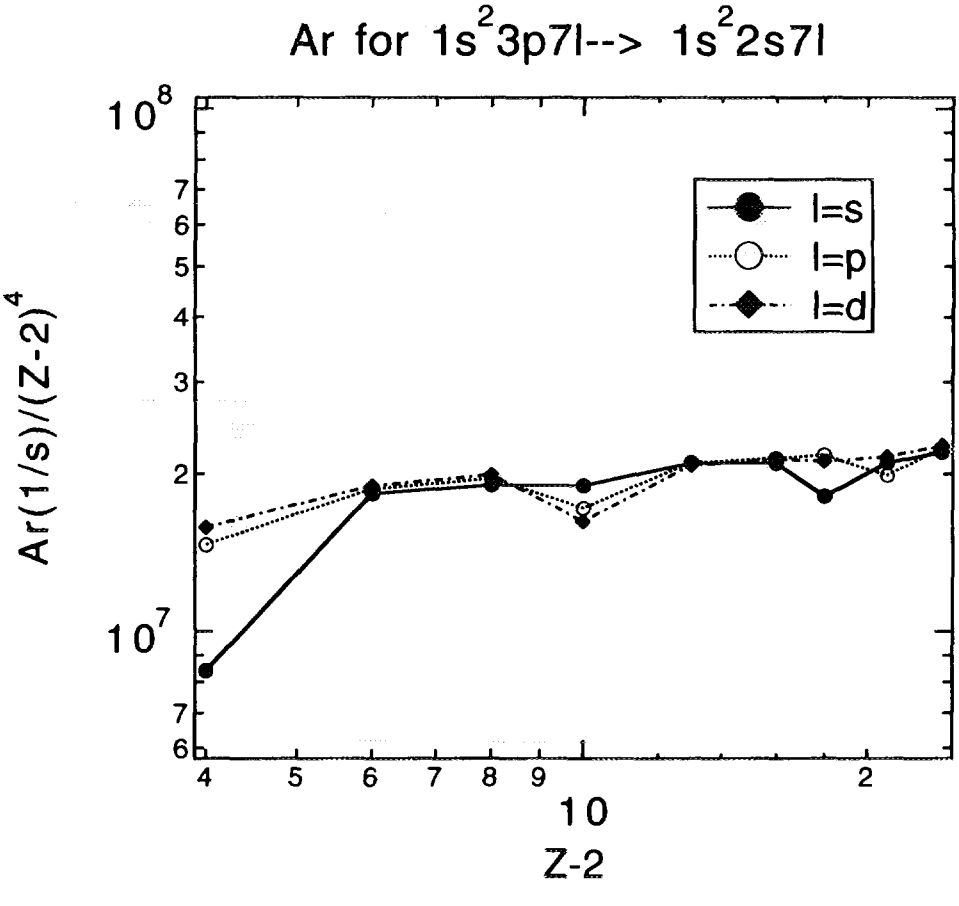

Fig.2-3(d)

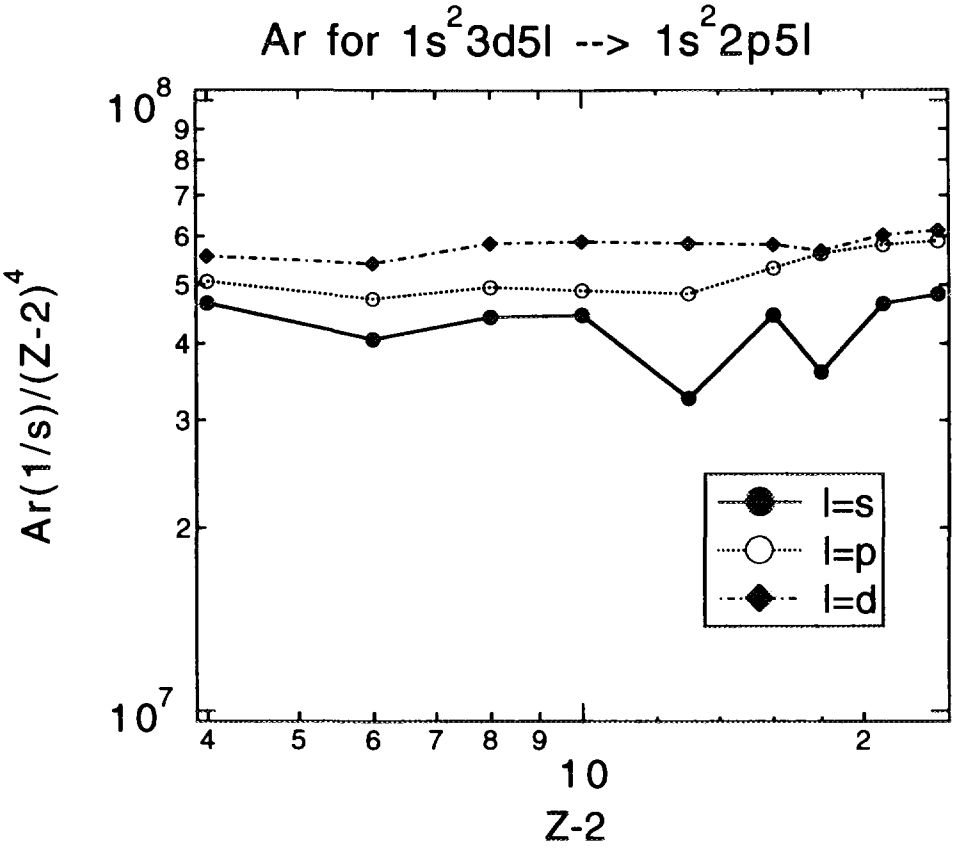

Fig.2-3(e)

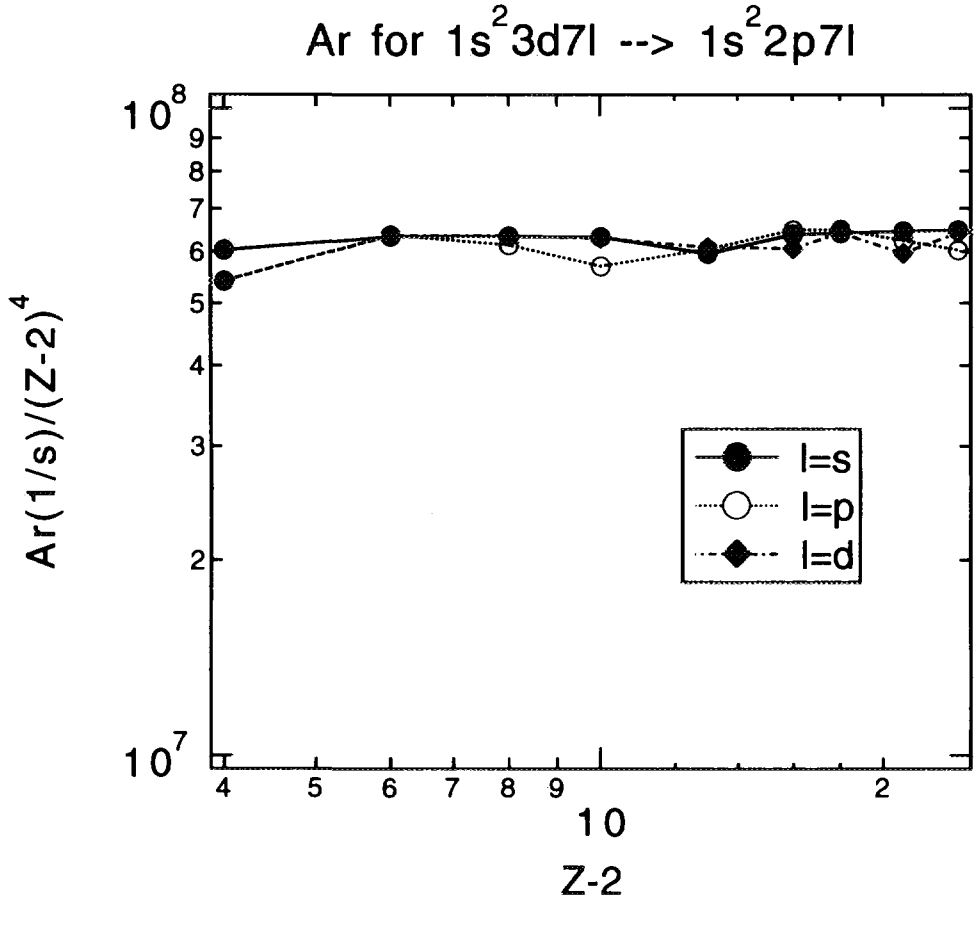

Fig.2-3(f)

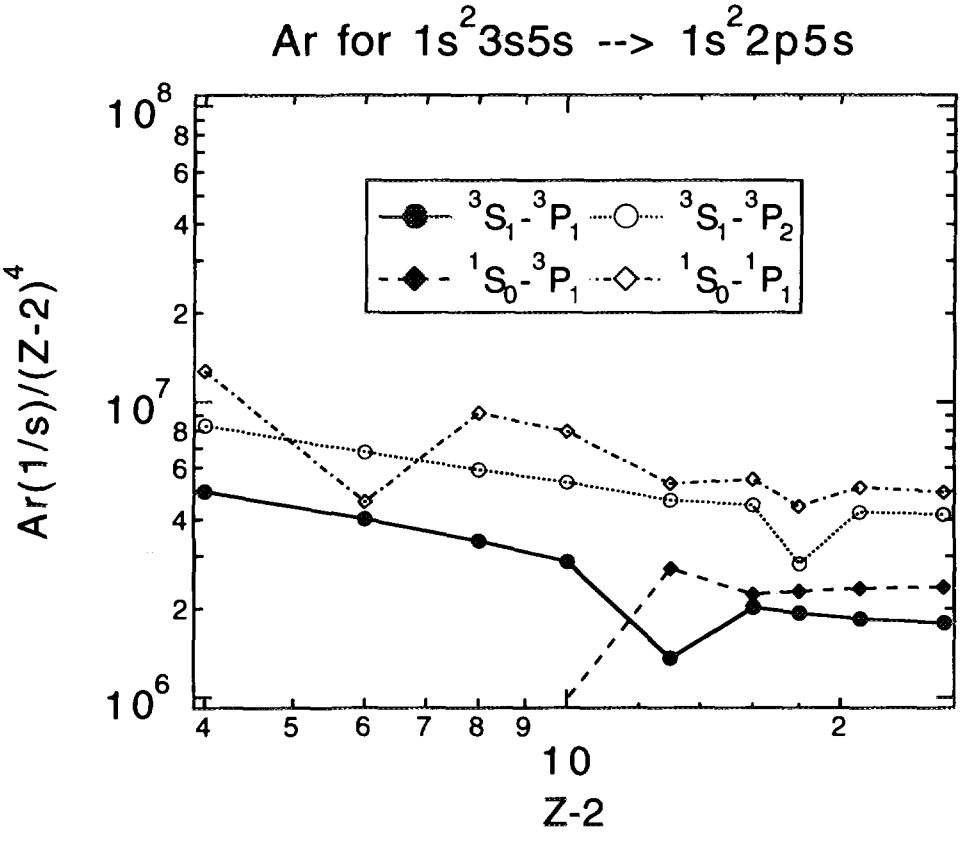

Fig.2-3-2(a)

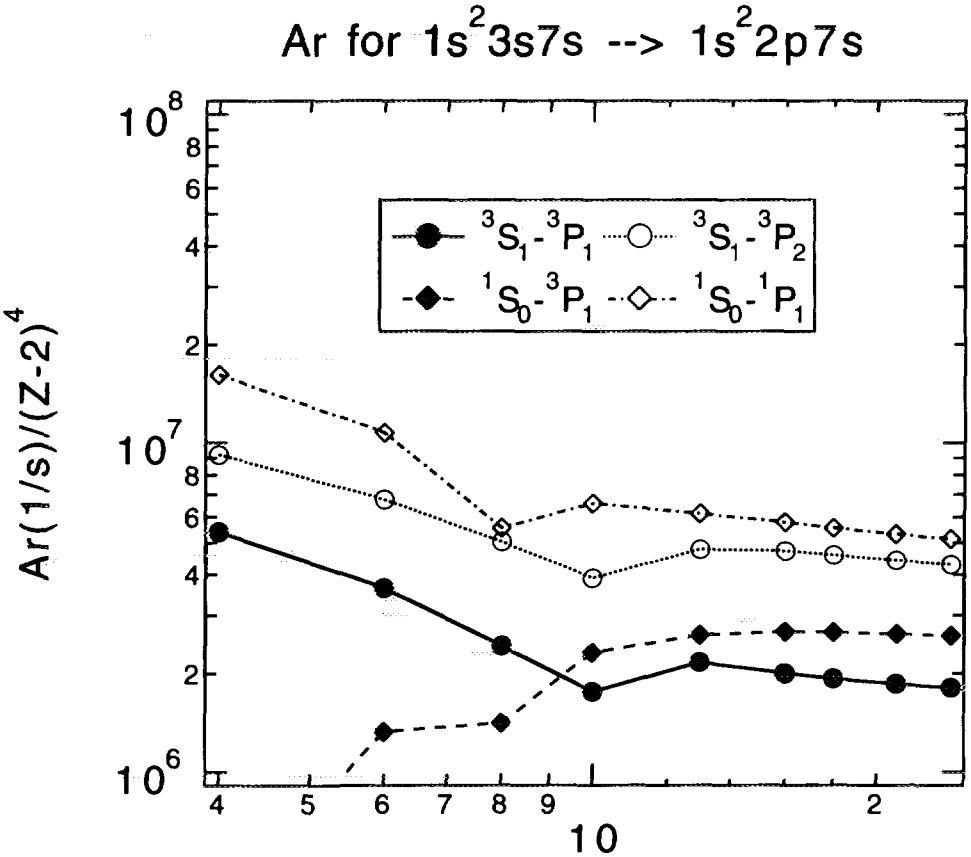

Fig.2-3-2(b)

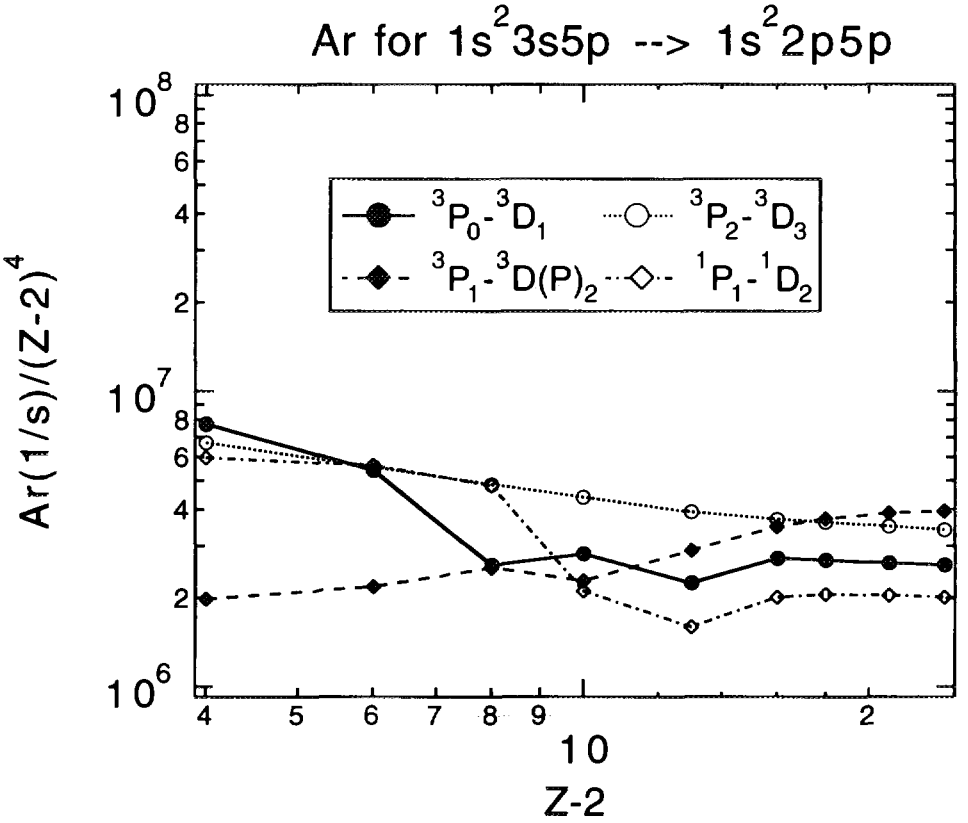

Fig.2-3-2(c)

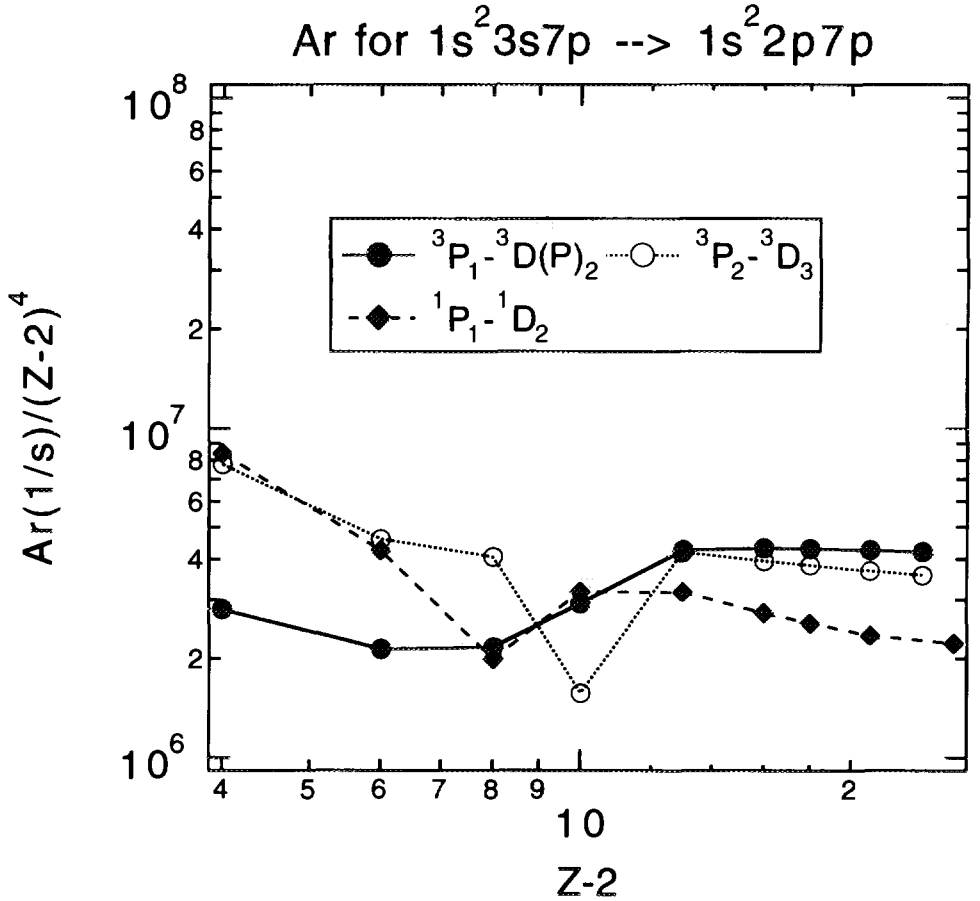

Fig.2-3-2(d)

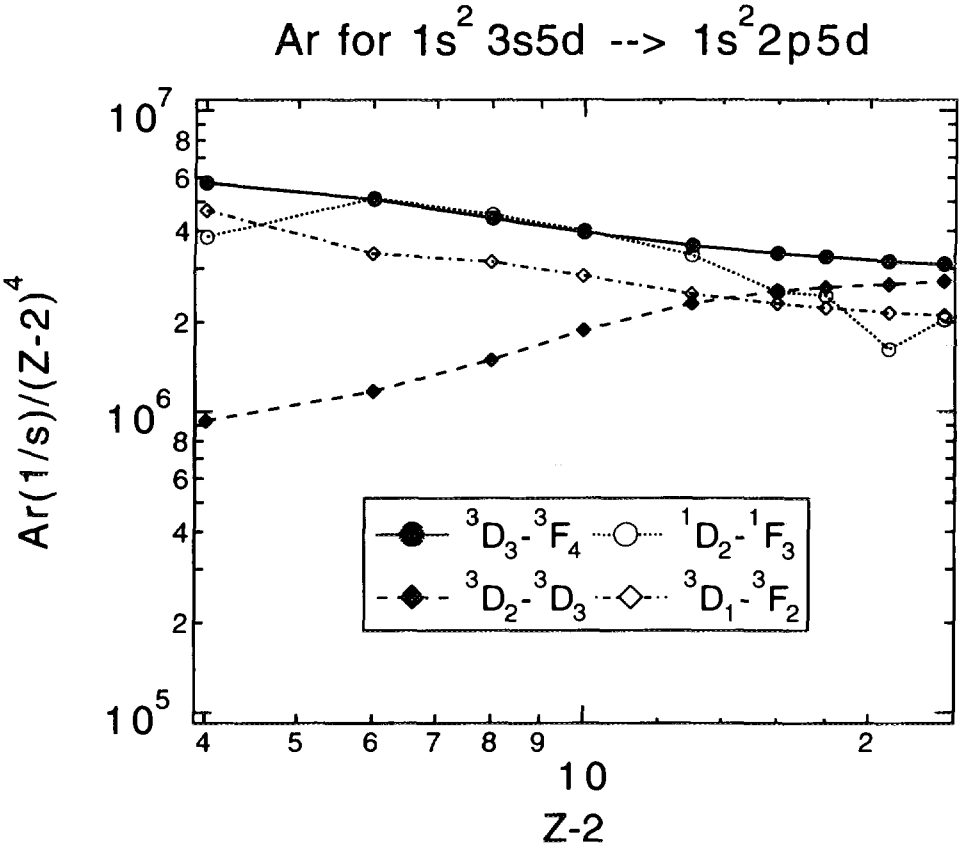

Fig.2-3-2(e)

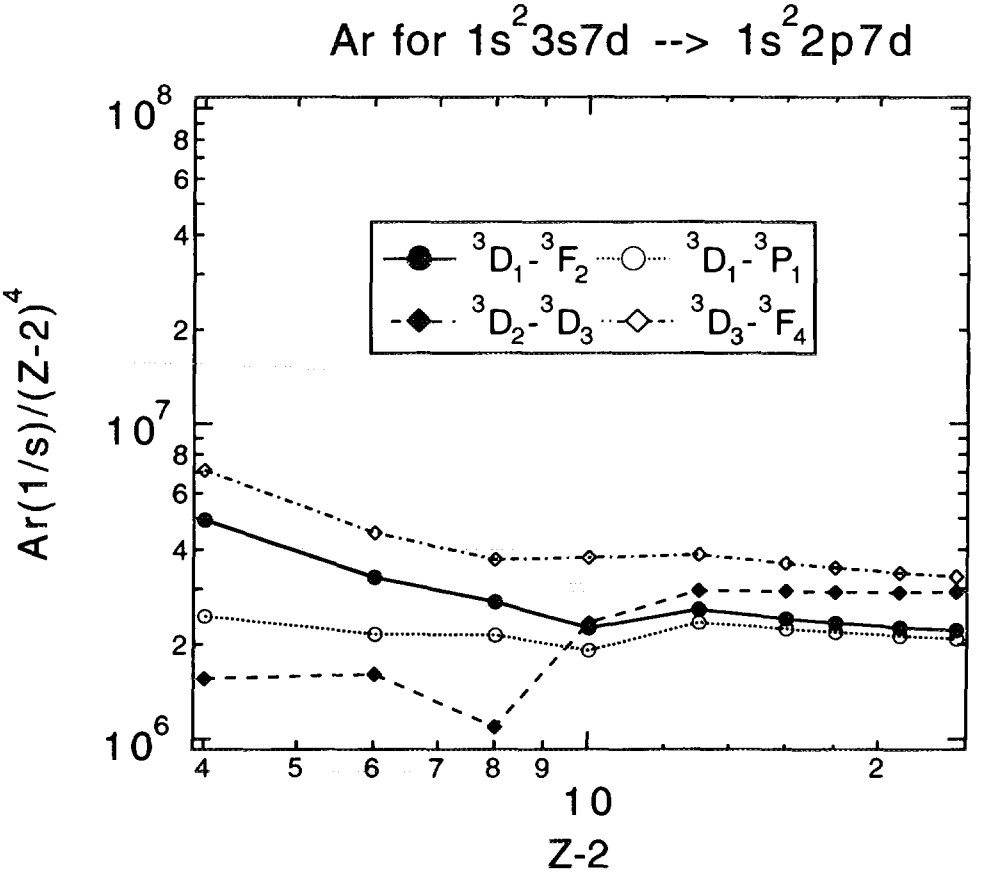

Fig.2-3-2(f)

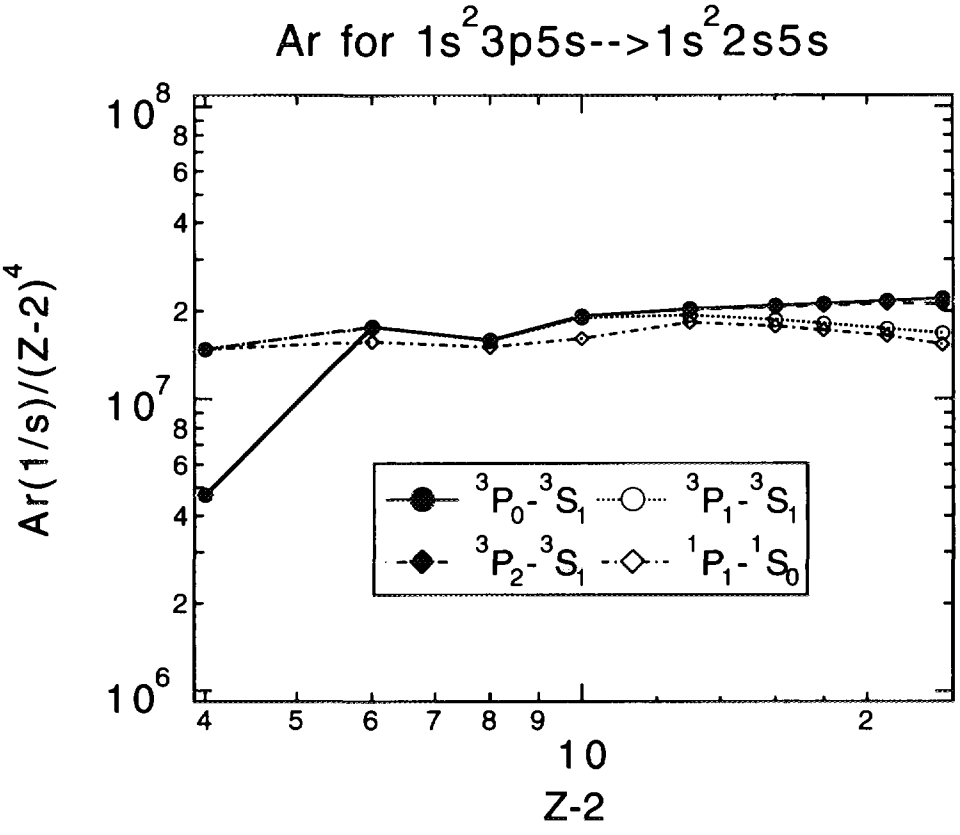

Fig.2-3-3(a)

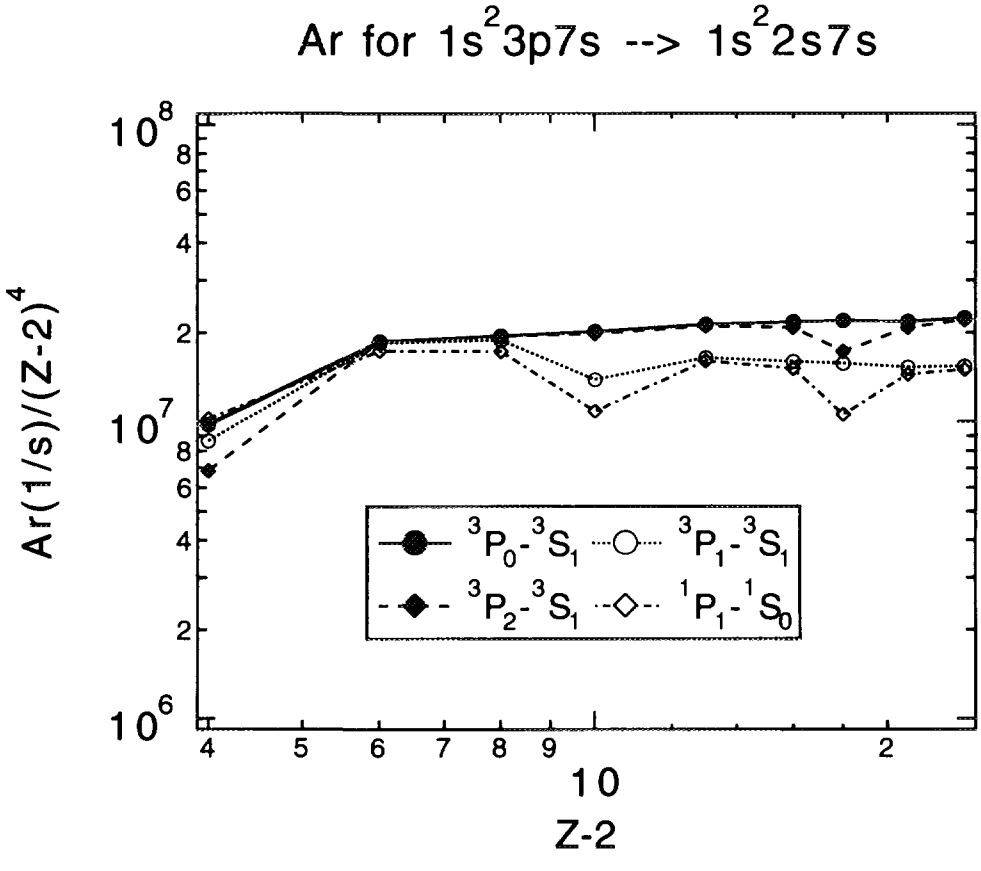

Fig.2-3-3(b)

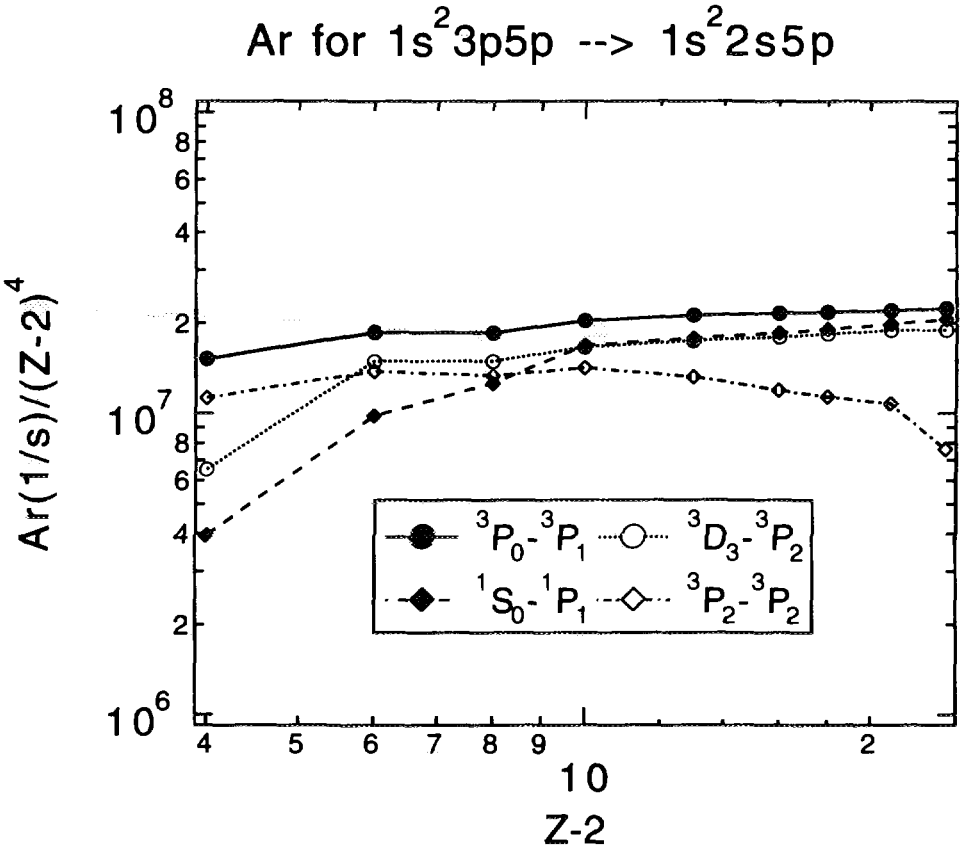

Fig.2-3-3(c)

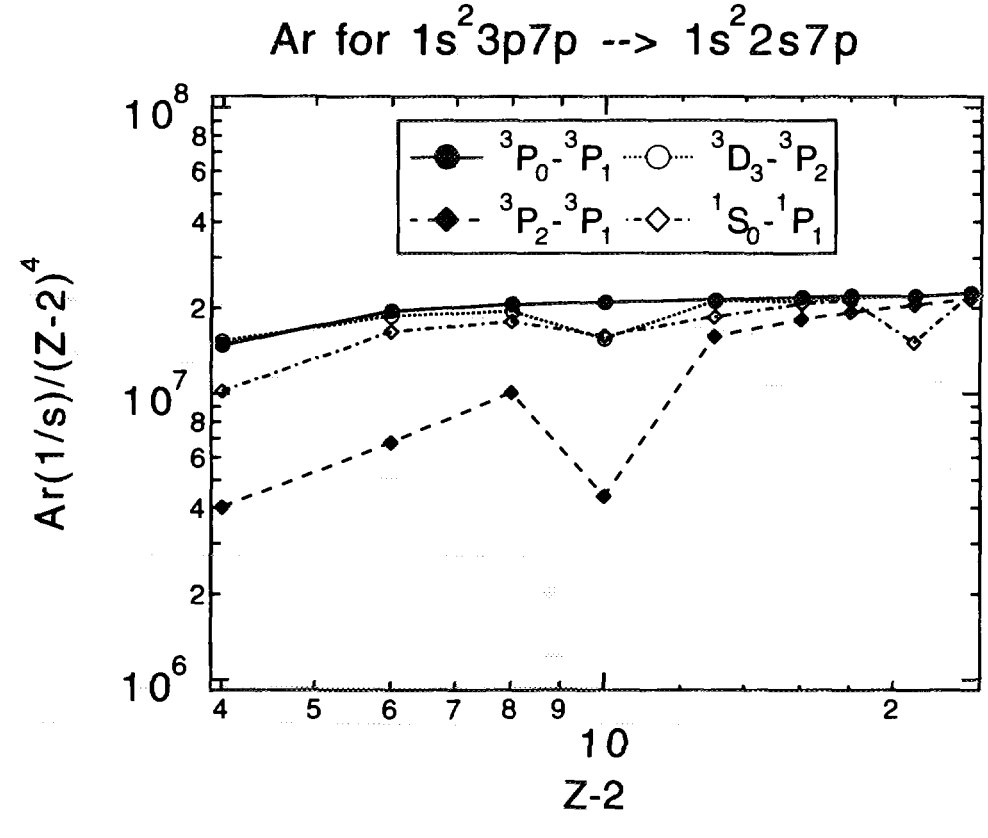

Fig.2-3-3(d)

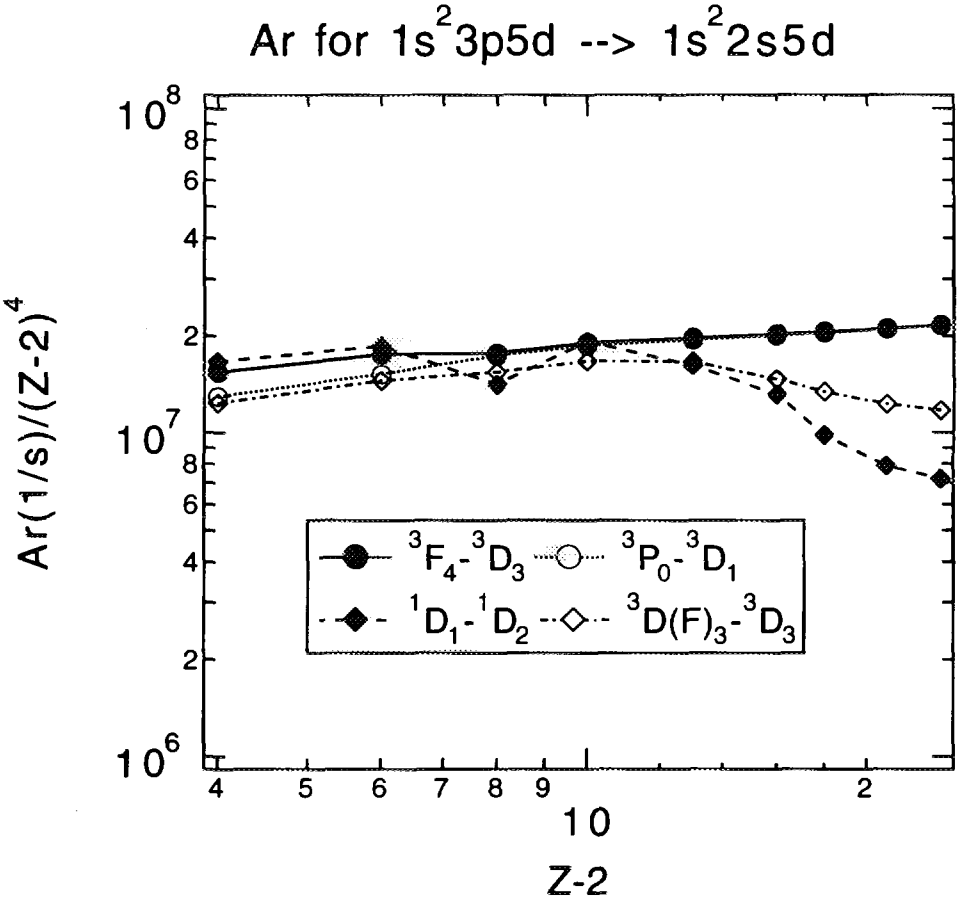

Fig.2-3-3(e)

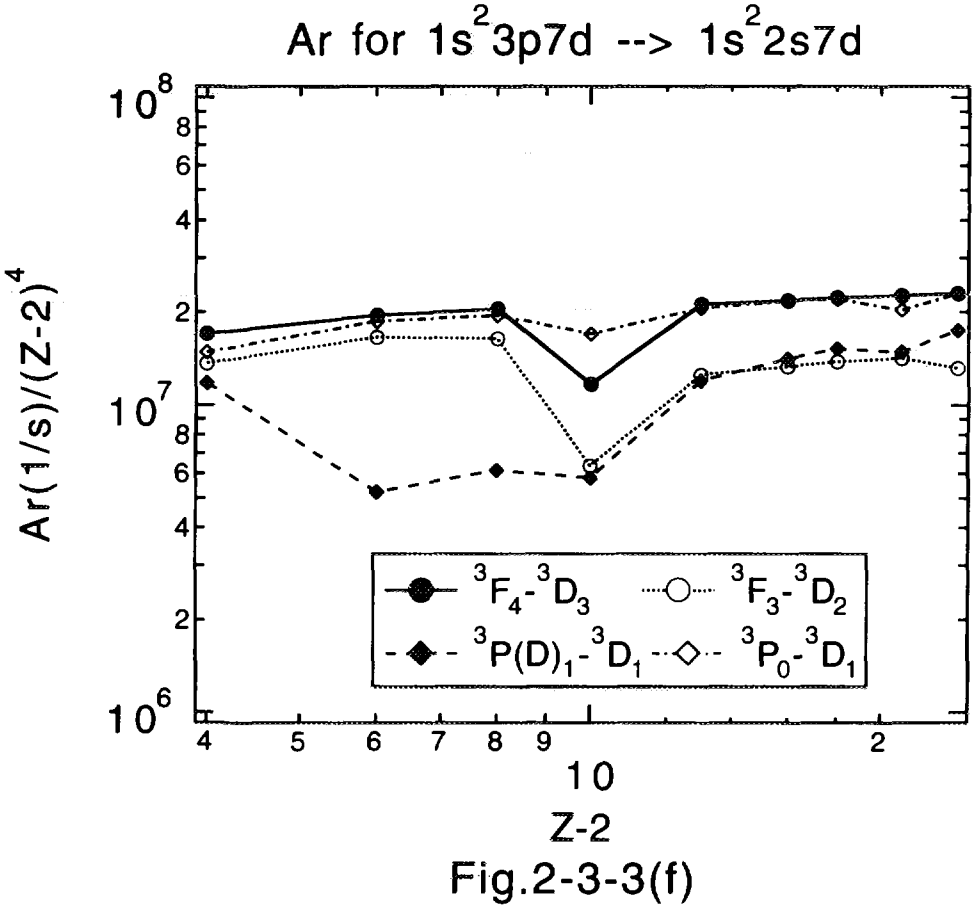

Fig.2-3-3(f)

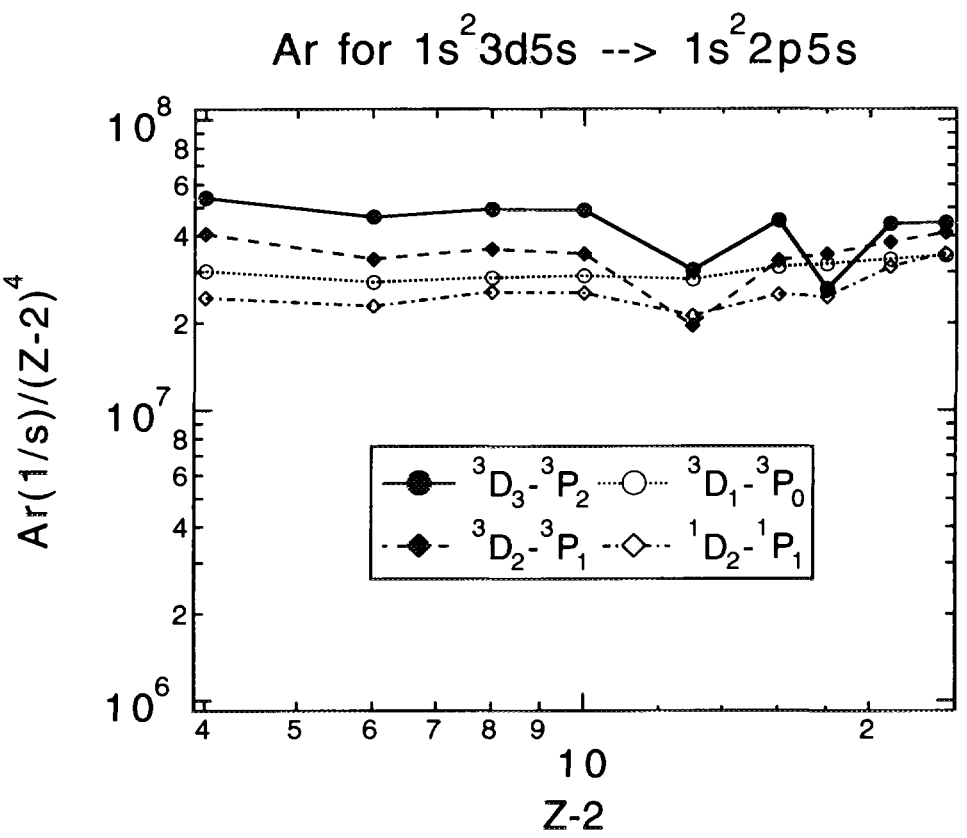

Fig.2-3-4(a)

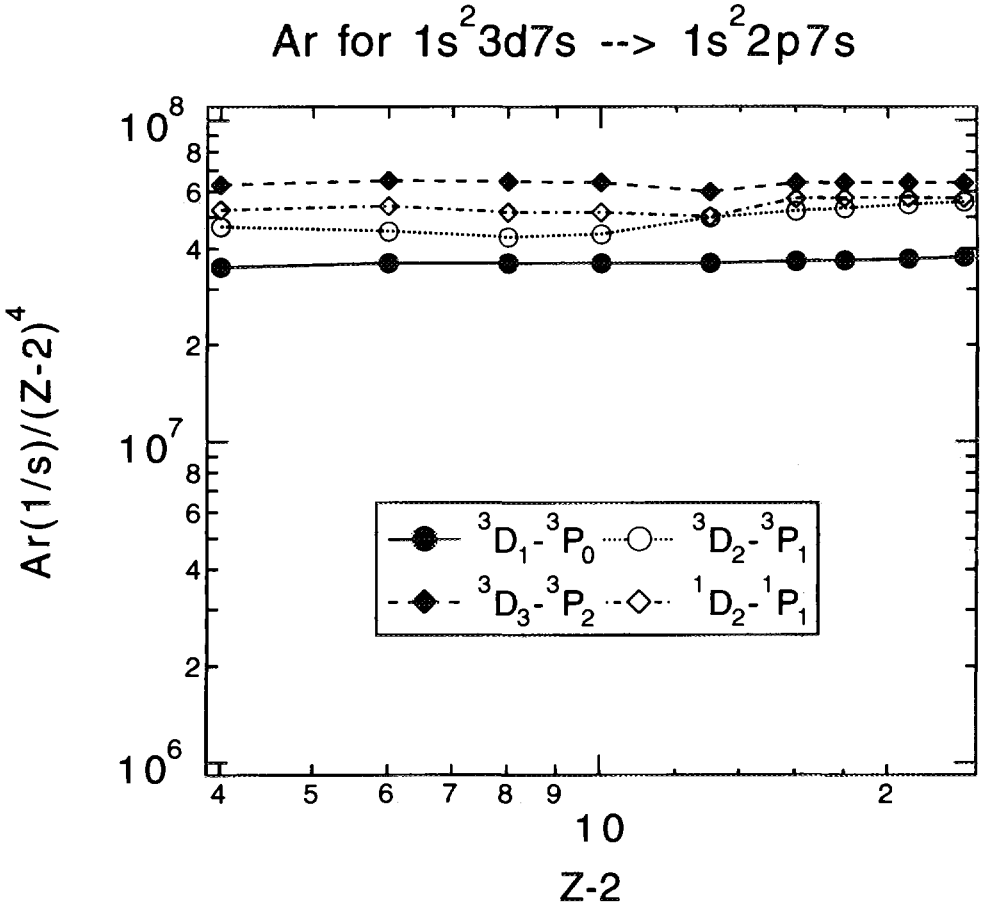

Fig.2-3-4(b)

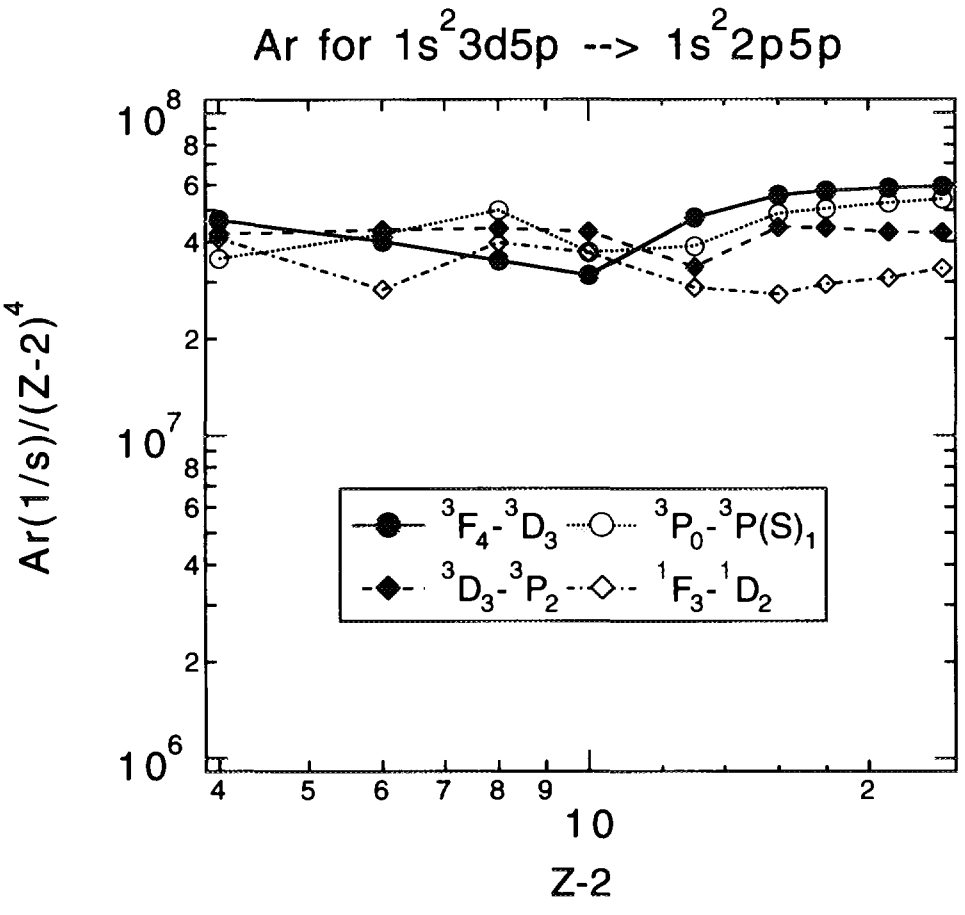

Fig.2-3-4(c)

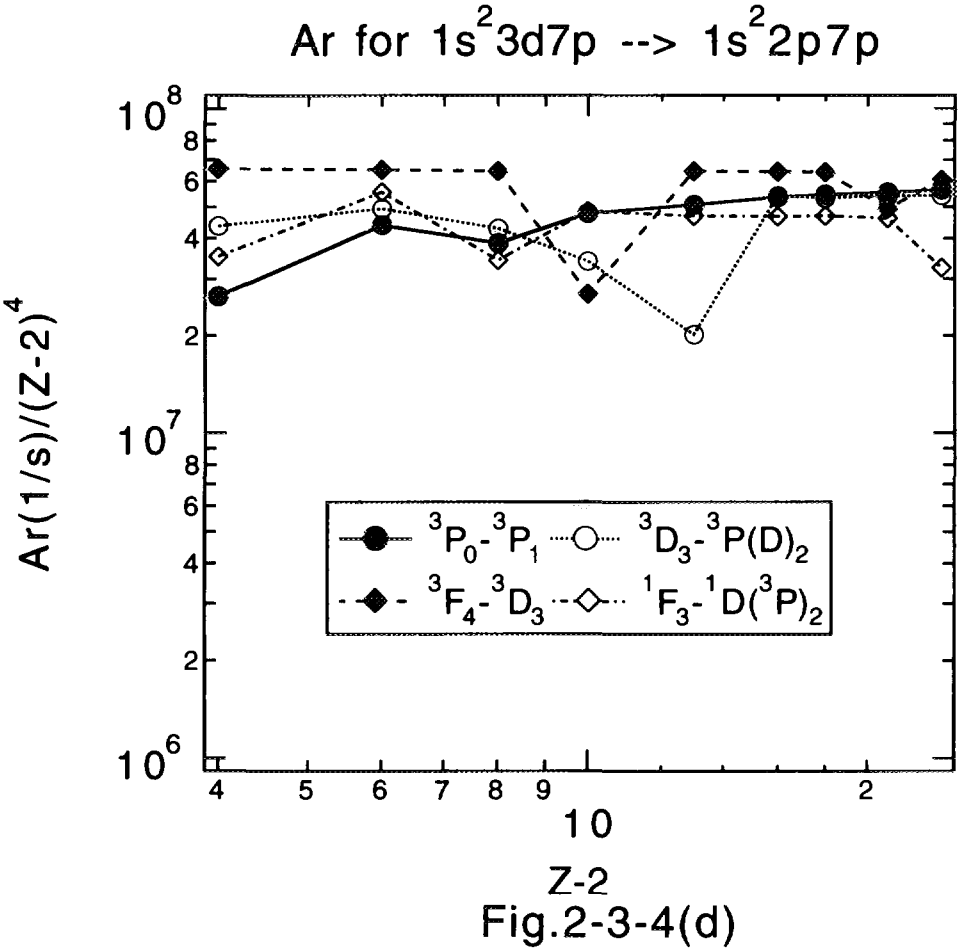

Fig.2-3-4(d)

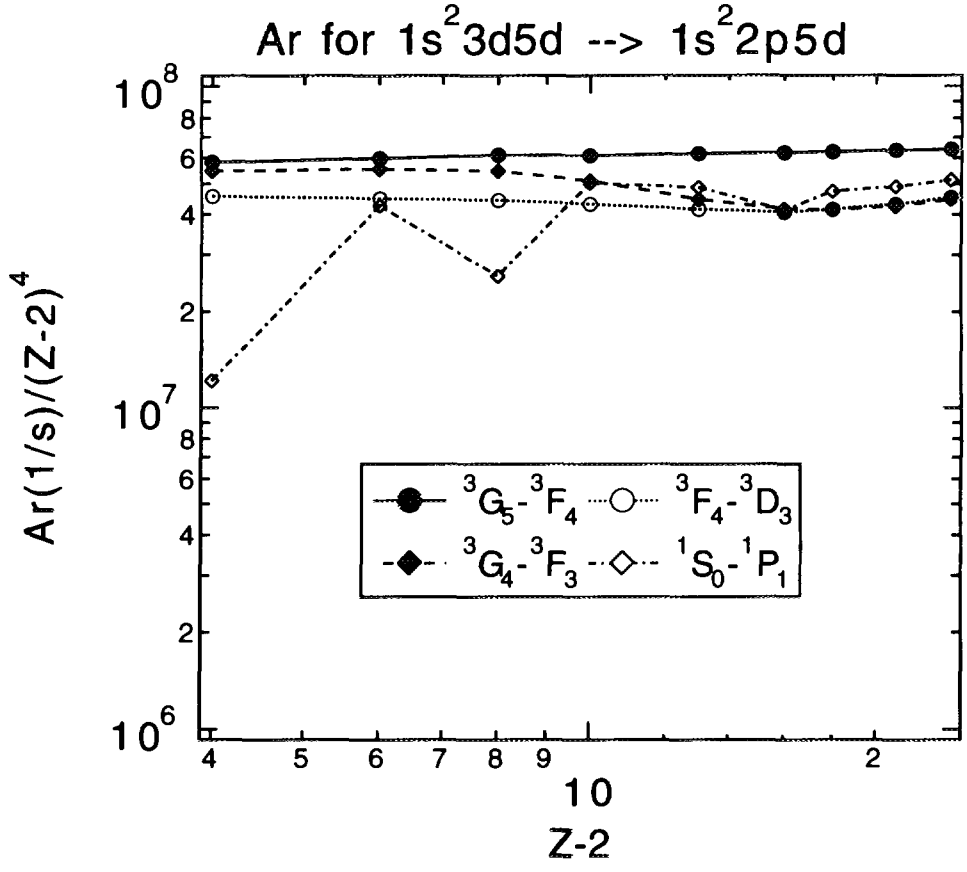

Fig.2-3-4(e)

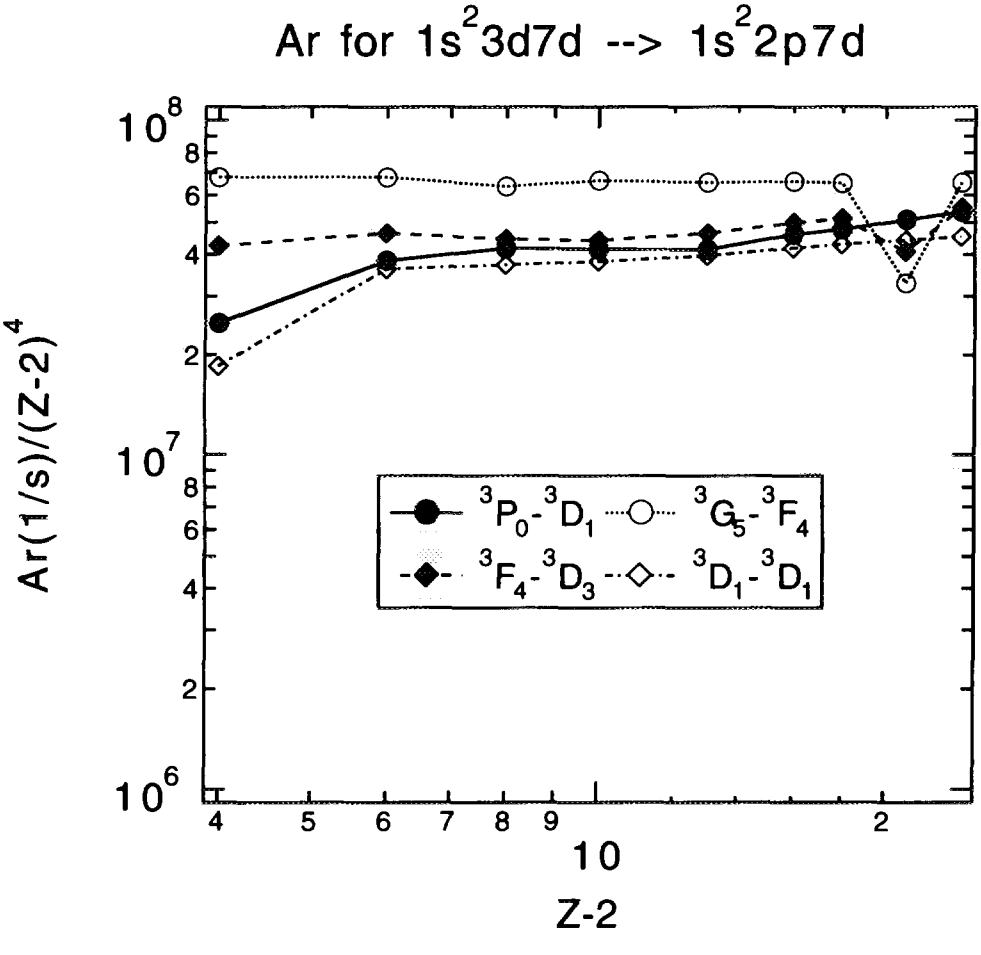

Fig.2-3-4(f)

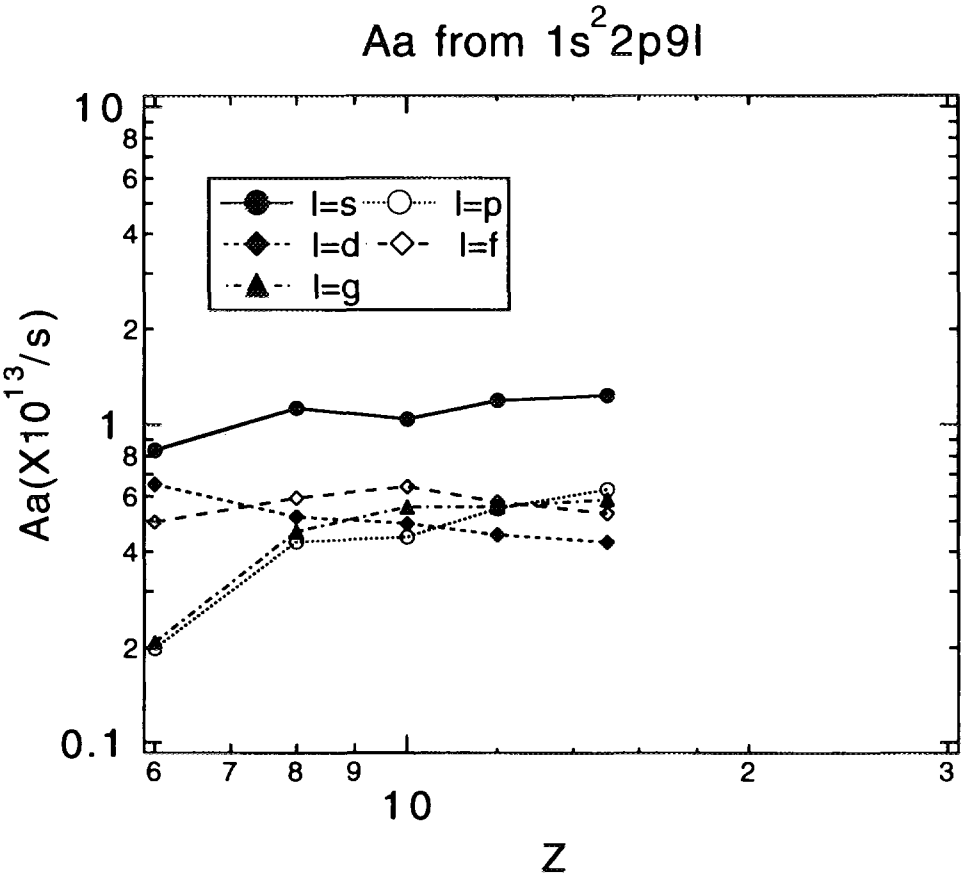

Fig.3-1(a)

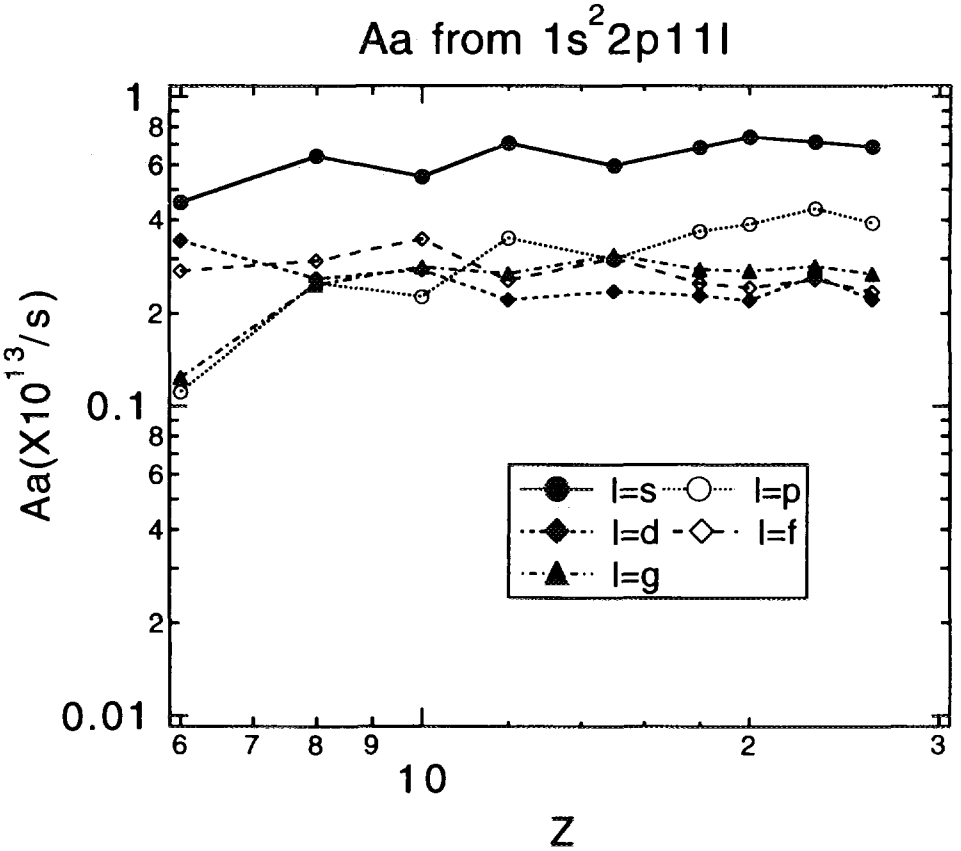

Fig.3-1(b)

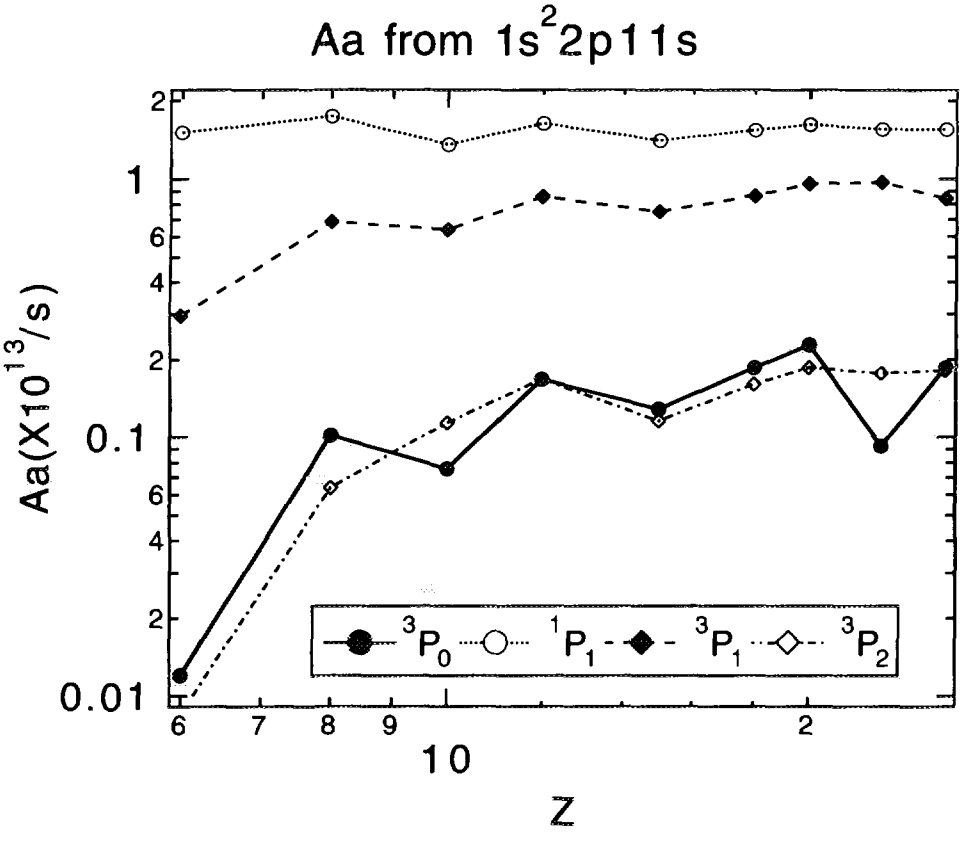

Fig.3-1-2(a)

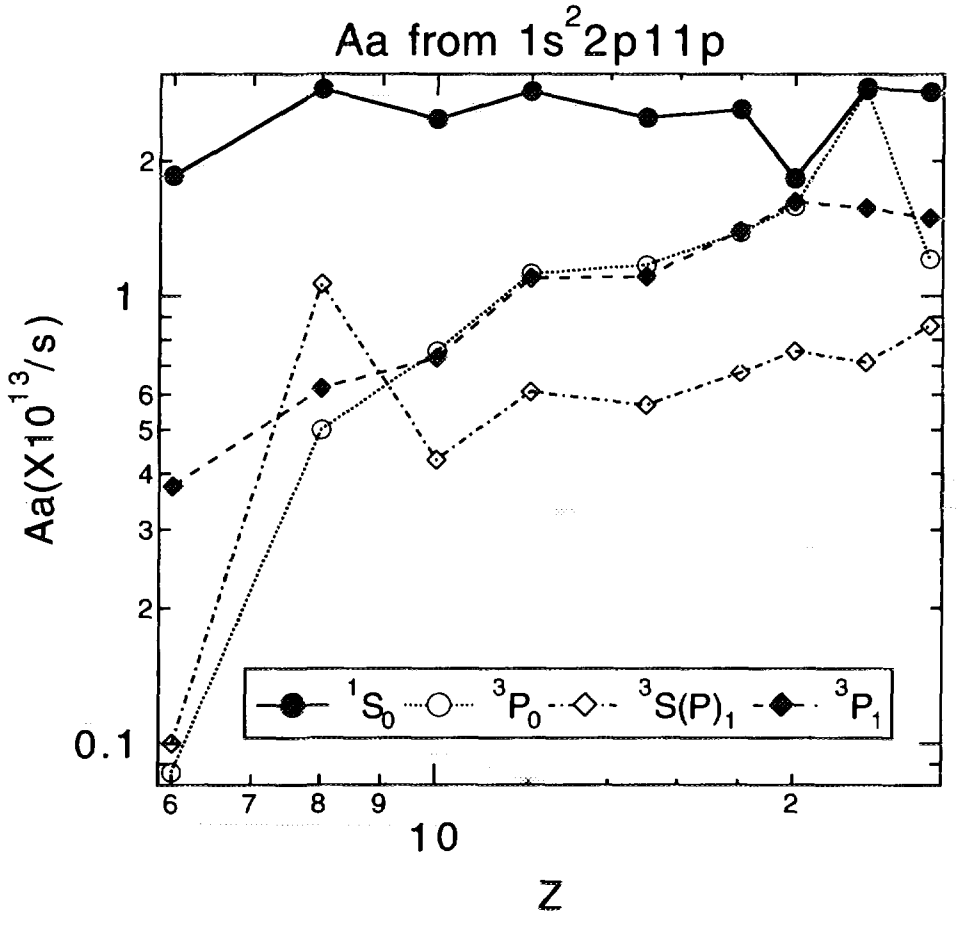

Fig.3-1-2(b)

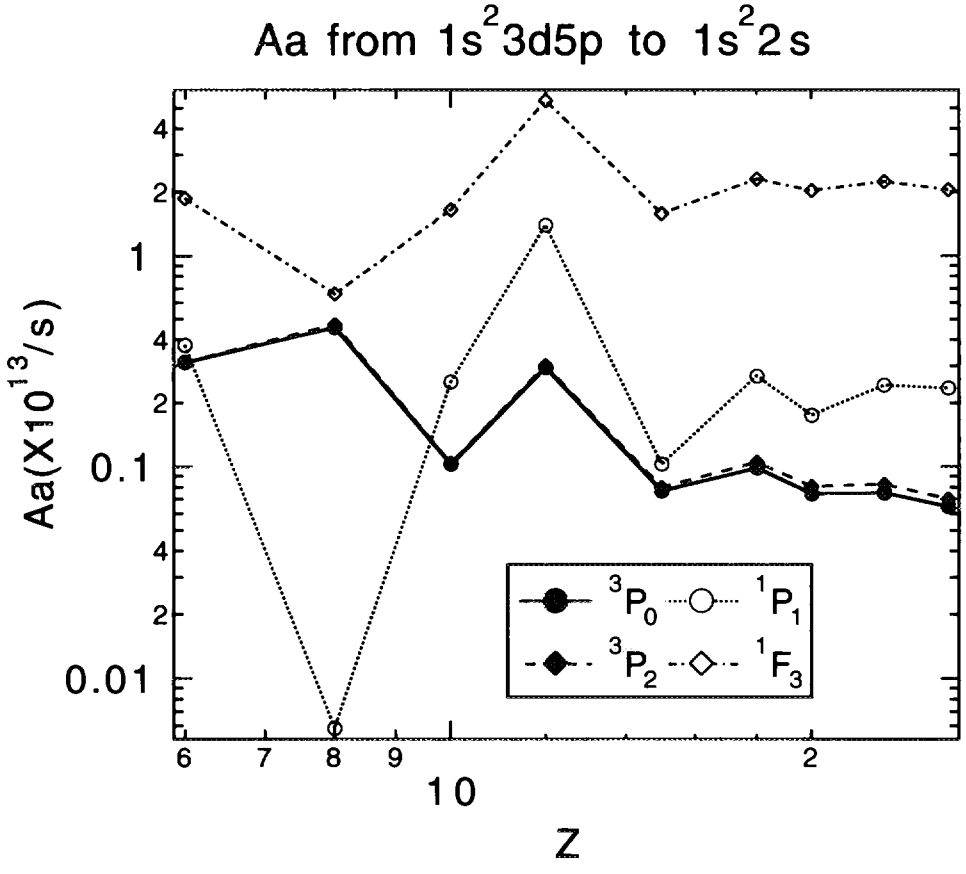

Fig.3-2-4(c)

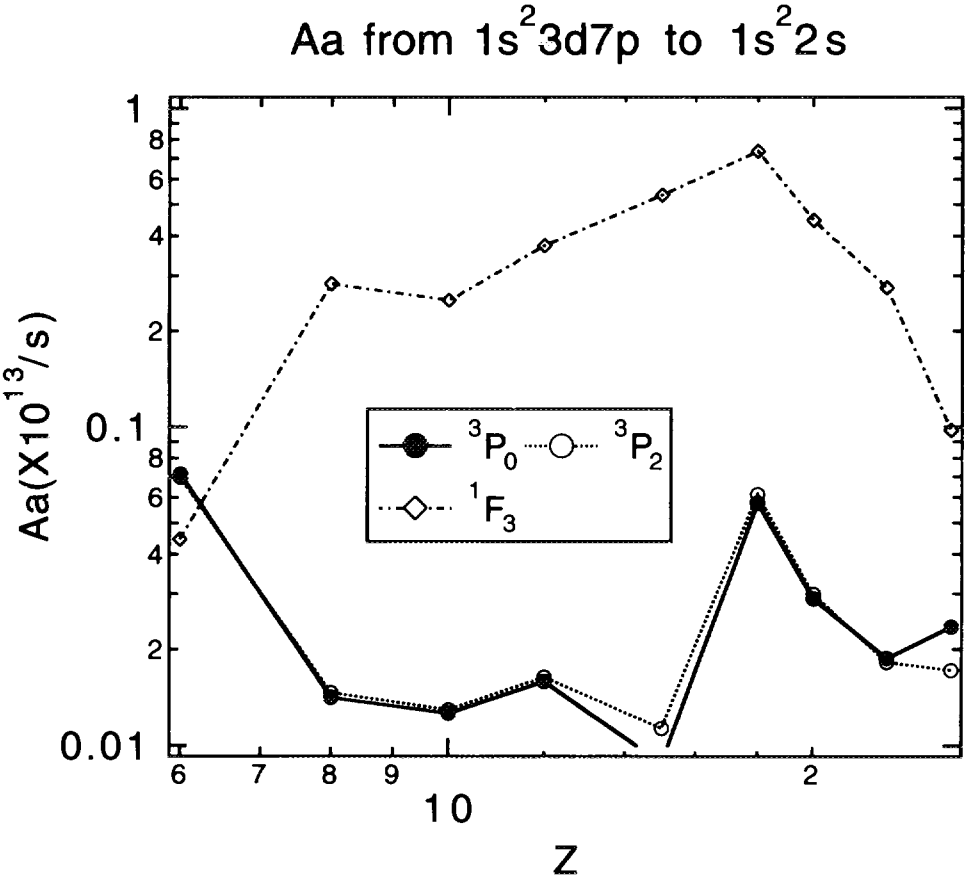

Fig.3-2-4(d)

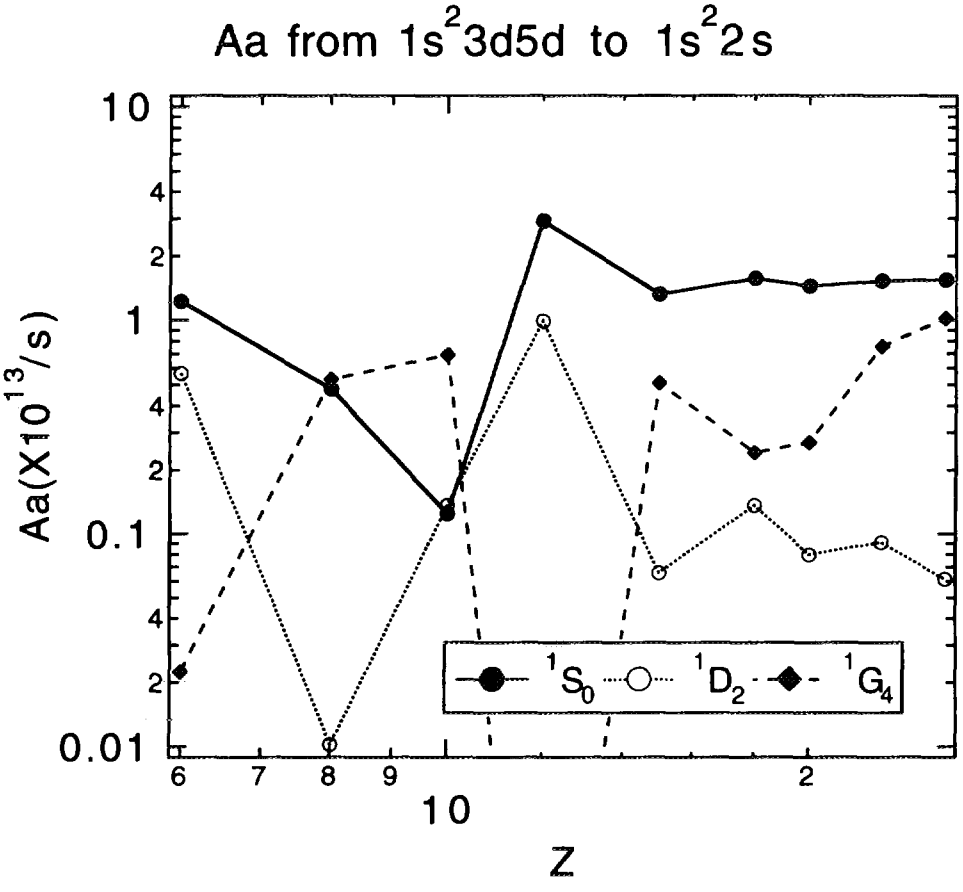

Fig.3-2-4(e)

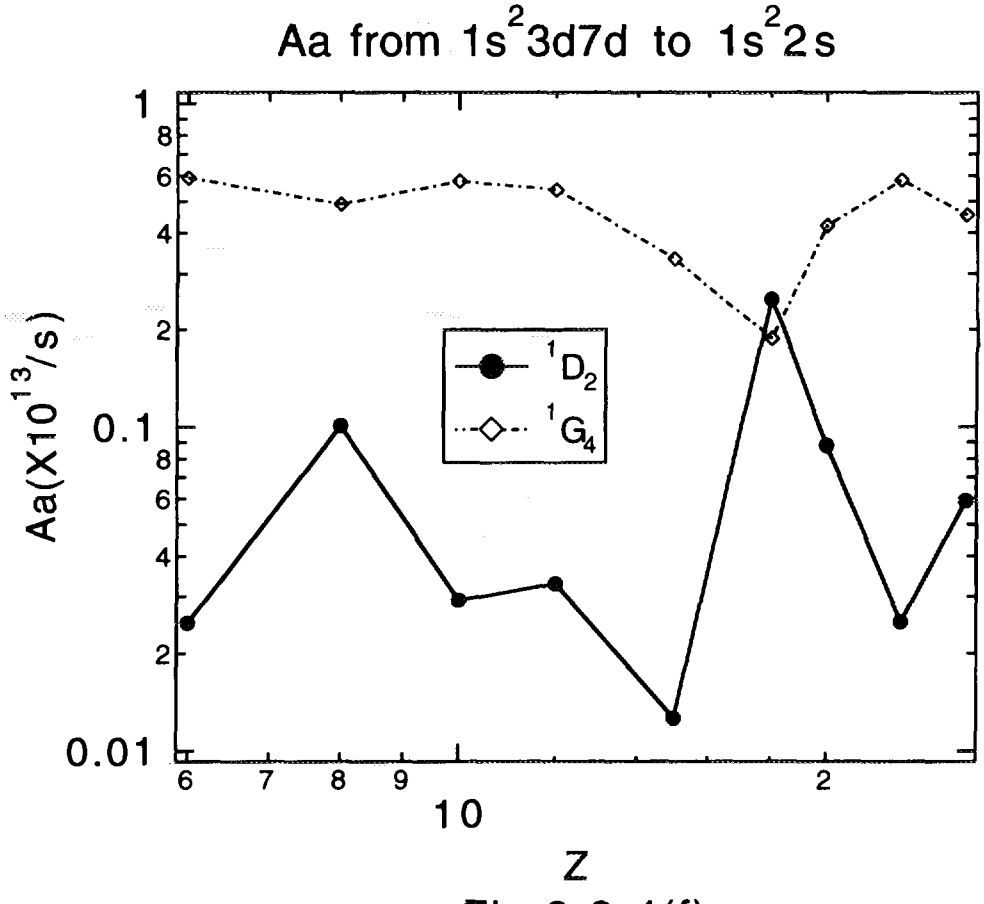

Fig.3-2-4(f)

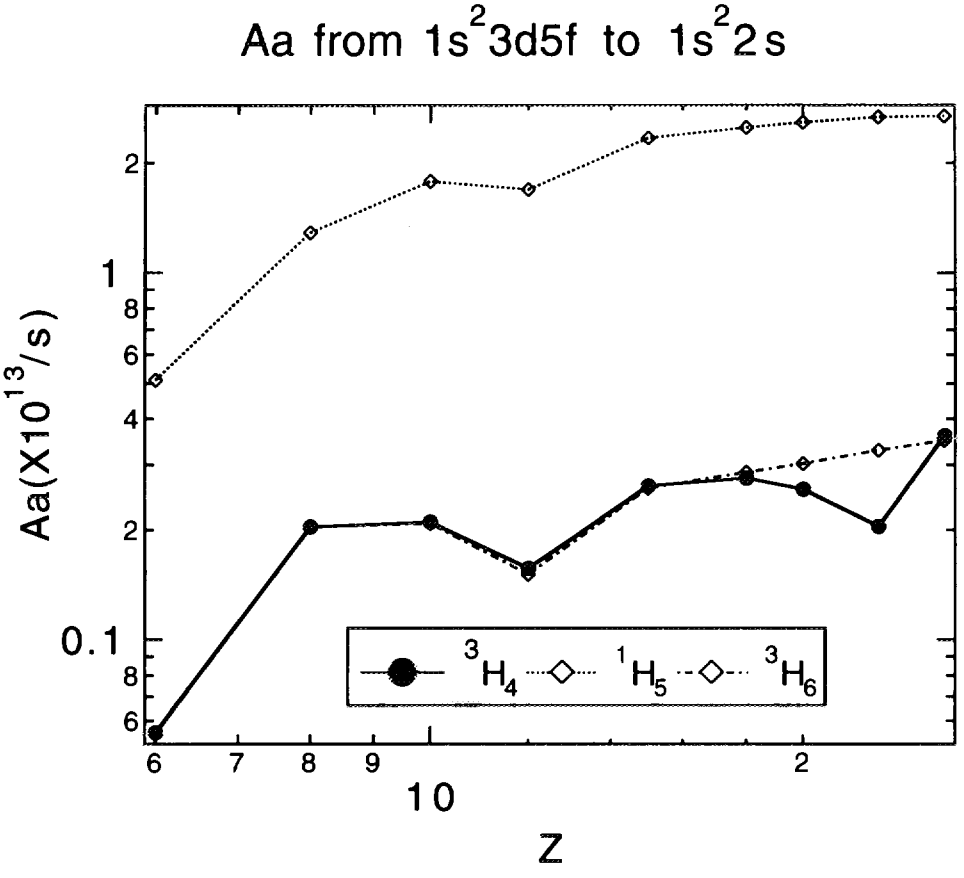

Fig.3-2-4(g)

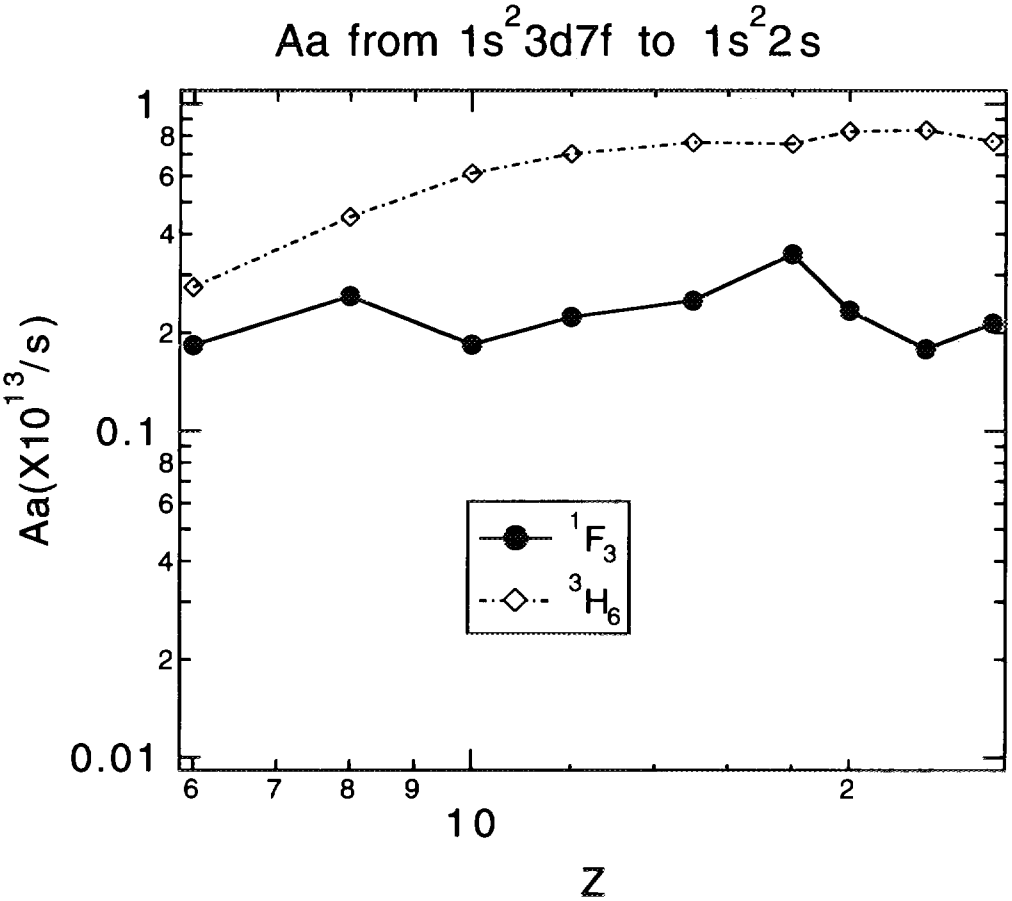

Fig.3-2-4(h)

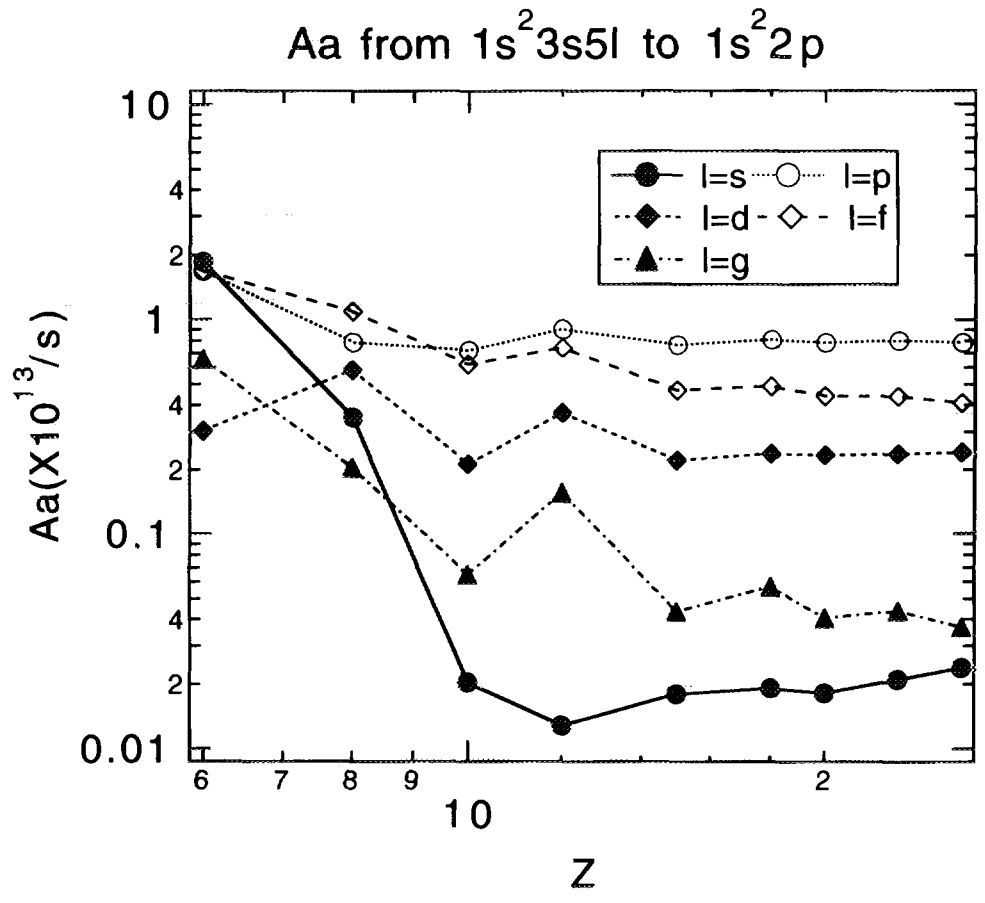

Fig.3-3(a)

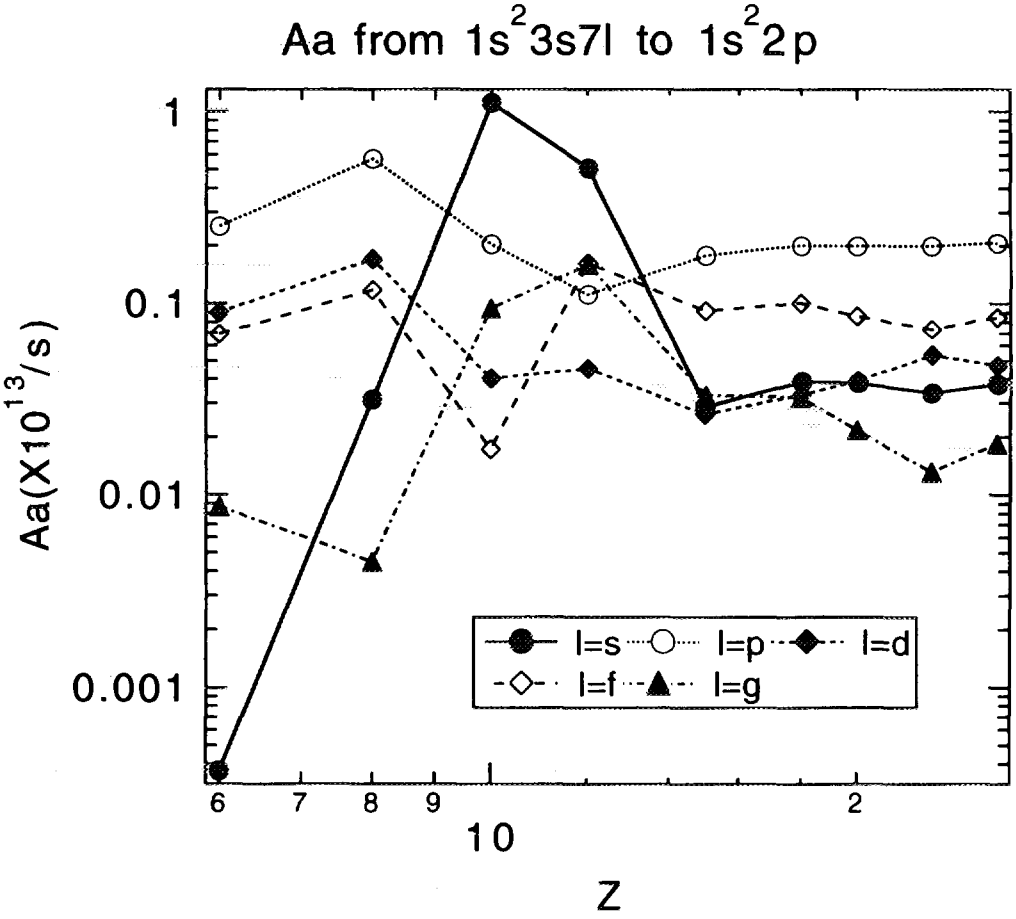

Fig.3-3(b)

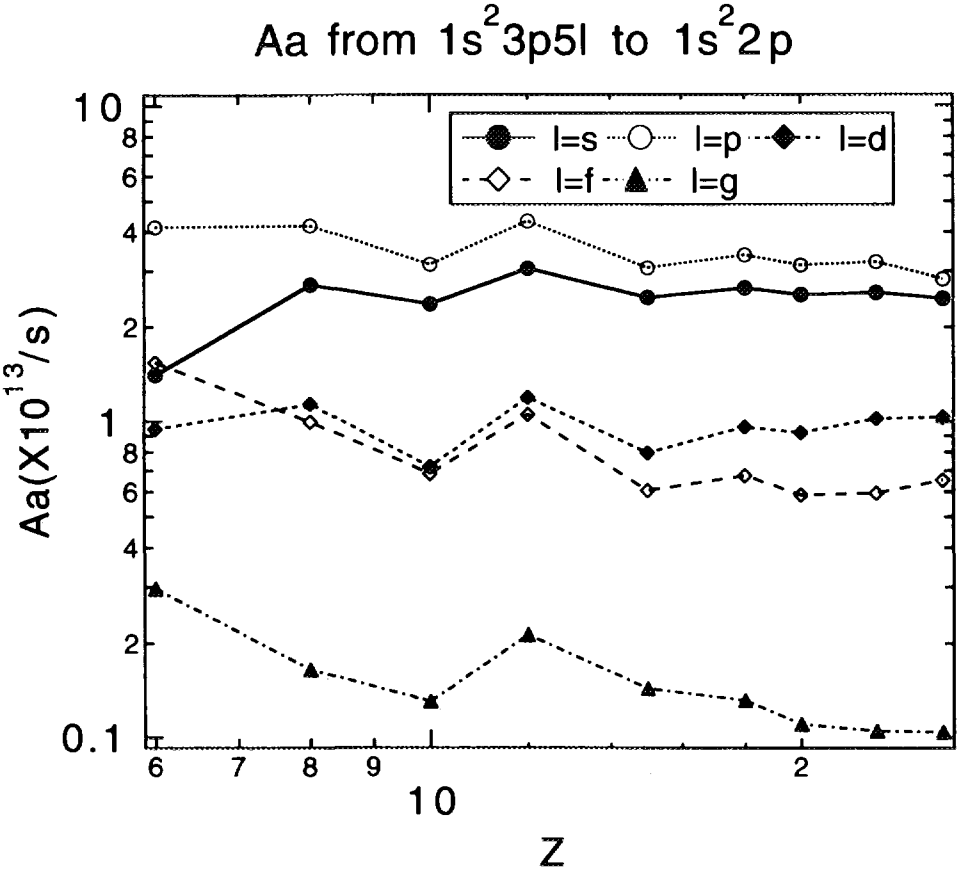

Fig.3-3(c)

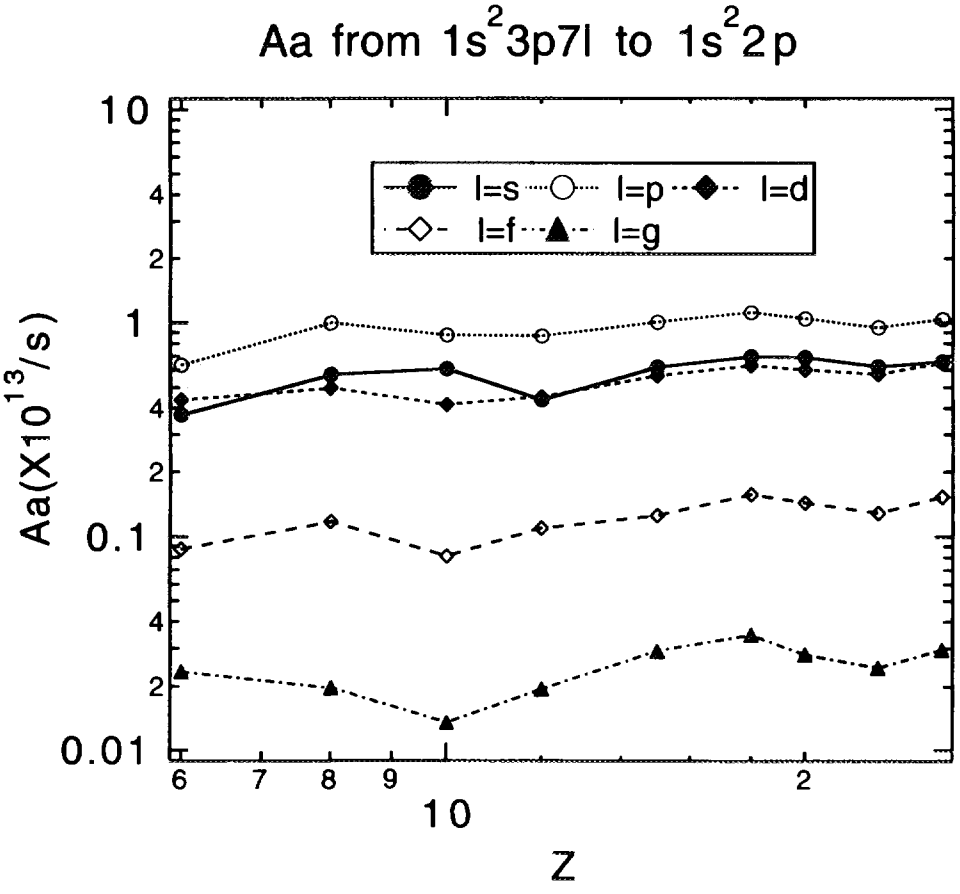

Fig.3-3(d)

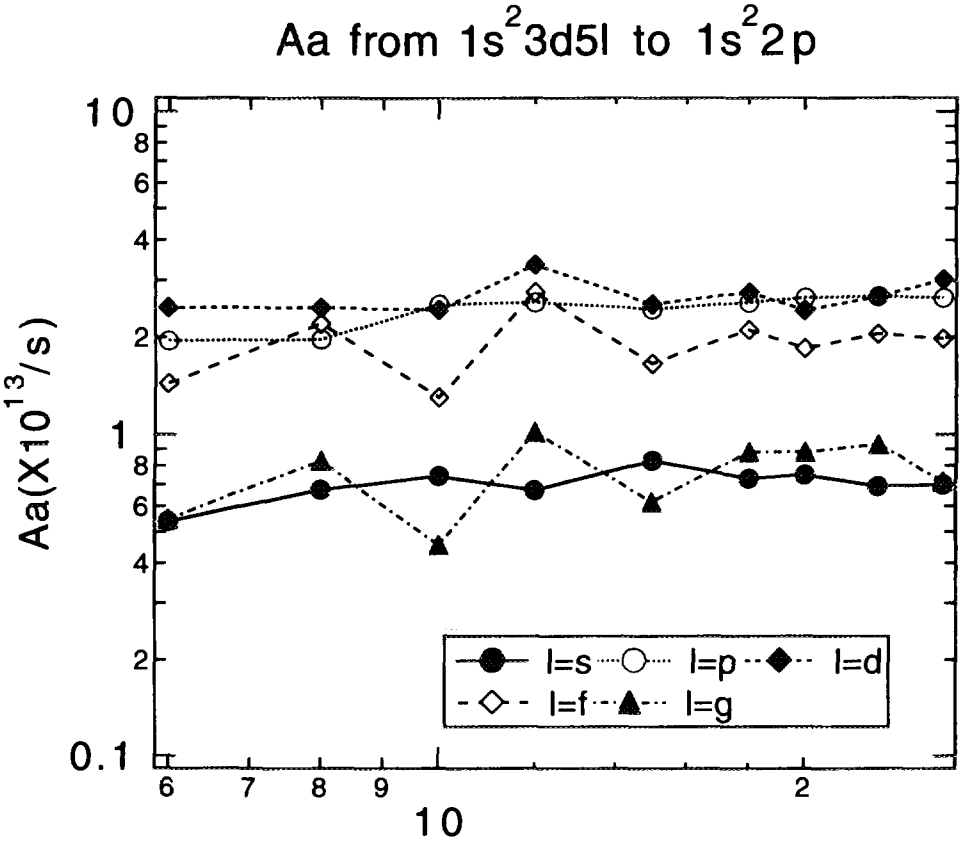

Fig.3-3(e)

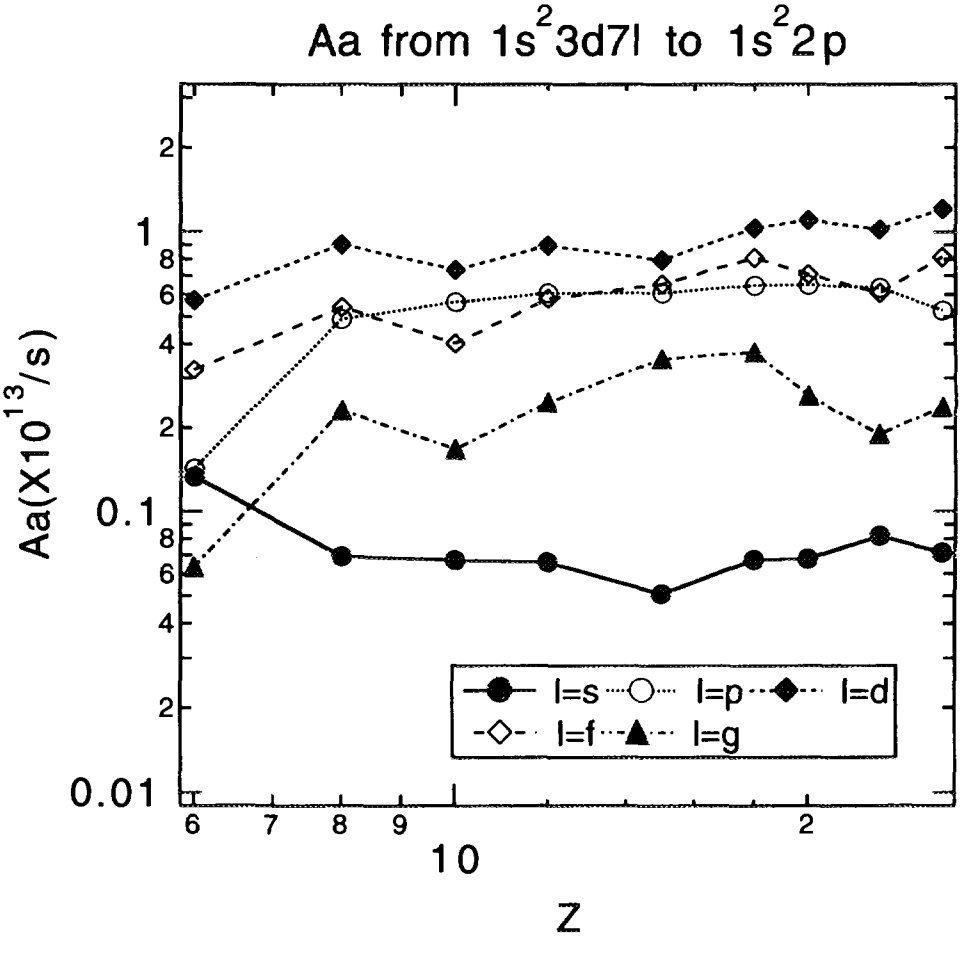

Fig.3-3(f)

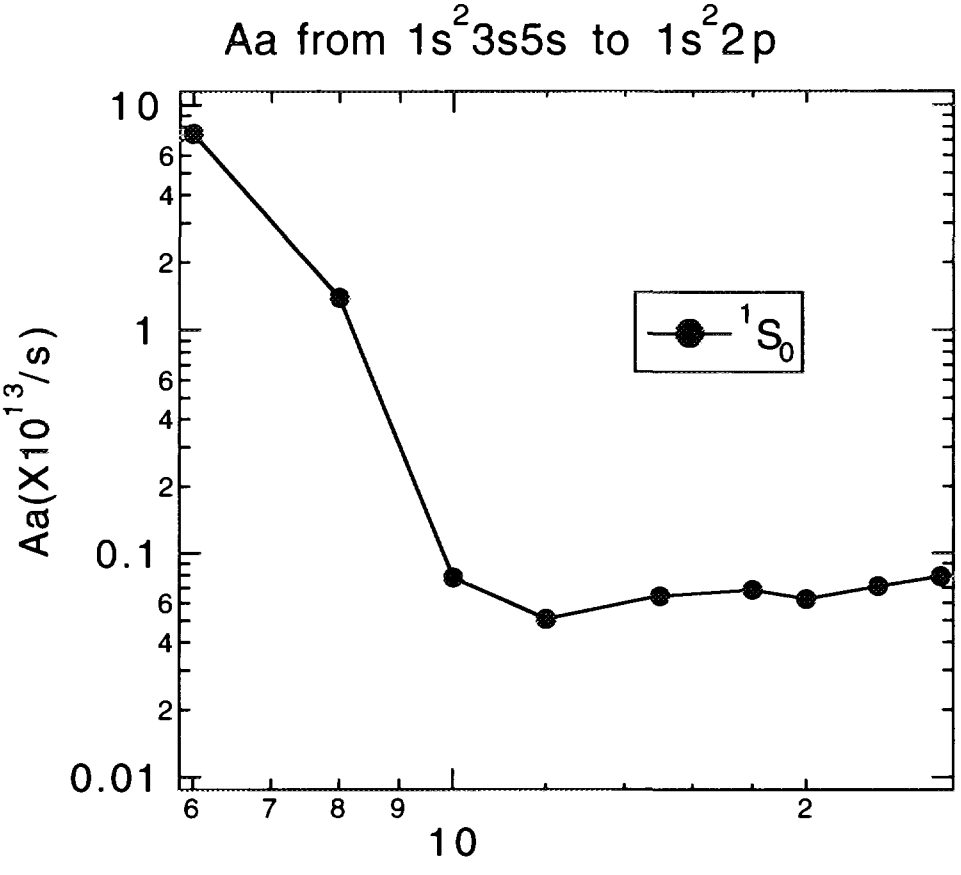

Fig.3-3-2(a)

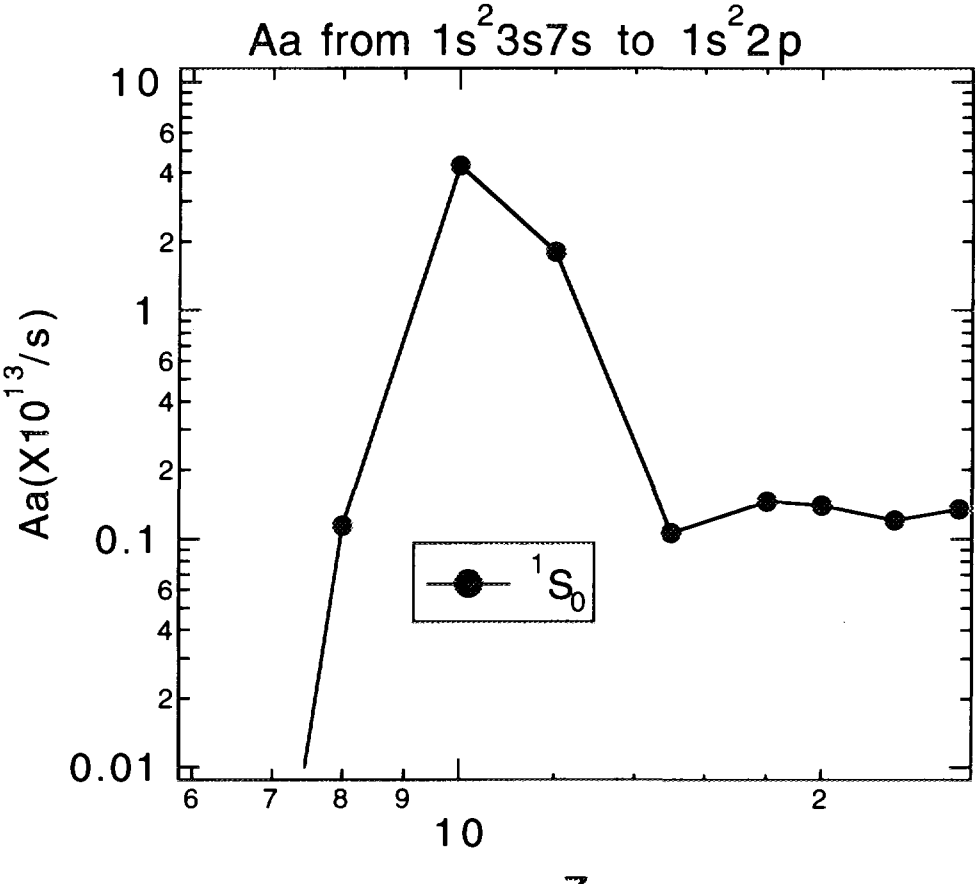

Fig.3-3-2(b)

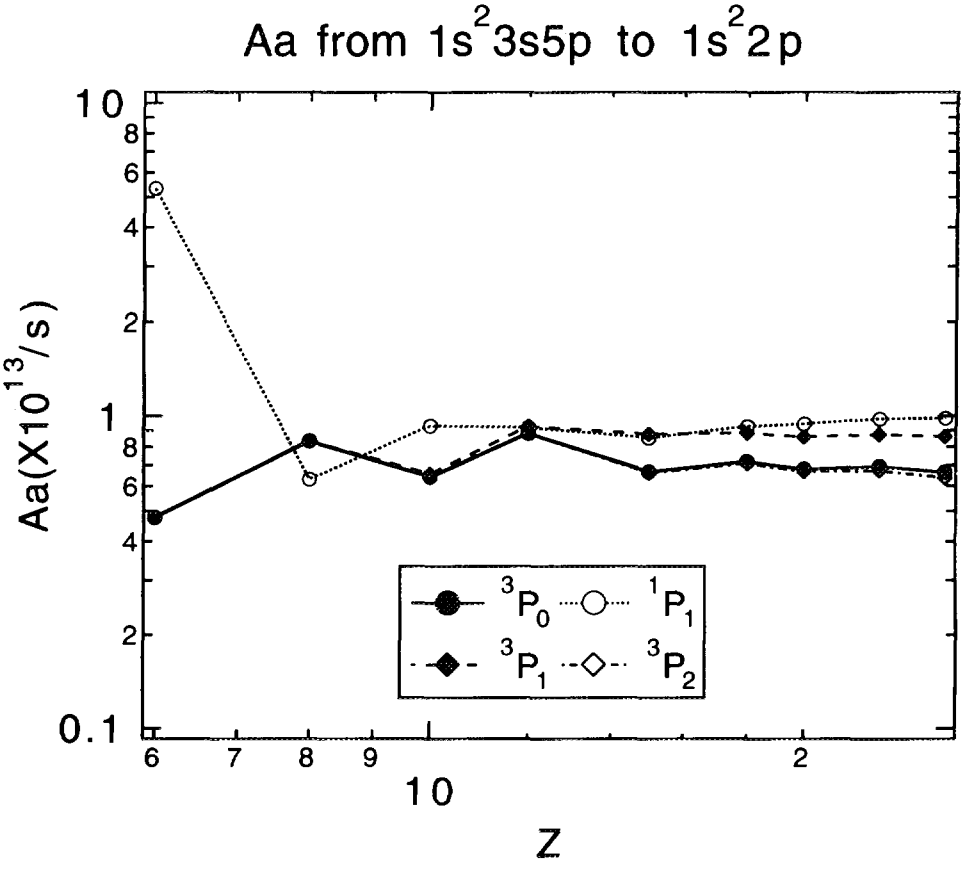

Fig.3-3-2(c)

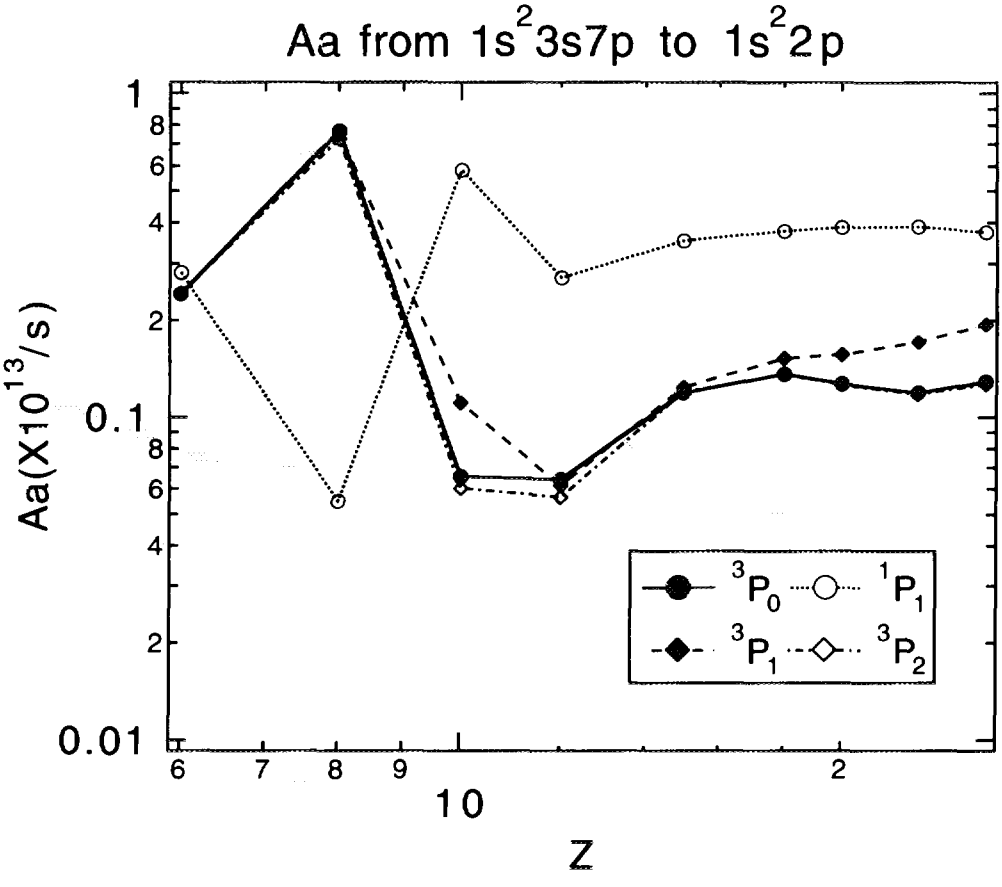

Fig.3-3-2(d)

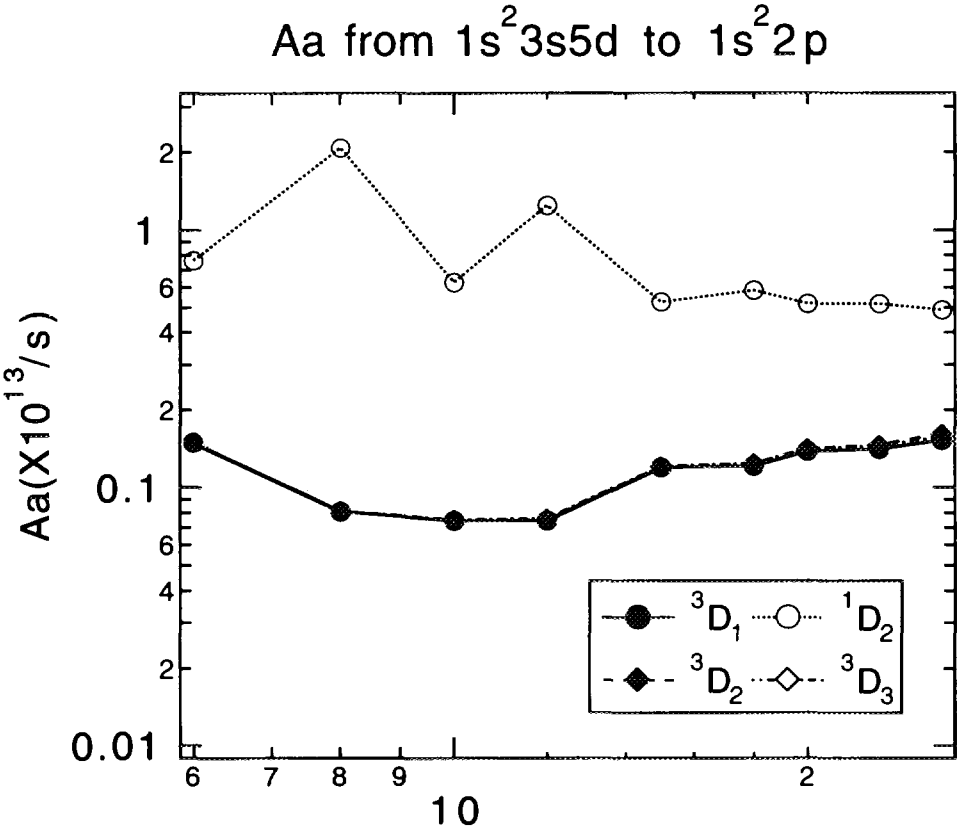

Fig.3-3-2(e)

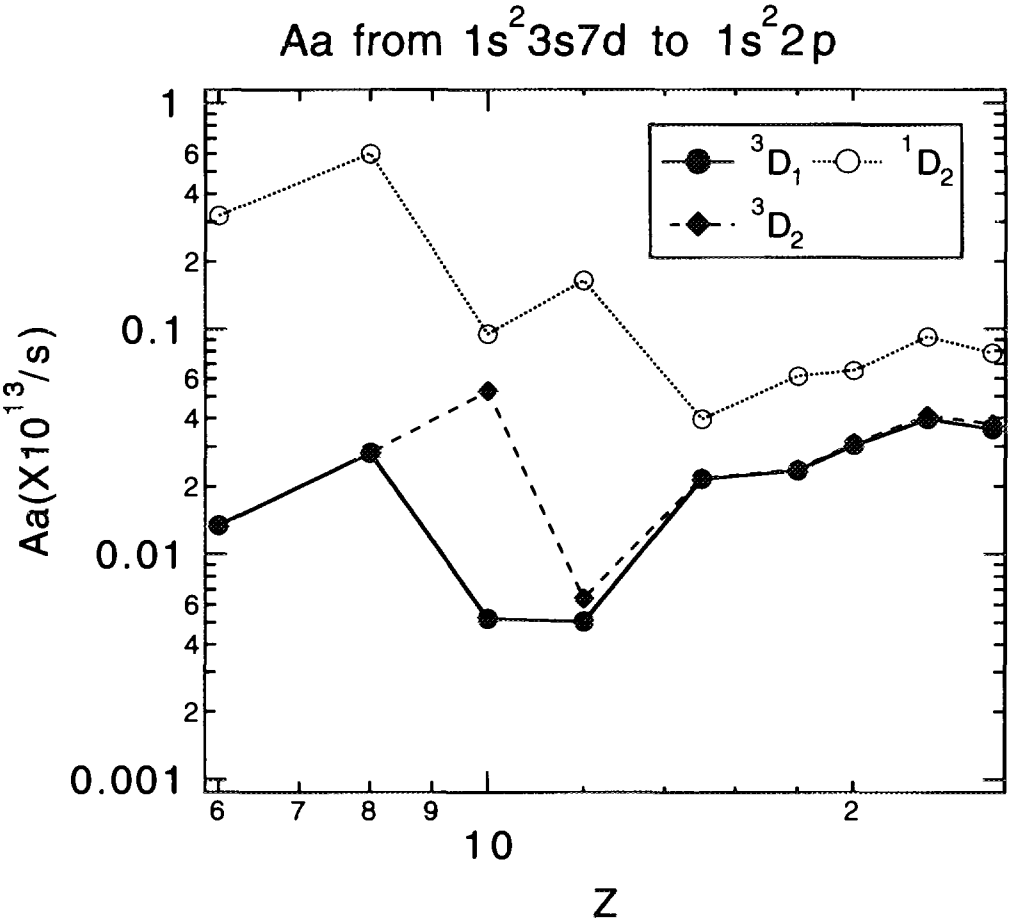

Fig.3-3-2(f)

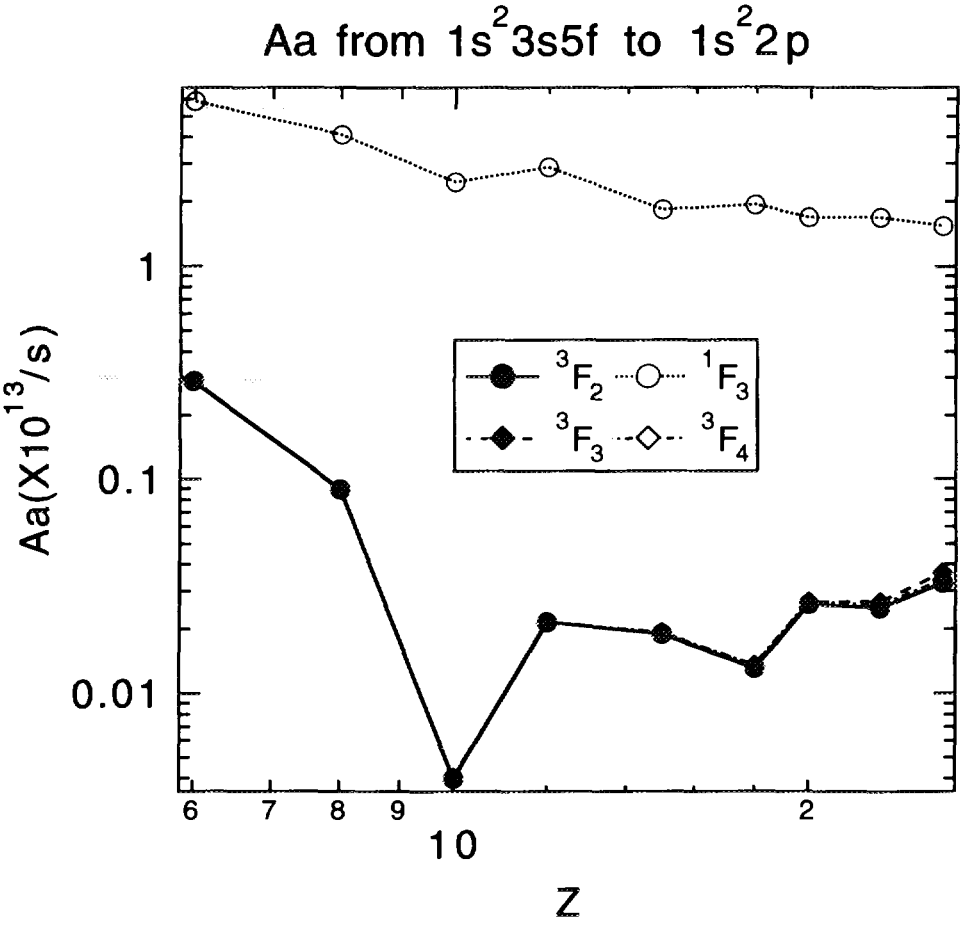

Fig.3-3-2(g)

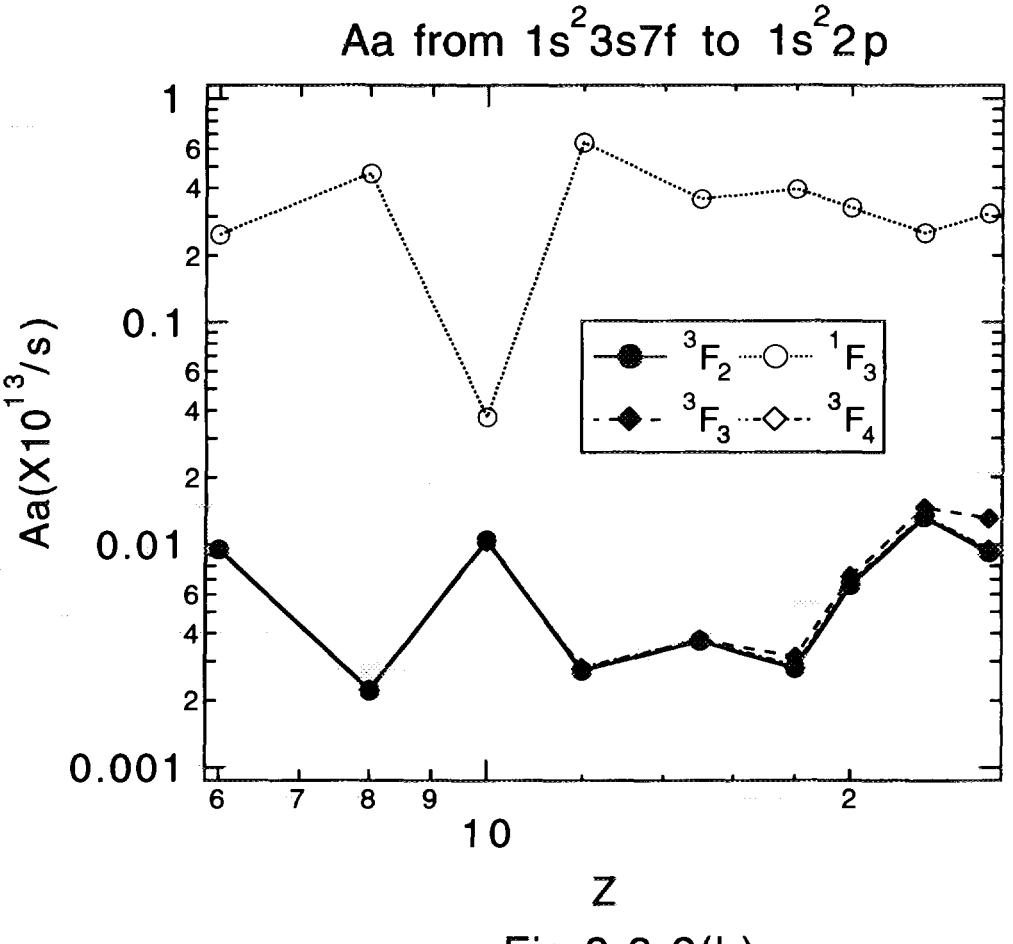

Fig.3-3-2(h)

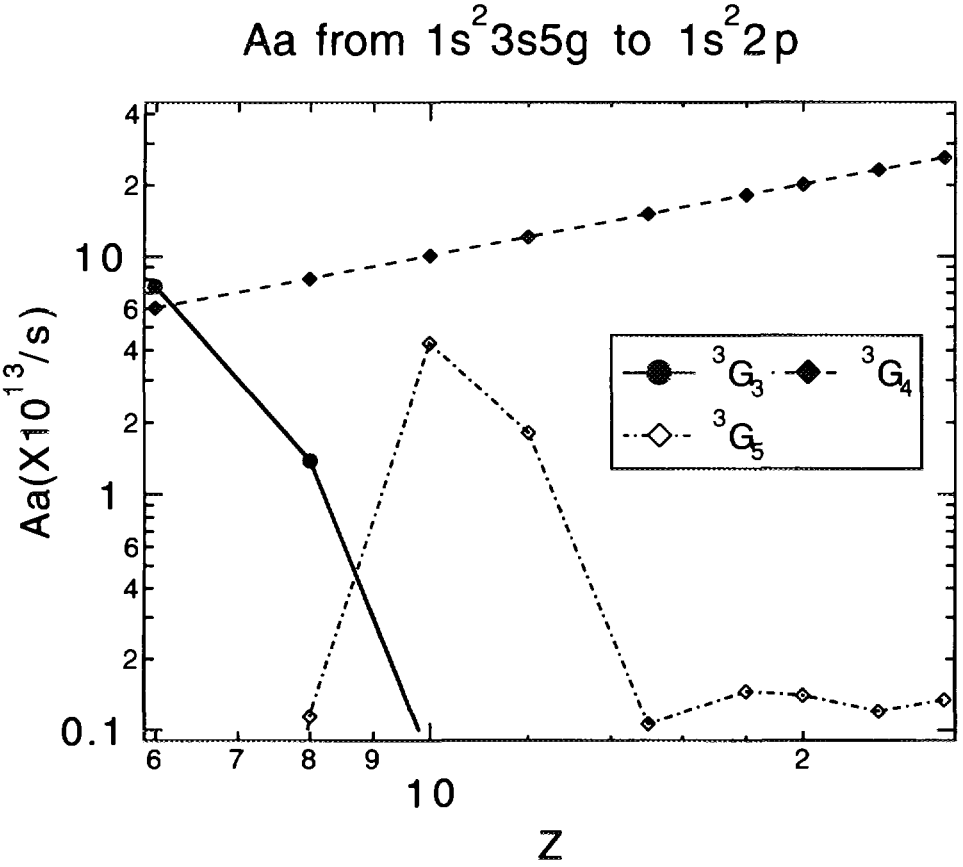

Fig.3-3-2(i)

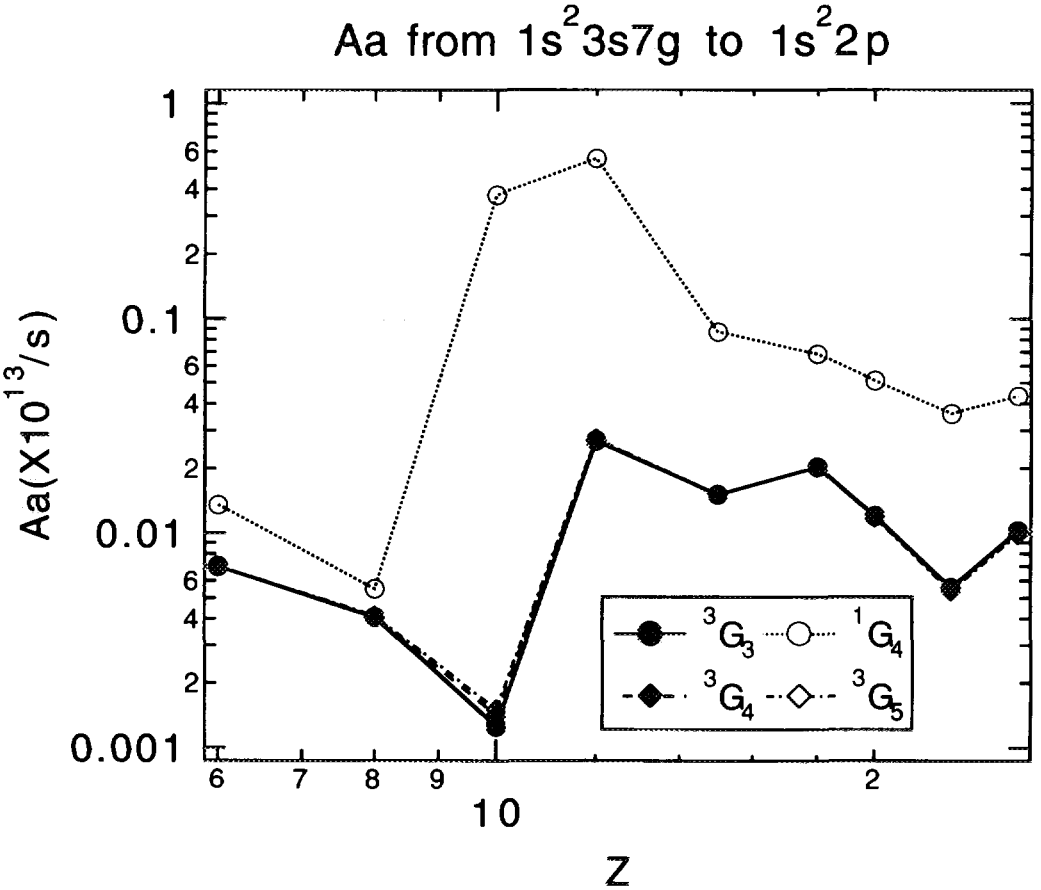

Fig.3-3-2(j)

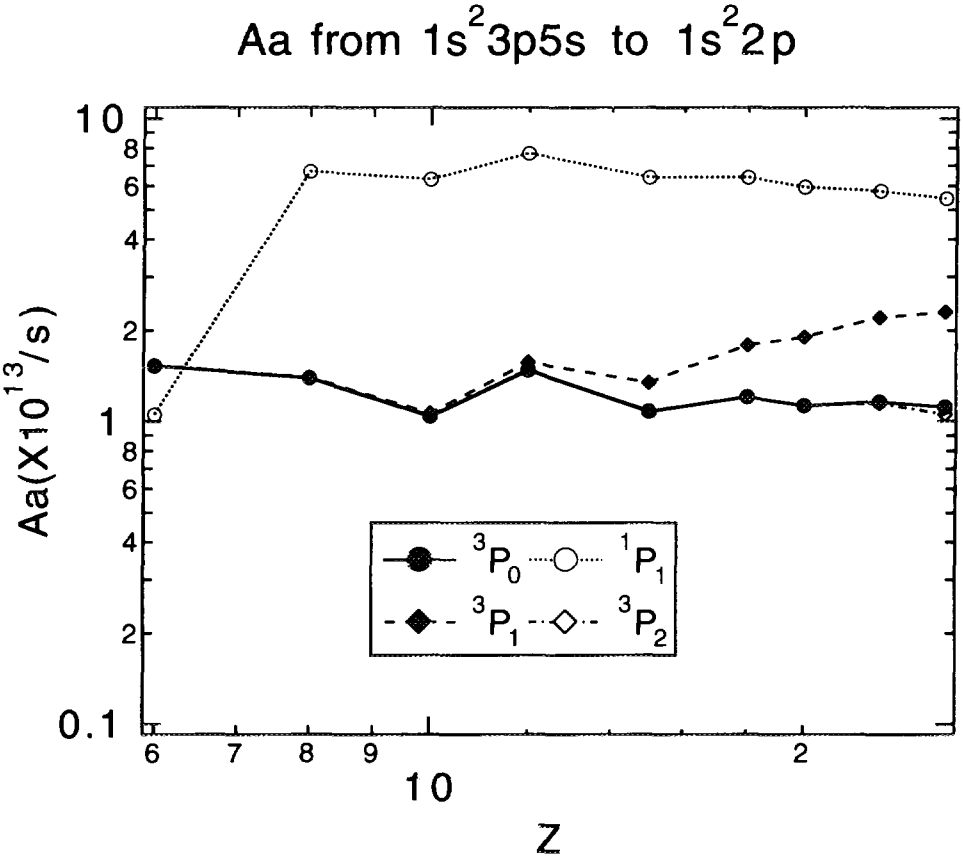

Fig.3-3-3(a)

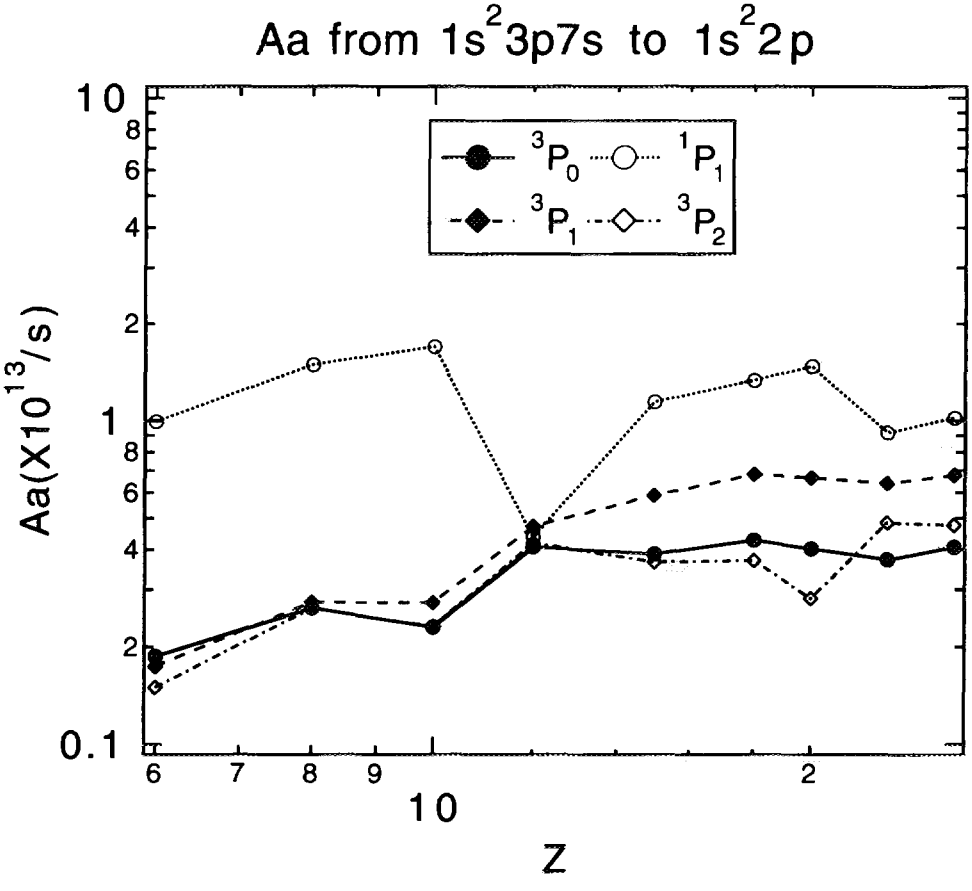

Fig.3-3-3(b)

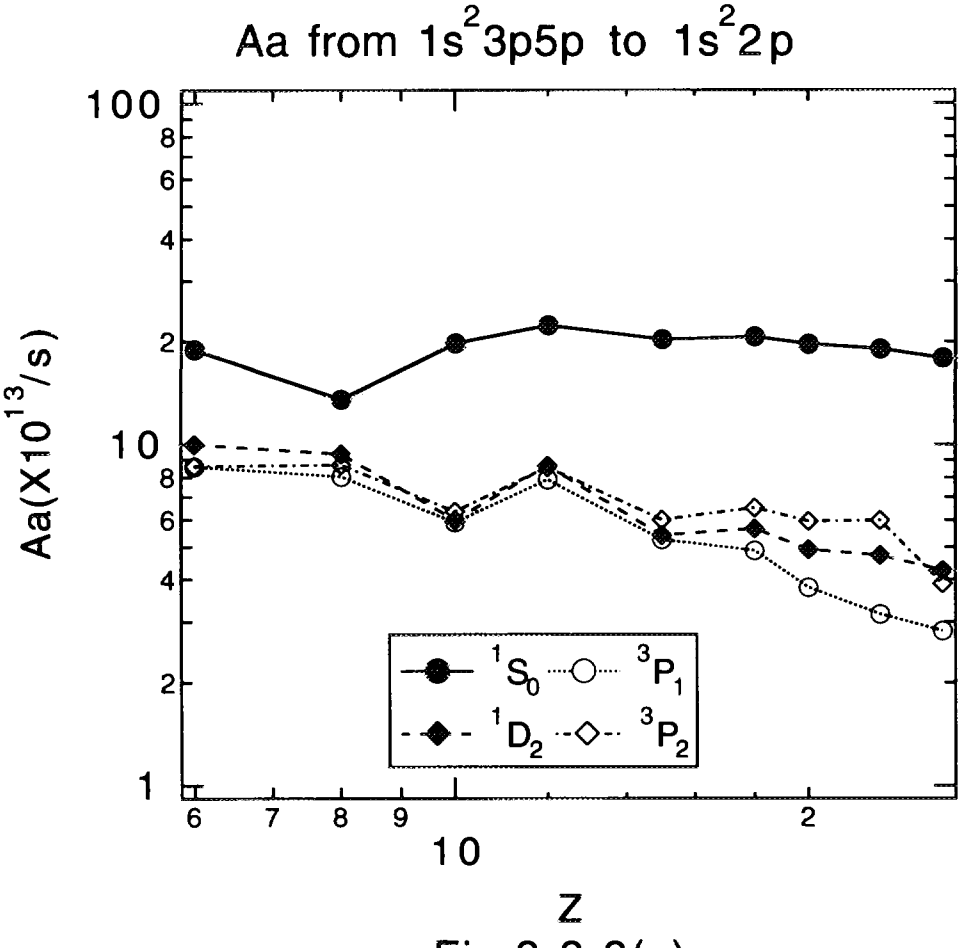

Fig.3-3-3(c)

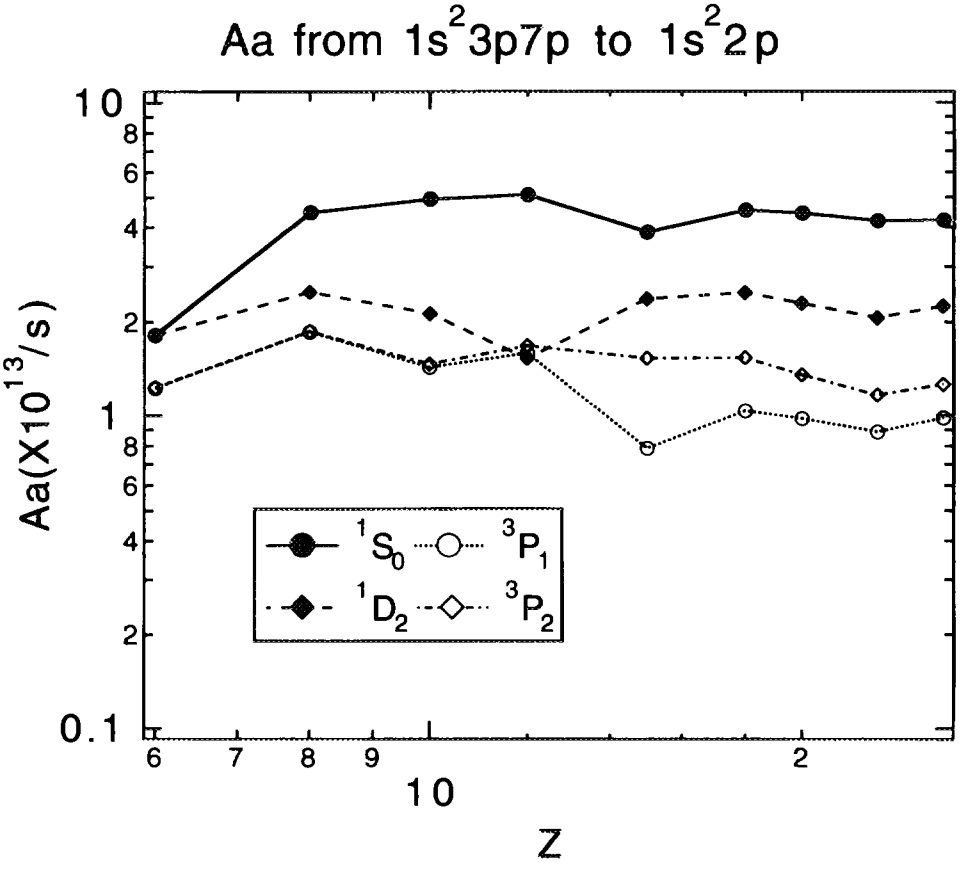

Fig.3-3-3(d)

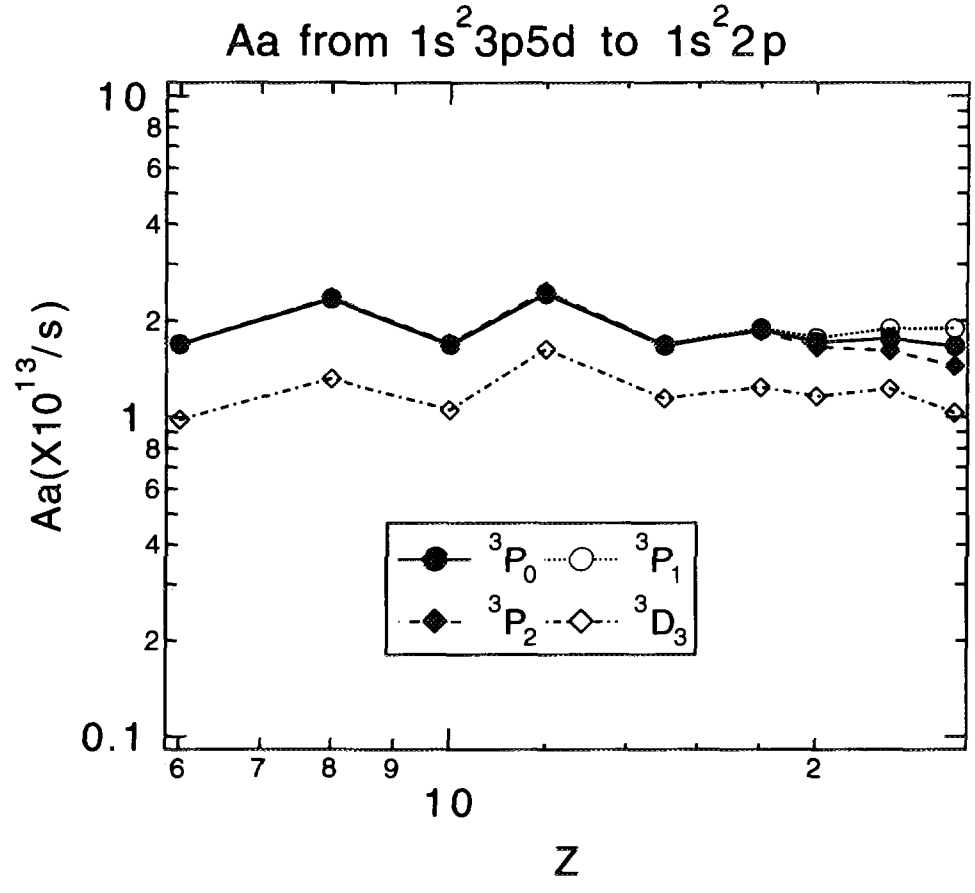

Fig.3-3-3(e)

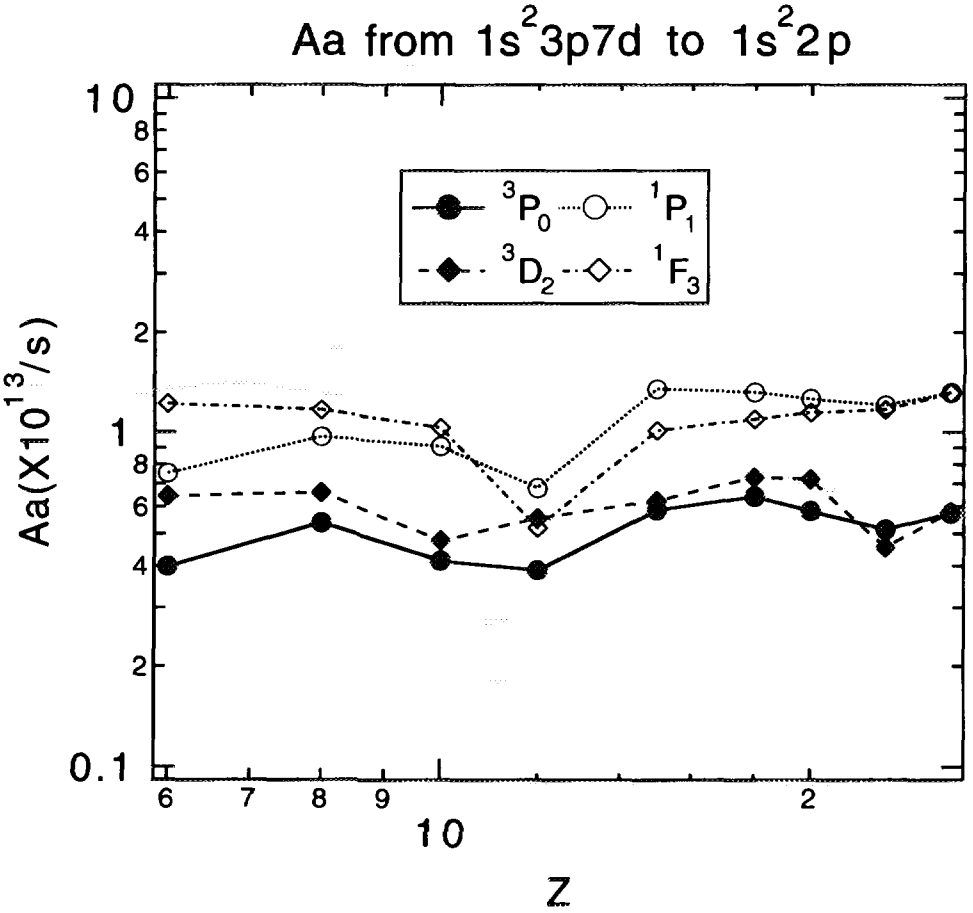

Fig.3-3-3(f)

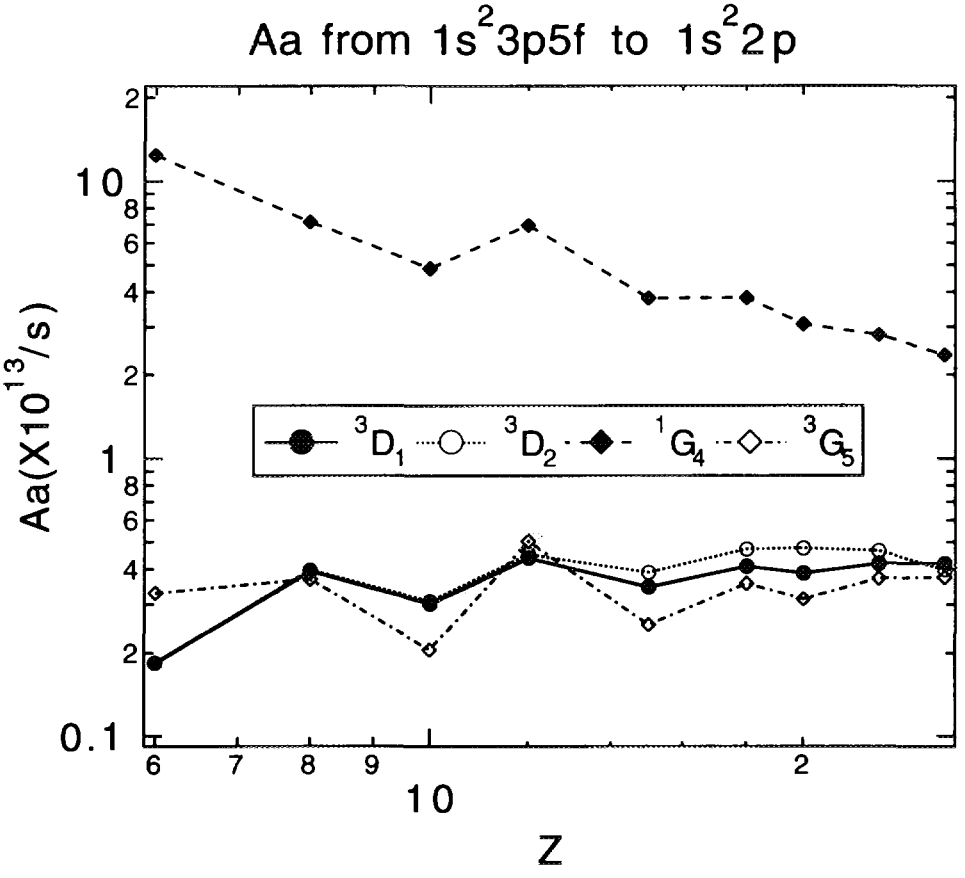

Fig.3-3-3(g)

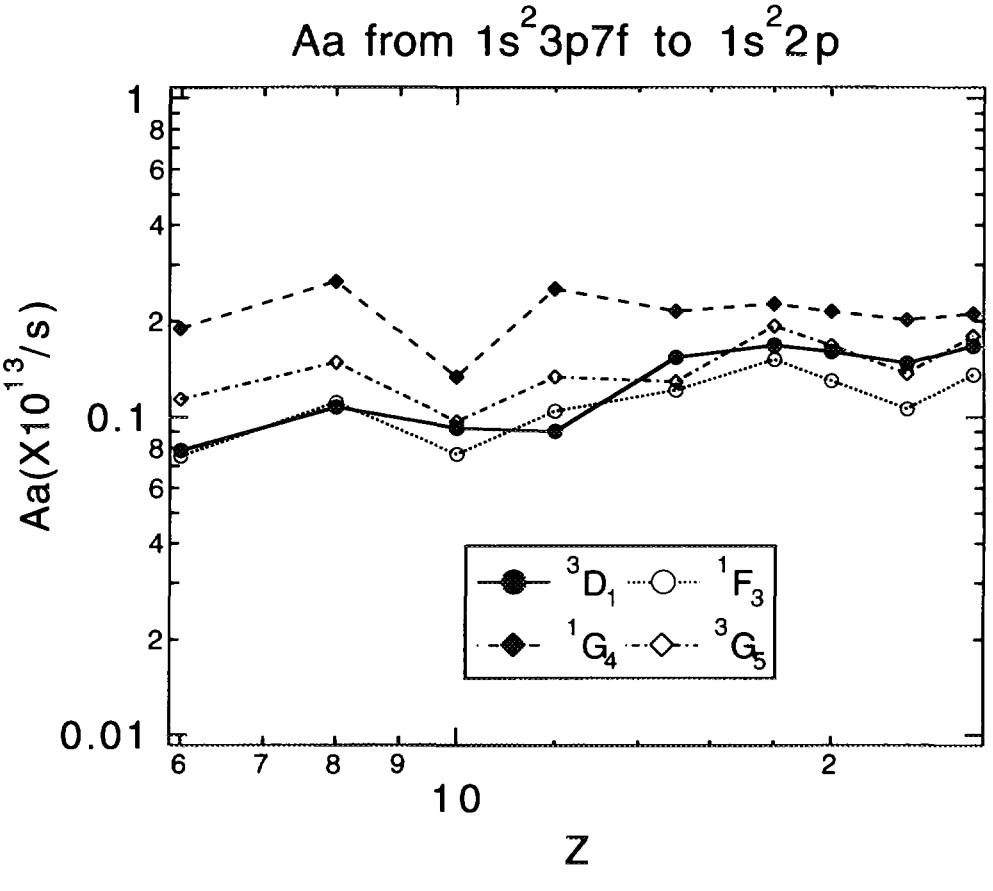

Fig.3-3-3(h)

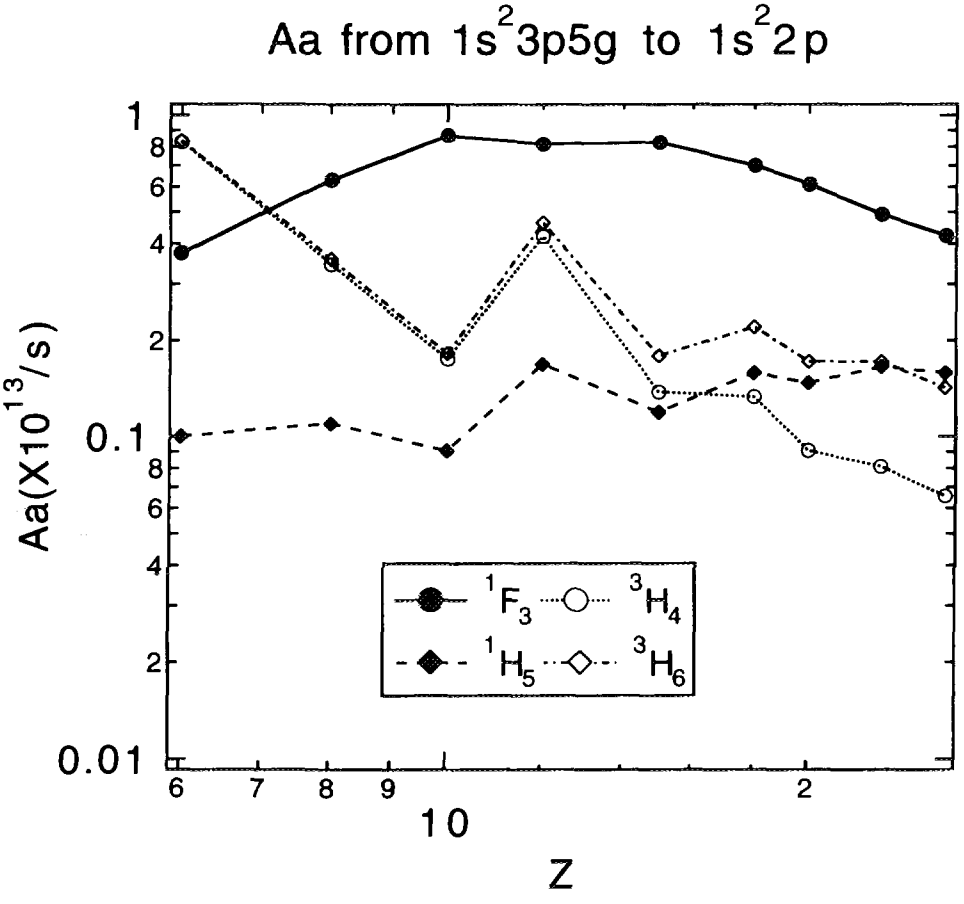

Fig.3-3-3(i)

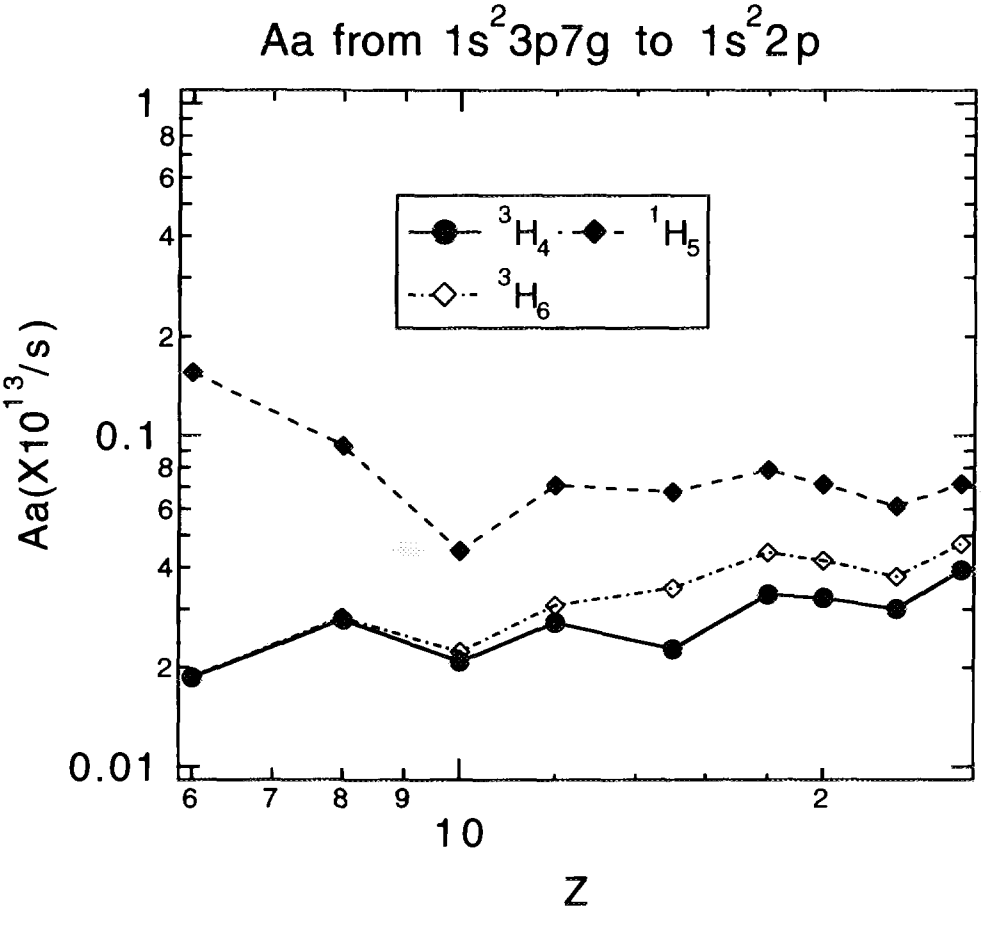

Fig.3-3-3(j)

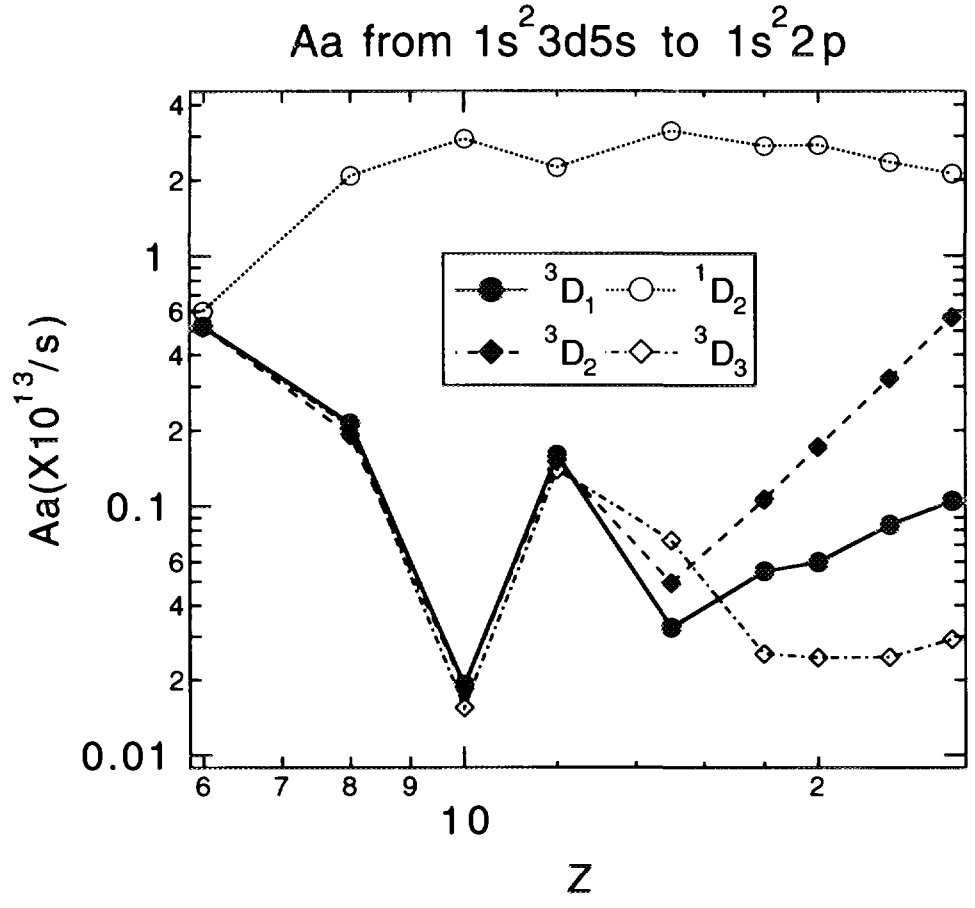

Fig.3-3-4(a)

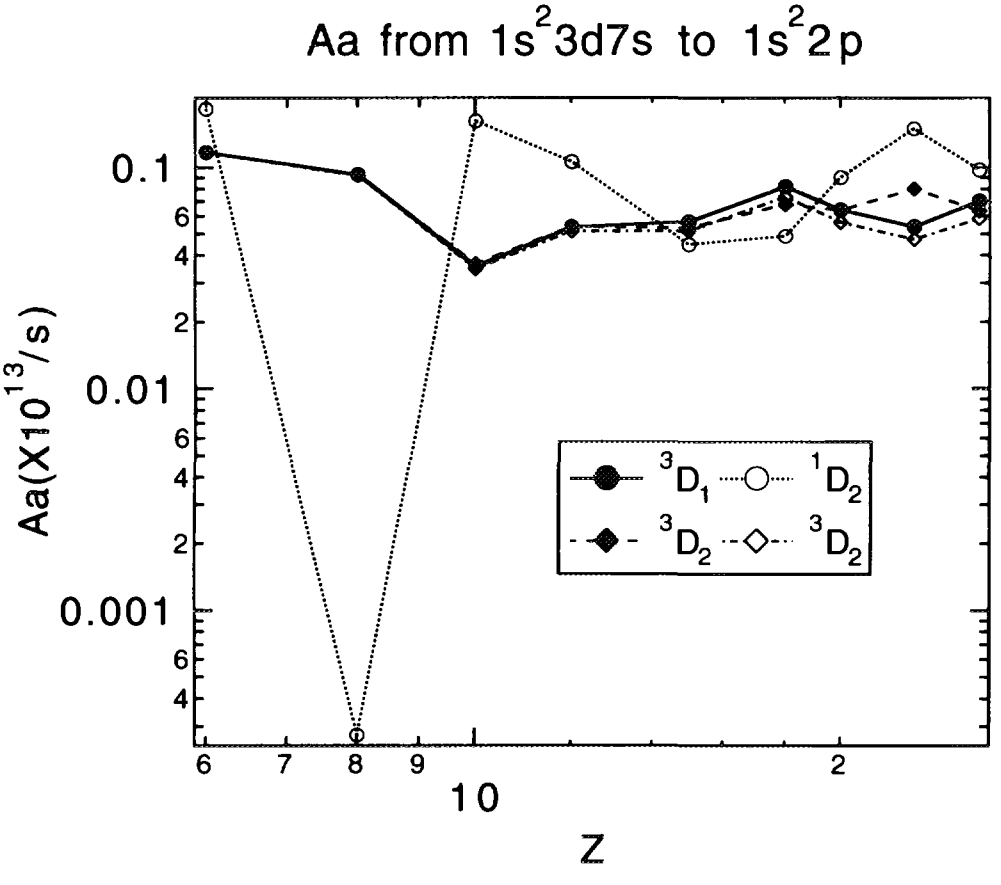

Fig.3-3-4(b)

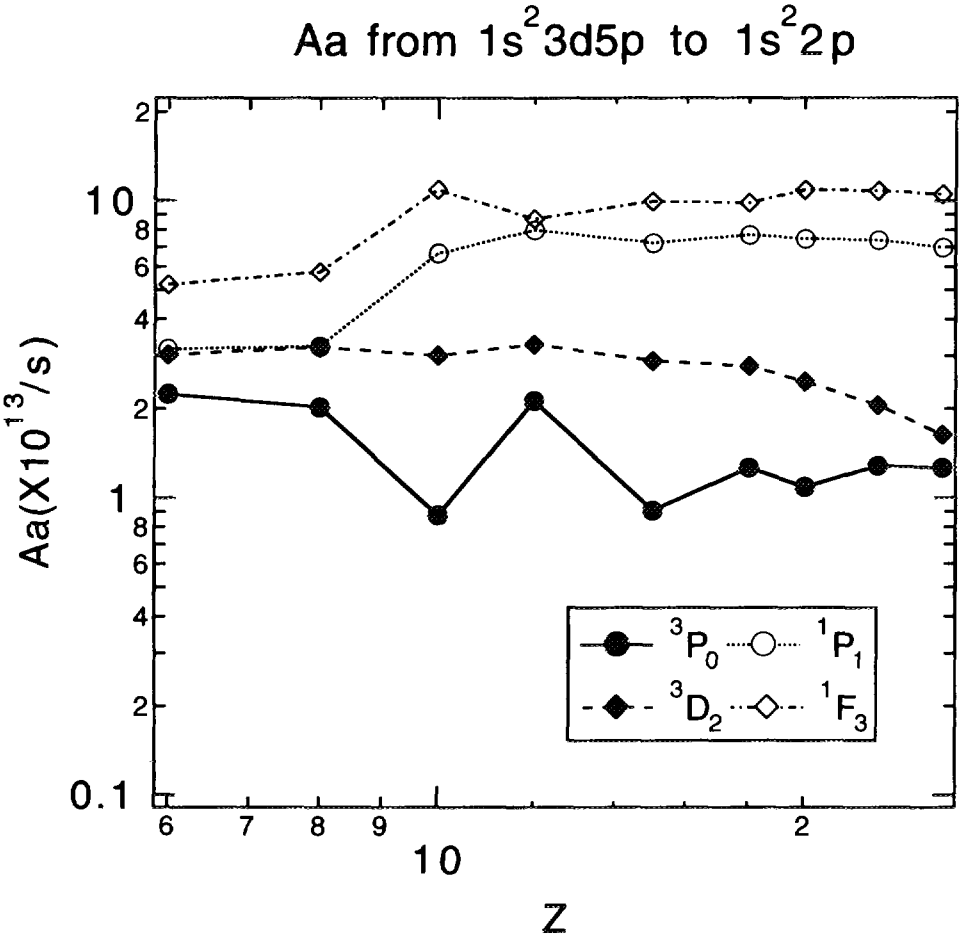

Fig.3-3-4(c)

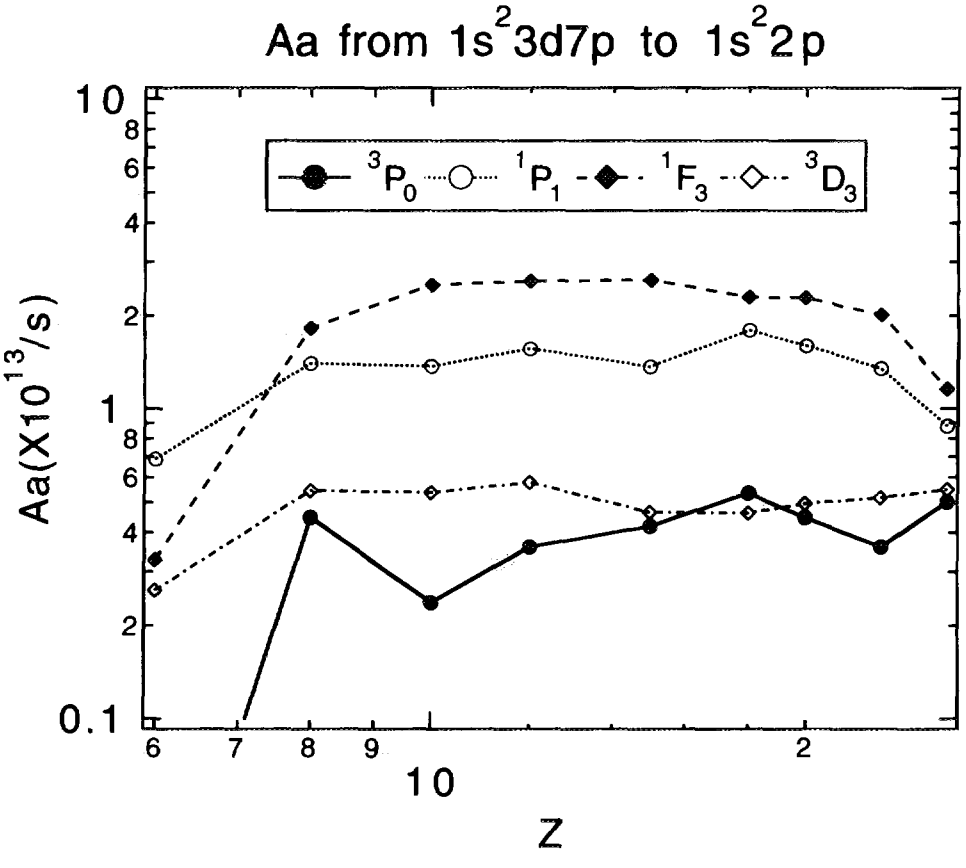

Fig.3-3-4(d)

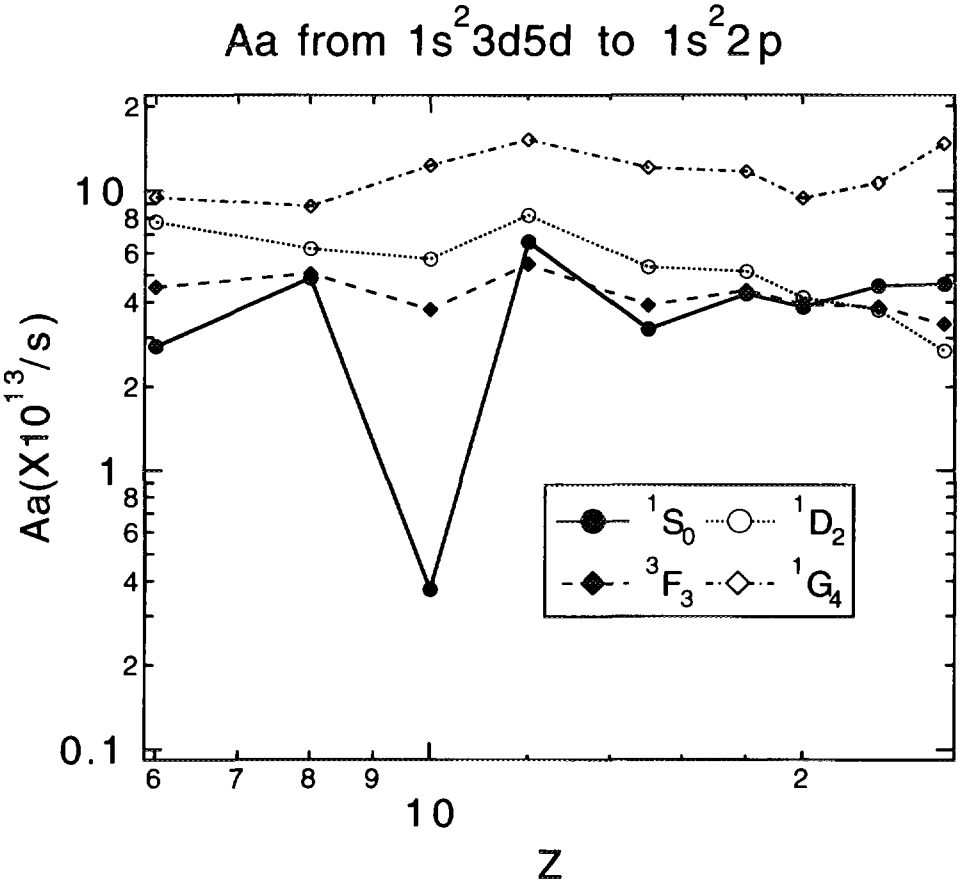

Fig.3-3-4(e)

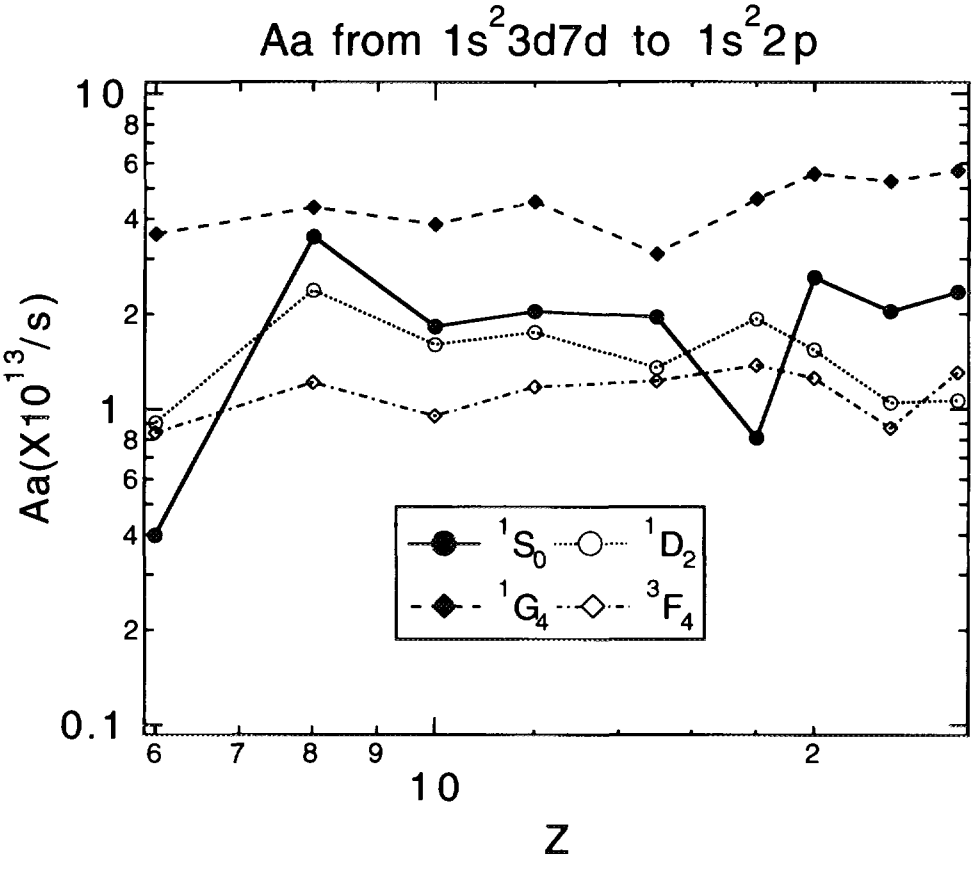

Fig.3-3-4(f)

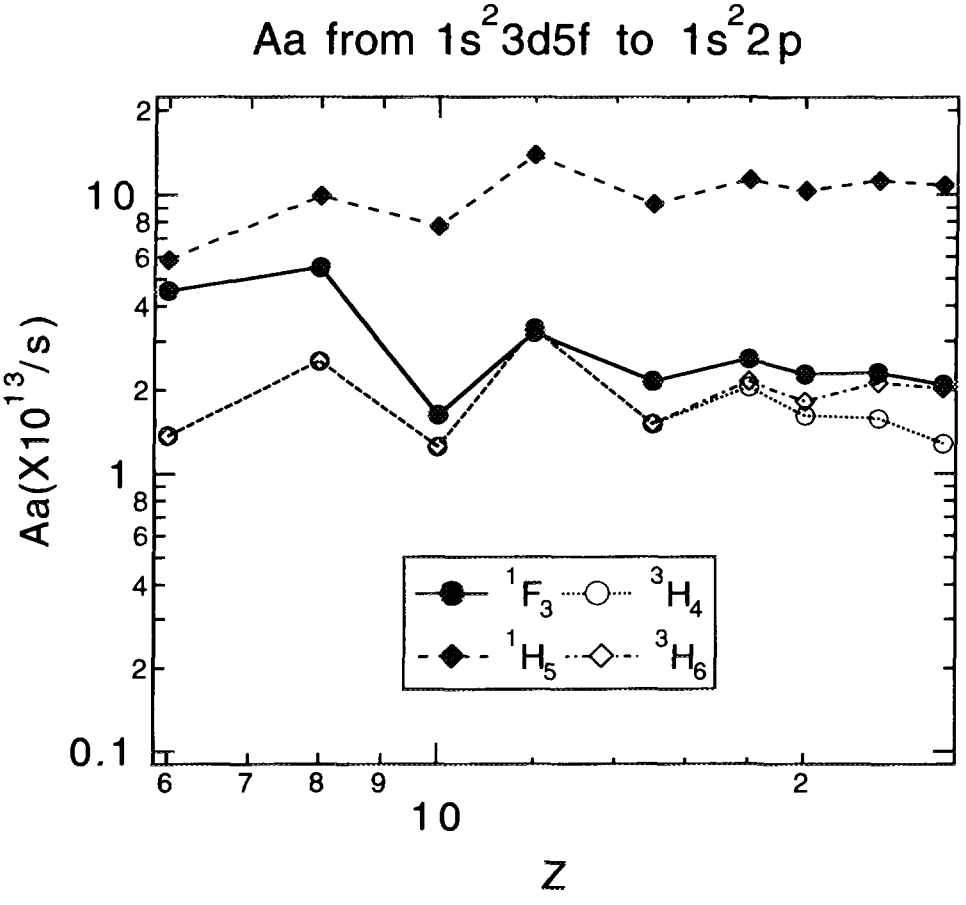

Fig.3-3-4(g)

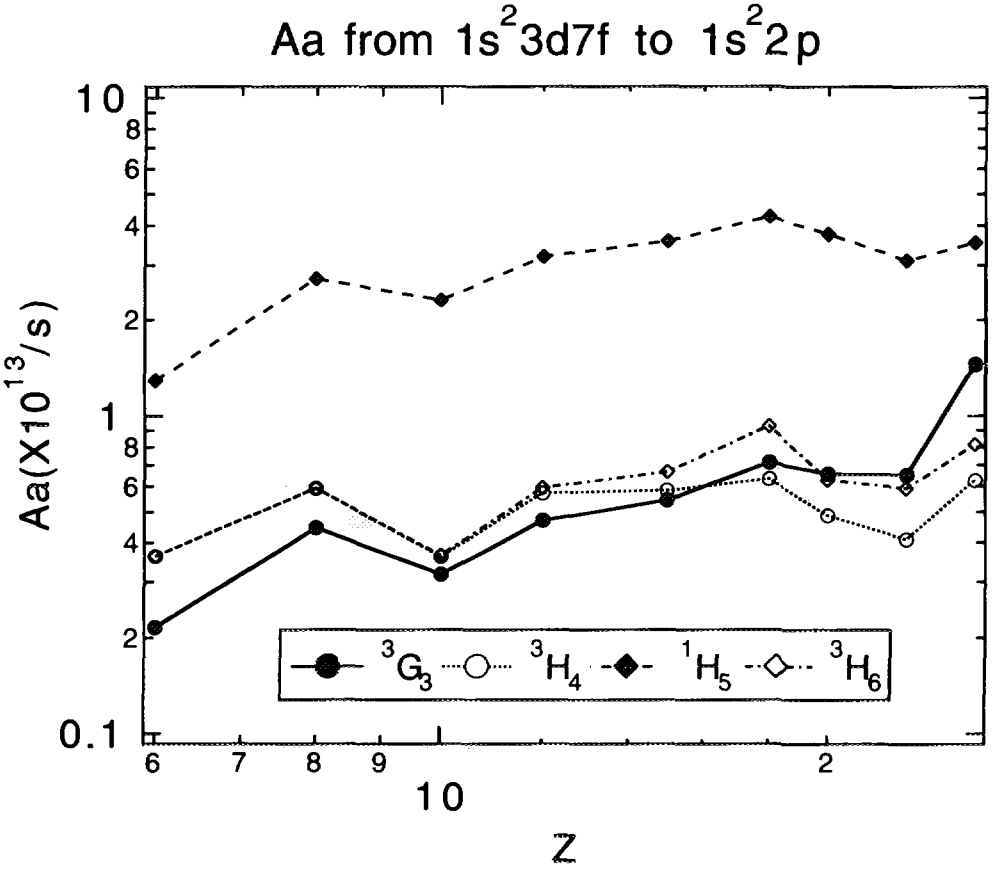

Fig.3-3-4(h)

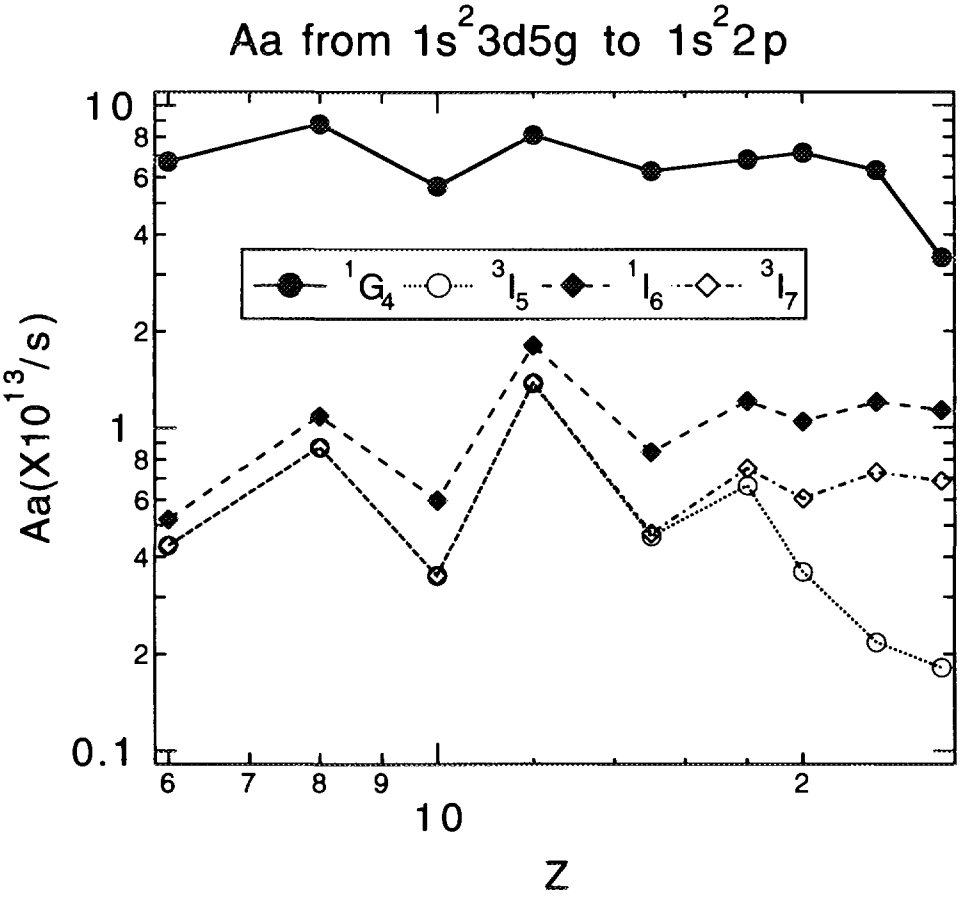

Fig.3-3-4(i)

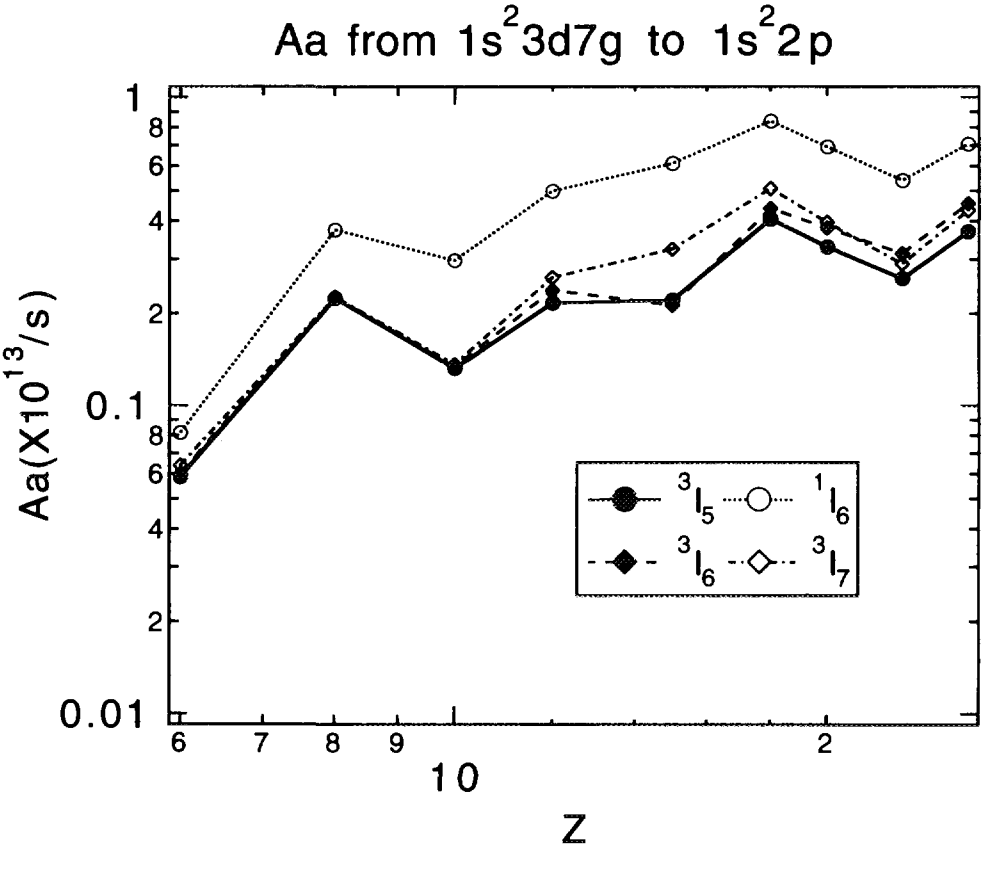

Fig.3-3-4(j)

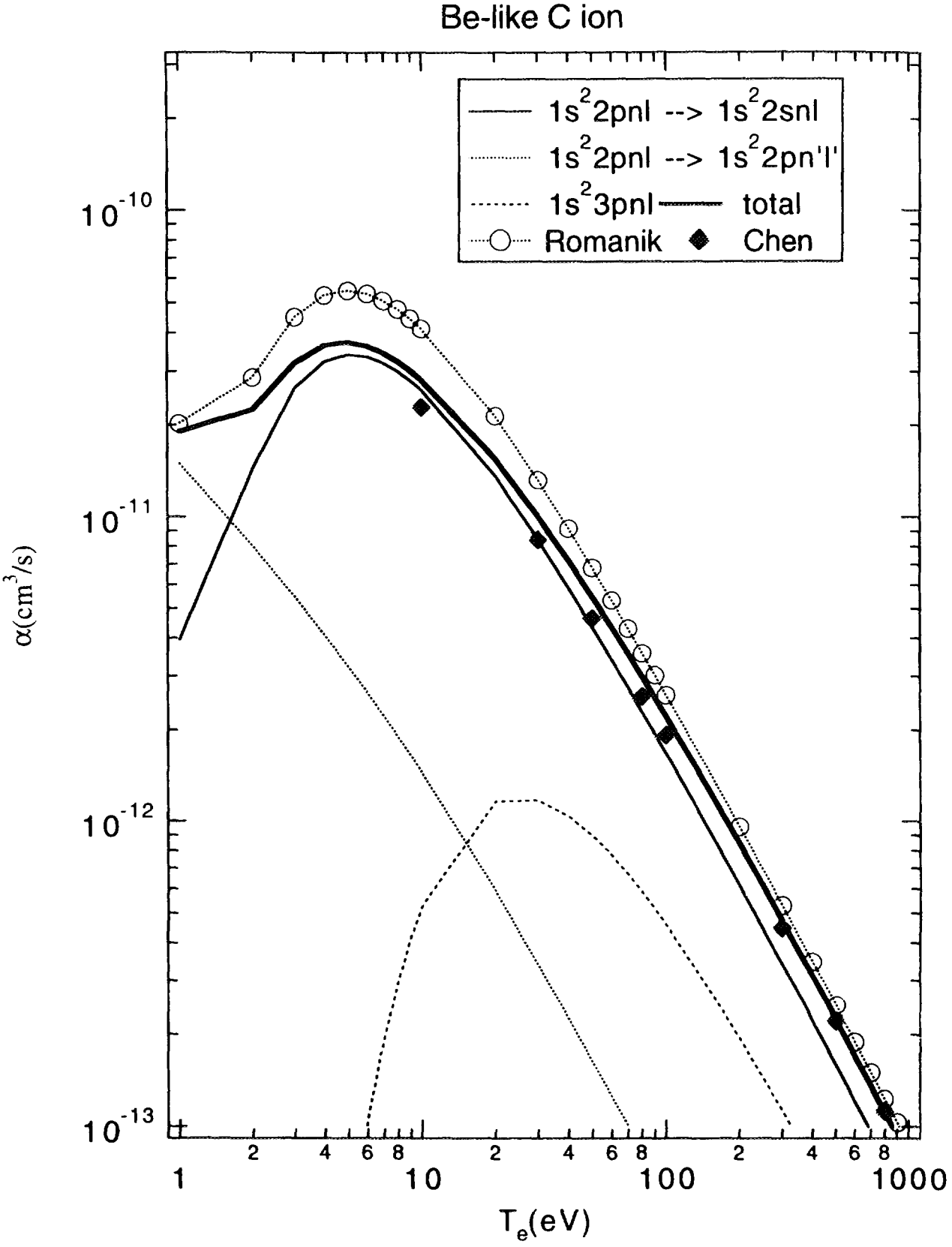
Be-like C ion
1s²2pnl --> 1s²2snl
1s²2pnl --> 1s²2pn'l'
1s²3pnl
total
Romanik
Chen
α(cm³/s)
10⁻¹⁰
10⁻¹¹
10⁻¹²
10⁻¹³
1
10
100
1000
T_e(eV)

Fig.4-1(a)

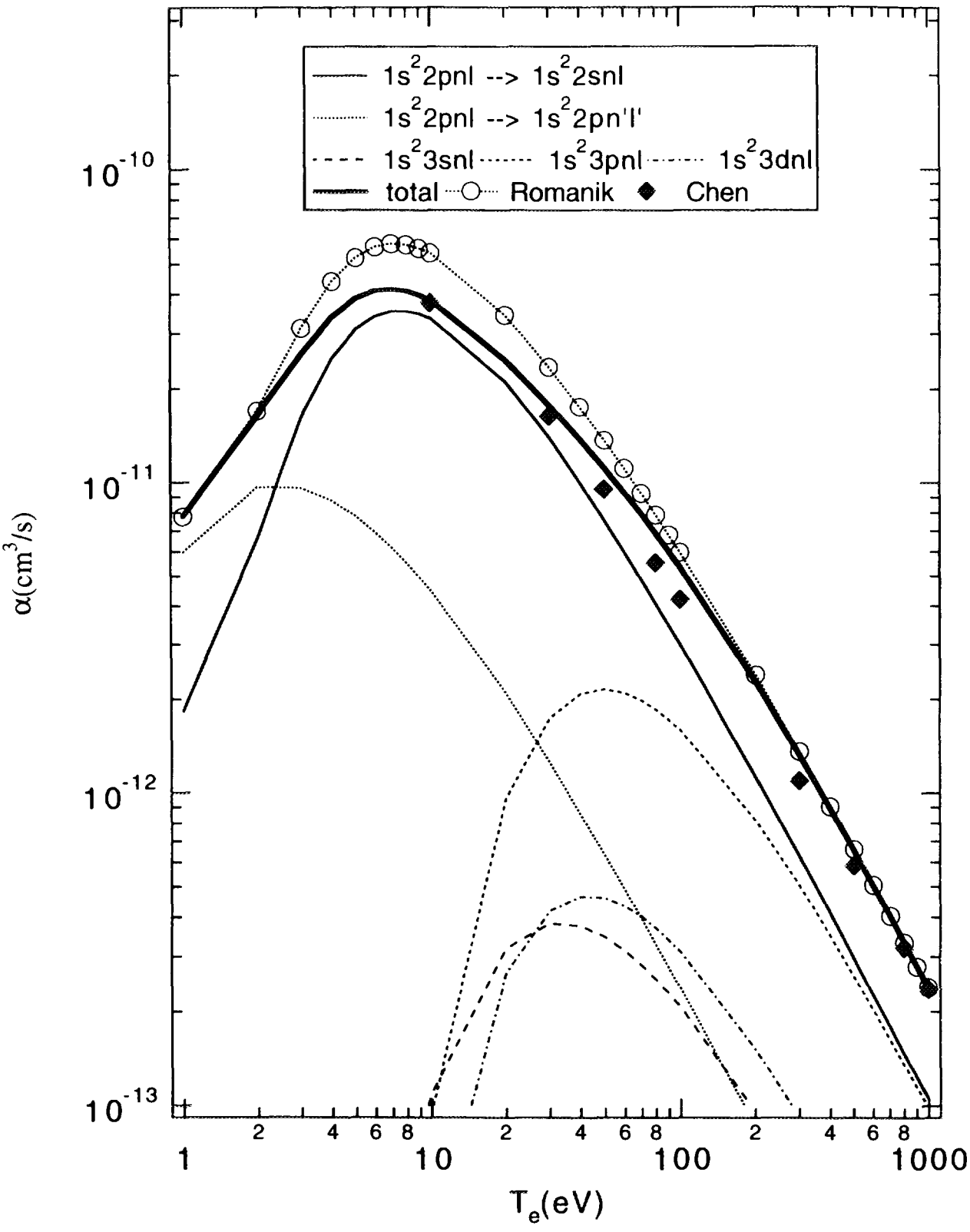
Be-like O ion
1s²2pnl --> 1s²2snl
1s²2pnl --> 1s²2pn'l'
1s²3snl
1s²3pnl
1s²3dnl
total
Romanik
Chen
10^-10
10^-11
10^-12
10^-13
α(cm³/s)
1
10
100
1000
T_e(eV)

Fig.4-1(b)

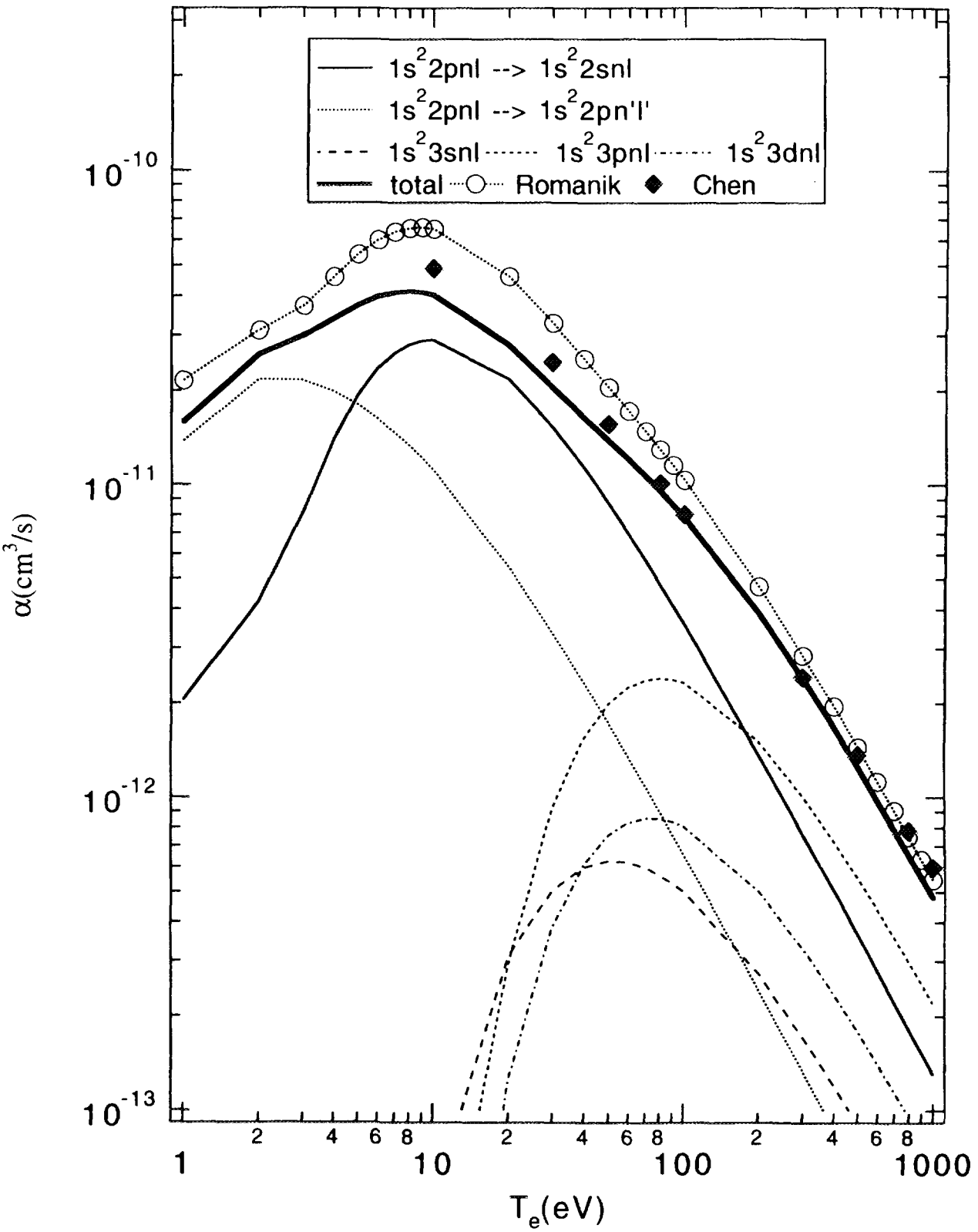
Be-like Ne ion
1s²2pnl --> 1s²2snl
1s²2pnl --> 1s²2pn'l'
1s²3snl
1s²3pnl
1s²3dnl
total
Romanik
Chen
10⁻¹⁰
10⁻¹¹
10⁻¹²
10⁻¹³
α(cm³/s)
1
10
100
1000
T_e(eV)

Fig.4-1(c)

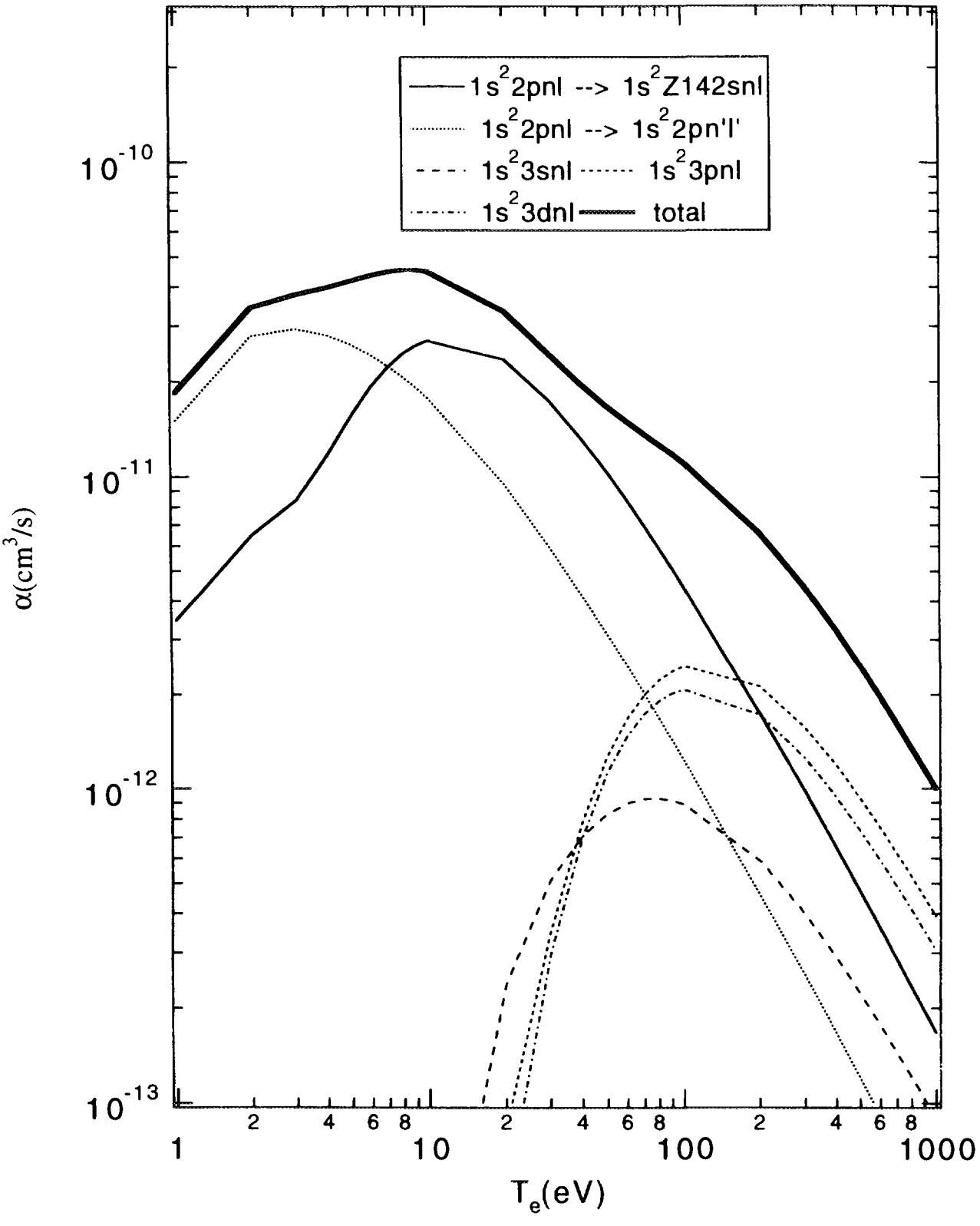
Be-like Mg ion
1s²2pnl --> 1s²Z142snl
1s²2pnl --> 1s²2pn'l'
1s²3snl
1s²3pnl
1s²3dnl
total
10⁻¹⁰
10⁻¹¹
10⁻¹²
10⁻¹³
α(cm³/s)
1
10
100
1000
T_e(eV)

Fig.4-1(d)

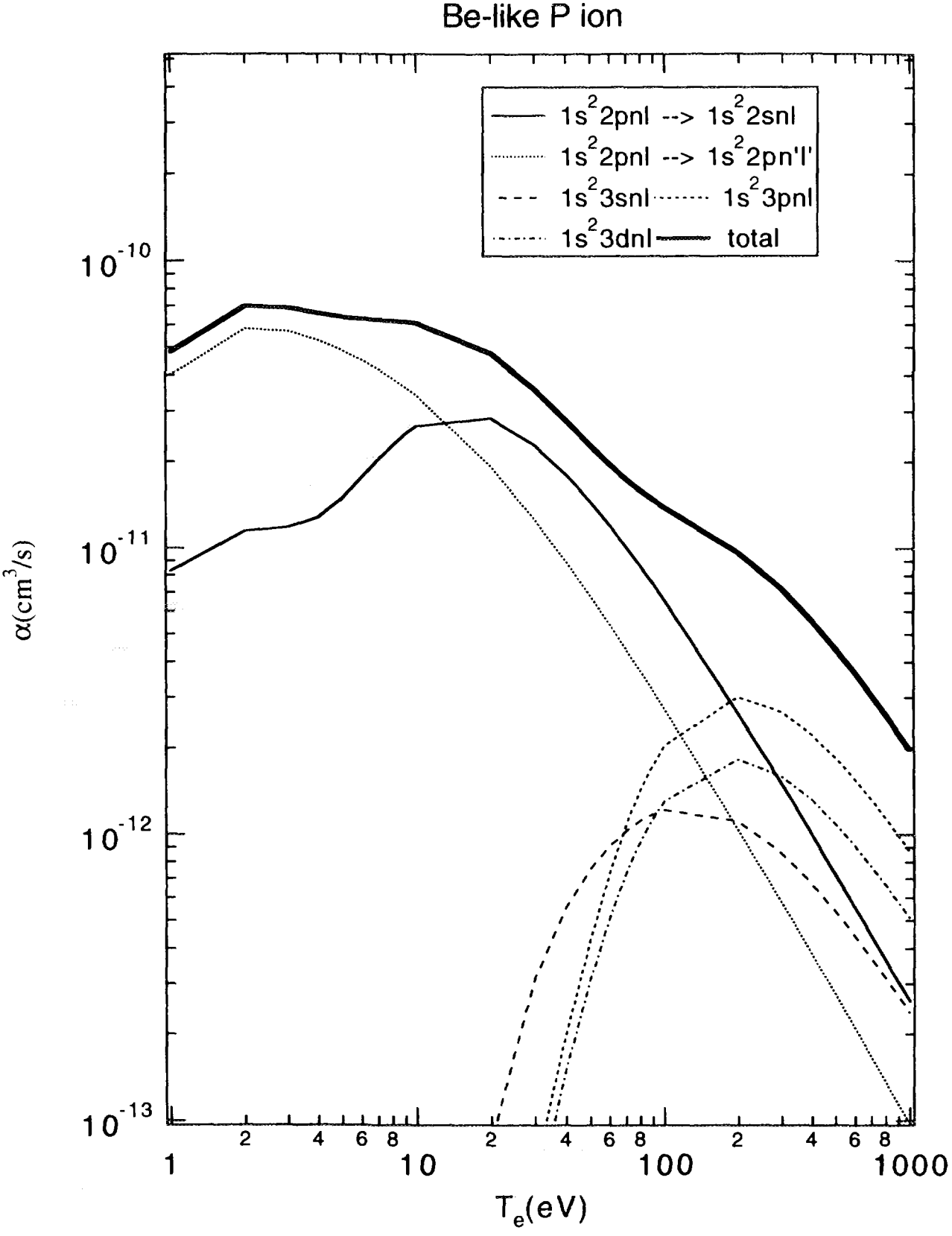
Be-like P ion
1s²2pnl --> 1s²2snl
1s²2pnl --> 1s²2pn'l'
1s²3snl
1s²3pnl
1s²3dnl
total
10⁻¹⁰
10⁻¹¹
10⁻¹²
10⁻¹³
α(cm³/s)
1
2
4
6
8
10
2
4
6
8
100
2
4
6
8
1000
Tₑ(eV)

Fig.4-1(e)

Be-like Ar ion

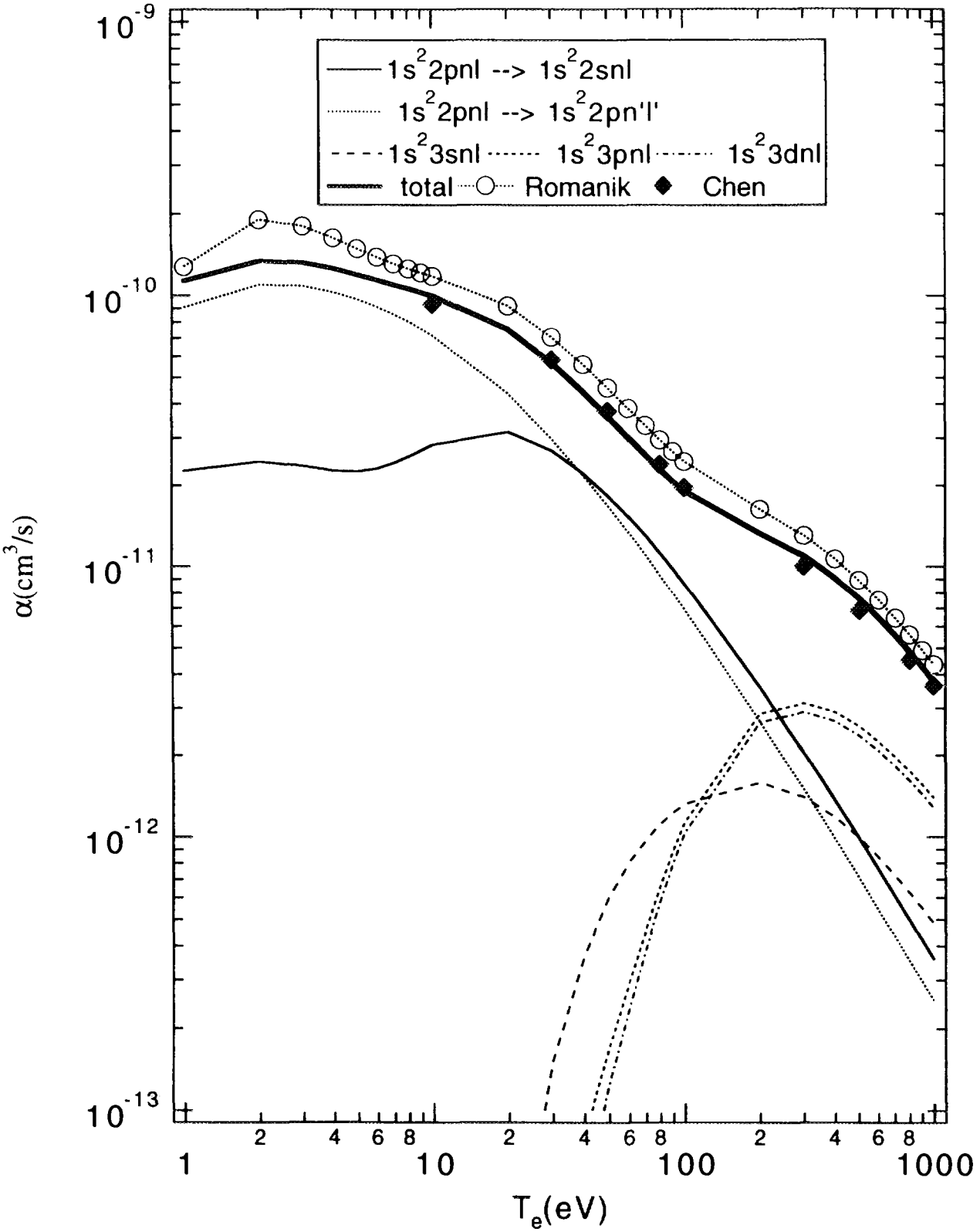

Fig.4-1(f)

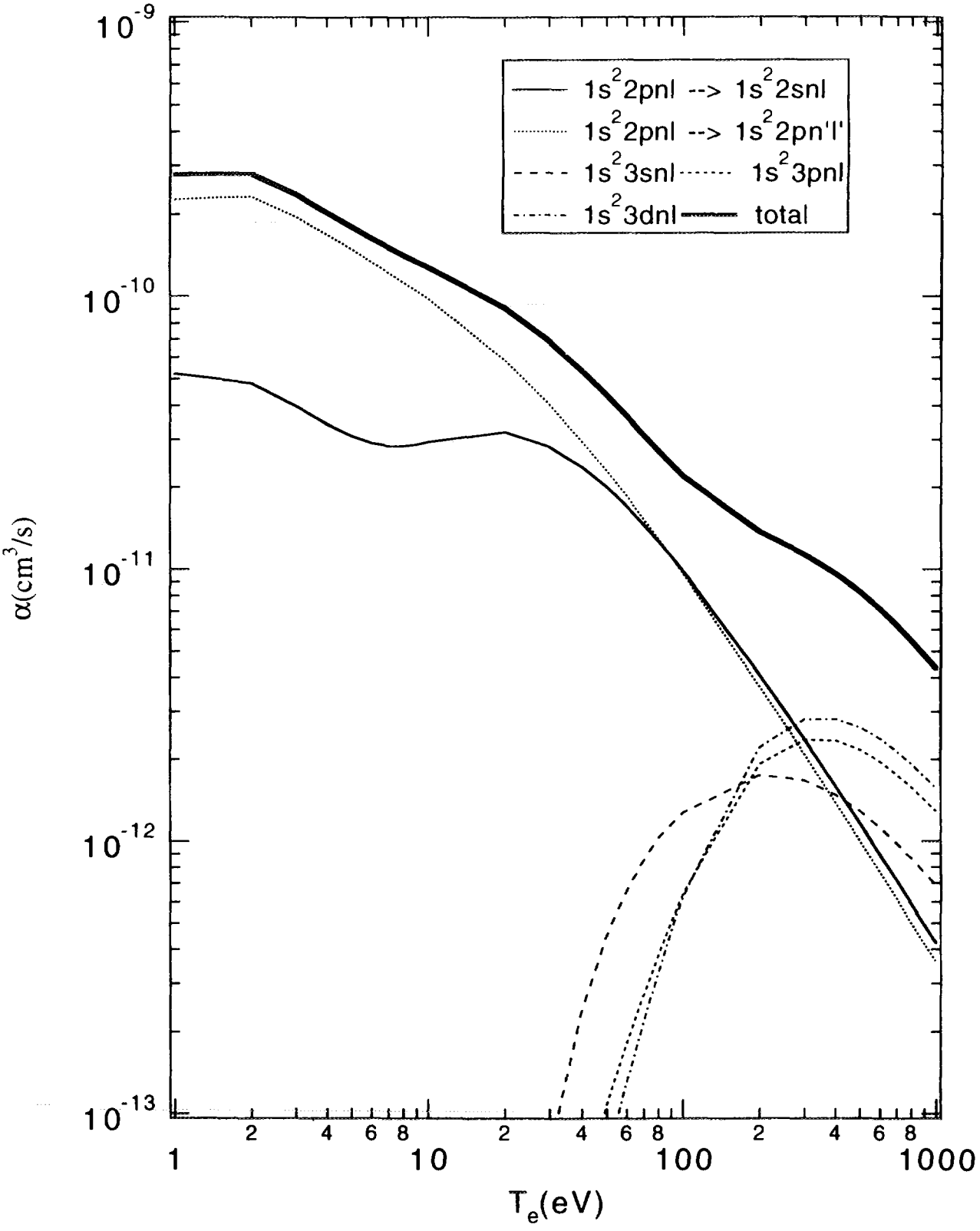
Be-like Ca ion
10^{-9}
10^{-10}
10^{-11}
10^{-12}
10^{-13}
$\alpha(cm^3/s)$
$1s^2 2pnl \rightarrow 1s^2 2snl$
$1s^2 2pnl \rightarrow 1s^2 2pn'l'$
$1s^2 3snl$
$1s^2 3pnl$
$1s^2 3dnl$
total
1
2
4
6
8
10
2
4
6
8
100
2
4
6
8
1000
$T_e(eV)$

Fig.4-1(g)

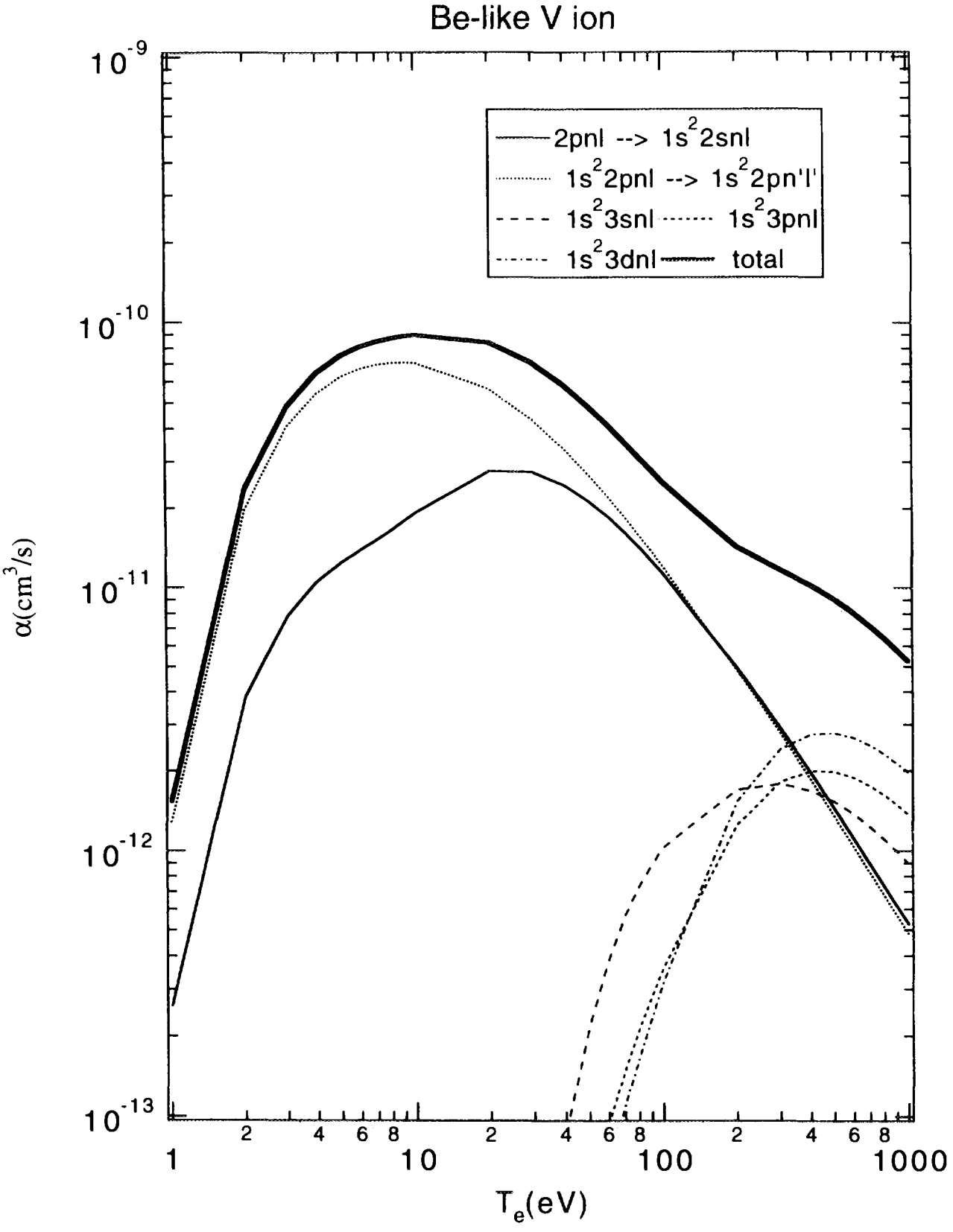
Be-like V ion
2pnl --> 1s²2snl
1s²2pnl --> 1s²2pn'l'
1s²3snl
1s²3pnl
1s²3dnl
total
α(cm³/s)
10⁻⁹
10⁻¹⁰
10⁻¹¹
10⁻¹²
10⁻¹³
1
10
100
1000
Tₑ(eV)

Fig.4-1(h)

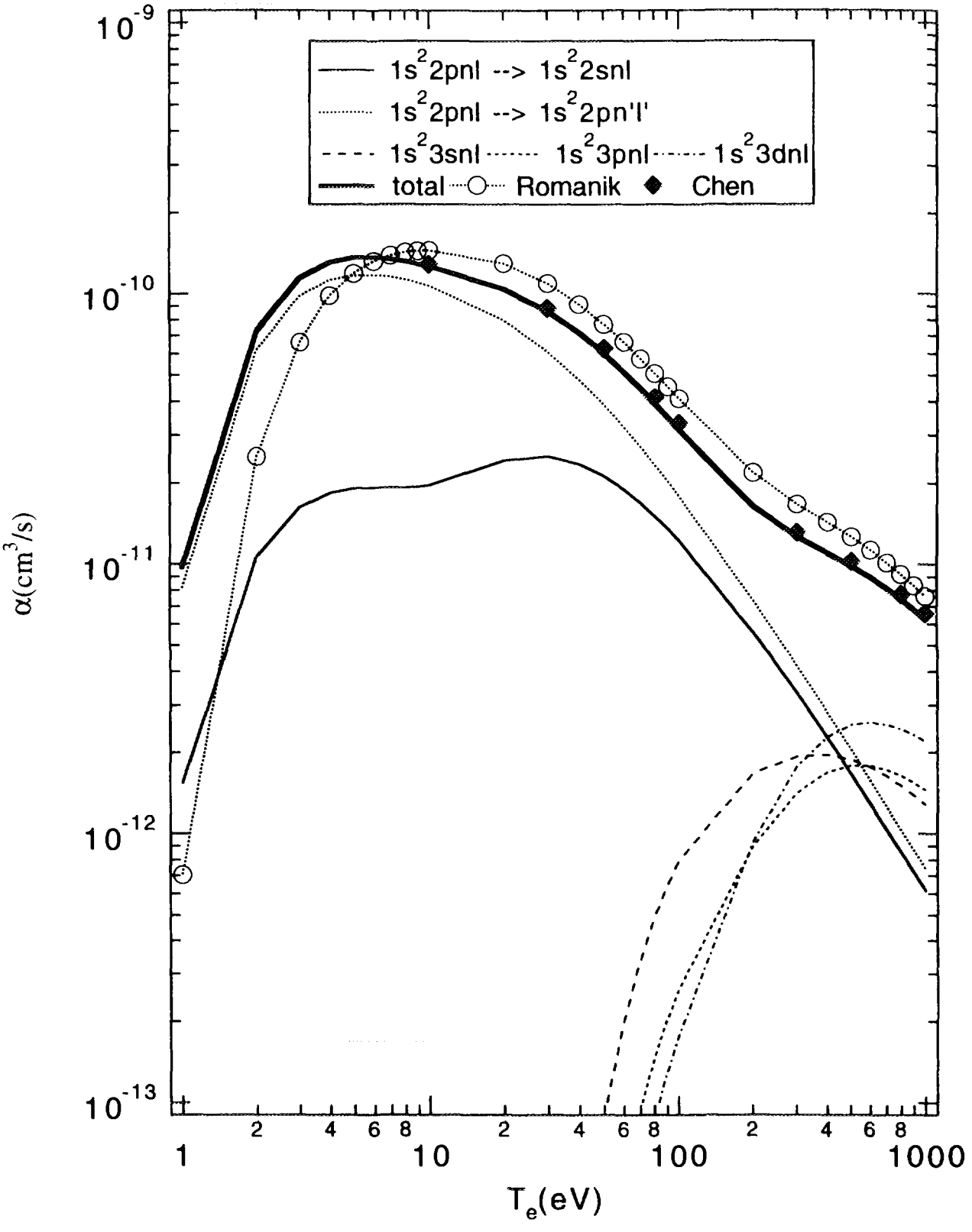
Be-like Fe ion
$1s^2 2pnl \rightarrow 1s^2 2snl$
$1s^2 2pnl \rightarrow 1s^2 2pn'l'$
$1s^2 3snl$
$1s^2 3pnl$
$1s^2 3dnl$
total
Romanik
Chen
10^{-9}
10^{-10}
10^{-11}
10^{-12}
10^{-13}
$\alpha(cm^3/s)$
1
10
100
1000
$T_e(eV)$

Fig.4-1(i)

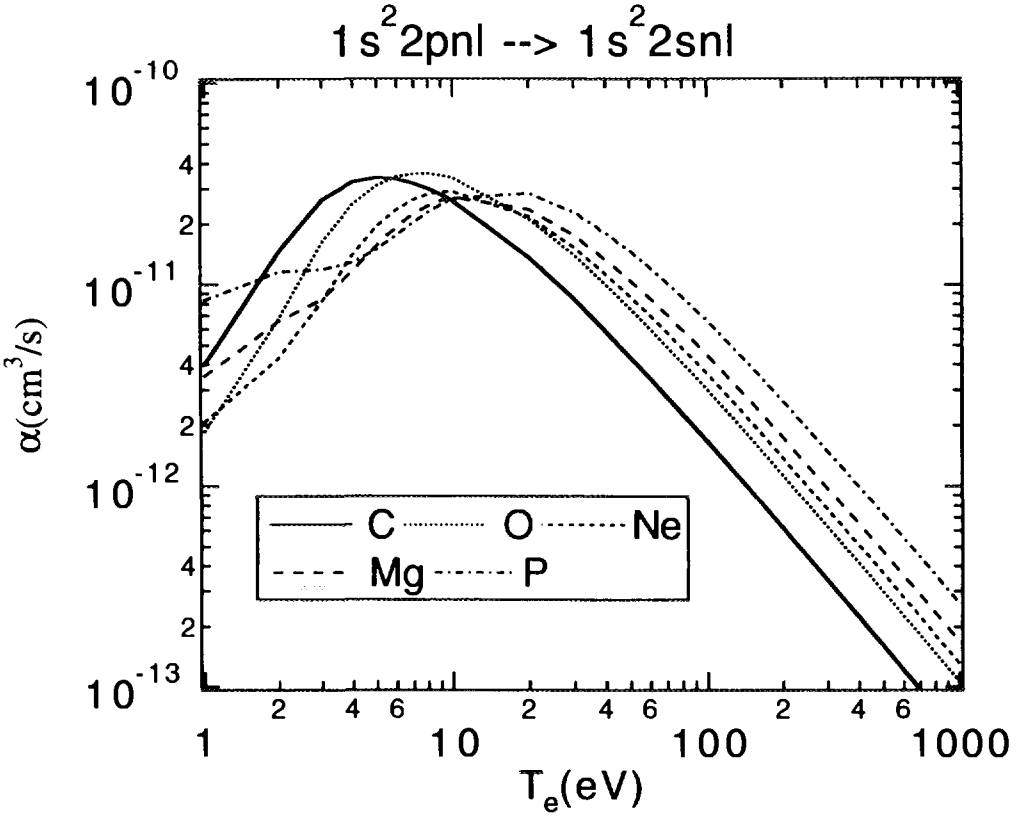

Fig.4-2(a)

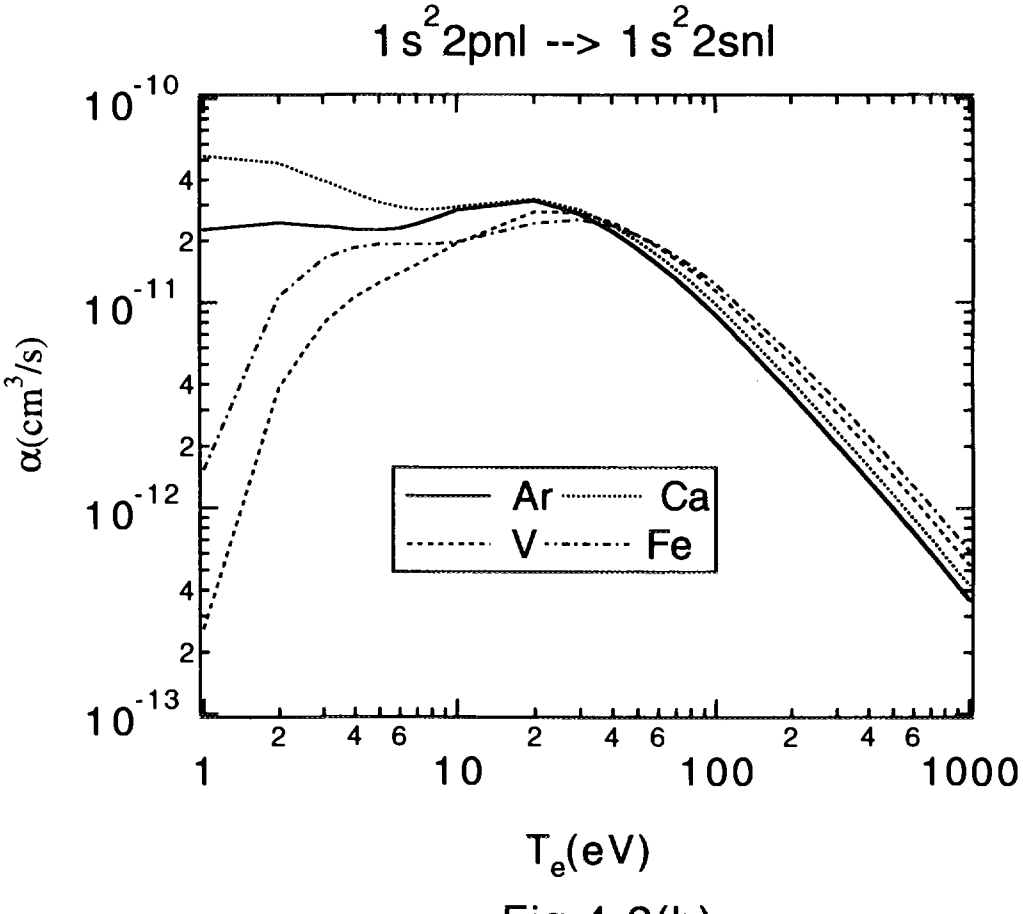

Fig.4-2(b)

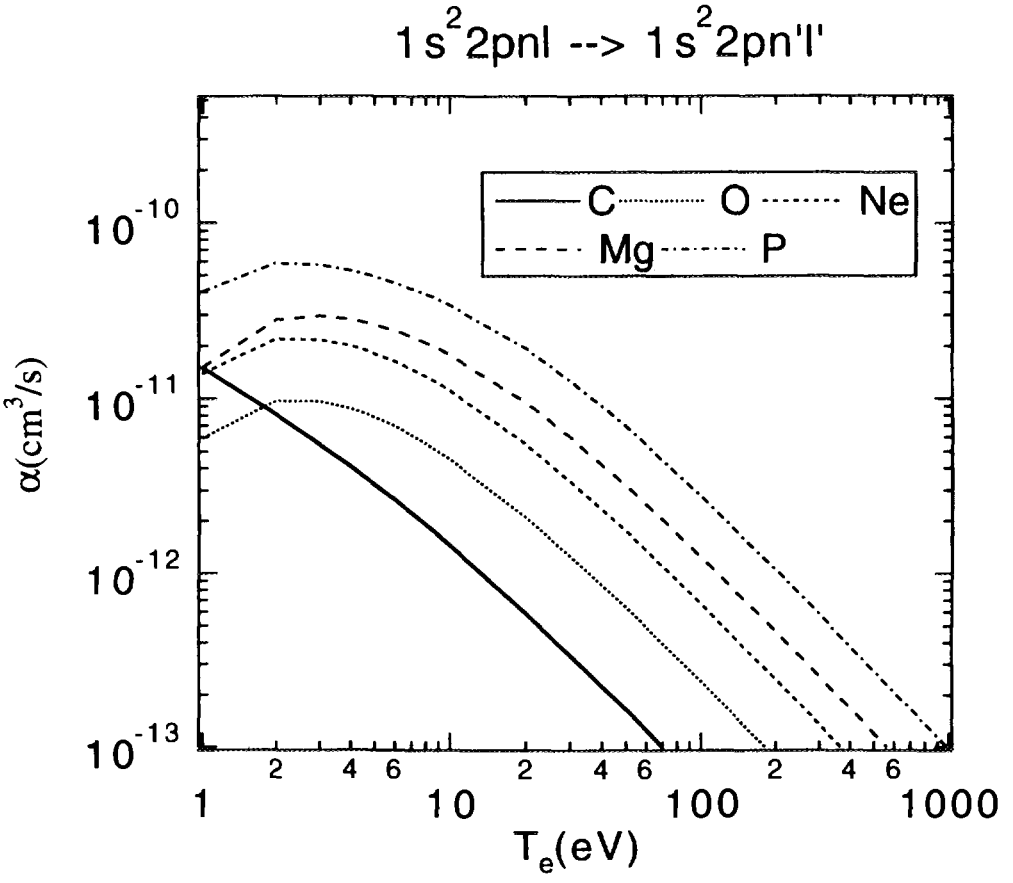

Fig.4-2(c)

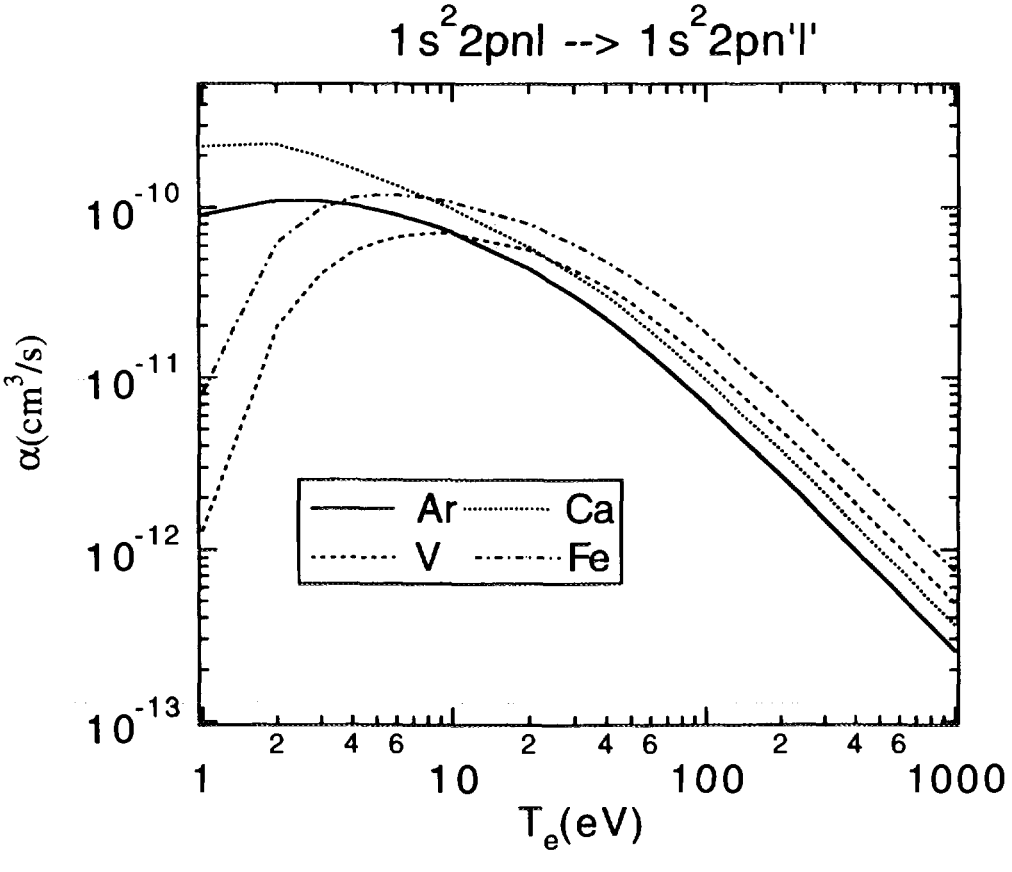

Fig.4-2(d)

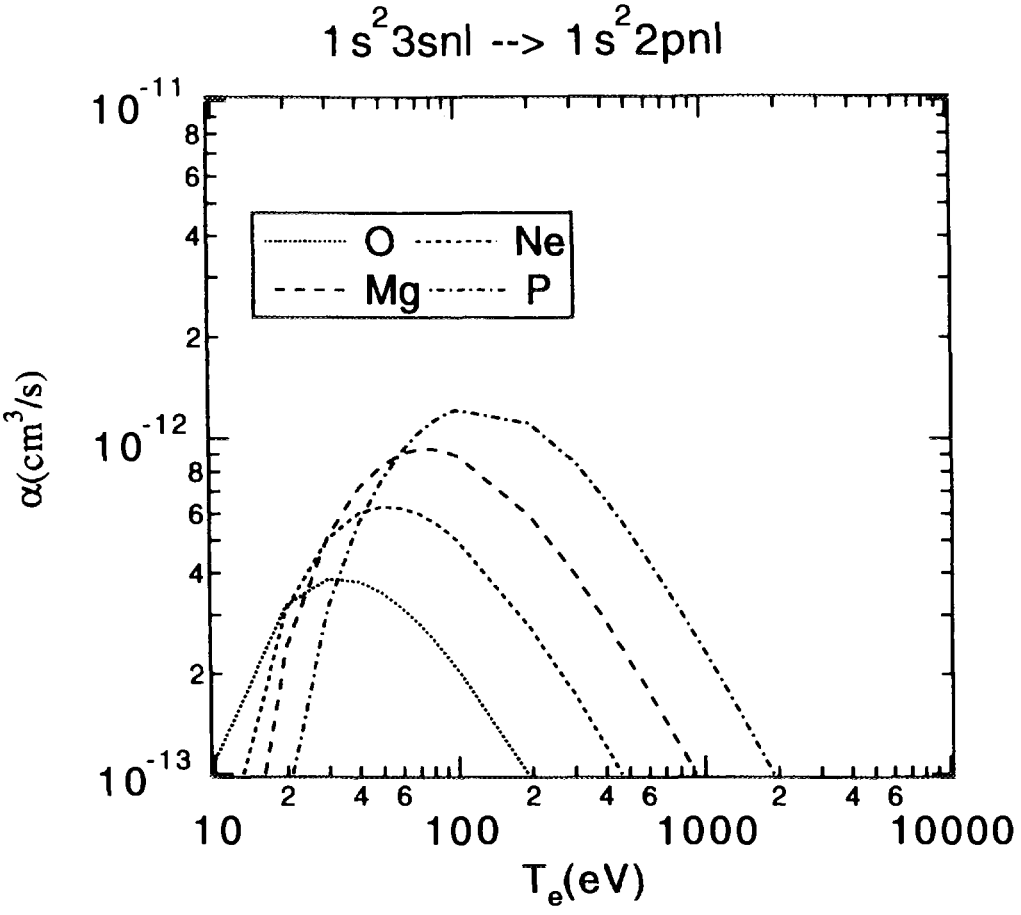

Fig.4-2(e)

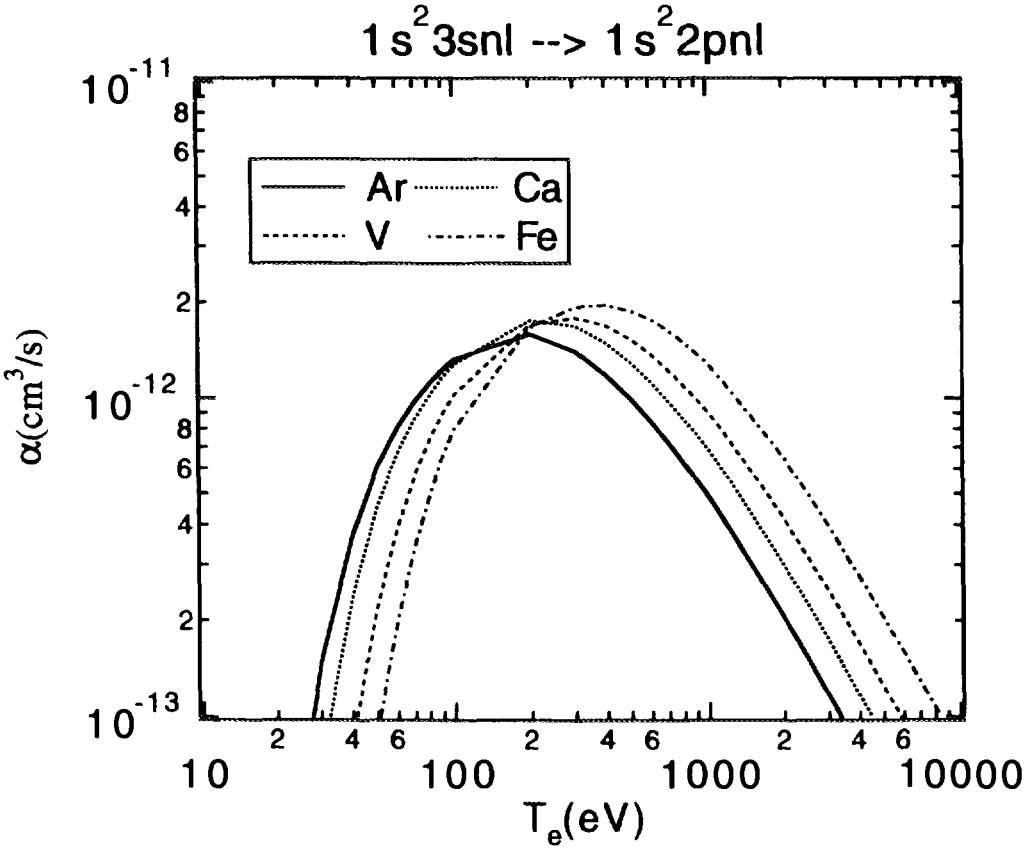

Fig.4-2(f)

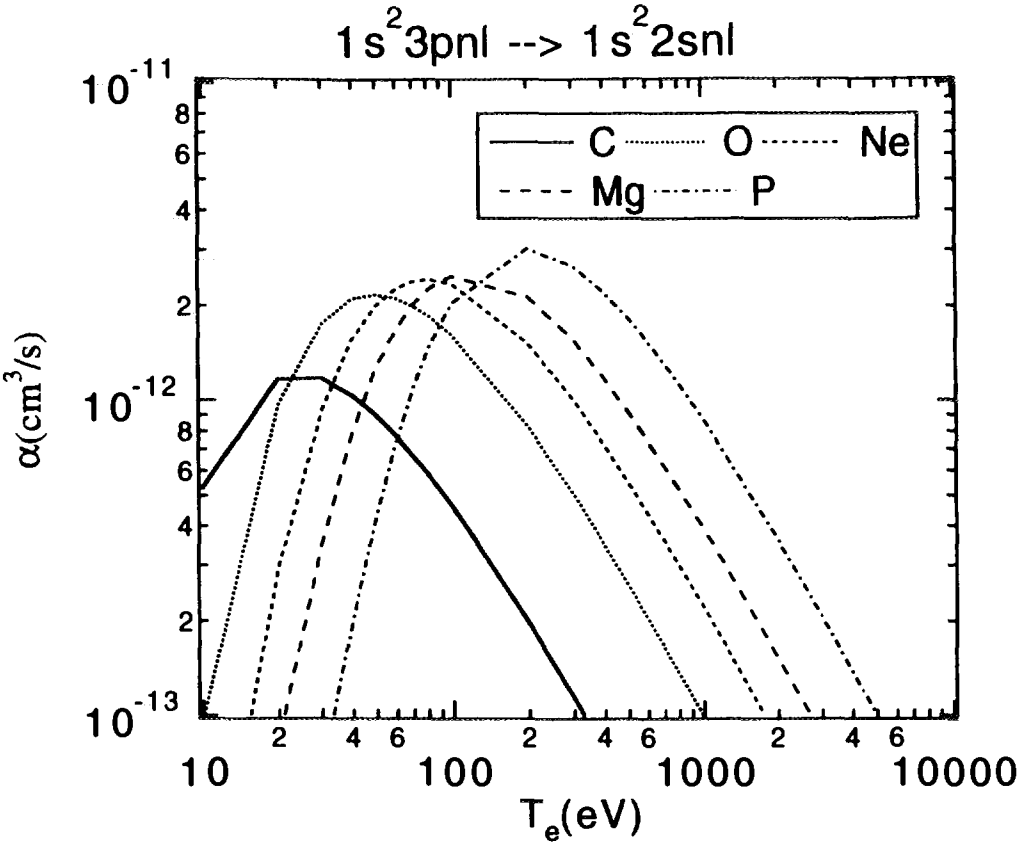

Fig.4-2(g)

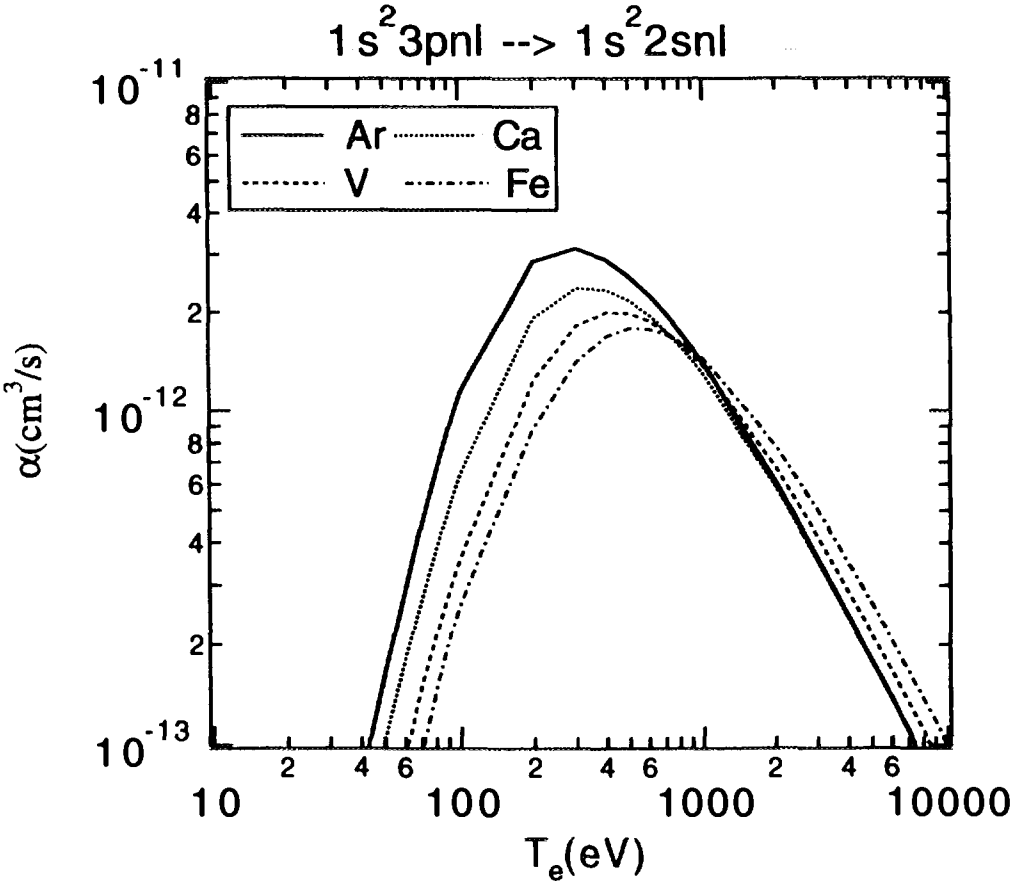

Fig.4-2(h)

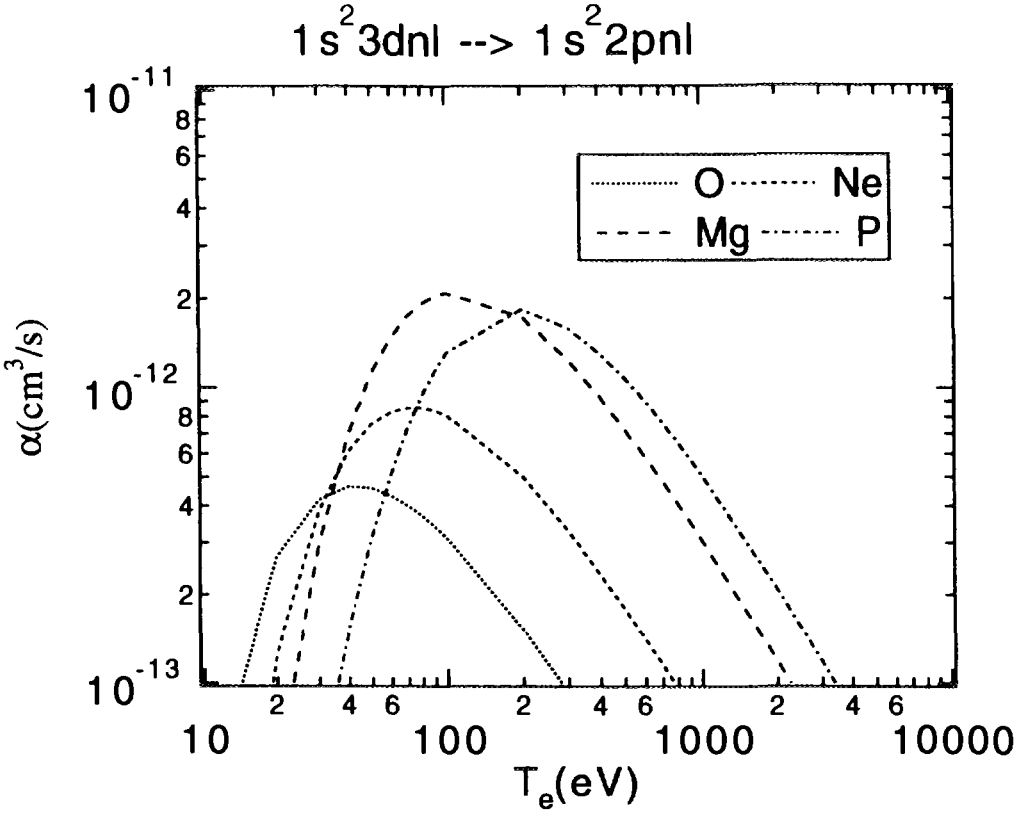

Fig.4-2(i)

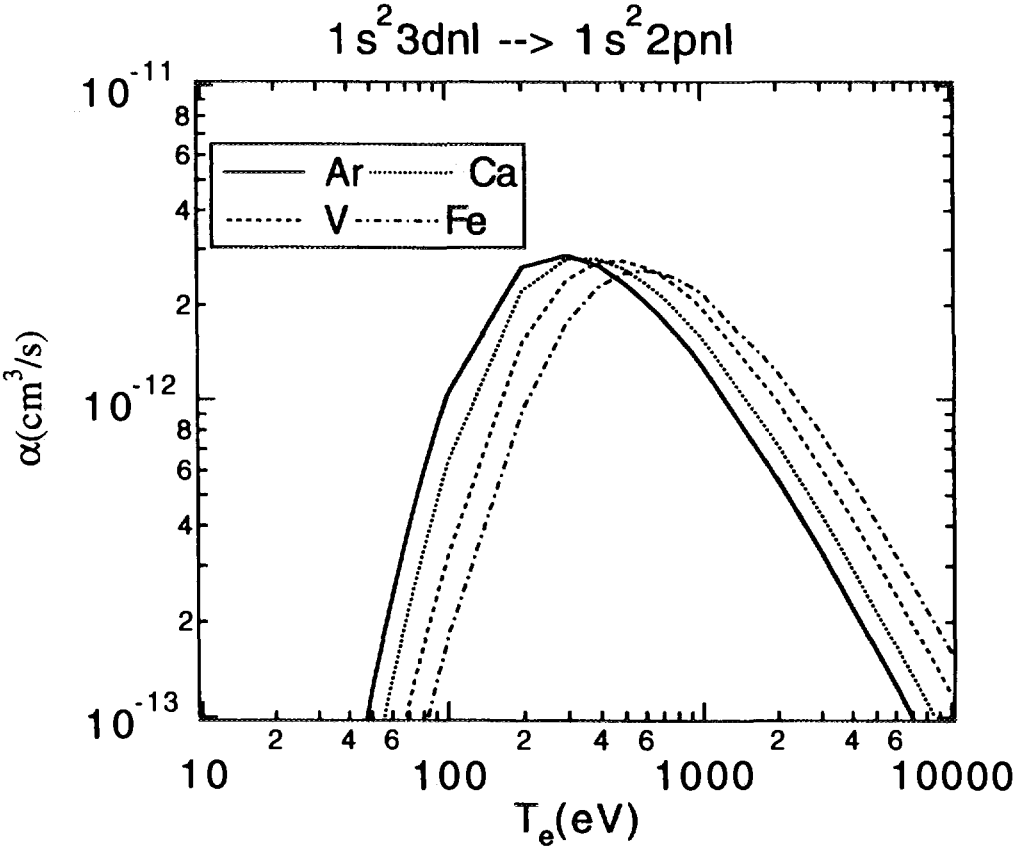

Fig.4-2(j)

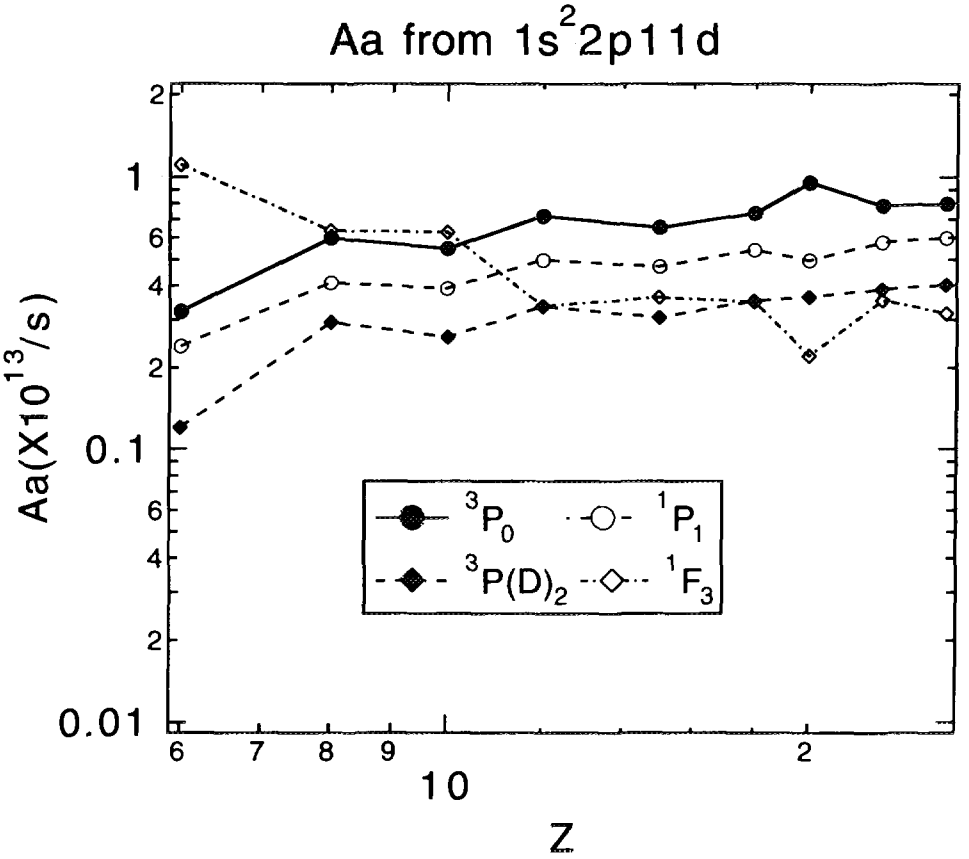

Fig.3-1-2(c)

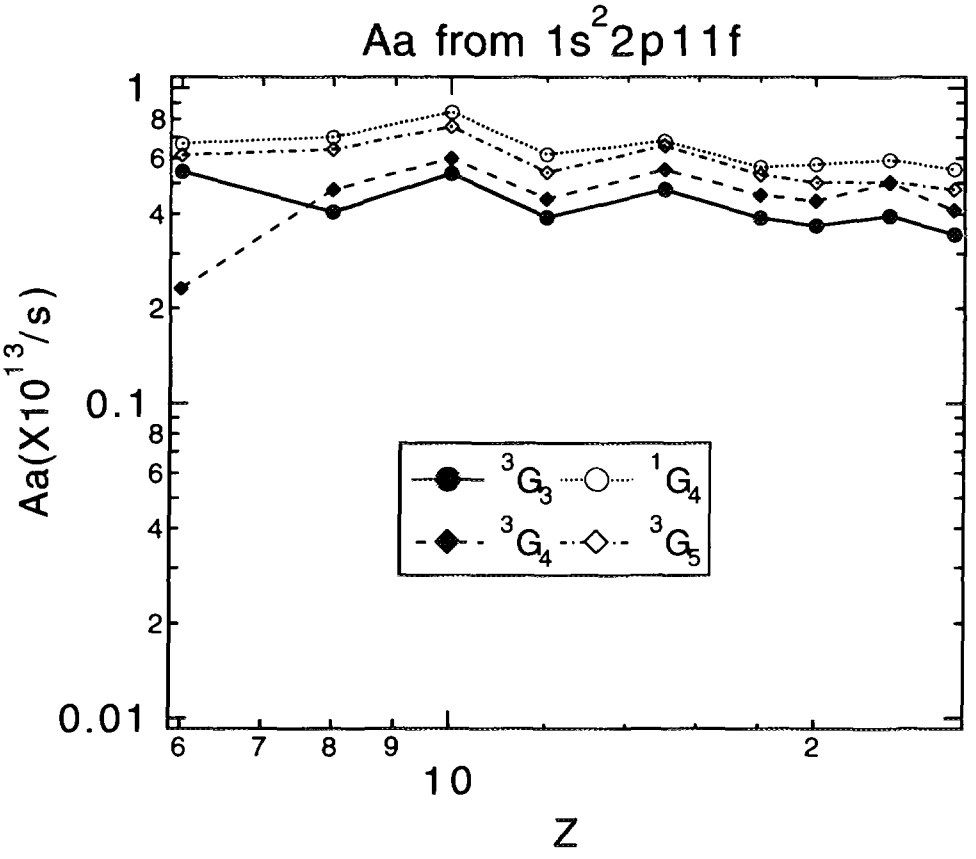

Fig.3-1-2(d)

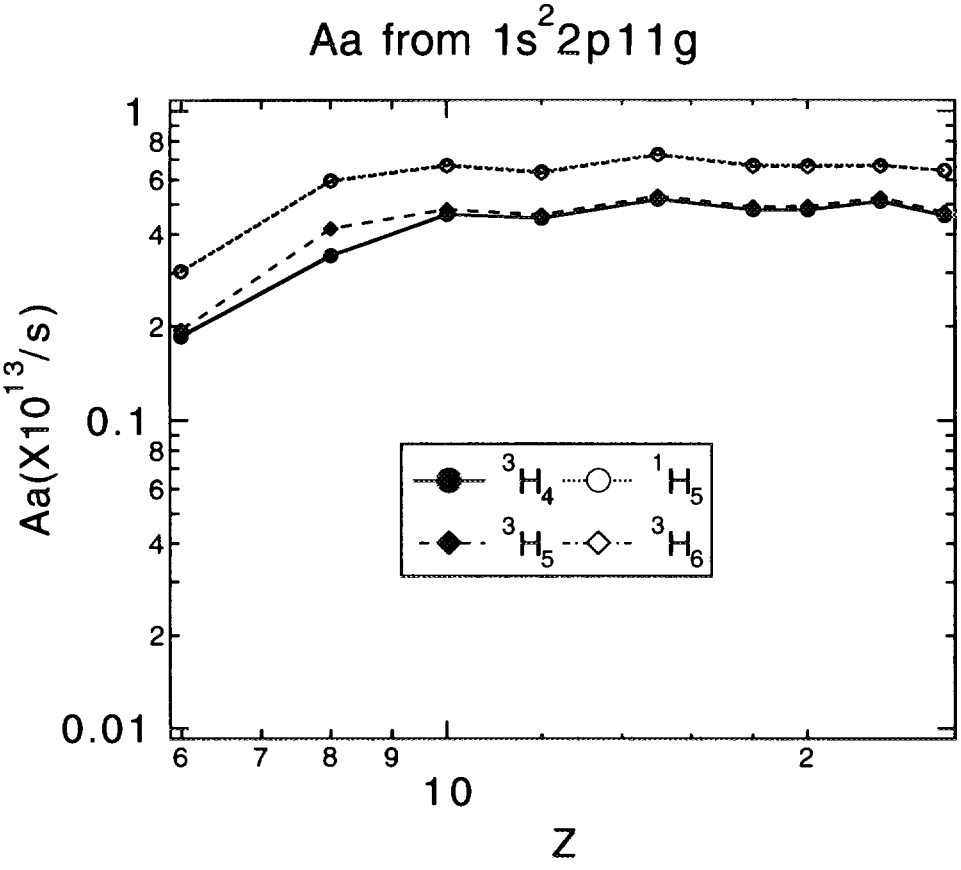
Aa from 1s²2p11g
Aa(X10¹³/s)
1
8
6
4
2
0.1
8
6
4
2
0.01
6
7
8
9
10
2
Z
³H₄
¹H₅
³H₅
³H₆

Fig.3-1-2(e)

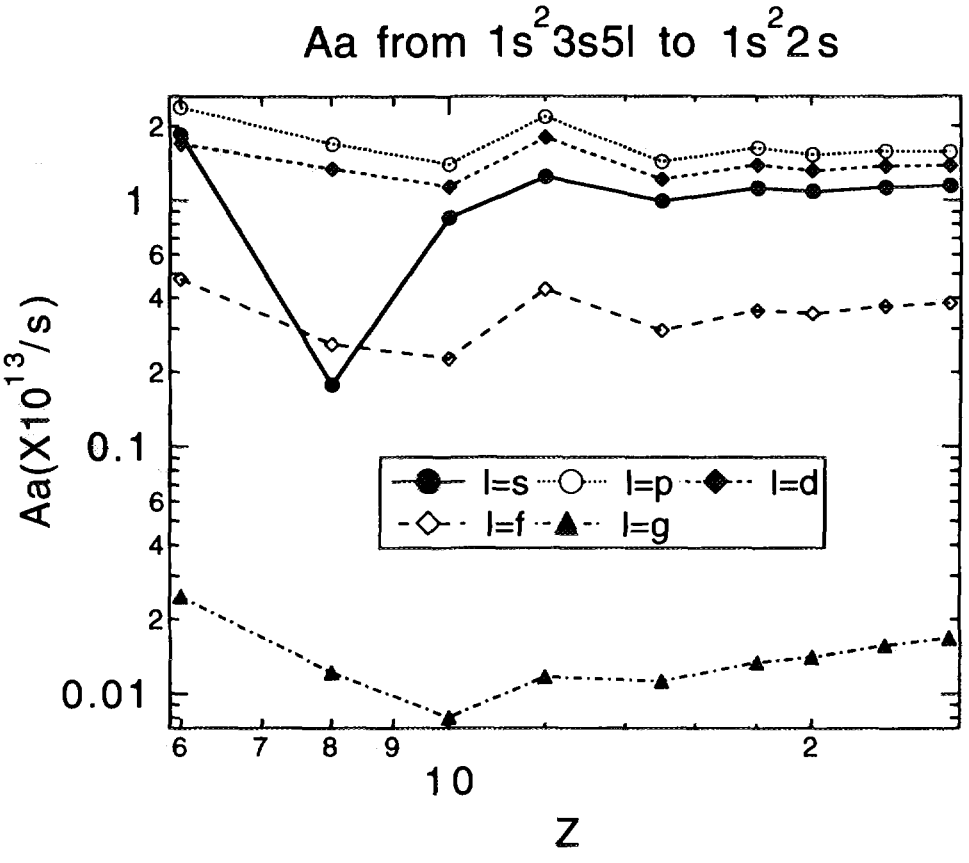

Fig.3-2(a)

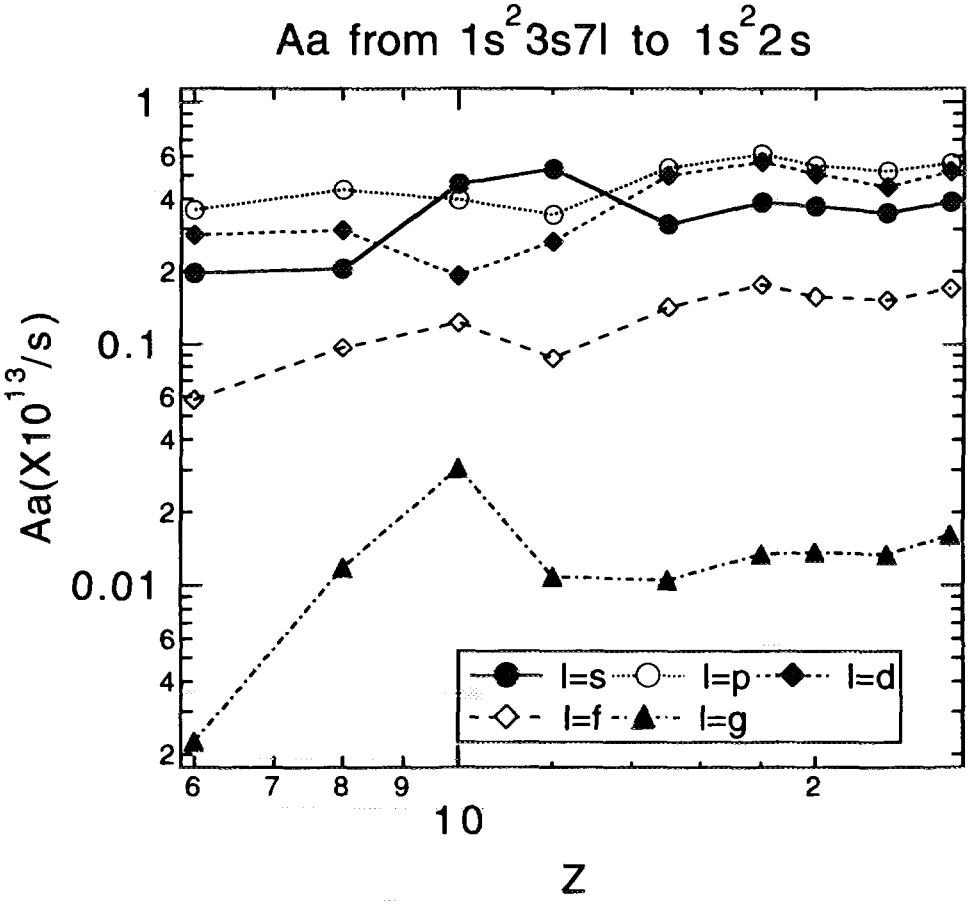

Fig.3-2(b)

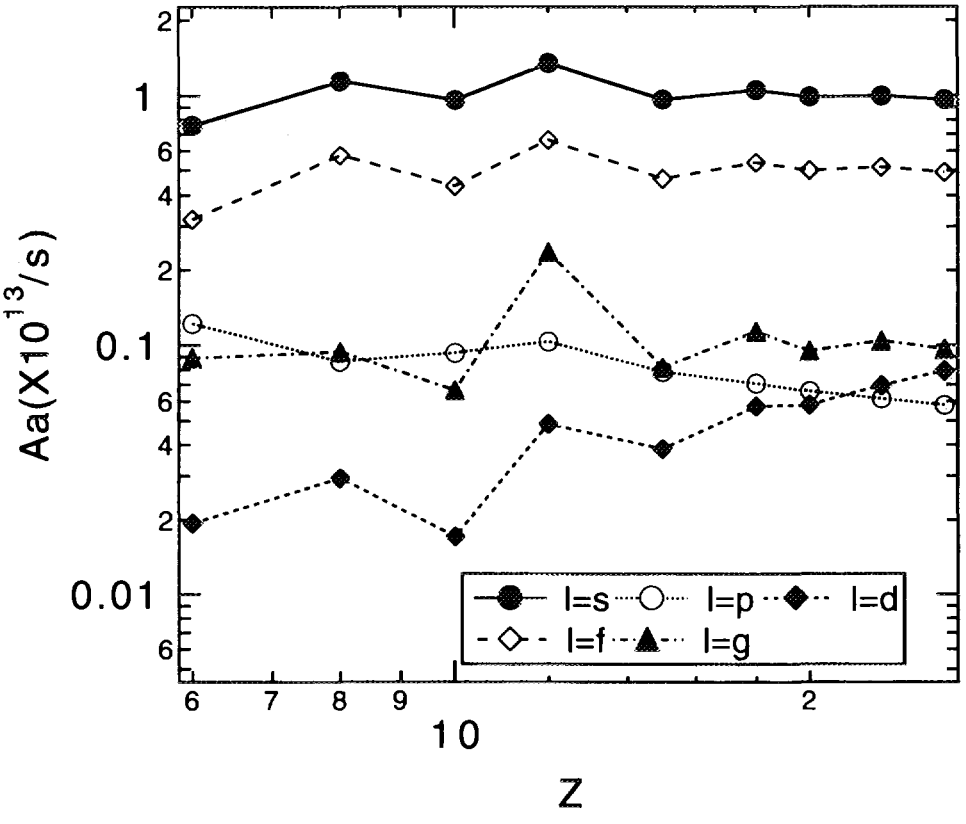

Fig.3-2(c)

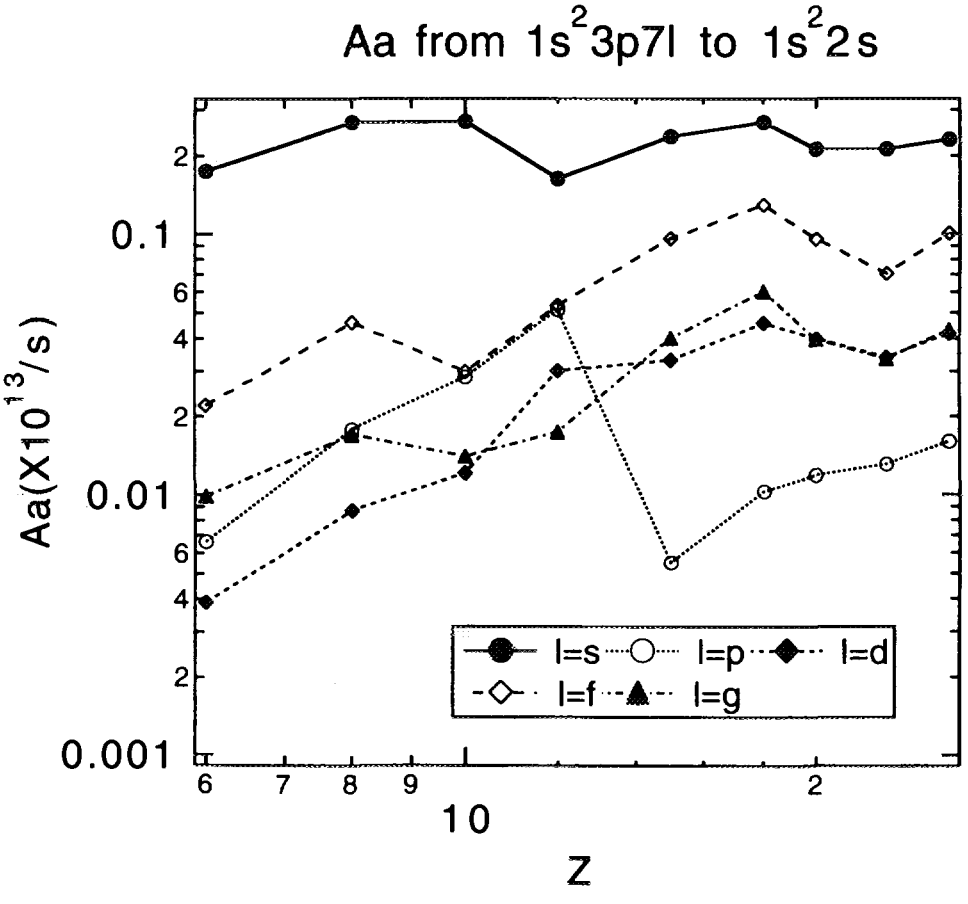

Fig.3-2(d)

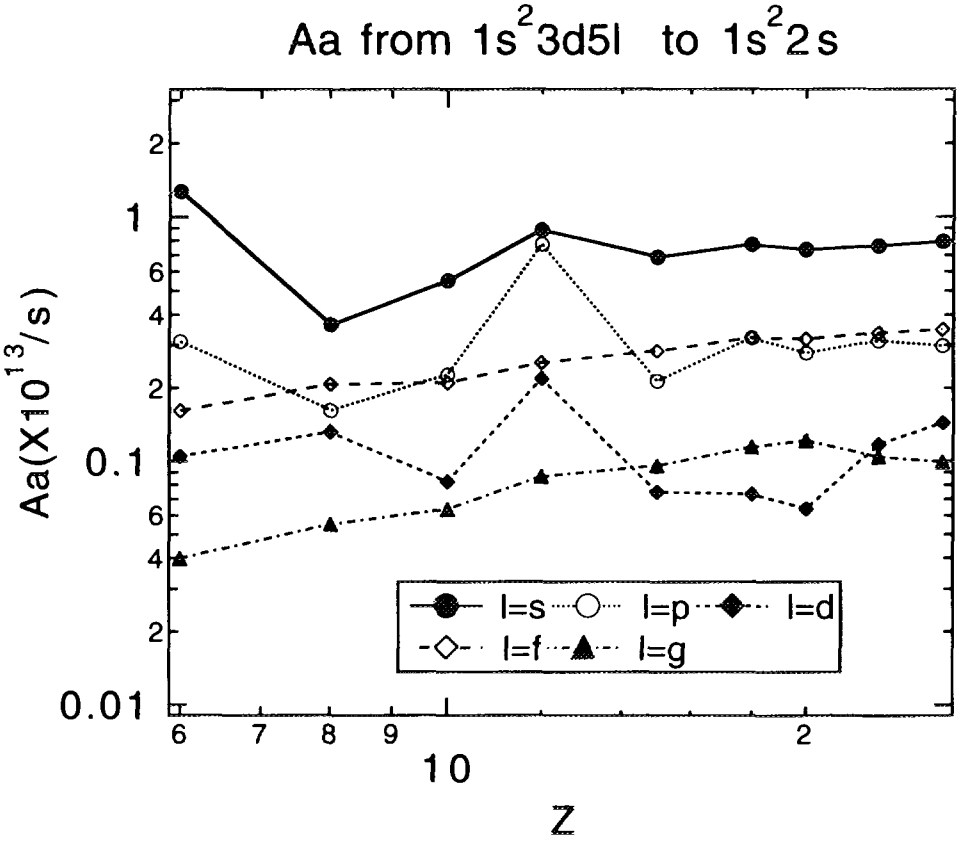

Fig.3-2(e)

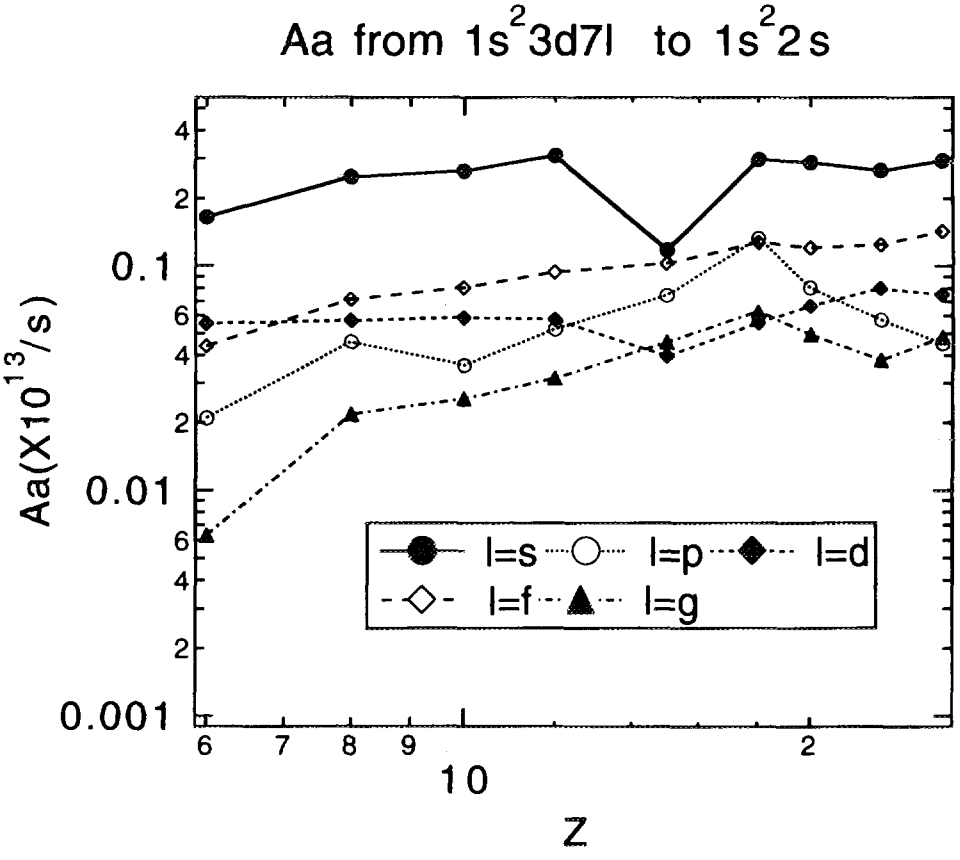

Fig.3-2(f)

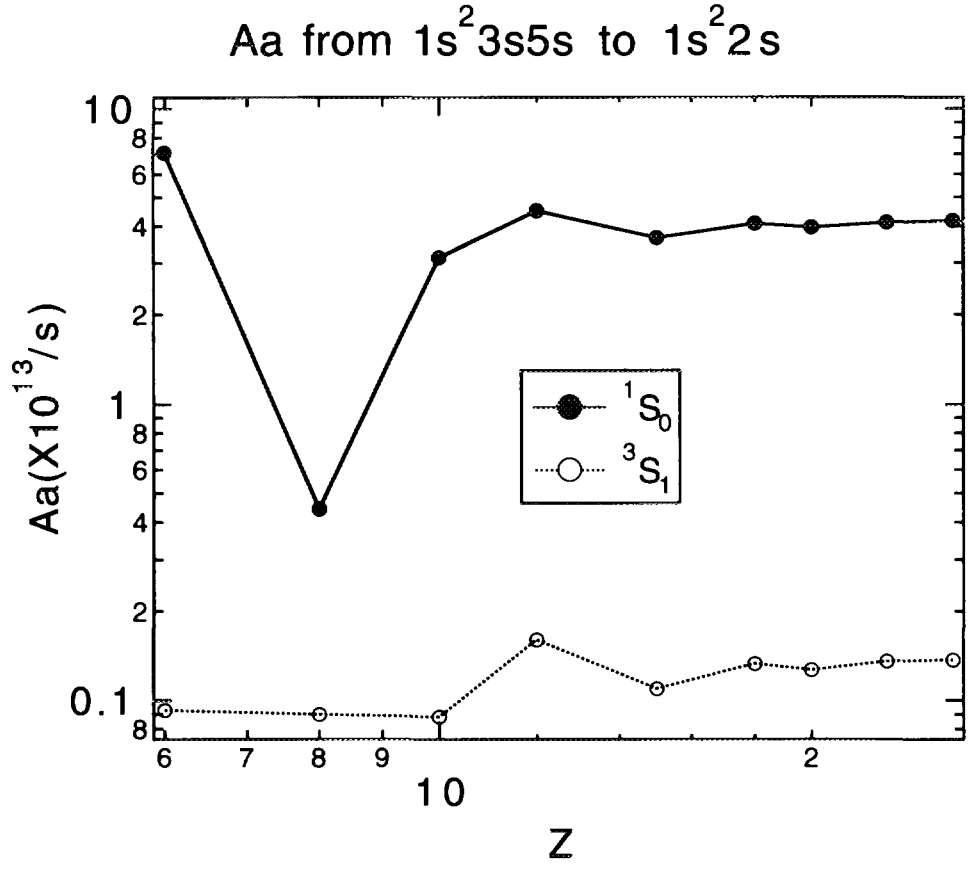

Fig.3-2-2(a)

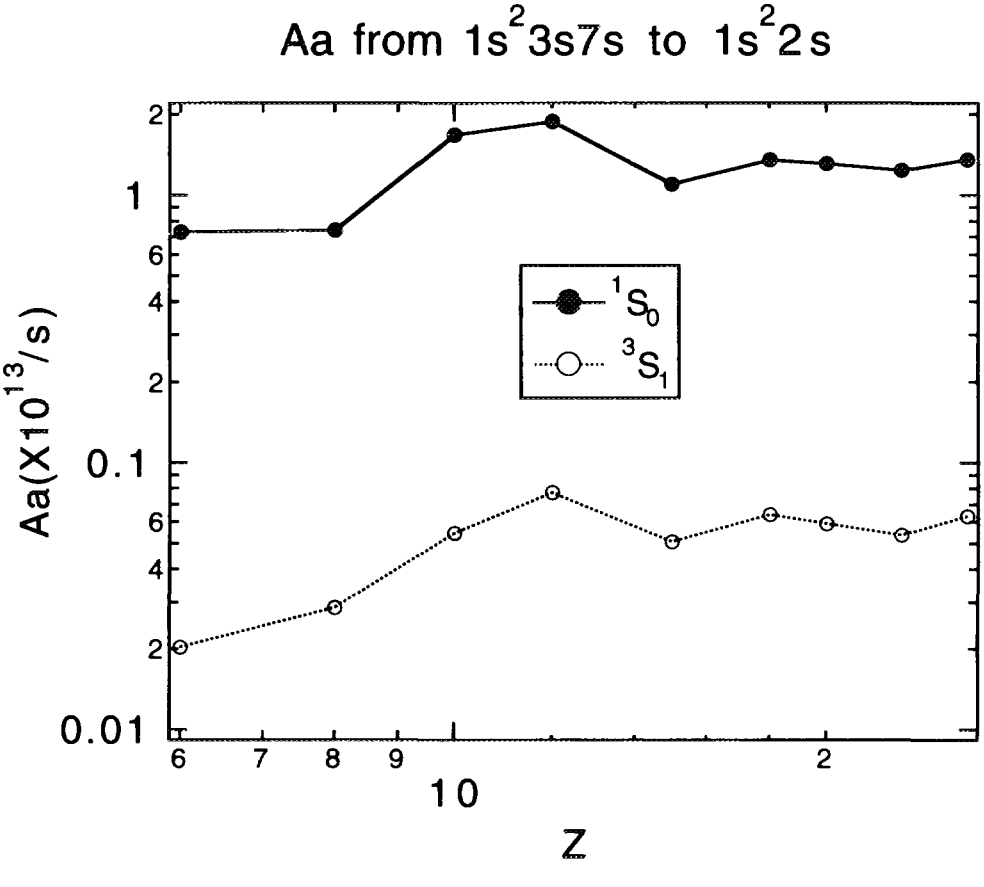

Fig.3-2-2(b)

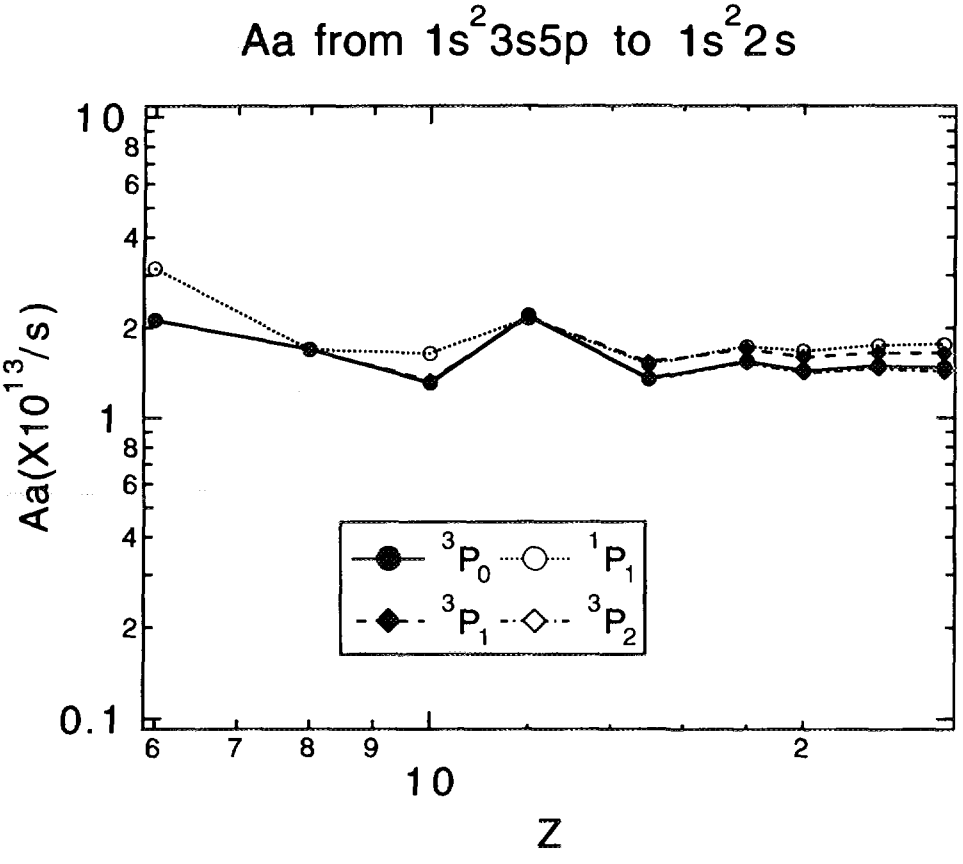

Fig.3-2-2(c)

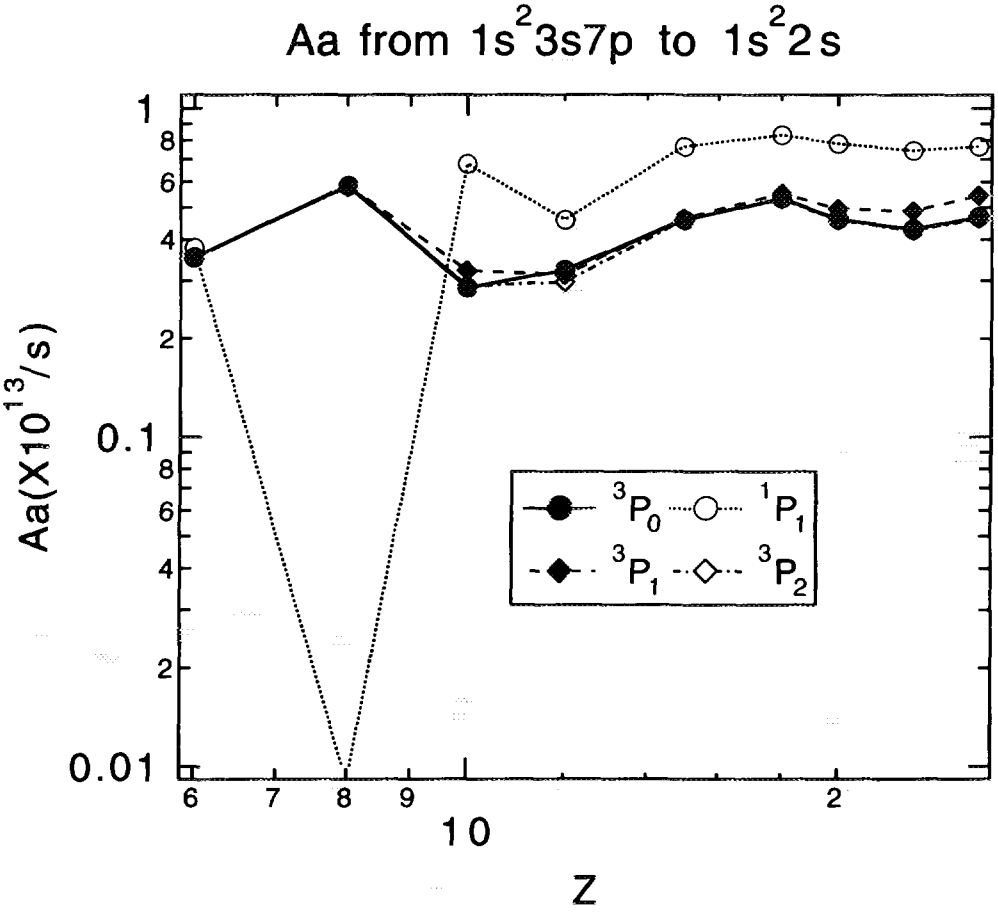

Fig.3-2-2(d)

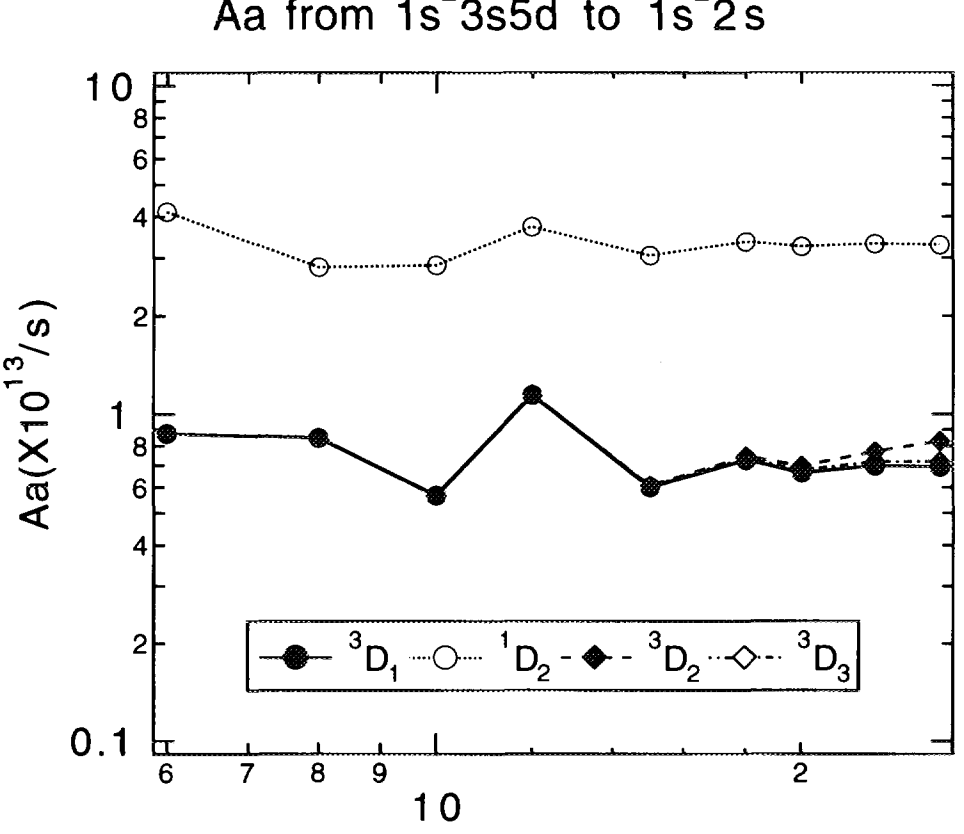

Fig.3-2-2(e)

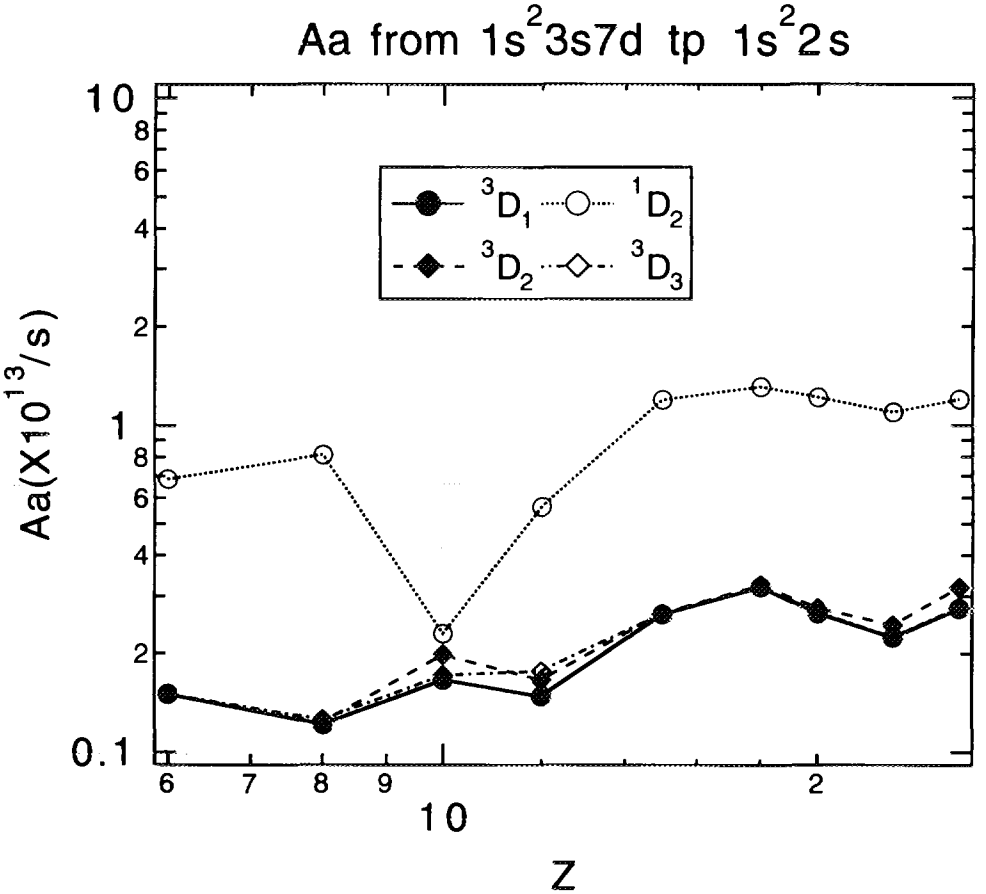

Fig.3-2-2(f)

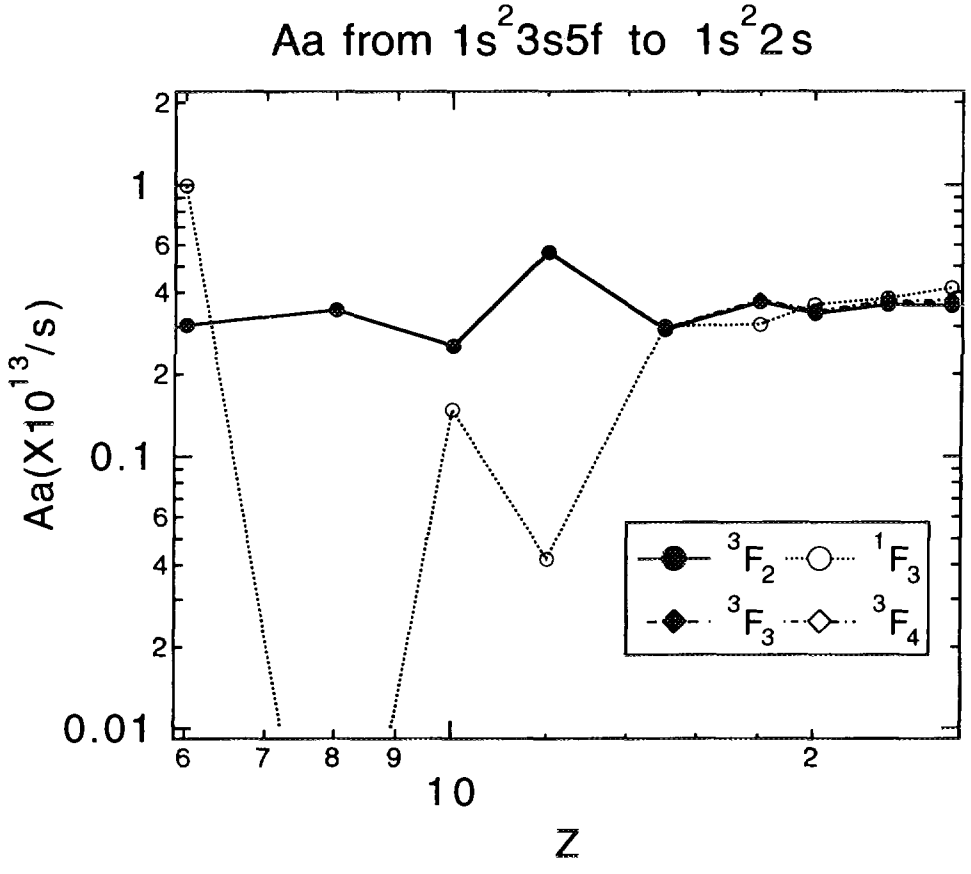

Fig.3-2-2(g)

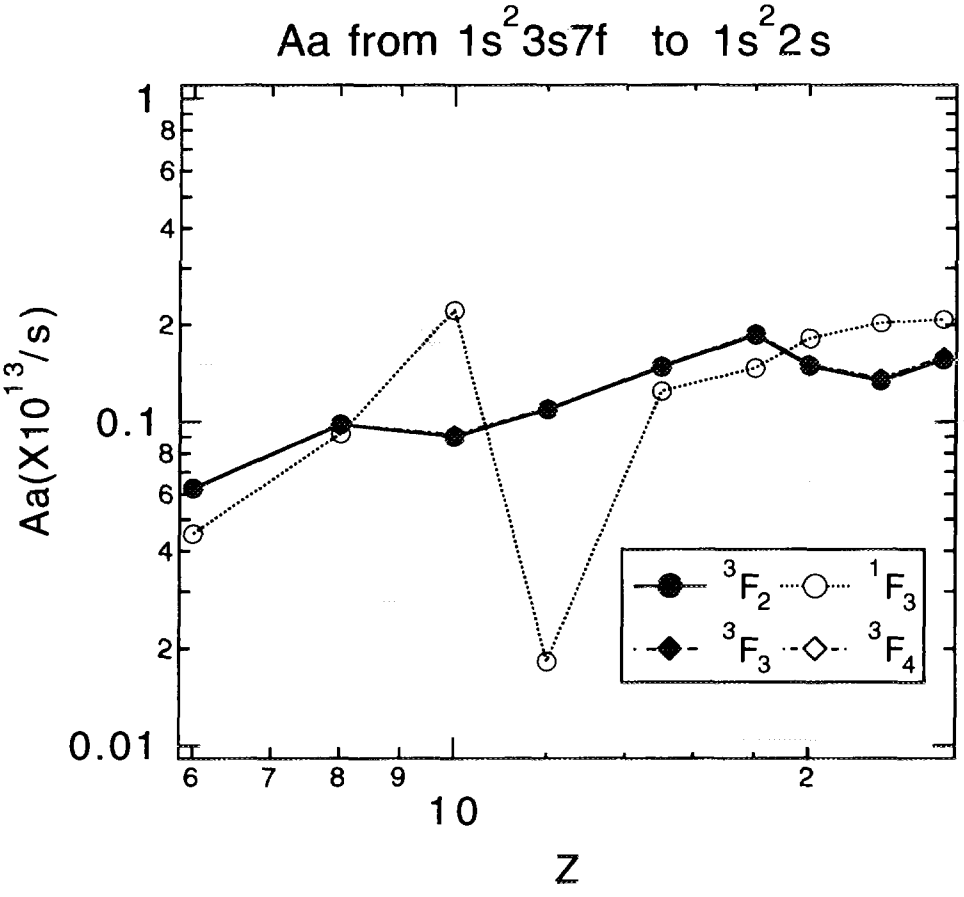

Fig.3-2-2(h)

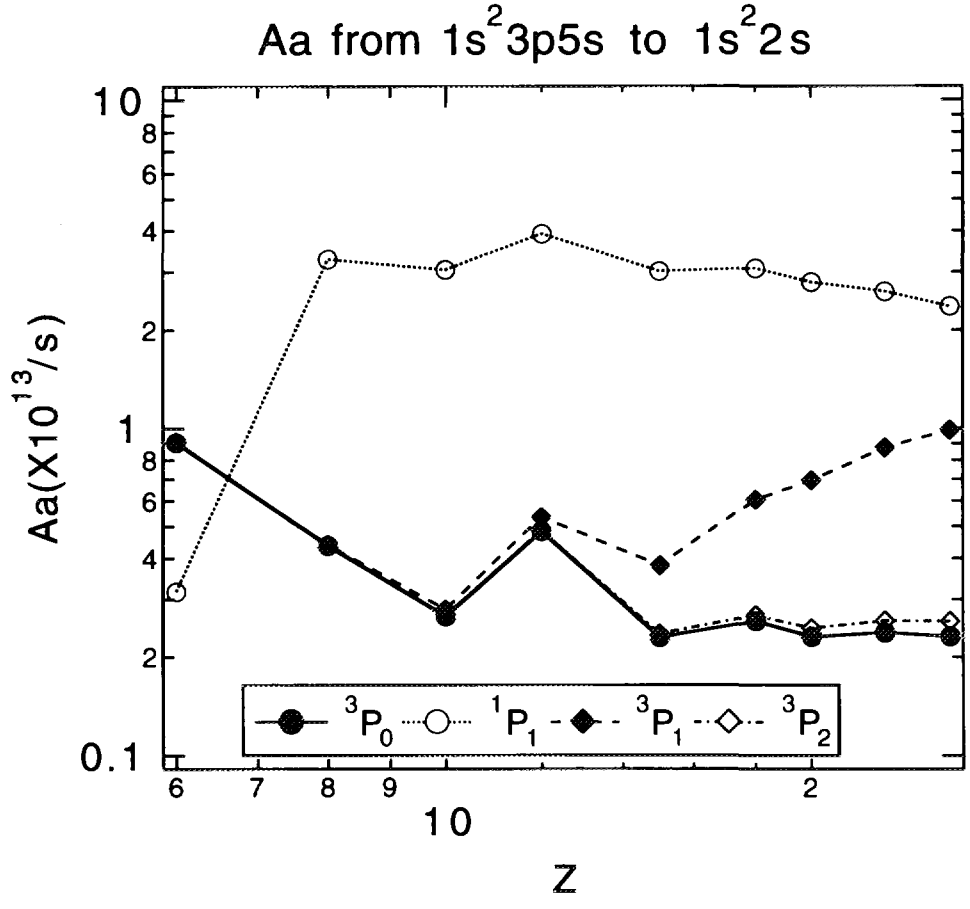

Fig.3-2-3(a)

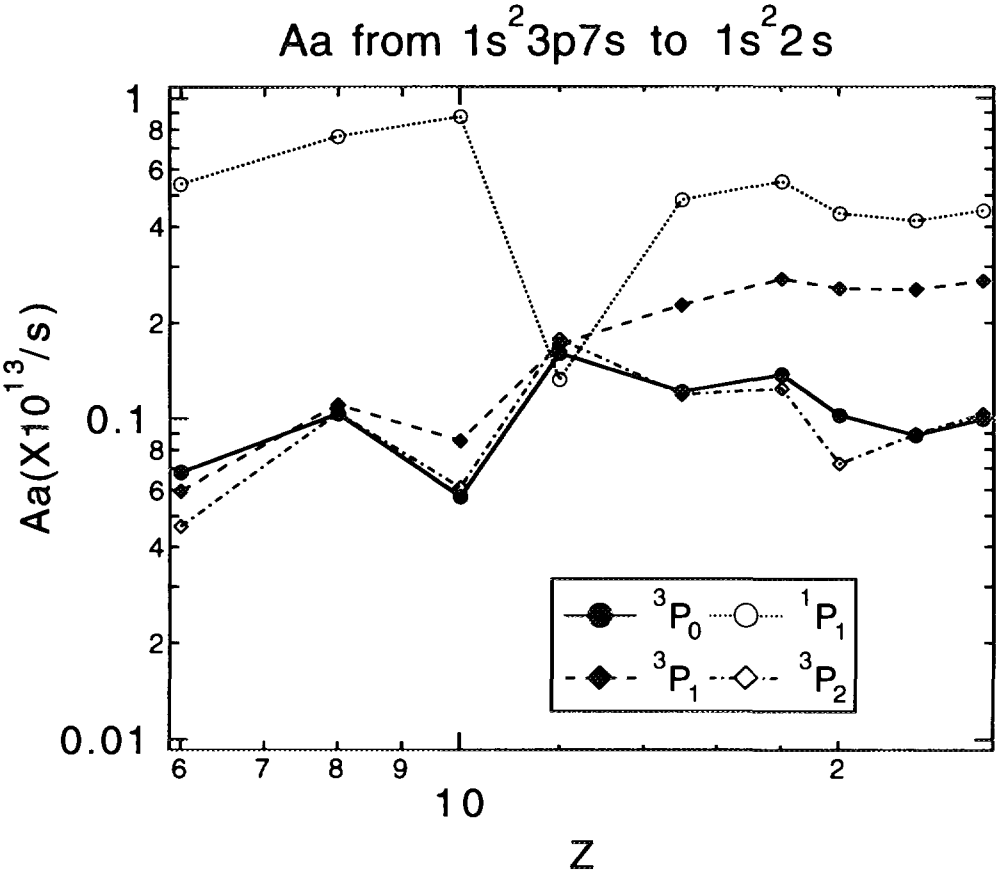

Fig.3-2-3(b)

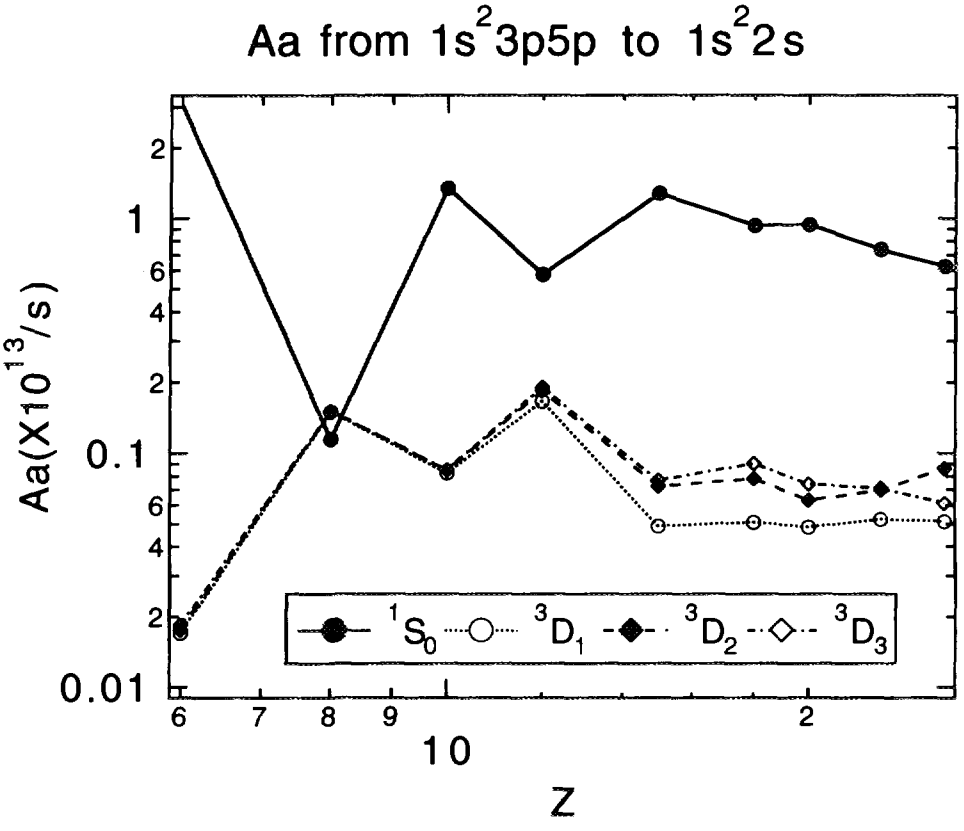

Fig.3-2-3(c)

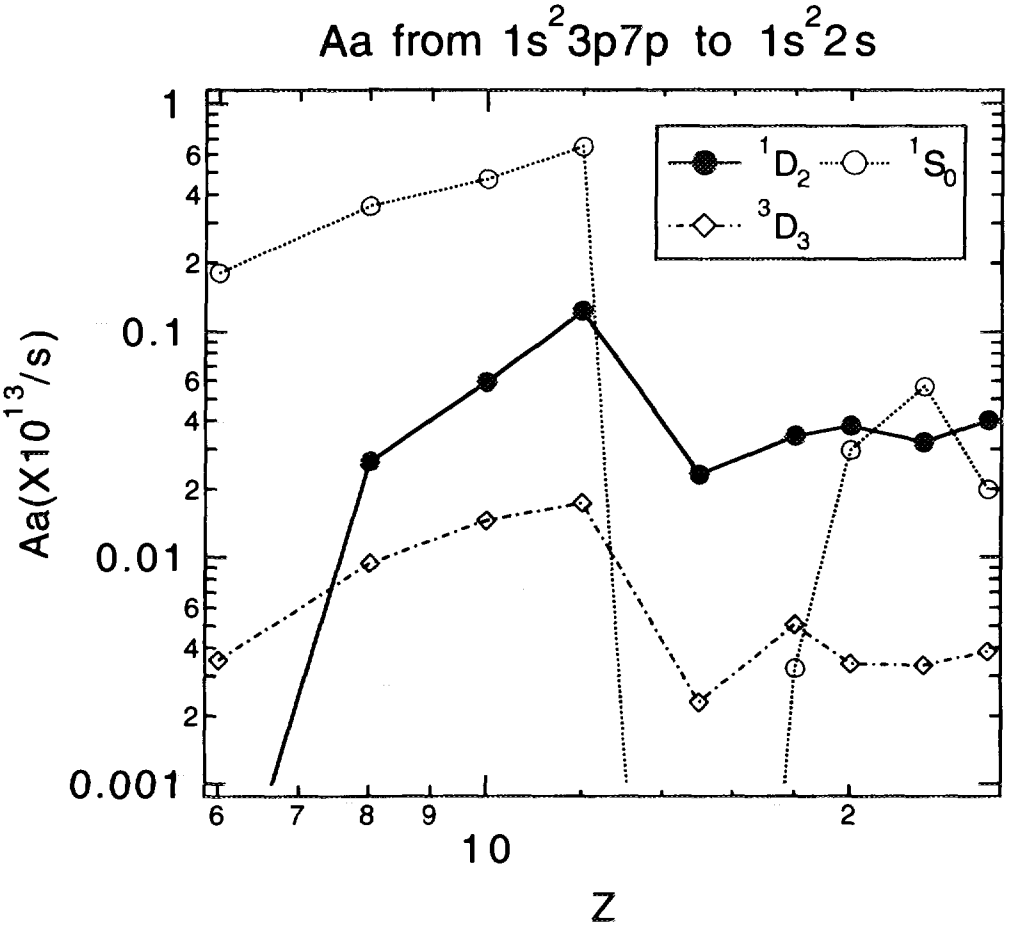

Fig.3-2-3(d)

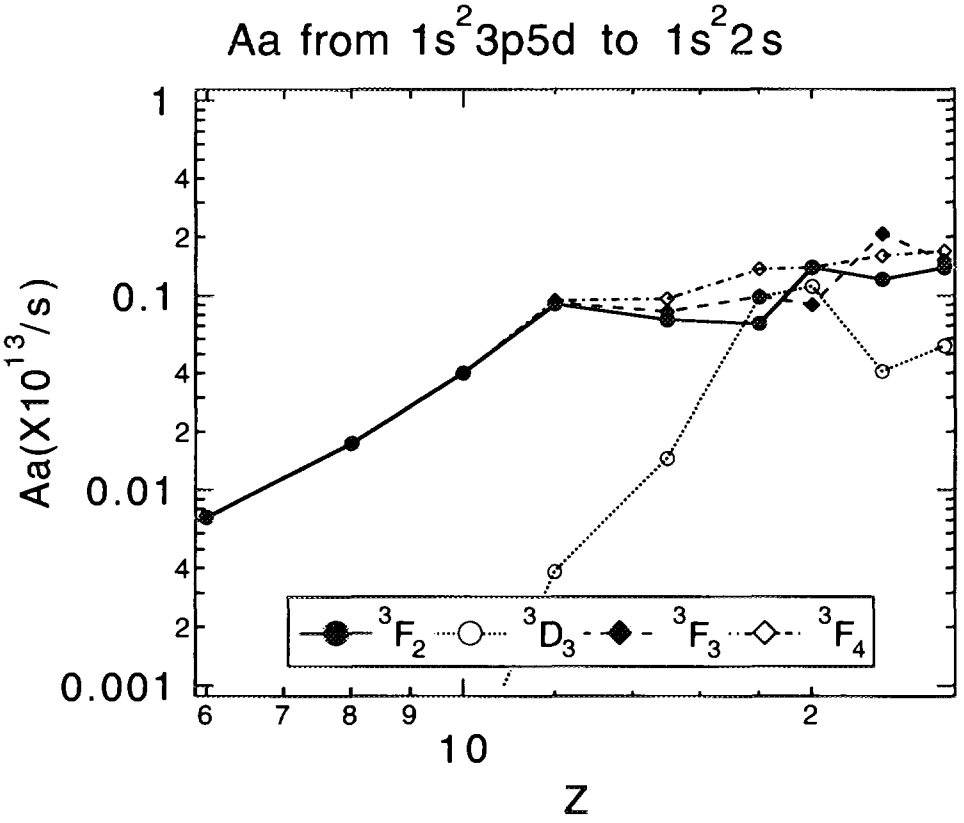

Fig.3-2-3(e)

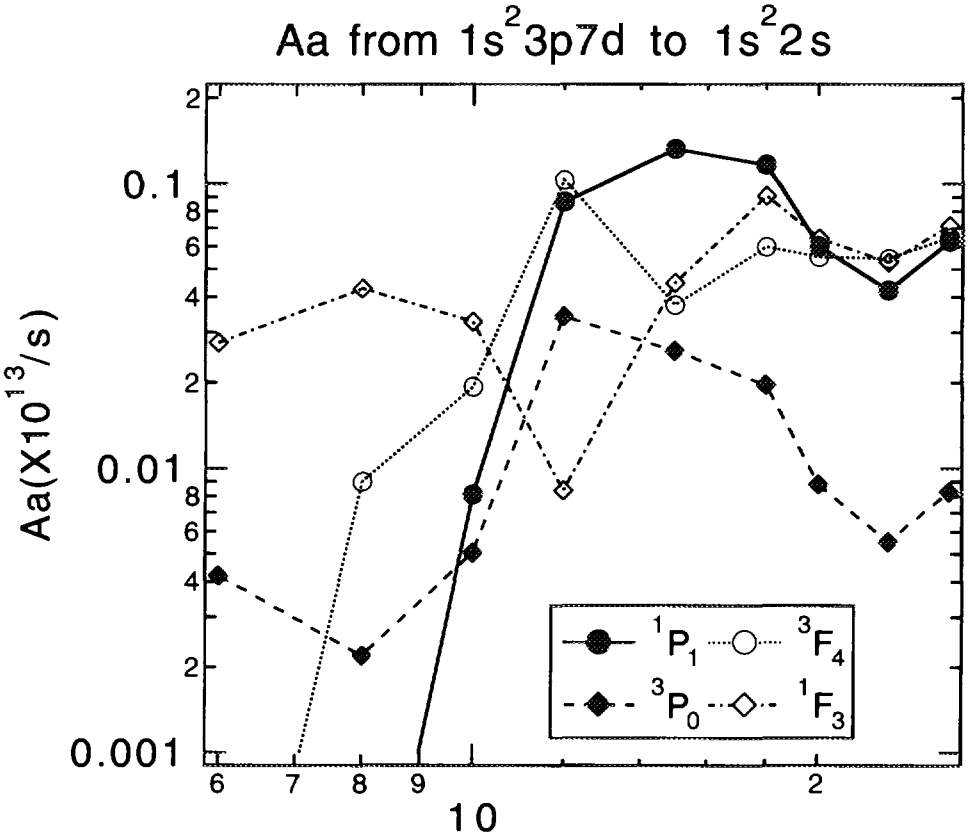

Fig.3-2-3(f)

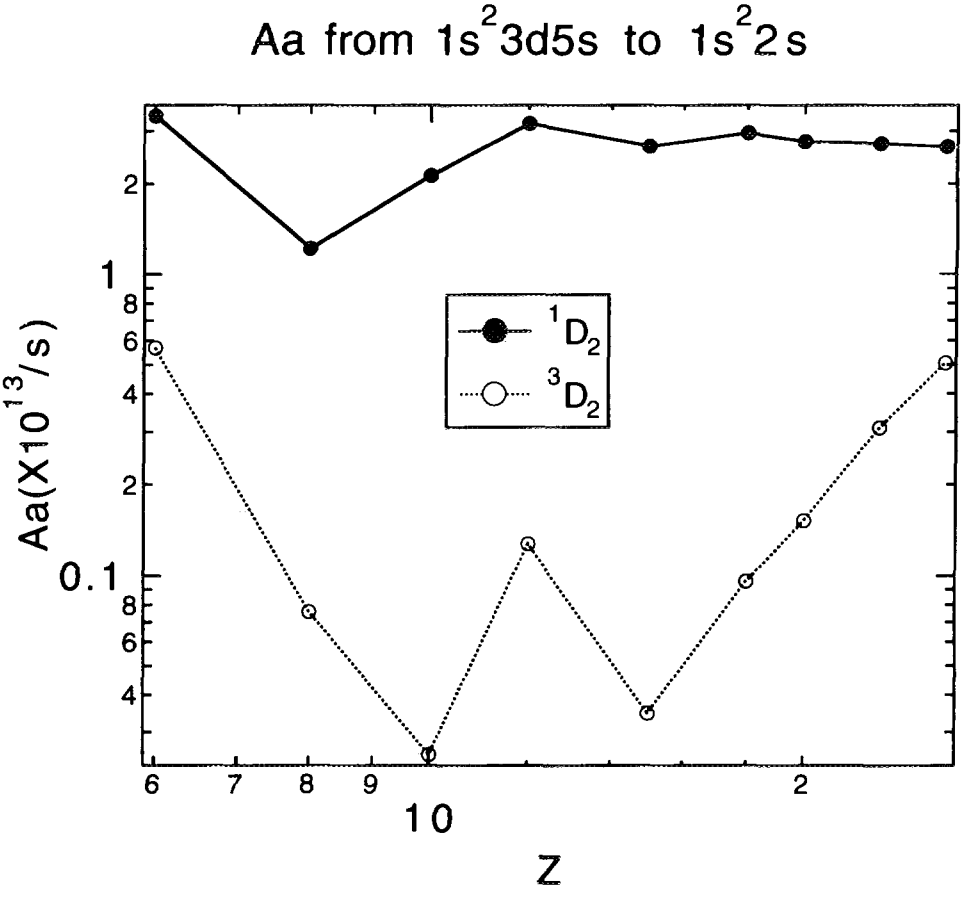

Fig.3-2-4(a)

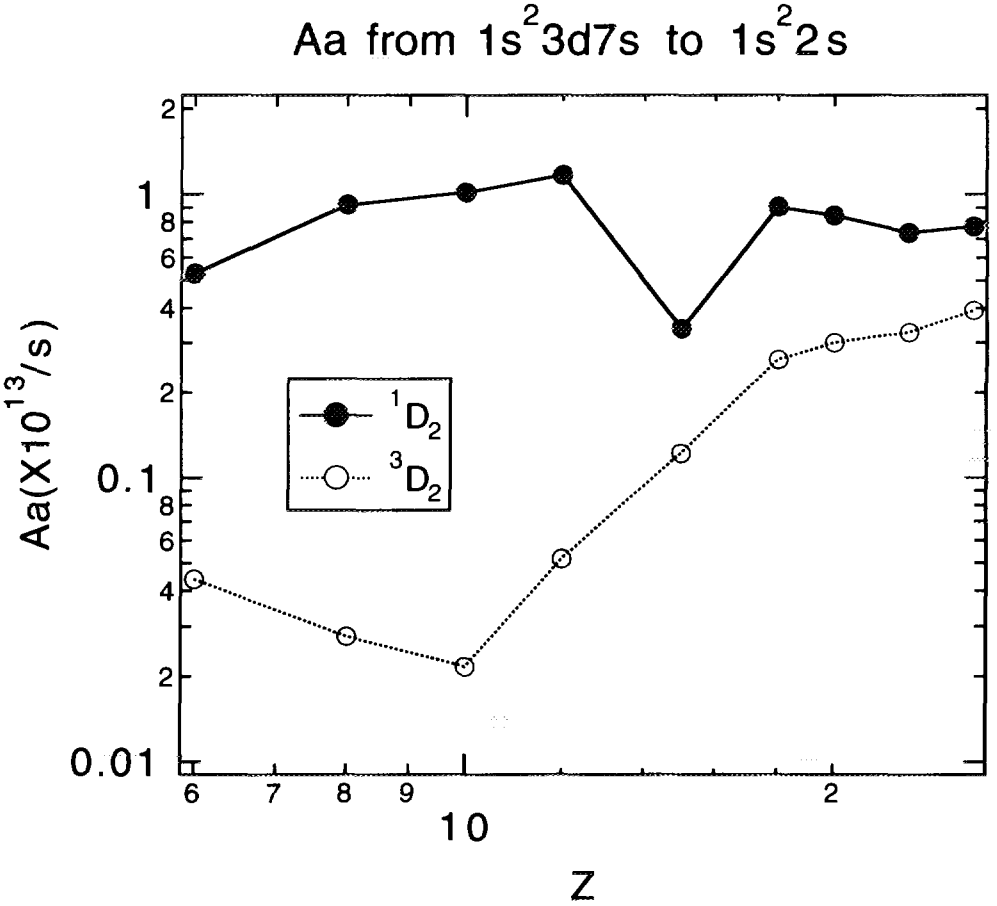

Fig.3-2-4(b)

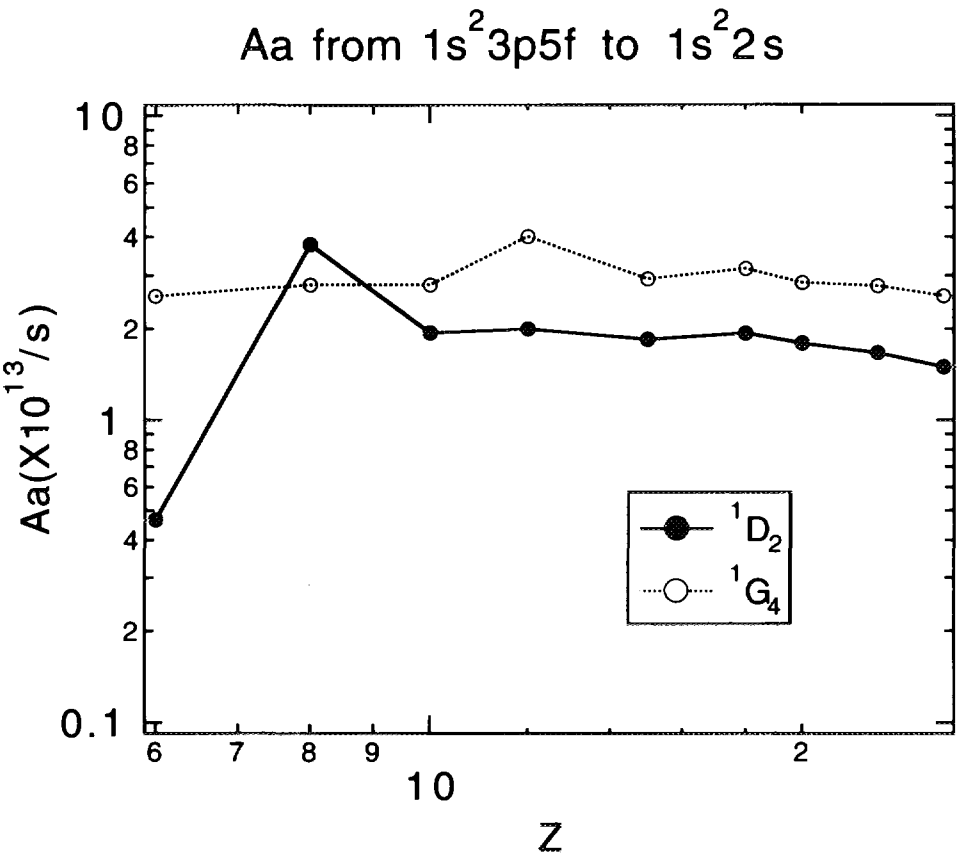

Fig.3-2-3(g)

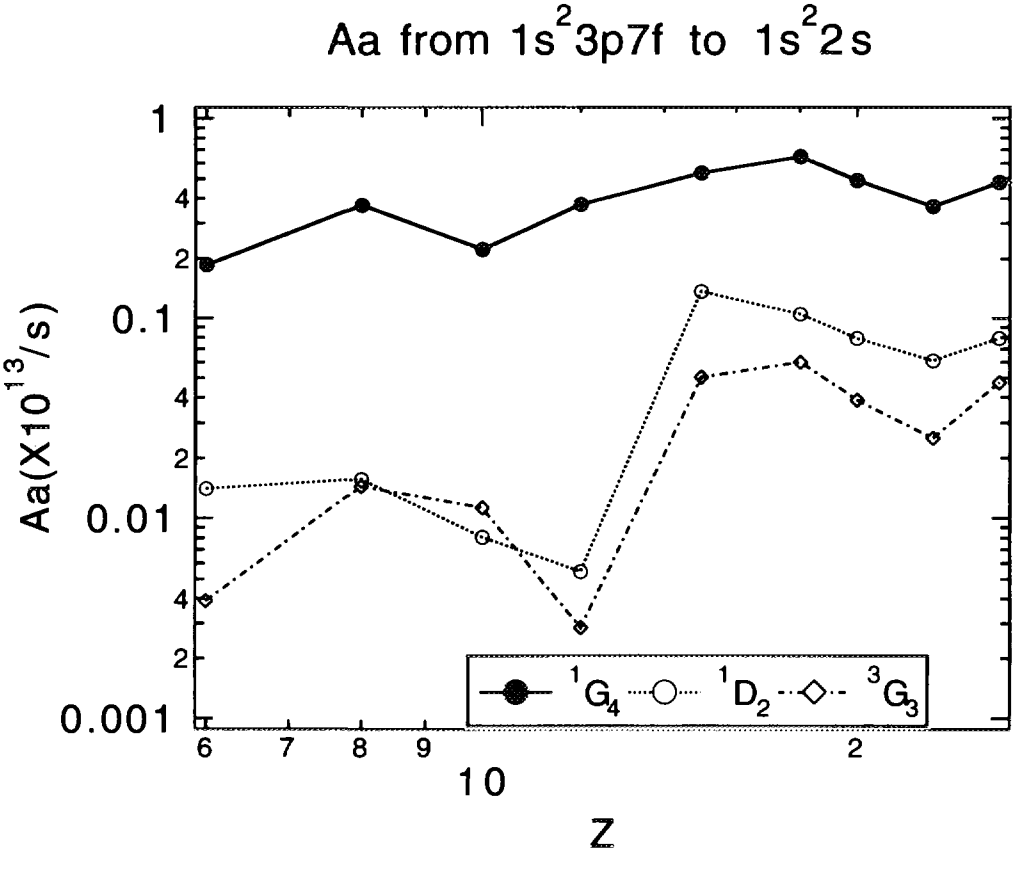

Fig.3-2-3(h)

Publication List of NIFS-DATA Series

NIFS-DATA-1 Y. Yamamura, T. Takiguchi and H. Tawara,
Data Compilation of Angular Distributions of Sputtered Atoms;
Jan. 1990

NIFS-DATA-2 T. Kato, J. Lang and K. E. Berrington,
Intensity Ratios of Emission Lines from OV Ions for Temperature and Density Diagnostics ; Mar. 1990 [At Data and Nucl Data Tables 44(1990)133]

NIFS-DATA-3 T. Kaneko,
Partial Electronic Straggling Cross Sections of Atoms for Protons;
Mar. 1990

NIFS-DATA-4 T. Fujimoto, K. Sawada and K. Takahata,
Cross Section for Production of Excited Hydrogen Atoms Following Dissociative Excitation of Molecular Hydrogen by Electron Impact ; Mar. 1990

NIFS-DATA-5 H. Tawara,
Some Electron Detachment Data for H^- Ions in Collisions with Electrons, Ions, Atoms and Molecules –an Alternative Approach to High Energy Neutral Beam Production for Plasma Heating– ;
Apr. 1990

NIFS-DATA-6 H. Tawara, Y. Itikawa, H. Nishimura, H. Tanaka and Y. Nakamura,
Collision Data Involving Hydro-Carbon Molecules; July 1990
[Supplement to Nucl. Fusion 2(1992)25]

NIFS-DATA-7 H.Tawara,
Bibliography on Electron Transfer Processes in Ion-Ion/Atom/Molecule Collisions –Updated 1990–; Aug. 1990

NIFS-DATA-8 U.I.Safronova, T.Kato, K.Masai, L.A.Vainshtein and A.S.Shlyapzeva,
Excitation Collision Strengths, Cross Sections and Rate Coefficients for OV, SiXI, FeXXIII, MoXXXIX by Electron Impact ($1s^22s^2$ - $1s^22s2p$-$1s^22p^2$ Transitions) Dec.1990

NIFS-DATA-9 T.Kaneko,
Partial and Total Electronic Stopping Cross Sections of Atoms and Solids for Protons; Dec. 1990

NIFS-DATA-10 K.Shima, N.Kuno, M.Yamanouchi and H.Tawara,
Equilibrium Charge Fraction of Ions of Z=4-92 (0.02-6 MeV/u) and Z=4-20 (Up to 40 MeV/u) Emerging from a Carbon Foil; Jan.1991
[AT.Data and Nucl. Data Tables 51(1992)173]

NIFS-DATA-11 T. Kaneko, T. Nishihara, T. Taguchi, K. Nakagawa, M. Murakami,

M. Hosono, S. Matsushita, K. Hayase, M.Moriya, Y.Matsukuma, K.Miura and Hiro Tawara,
Partial and Total Electronic StoppingCross Sections of Atoms for a Singly Charged Helium Ion: Part 1;Mar. 1991

NIFS-DATA-12 Hiro Tawara,
Total and Partial Cross Sections of Electron Transfer Processes for Be^{q+} *and* B^{q+} *Ions in Collisions with H,* H_2 *and He Gas Targets - Status in 1991-*; June 1991

NIFS-DATA-13 T. Kaneko, M. Nishikori, N. Yamato, T. Fukushima, T. Fujikawa, S. Fujita, K. Miki, Y. Mitsunobu, K. Yasuhara, H. Yoshida and Hiro Tawara,
Partial and Total Electronic Stopping Cross Sections of Atoms for a Singly Charged Helium Ion : Part II; Aug. 1991

NIFS-DATA-14 T. Kato, K. Masai and M. Arnaud,
Comparison of Ionization Rate Coefficients of Ions from Hydrogen through Nickel ; Sep. 1991

NIFS-DATA-15 T. Kato, Y. Itikawa and K. Sakimoto,
Compilation of Excitation Cross Sections for He Atoms by Electron Impact; Mar. 1992

NIFS-DATA-16 T. Fujimoto, F. Koike, K. Sakimoto, R. Okasaka, K. Kawasaki, K. Takiyama, T. Oda and T. Kato,
Atomic Processes Relevant to Polarization Plasma Spectroscopy ; Apr. 1992

NIFS-DATA-17 H. Tawara,
Electron Stripping Cross Sections for Light Impurity Ions in Colliding with Atomic Hydrogens Relevant to Fusion Research; Apr. 1992

NIFS-DATA-18 T. Kato,
Electron Impact Excitation Cross Sections and Effective Collision Strengths of N Atom and N-Like Ions -A Review of Available Data and Recommendations- ; Sep. 1992

NIFS-DATA-19 Hiro Tawara,
Atomic and Molecular Data for H_2O, CO & CO_2 *Relevant to Edge Plasma Impurities*, Oct. 1992

NIFS-DATA-20 Hiro. Tawara,
Bibliography on Electron Transfer Processes in Ion-Ion/Atom/Molecule Collisions -Updated 1993-; Apr. 1993

NIFS-DATA-21 J. Dubau and T. Kato,
Dielectronic Recombination Rate Coefficients to the Excited

States of C I from C II; Aug. 1994

NIFS-DATA-22 T. Kawamura, T. Ono, Y. Yamamura,
Simulation Calculations of Physical Sputtering and Reflection Coefficient of Plasma-Irradiated Carbon Surface; Aug. 1994

NIFS-DATA-23 Y. Yamamura and H. Tawara,
Energy Dependence of Ion-Induced Sputtering Yields from Monoatomic Solids at Normal Incidence; Mar. 1995

NIFS-DATA-24 T. Kato, U. Safronova, A. Shlyaptseva, M. Cornille, J. Dubau,
Comparison of the Satellite Lines of H-like and He-like Spectra; Apr. 1995

NIFS-DATA-25 H. Tawara,
Roles of Atomic and Molecular Processes in Fusion Plasma Researches - from the cradle (plasma production) to the grave (after-burning) -; May 1995

NIFS-DATA-26 N. Toshima and H. Tawara
Excitation, Ionization, and Electron Capture Cross Sections of Atomic Hydrogen in Collisions with Multiply Charged Ions; July 1995

NIFS-DATA-27 V.P. Shevelko, H. Tawara and E.Salzborn,
Multiple-Ionization Cross Sections of Atoms and Positive Ions by Electron Impact; July 1995

NIFS-DATA-28 V.P. Shevelko and H. Tawara,
Cross Sections for Electron-Impact Induced Transitions Between Excited States in He: n, n'=2,3 and 4; Aug. 1995

NIFS-DATA-29 U.I. Safronova, M.S. Safronova and T. Kato,
Cross Sections and Rate Coefficients for Excitation of $\Delta n = 1$ Transitions in Li-like Ions with $6<Z<42$; Sep. 1995

NIFS-DATA-30 T. Nishikawa, T. Kawachi, K. Nishihara and T. Fujimoto,
Recommended Atomic Data for Collisional-Radiative Model of Li-like Ions and Gain Calculation for Li-like Al Ions in the Recombining Plasma; Sep. 1995

NIFS-DATA-31 Y. Yamamura, K. Sakaoka and H. Tawara,
Computer Simulation and Data Compilation of Sputtering Yield by Hydrogen Isotopes ($^1H^+$, $^2D^+$, $^3T^+$) and Helium ($^4He^+$) Ion Impact from Monatomic Solids at Normal Incidence; Oct. 1995

NIFS-DATA-32 T. Kato, U. Safronova and M. Ohira,
Dielectronic Recombination Rate Coefficients to the Excited States of CII from CIII; Feb. 1996

NIFS-DATA-33 K.J. Snowdon and H. Tawara,
Low Energy Molecule-Surface Interaction Processes of Relevance to Next-Generation Fusion Devices; Mar. 1996

NIFS-DATA-34 T. Ono, T. Kawamura, K. Ishii and Y. Yamamura,
Sputtering Yield Formula for B_4C Irradiated with Monoenergetic Ions at Normal Incidence; Apr. 1996

NIFS-DATA-35 I. Murakami, T. Kato and J. Dubau,
UV and X-Ray Spectral Lines of Be-Like Fe Ion for Plasma Diagnostics; Apr. 1996

NIFS-DATA-36 K. Moribayashi and T. Kato,
Dielectronic Recombination of Be-like Fe Ion; Apr. 1996

NIFS-DATA-37 U. Safronova, T. Kato and M. Ohira,
Dielectronic Recombination Rate Coefficients to the Excited States of CIII from CIV; July 1996

NIFS-DATA-38 T. Fujimoto, H. Sahara, G. Csanak and S. Grabbe,
Atomic States and Collisional Relaxation in Plasma Polarization Spectroscopy: Axially Symmetric Case; Oct. 1996

NIFS-DATA-39 H. Tawara (Ed.)
Present Status on Atomic and Molecular Data Relevant to Fusion Plasma Diagnostics and Modeling; Jan. 1997

NIFS-DATA-40 Inga Yu. Tolstikhina,
LS-Averaged 1/Z Method as a Tool of Studying the Interactions of Highly Charged Ions with a Metal Surface; Jan. 1997

NIFS-DATA-41 K. Moribayashi and T. Kato,
Atomic Nuclear Charge Scaling for Dielectronic Recombination to Be-like Ions; Apr. 1997